
**Time-resolved measurements on a single
molecular target
and
Discrete Kink Solitons in Ion traps**

Dissertation der Fakultät für Physik
der
Ludwig-Maximilians-Universität München



vorgelegt von Günther Leschhorn
aus München

München, den 8. Dezember 2011

Erstgutachter: Prof. Dr. Tobias Schätz

Zweitgutachter: Prof. Dr. Ferenc Krausz

Tag der mündlichen Prüfung: 17. Januar 2012

for my family



for Sandy

Contents

Summary	viii
Zusammenfassung	xi
Introduction	4
1 Theoretical elements	5
1.1 Confinement and cooling of charged particles	5
1.1.1 The linear Paul-trap	6
1.1.2 The Quadrupole Mass Filter and the Quadrupole ion-guide	9
1.1.3 Doppler-cooling in a two and three level system	11
1.2 Elements of ultra-fast physics	17
1.2.1 Description and properties of electromagnetic pulses	17
1.2.2 Pulse propagation and third order non-linear effects	19
1.3 Dynamic quantum chemical calculation on $^{24}\text{MgH}^+$	22
2 Experimental setup	25
2.1 Apparatus	25
2.1.1 Mg trap apparatus	25
2.1.2 Ba trap apparatus	31
2.2 Laser systems	33
2.2.1 $^{24}\text{Mg}^+$ Doppler-cooling and photoionization	33
2.2.2 $^{138}\text{Ba}^+$ Doppler-cooling and photoionization	35
2.2.3 Few-cycle NIR/VIS pulses	43
2.2.4 UV-pulse pair generation and connection to the trap	46

2.3	Electro-Spray Ionization source	53
2.3.1	Apparatus and concept	53
2.3.2	Characterization	58
3	Time-resolved spectroscopy on single molecular $^{24}\text{MgH}^+$ -ions	64
3.1	Ion trapping and transfer	64
3.1.1	Ion trapping and molecular ion preparation	64
3.1.2	Deterministic ion-transfer protocol	68
3.2	Experimental concepts and procedure	74
3.2.1	A pump-probe experiment on single $^{24}\text{MgH}^+$ -ions	75
3.2.2	Experimental routine	77
3.3	Measurements on the time-resolved dissociation of single molecular ions . .	79
4	Experimental studies towards heavier atomic and molecular ions	85
4.1	Photoionization of neutral Barium	85
4.2	Trapping and laser cooling of $^{138}\text{Ba}^+$ -ions	95
4.3	Sympathetic cooling of molecular ions with $^{138}\text{Ba}^+$	97
5	Discrete Kink Solitons in Ion-traps	100
5.1	Introduction and motivation	100
5.2	Experimental observation of static extended and discrete kinks	103
5.3	Towards a measurement of the dispersion relation of kinks in ion-crystals .	109
6	Conclusion and outlook	114
6.1	Time-resolved measurement on a single molecular target	114
6.2	Discrete kink solitons in ion-traps	117
6.3	Guiding of neutral polar molecules with electric fields in the radio-frequency regime	119
A	Publications	120
A.1	Deterministic delivery of externally cold and precisely positioned single molecular ions. <i>Submitted to Appl. Phys. B, ArXiv:1110.4254</i>	120
A.2	Controlled delivery of single molecules into ultra-short laser pulses: A molecular conveyor belt. <i>Accepted for publication in Nature Physics</i>	132

A.3 Efficient photoionization for barium ion trapping using a dipole-allowed resonant two-photon transition. *Submitted to Appl. Phys. B, ArXiv:1110.4040* 139

Bibliography

152

Summary

In this thesis, two experiments are presented that are both based on trapped ions, laser-cooled into Coulomb-crystalline structures, but contribute to two, nearly independent fields of research. On the one hand, a pump-probe experiment on trapped and sympathetically cooled molecular ions contributes to the field of single molecule imaging. On the other hand, the observation of topological defects in Coulomb-crystals opens new possibilities in exploring defect nucleation with applications in classical and quantum physics. In addition, this experiment contributes to improvements in quantum information processing, for example in experimental quantum simulations with trapped ions.

The first experiment is performed within a collaboration of members of the Munich-Center of Advanced Photonics (MAP) cluster of excellence and is motivated by envisioned applications in structural imaging of matter, ultimately single molecules, on the atomic scale using ultra-short X-ray free-electron laser pulses. To image a single molecule, the pulse has to contain on the order of 10^{13} X-ray photons, has to have a duration of a few femtoseconds ($1 \text{ fs} = 10^{-15} \text{ s}$) or below and must be focused to a spot size of approximately $(100 \text{ nm})^2$. This part of the thesis, covers a proof-of-method experiment that demonstrates the feasibility of combining the fields of ultra-short and intense laser pulses, providing excellent time-control of electromagnetic fields, with the field of trapping and laser-cooling of charged particles, providing unique spatial control capabilities limited only by the laws of quantum mechanics. For this purpose a trap apparatus and a laser system optimized for the simultaneously trapping and cooling of atomic and molecular ions was planned, designed and built. This apparatus provides trapped magnesium or barium ions that are directly laser-cooled and act as cooling agents for the sympathetic cooling of a reservoir of nearly generic molecular ions in ultra-high vacuum. A test on the feasibility of the proposed scheme for the envisioned applications with X-ray pulses requires a molecular ion providing internal dynamics on the timescale of a few femtoseconds. The diatomic molecular ion magnesium hydrid ($^{24}\text{MgH}^+$), featuring correspondingly fast vibrational dynamics, is sympathetically cooled in the trap apparatus by atomic $^{24}\text{Mg}^+$ -ions and deterministically transferred to an ultra-high vacuum chamber. A femtosecond pump-probe spectroscopy scheme, based on single reaction events, with 5 fs ultraviolet (UV) pulses on the fast internal dynamics of this molecular ion is applied. Inspired by a proposed experiment on $^{24}\text{MgH}^+$ using picosecond pulses, an extension to explore the fast (fs) vibrational dynamics of this molecular ion using UV-pulses in the few-cycle regime has been developed. The laser system for the ultra-short UV-pulses is an extension of an evacuated beamline based on the third gas-harmonic of few-cycle laser pulses in the visible and near-infrared region. The optimization and extension of this laser system and the link

to the ion trap apparatus was also designed and built in the framework of this thesis. The experiment reveals the observation of the 30 fs internal vibration with a resolution of 4-5 fs of individual magnesium hydrid ions in nearly background free environment. In addition, due to the isolated preparation of the molecular ion in ultra-high vacuum, strong evidence for long coherence times was found and a unconcealed measurement even near zero pump-probe delay was possible (absence of a coherence spike). Fundamental steps towards an extension of the presented scheme to biologically relevant molecular ions have been implemented already. To allow for a suitable preparation of nearly generic molecular ions out of solution, an Electrospray-Ionization (ESI) source for ionization of molecules via protonation and an appendant filtering setup that selects the required charge-to-mass ratio of the molecular ions via a mass filter has been built up. This source is characterized and tested fully functional within this thesis. To provide sufficient cooling atoms at the repetition rate of the X-ray source (~ 100 Hz), a novel photoionization scheme for barium atoms has been developed and implemented, exceeding the loading efficiency of established schemes by two orders of magnitude. With their almost six-times larger mass compared to magnesium ions, barium ions are better suited to sympathetically cool larger molecular ions. The successful trapping of barium ions, as well as the embedding of molecular ions into the structure of barium crystals, is presented.

The second part of this thesis focuses on the physics of the crystalline structures of confined, laser-cooled ions itself. Crystalline structures of Coulomb-crystals in a Paul-trap have been first observed in 1987 by the groups of Walther and Wineland. Their properties, such as the accompanying phase transition between structures of different dimensionality, have been investigated in detail experimentally and in theory, for example transitions between a linear chain and a zig-zag configuration. These structures are in the center of numerous applications such as quantum information processing or the experiment described above. Recently, in 2010, it was predicted that a fast, non-adiabatic change of the order parameter (displacement of the ions from the trap axis) could lead to topological defects within the crystalline structure. These defects, reveal a solitonic behavior and separate two domains of undisturbed crystalline parts within the crystal. The first-time, experimental observation of topological defects, also called kinks, in ion traps is presented. One of the ion-traps, built in the framework of the time-resolved pump-probe experiment on molecular ions, has been successfully modified to allow for an observation of all predicted types of kink structures with crystals of laser-cooled $^{24}\text{Mg}^+$ -ions. The so-called extended kink where an ensemble of ions within the crystal contributes to the defect structure, as well as the localized kink where only the core ion and its direct neighbors contribute significantly are experimentally observed. In a cooperation with the University of Tel-Aviv, the topological defects are compared to the predictions made by theory for the experimentally used parameters. Finally, attempts to extend the lifetime of the kink structures in the current apparatus are performed and their impact is discussed. In addition to single kinks with a specific topological charge in one ion-crystal, the simultaneous creation of two kinks is experimentally demonstrated which might allow a deeper insight into dynamics, collisions or annihilation of kinks in the future. An investigation of the properties of structural defects in ion-traps is already interesting by itself, because topological defects are a perseverative phenomena in nature, spanning from particle creation within the inflationary expansion of the early universe to solid-state physics. The topo-

logical defects in the ion-trap system can be seen as an experimental simulation tool with unprecedented control for investigations on solitons and their quantum behavior and they are predicted to allow for new approaches as a carrier for quantum information in the field of quantum information processing. In addition, theories covering the nucleation of defects during an inhomogeneous phase transition of second order (inhomogeneous Kibble-Zurek mechanism) that lack experimental verification up to date can be tested experimentally for the first time.

Zusammenfassung

In der vorliegenden Arbeit werden zwei Experimente vorgestellt und diskutiert, die beide auf kristalline Strukturen, sogenannten Coulomb-Kristallen, aus Laser-gekühlten und gefangenen Ionen basieren. Trotz der Ähnlichkeit der untersuchten Objekte, tragen die beiden Experimente zu sehr unterschiedlichen Forschungsfeldern bei. Das eine Experiment untersucht einzelne, gefangene und sympathetisch gekühlte molekulare Ionen mit Hilfe eines Pump-Abfrage Schemas und trägt damit zu dem Forschungsgebiet der Strukturbestimmung einzelner Moleküle bei. Das andere Experiment beschäftigt sich mit sogenannten topologischen Defekten in Coulomb-Kristallen. Diese Defekte haben Anwendungen in der klassischen-, sowie in der Quanten-Physik. Sie tragen insbesondere zu den Forschungen der Quanten-Informationsverarbeitung und der Simulation von Quantensystemen in Ionenfallen bei.

Das erste Experiment wurde im Rahmen des Exzellenz-Clusters "Munich-Center for Advanced Photonics (MAP)" der Deutschen Forschungsgemeinschaft entwickelt und durchgeführt. Als Motivation dienen erwogene Strukturuntersuchungen mit atomarer Auflösung an einzelnen Molekülen mit Hilfe der sogenannten vierten Generation von ultra-kurzen Laserpulsen im Röntgen-Bereich, erzeugt durch Röntgen-Freie-Elektronen Laser. Die vorgeschlagene Technik benötigt Pulse mit einer Dauer von wenigen Femtosekunden ($1 \text{ fs} = 10^{-15} \text{ s}$) und etwa 10^{13} Röntgenphotonen pro Puls. Außerdem müssen diese Pulse auf eine Fläche in der Größenordnung von etwa $(100 \text{ nm})^2$ fokussiert werden. Das durchgeführte Experiment in diesem Teil der Arbeit versteht sich als Machbarkeitsstudie, die zwei fruchtbare Forschungsfelder der Physik zusammenführt. Auf der einen Seite die Forschung an ultra-kurzen und intensiven Laserpulsen, die eine unübertroffene Präzision in der Kontrolle elektromagnetischer Felder bietet und auf der anderen Seite das Gebiet der gefangenen und Laser-gekühlten Ionen in Radio-Frequenz Fallen, das in Präzision und Lokalisierung lediglich durch die Gesetze der Quantenmechanik limitiert ist. Für die Ausführung des Experimentes wurde ein Apparat geplant, entwickelt und gebaut, der das gleichzeitige Speichern und Kühlen von atomaren und molekularen Ionen erlaubt. Mit diesem Experiment ist es möglich ein Reservoir von fast beliebigen und kalten molekularen Ionen freischwebend im ultra-Hochvakuum zu Verfügung zu stellen. Gefangene und direkt Laser-gekühlte Magnesium oder Barium Ionen dienen als Kältebad für das über die Coulomb-Wechselwirkung übertragene sympathetische Kühlen der molekularen Ionen. Für den Machbarkeitstest der angedachten Röntgen-Streuung mit bereits zu Verfügung stehenden Pulsen im ultravioletten Spektralbereich, ist ein leichtes molekulares Ion mit schneller interner Dynamik erforderlich. Das zweiatomige Molekül-Ion Magnesium-Hydrid ($^{24}\text{MgH}^+$), das eine Vibrations Dynamik auf der Zeitskala von wenigen Femtosekunden besitzt, wurde im Ex-

periment sympathetisch von atomaren Magnesium-Ionen gekühlt und deterministisch in eine ultra-Hochvakuums Umgebung des Apparates transferiert. Die schnelle interne Dynamik des einzelnen molekularen Ions wurde mit Hilfe eines Pump-Abfrage Experimentes mit 5 fs langen Pulsen im ultra-violetten (UV) Spektralbereich aufgelöst. Dieses Experiment versteht sich als Erweiterung von vorgeschlagenen Experimenten an $^{24}\text{MgH}^+$ mit pico-Sekunden Laserpulsen. Das Lasersystem für die ultra-kurzen UV-Pulse ist eine Erweiterung eines Systems, das auf der Produktion von Gas-Harmonischen von Pulsen basiert, die nur wenige Oszillations-Zyklen lang sind und die spektral vom Sichtbaren bis ins Nah-Infrarote reichen. Im Rahmen dieser Arbeit wurde die Erweiterung und der Anschluss dieses Systems an den Fallenapparat entwickelt und gebaut. Das durchgeführte Experiment bildet die 30 fs lange Vibrationsperiode im ersten angeregten Zustand von einzelnen, störungsfrei gespeicherten $^{24}\text{MgH}^+$ -Ionen mit einer Auflösung von 4-5 fs ab. Zudem wurde gezeigt, dass das Experiment aufgrund der Isolation von einzelnen Ionen lange Kohärenz-Zeiten und sogar eine Messung nahe verschwindender Verzögerung zwischen Pump und Abfrage-Puls zulässt. Letzteres ist in Lösung normalerweise nicht oder nur sehr eingeschränkt möglich, da zum Beispiel ein sogenannter Kohärenz-Artefakt die Umgebung durch den überlappenden Pump und Abfrage-Puls polarisiert und die Messung beeinträchtigt. Die wichtigsten Schritte in Richtung einer Erweiterung des demonstrierten Schemas zu biologisch relevanten molekularen Ionen wurden in dieser Arbeit bereits durchgeführt. Es wurde eine sogenannte Electrospray Ionizations Quelle aufgebaut, die es ermöglicht nahezu beliebige Moleküle, die ursprünglich in Lösung vorliegen, zu protonieren und damit einen Fluss einzelner, molekularen Ionen im ultra-Hochvakuum bereitzustellen. Eine angehängte Filter-Stufe, bestehend aus einem Paulschen Massenfilter, der die molekularen Ionen nach Ladungs-zu-Masse Verhältnis selektiert, macht die Quelle zu einem vielseitig einsetzbaren Werkzeug, das in dieser Arbeit aufgebaut und charakterisiert wurde. Ein weiterer wichtiger Schritt wurde mit einem neuartigen und sehr effektivem Photoionizations Schema für Barium Atome erreicht. Um bei den angedachten Experimenten mit Röntgen-Lasern die Wiederholrate von ~ 100 Hz voll auszunutzen, müssen effektiv eine große Anzahl von Barium Ionen für die sympathetische Kühlung von molekularen Ionen bereitgestellt werden. Im Experiment wurde gezeigt, dass das neue Photoionizations-Schema aufgrund seiner Effektivität in der Lage ist die benötigten zwei Größenordnungen mehr Barium Ionen im Vergleich zu etablierten Methoden zu Verfügung zu stellen. Barium Ionen können aufgrund ihrer fast sechs-mal höheren Masse im Vergleich zu Magnesium Ionen viel schwerere molekulare Ionen sympathetisch kühlen. In dieser Arbeit wurden Barium Ionen erfolgreich gefangen und molekulare Ionen in den Kristallverbund von gefangenen Barium Ionen eingebaut.

Das zweite durchgeführte Experiment dieser Arbeit führt Untersuchungen zu den Strukturen von gefangenen und Laser-gekühlten Ionen durch. Coulomb-Kristalle in einer Paul-Falle wurden erstmals 1987 von den Gruppen unter Führung von Walther und Wineland experimentell beobachtet. Die Eigenschaften solcher Kristalle, wie die involvierten Phasenübergänge wurden theoretisch und experimentell im Detail untersucht. Anwendungen finden sich häufig, wie zum Beispiel in der Quanteninformationsverarbeitung oder dem oben beschriebenen Experiment. Erst vor kurzem, Anfang 2010, wurde vorgeschlagen, dass ein schneller diabatischer Wechsel in dem Phasenübergang zugeordnetem Ordnungsparameter zu sogenannten topologischen Defekten in Coulomb-Kristallen führen kann. Diese

Defekte separieren zwei Domänen ungestörter Ordnung im Kristall und besitzen Eigenschaften von Solitonen. Diese Defekt-Solitonen werden auch als Kinks bezeichnet und ihre Erzeugung in einer linearen Paul-Falle ist im Rahmen dieser Arbeit erstmalig gelungen. Alle theoretisch vorhergesagten Typen von Kinks konnten in derselben Falle erzeugt werden, in der auch die zeit-aufgelösten Experimente an einzelnen Molekülonen durchgeführt wurden. In dieser Falle, mit leicht modifizierten Parametern, wurden die Defekte in Lasergekühlten Coulomb-Kristallen aus $^{24}\text{Mg}^+$ -Ionen nachgewiesen. Nicht nur der sogenannte "extended kink", bei dem mehrere Ionen im Ensemble der Struktur des Defektes zugeordnet sind, sondern auch der "localized kink", bei dem nur das zentrale Ion und seine direkten Nachbarn signifikant beitragen, konnten erzeugt werden. Im Rahmen einer Kooperation mit der Universität von Tel-Aviv, vergleicht diese Arbeit die experimentellen Ergebnisse mit den Vorhersagen der Theorie. Im Anschluss werden die ersten Versuche beschrieben und bewertet, die strukturelle Lebensdauer der Kinks in der derzeitigen Falle zu verlängern. Nicht nur einzelne Defekte wurden im Kristall erzeugt, sondern auch die gleichzeitige Erzeugung mehrerer Kinks mit unterschiedlichen topologischen Vorzeichen (Kinks und Anti-Kinks) wurden demonstriert. Dies gibt die Möglichkeit tiefere Einblicke in die Dynamik oder auch die Kollision oder Annihilation von topologischen Defekten in Ionenfallen zu untersuchen. Eine eingehende Untersuchung von strukturellen Defekt-Solitonen in Ionenfallen ist allgemein interessant, da diese in vielen physikalischen Phänomenen in der Natur eine entscheidende Rolle spielen. Dies reicht von der Erzeugung von Teilchen im inflationär expandierenden, frühen Universum bis hin zur modernen Festkörperphysik. Das sich eröffnende Gebiet der topologischen Defekte in Ionenfallen kann als Simulator mit unerreichter Präzision für Effekte mit Solitonen, deren Quantenverhalten oder auch als neuer Ansatz in der Quanteninformationsverarbeitung verstanden werden. Zudem erlaubt es erstmals, Theorien über die Erzeugung von Defekten während eines inhomogenen Phasenübergangs zweiter Ordnung (der sogenannte inhomogene Kibble-Zurek Mechanismus) zu testen.

Introduction

Introduction to time-resolved measurements on a single molecular target X-ray crystallography is the most widely used experimental technique in the science of determination of molecular conformations [1]. A major part of the knowledge obtained so far in the field of structural determination of macromolecules, such as protein and nucleic acids, is due to this technique. Further information can be obtained in combination with neutron and electron crystallography [2], sometimes used for refinement purposes only. The structural determination of ensembles of molecules is possible with X-ray beams from synchrotrons [3]. This technique strongly relies on the enhancement of the signal by Bragg diffraction and thus on the possibility to crystallize the probe [4, 5]. However, many molecules, such as proteins, do not occur naturally as crystals [2, 6]. Typically, the crystallization is achieved with methods like vapor diffusion [7, 8]. For rather simple molecules or for the determination of the coarse structure of a more involved molecule, X-ray diffraction from powders or fibers might be sufficient [9, 10]. It is important to note that many biological molecules, such as most of the membrane proteins, are difficult or impossible to crystallize [2]. The prerequisite of crystallization can thus be interpreted as the major shortfall of standard X-ray diffraction crystallography [4].

The proposed scheme that might allow to record sufficient information out of the diffraction pattern of single, isolated molecules changes the situation completely [6, 11, 12]. The detection of diffracted X-rays does not feature the discrete interference pattern of crystals but is of continuous nature. It allows to fully reveal the structure of the target by appropriate methods [4, 13]. The technique of oversampling even allows for the compensation of the lost phase information of the X-rays. However, the intensity provided by the X-ray pulses from synchrotrons is far too low and the pulse duration by orders of magnitude too long to allow for the implementation of the proposal. An intense X-ray pulse with a duration on the order of a few femtoseconds (10^{-15} seconds) is required to outrun radiation damage. Currently, long exposures of synchrotron radiation would be necessary to accumulate a sufficient number of scattering events. During this exposure, the X-rays alter the nuclear skeleton or even lead to the Coulomb explosion of the sample molecule. In addition, resolving fast dynamics by time-resolved pump-probe experiments to analyze short-lived intermediates is excluded.

Very intense X-ray pulses [14] that last only a few femtoseconds, contain on the order of 10^{13} photons per pulse and are focused to approximately $(100\text{ nm})^2$ (the size of a large molecule). They are predicted to overcome the shortfall and limitations of conventional sources [15, 16, 17, 18, 19]. The duration of the pulses is sufficiently short that the "fatal

overdose” can be applied such that the recording of the diffraction pattern occurs before the single sample molecule is degraded or destroyed. In addition, the mentioned time-resolved experiments get into reach. To image a single molecule with this technique, conceptional different X-ray sources like the new generation of accelerator based X-ray free-electron lasers (X-FEL) are required. Examples are the hard X-ray free-electron laser, Linac-Coherent-Light-Source (LCLS) in Stanford and the European X-FEL in Hamburg, the latter still under construction. The pulses of wavelengths in the Å-regime, required to resolve structures on the atomic scale, have been already focused to a micrometer spot size with tens of Hertz repetition rate to reach towards the required photon flux [18, 16, 17]. The improvement to a 100 nm spot size is already work in progress [20]. In addition, tremendous progress has been made in the attempt of the Munich-Center of Advanced Photonics (MAP) to substitute the accelerator based free-electron lasers (like LCLS) with small-scale, table-top setups that accelerate electrons to relativistic energies by laser wake-field acceleration [21].

However, the scheme described above assumes a deterministically prepared target molecule, well separated from the environment that can be positioned reliably within each single pulse and is replaceable at the repetition rate of the laser source. Conventional target preparation schemes, for example by Electro-spray ionization [22, 23], suffer from randomly released molecules, a dilution by free expansion and mutual Coulomb repulsion, in the case of molecular ions. Indeed, exploring the target as an isolated ion might even help to understand fundamental processes since many molecules occur charged in nature [24, 25]. The probability to hit a molecule provided by the currently best sources, that is in a sprayed sample, with the discussed laser parameters is very low (below 10^{-5}). Thus, established sources for the target defy the desired level of control and a sufficiently precise preparation of the target is a challenge for the envisioned experiments [4].

In contrast, confined charged particles in an linear ion-trap provide unique control capabilities reaching the quantum limits [26, 27, 28]. Ions can be laser-cooled to the quantum mechanical ground state of motion in the confining potential and thus can be positioned with sub-10 nm precision. In addition, it has been demonstrated that a transfer between separate traps at rates of kilohertz is possible by changing the related electric fields [28], responsible for the axial confinement in the trap. Although, a direct laser-cooling of molecular ions is difficult due to their rich ro-vibrational states and the related lack of a closed cycling transition, it has been shown that sympathetic cooling is sufficiently efficient. Using the Coulomb interaction as a mediator to a directly laser-cooled heat sink of atomic ions again allows to reach the motional ground state [29, 30]. In addition, the absolute position of such a sympathetically cooled molecular ion embedded in a so called heterogeneous Coulomb-crystal can be measured by detecting the fluorescence light of the neighboring atomic cooling agents on their lattice sites with an accuracy down to half of its wavelength (UV-regime in the case of this thesis). Thus, the ion trap technology is capable of providing externally cold single molecular ions, well isolated from the environment, deterministically delivered into the spot size of the X-FEL beam of approximately 100 nm and replaceable with the repetition rate of the laser source [31]. Moreover this scheme is not severely limited in its scalability to biologically relevant molecules. Protonated proteins with a mass of approximately 10^4 amu and a charge state $Z = 12$ have already been shown to be sympathetically cooled in an ion-trap [32] and a further extension in the

charge-to-mass range is proposed [31]. In addition to the control schemes and the cooling of the external degrees of freedom, ion traps provide the possibility to implement sophisticated cooling schemes for the internal degrees of freedom of a molecular ion. Buffer gas [33], as well as optical cooling schemes [34, 35] have been shown to be applicable.

The experiment presented in this thesis bridges the gap between the two fields of research, ultra-short pulses and the manipulation of single particles in ion-traps. By performing a time-resolved pump-probe experiment with ultra-short, ultraviolet laser pulses on single, sympathetically cooled molecular ions, it demonstrates a method relying on the combination of these two fields. Moreover, the experiment reveals that providing single molecules into each pulse of a X-FEL beamline is possible since the used, ultra-short optical pulses in the ultraviolet spectral region request nearly identical requirements. In addition, this experiment already presents the first time-resolved measurement of this kind.

Introduction to discrete kink solitons in ion traps The first crystalline structures in a Paul-trap have been reported in 1987 by the publications of Walther and Wineland [36, 37]. When several ions, confined in a common trapping potential, are sufficiently cooled by lasers, they undergo a second order phase transition and form a crystalline structure, often called Coulomb or Wigner crystals. In contrast to crystals in solid state physics, the mutual distance between ions, the lattice parameter of this quasi-crystal, is on the order of $10\ \mu\text{m}$. For more than 20 years the structure of cold ions in Paul-traps has been studied intensively, both experimentally [38] and theoretically [39]. Different sizes, shapes and aspect ratios have been explored. For linear Paul-traps, it was commonly accepted that the minimal energy configurations in the trapping potential, ranging from linear strings and two-dimensional zig-zag to helical and multiple shell structures were the crystalline structures that can be observed [40, 41]. Very recently, it was proposed to observe topologically protected localized distortions of the "normal" two-dimensional zig-zag structure in an ion trap, already with a moderate number of ions ($N\sim 20$) [42, 43]. The proposal claims that these metastable distortions would not be destroyed by thermal fluctuations at up to 15 times the Doppler limit temperature of the ions and could be realized with already existing traps and cooling techniques. Defining a soliton as a localized, non-perturbative solutions of a non-linear system that is topologically protected, the defects in an ion crystal, also referred to as kinks, indeed reveal a solitonic behavior [42]. Solitons are often found in classical systems and have been studied intensively in the literature. The first-time experimental creation and observation of those kink solitons in an ion trap is presented in this thesis.

Apart from the classical aspect, quantum mechanical properties and quantum dynamics of solitons can be studied in this system. The internal modes can be canonically quantized. The results are quantum internal oscillation modes about the classical kink configuration [42]. This gives the possibility to study quantum mechanical effects with solitons in an ion trap, a system providing unique control. Furthermore, it is proposed to use this internal modes as a carrier for quantum information [42]. Schemes for quantum information processing (QIP) that rely on the coherent manipulation of motional modes normally reveal a conflicting requirement on the trap frequency when scaling the number of particles in the trap. The theoretically predicted separation in energy of the modes of the kink in

the linearized normal mode spectrum from the rest of the vibrational band makes the topological defects suited for QIP-schemes because this energy gap does not scale with the number of ions in the trap.

Another application of the kink solitons in ion traps relies on the type of phase transition from a linear chain of ions to a zig-zag configuration. It has been shown that this structural change is a phase transition of second order and that the assigned order parameter is the displacement of the ions in the crystal from the trap axis [38]. The famous Kibble-Zurek mechanism (KZM) [44, 45] applies to infinite systems with a phase transition of second order that is described by Landau theory. It is expected to account for the formation of cosmic strings in the early universe. The great advantage of laboratory scale systems that mimic this process is most intriguing [46]. Several of those small-size systems have been studied that rely on the homogeneous KZM [47, 48, 49, 50]. In the case of a linear ion-trap, the inter-ion distances are inhomogeneous. Thus the phase transition becomes inhomogeneous because the critical point is first crossed in the center of the trap and the front of the mechanical instability moves from the center to the edges. Kink solitons in ion traps therefore provide a test setup with unprecedented control for the inhomogeneous extension of the Kibble-Zurek mechanism that lacks experimental verification up to date [43, 51].

Chapter 1

Theoretical elements

This chapter provides the basic theoretical framework needed for the description of various experimental building blocks of this thesis. The first section discusses the theory of trapped charged particles including the linear Paul-trap, the quadrupole mass filter and the quadrupole ion guide. Additionally, the relevant methods of laser Doppler cooling of effective two- and three-level atomic ions as well as the technique of sympathetic cooling are briefly addressed. The second section deals with the physics of ultra-short laser pulses and especially discusses the concept of gas-harmonic generation. The last part gives an introduction to the theoretical concept and the theoretical description of a time-resolved pump-probe experiment on $^{24}\text{MgH}^+$, presented in chapter 3.

1.1 Confinement and cooling of charged particles

Various different concepts of traps for atoms or ions have been developed and are widely used in modern physics. Two main trapping principals exist for ions. The Penning-trap uses a superposition of static magnetic and electric fields [52], whereas the trapping potential of a Paul-trap is generated by time-varying and static electric fields [53, 54]. In the purely electrostatic case, Laplace's equation ($\Delta\phi = 0$) forces the trapping potential to take its extreme values inside an electrode, but never outside. This fundamental physical limitation leads to the mentioned trap designs, that either use additional magnetic or time-varying electric fields to form a field minimum in free space. The time-varying potential ϕ corresponding to a confining force that is directly proportional to the distance to the trap center ($\vec{F}(\vec{r}) \sim -|\vec{r}|$) is given by:

$$\phi(x, y, z, t) = \phi_0(t) \cdot (\alpha x^2 + \beta y^2 + \gamma z^2)$$

To satisfy Laplace's equation, the coefficients have to sum up to zero. The first possibility ($\alpha = \beta, \gamma = -2\alpha$) forms the time-varying potential of a three-dimensional Paul-trap. In this case, only a single ion can be trapped without micro-motion (refer to section 1.1.1). If, like in this thesis, a micro-motion free trapping of multiple ions is desired, the choice

($\alpha = -\beta, \gamma = 0$) is more convenient. Without additional axial fields, this choice for the coefficients leads to the quadrupole mass filter that will be discussed in 1.1.2. An additional static confining field in z -direction forms the potential of the linear Paul-trap, discussed in section 1.1.1.

1.1.1 The linear Paul-trap

The three-dimensional potential of the linear Paul-trap, used in this thesis can be written as

$$\phi(\vec{r}, t) = \phi_0(t) \frac{x^2 - y^2}{2r_0^2} + \frac{1}{2} \xi U_z z^2 - \frac{1}{2} \xi U_z (x^2 + y^2) \quad (1.1)$$

,where r_0 is the distance from the center of the trap to the surface of the electrodes that are arranged in a configuration producing this quadrupole potential. The time-dependent part of the potential is given by

$$\phi_0(t) = U_{\text{DC}} - U_{\text{RF}} \cdot \cos \Omega t \quad (1.2)$$

where U_{RF} is the alternating current of frequency Ω applied to the quadrupole electrodes superimposed by the direct current voltage U_{DC} . In the z -direction the potential is static and formed by a DC-voltage U_z applied to a pair of ring-electrodes. The expansion of the potential ϕ_z in this direction up to the second order, leads to the harmonic potential

$$\psi_z(z) = \frac{1}{2} \xi U_z z^2$$

and the expansion coefficient ξ is given by $\xi = \frac{d^2}{dz^2} \left(\frac{\phi_z(z)}{U_z} \right) |_{z=0}$. The potential of the linear Paul-trap of equation 1.1 satisfies Laplace's equation $\Delta\phi = 0$ at all times.

The equations of motion

$$\frac{d^2 u_i}{dt^2} = \frac{-Z |e|}{m} \frac{\partial \Phi}{\partial u_i} \quad i = x, y, z$$

for a particle carrying a charge $Z |e|$ and mass m in the potential ϕ are given by

$$\begin{aligned} m \frac{d^2 x}{dt^2} + Z |e| \left(\frac{\phi_0(t)}{r_0^2} - \xi U_z \right) x &= 0 \\ m \frac{d^2 y}{dt^2} - Z |e| \left(\frac{\phi_0(t)}{r_0^2} + \xi U_z \right) y &= 0 \\ m \frac{d^2 z}{dt^2} + Z |e| \xi U_z z &= 0 \end{aligned} \quad (1.3)$$

It is convenient to rewrite this decoupled set of equations into Mathieu's differential equation

$$\frac{d^2 u_i}{d\tau^2} + (\tilde{a}_i - 2q_i \cos 2\tau)u_i = 0 \quad i = x, y, z \quad (1.4)$$

with the help of the stability parameters \tilde{a}_i , q_i and the normalized time τ :

$$\begin{aligned} \tilde{a}_x = -\tilde{a}_y &= \frac{4Z |e| U_{\text{DC}}}{m\Omega^2 r_0^2} - \tilde{a}_z \\ \tilde{a}_z &= \frac{4\xi Z |e| U_z}{m\Omega^2} \\ q_x = -q_y &= \frac{2Z |e| U_{\text{RF}}}{m\Omega^2 r_0^2} \\ q_z &= 0 \\ \tau &= \frac{1}{2}\Omega t \end{aligned} \quad (1.5)$$

The series

$$u(\tau) = A \exp(\mu\tau) \sum_{n=-\infty}^{n=+\infty} C_n \exp(2in\tau) + B \exp(-\mu\tau) \sum_{n=-\infty}^{n=+\infty} C_n \exp(-2in\tau) \quad (1.6)$$

is a general solution of Mathieu's equation 1.4. The coefficients A and B are determined only by the initial conditions. The amplitude coefficients C_n and the frequency constants μ are functions of the stability parameters \tilde{a}_i and q_i and are independent of the initial conditions. The choice of the stability parameters can lead to stable or unstable oscillating trajectories. A real component of μ would lead to an exponential increase in the ion's motional amplitudes. Only non-integral μ with $Re(\mu) = 0$ lead to finite amplitude trajectories and hence to stable trapping conditions. A so-called a-q stability diagram, as shown in figure 1.2 is conveniently used to illustrate the stable zones.

For sufficiently small stability parameters a and q ($|\tilde{a}_i| \ll |q_i| \ll 1$) the series in equation 1.6 simplifies to the adiabatic or pseudo-potential approximation and only the terms $|n| = 0, 1$ contribute. Using this approximation, the general solution to the differential equation 1.4 reduces to

$$u_i(t) = u_{\text{max}} \left(1 + \frac{q_i}{2} \cos(\Omega t) \right) \cos(\omega_{\text{sec},i} t) \quad (1.7)$$

The initial conditions $u(t)|_{t=0} = u_{\text{max}}$ and $\left. \frac{du(t)}{dt} \right|_{t=0} = 0$ deduce the coefficients $A = B = u_{\text{max}}/2$ and the amplitude coefficients can be written as $C_1 = C_{-1} = -q_i C_0/4$. The expression for μ_i simplifies to $\mu_i^2 = \tilde{a}_i + q_i^2/2$. The motion of a charged particle in a linear Paul-trap is thus a superposition of a slowly varying oscillation with frequency $\omega_{\text{sec},i} = -i\mu_i\Omega/2$ (secular motion) and a fast oscillation (micro-motion), driven by the RF frequency Ω . The secular motion is harmonic and a time-independent pseudo potential

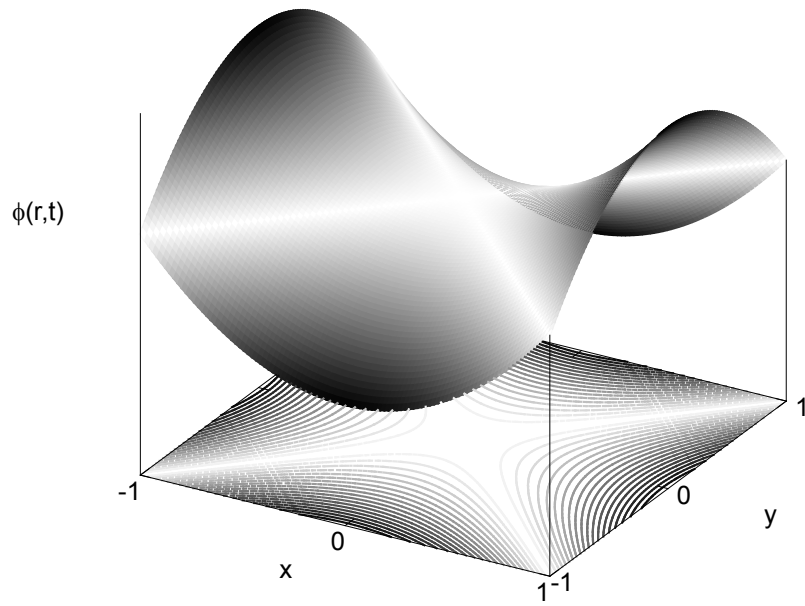


Figure 1.1: The quadrupole potential for a fixed time instant.

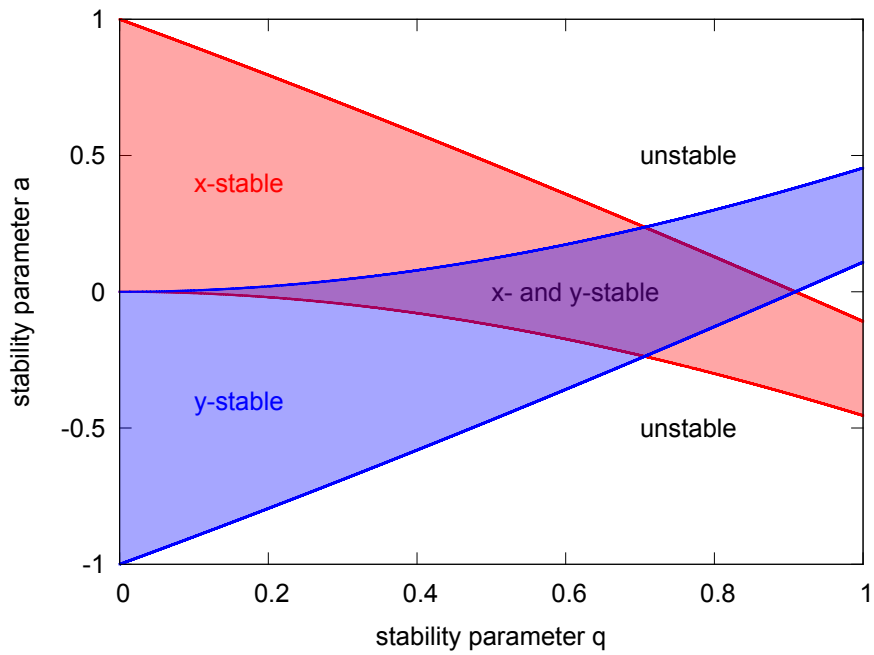


Figure 1.2: The lowest lying part of the stability diagram spanned by the stability parameters a and q . Stable trajectories in both radial directions are realized only in the intersection of the red and blue shaded stable zones in one direction.

$$\phi_{\text{Pseudo}}(\vec{r}) = \frac{m}{2Z|e|}(\omega_{\text{sec},x}^2 x^2 + \omega_{\text{sec},y}^2 y^2 + \omega_z^2 z^2)$$

can be defined.

1.1.2 The Quadrupole Mass Filter and the Quadrupole ion-guide

Using suitable restrictions and simplifications, the theoretical framework of the linear Paul-trap that was developed in the last section, can be applied to the Quadrupole Mass Filter (QMF) and the quadrupole ion-guide.

The quadrupole mass filter is a widely used experimental technique and tool, that confines charged particles in x- and y-direction and transmits only a selectable part of the mass spectrum in z-direction. Omitting the static potential in z-direction ($U_z = 0$), the potential of the linear Paul-trap reduces to the potential of the quadrupole mass filter:

$$\phi(x, y, t) = \phi_0(t) \frac{x^2 - y^2}{2r_0^2}, \quad \phi_0(t) = U_{\text{DC}} - U_{\text{RF}} \cdot \cos \Omega t \quad (1.8)$$

The decoupled set of equations of motion

$$\begin{aligned} m \frac{d^2 x}{dt^2} + \frac{Z|e|}{r_0^2} \phi_0(t) x &= 0 \\ m \frac{d^2 y}{dt^2} - \frac{Z|e|}{r_0^2} \phi_0(t) y &= 0 \\ m \frac{d^2 z}{dt^2} &= 0 \end{aligned} \quad (1.9)$$

can be rewritten in the form of Mathieu's equation

$$\frac{d^2 u_i}{d\tau^2} + (a_i - 2q_i \cos 2\tau) u_i = 0 \quad i = x, y \quad (1.10)$$

using the simplified ($\tilde{a}_z = 0$) stability parameters a_i and q_i and the normalized time τ

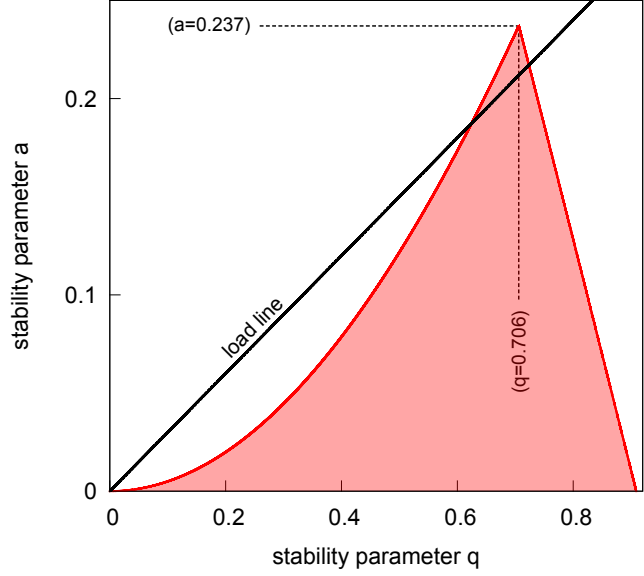
$$a_x = -a_y = a = \frac{4Z|e|U_{\text{DC}}}{m\Omega^2 r_0^2}, \quad q_x = -q_y = q = \frac{2Z|e|U_{\text{RF}}}{m\Omega^2 r_0^2}, \quad \tau = \frac{1}{2}\Omega t \quad (1.11)$$

The solution of 1.10 has been discussed in 1.1.1. The adiabatic approximation in this case leads to radial secular frequencies

$$\omega_{\text{sec},x}^2 = \frac{\Omega^2}{4} \left(\frac{q_x^2}{2} + a_x \right) = \frac{(Z|e|)^2 U_{\text{RF}}^2}{2m^2 r_0^4 \Omega^2} + \frac{Z|e|U_{\text{DC}}}{mr_0^2} \quad (1.12)$$

$$\omega_{\text{sec},y}^2 = \frac{\Omega^2}{4} \left(\frac{q_y^2}{2} + a_y \right) = \frac{(Z|e|)^2 U_{\text{RF}}^2}{2m^2 r_0^4 \Omega^2} - \frac{Z|e|U_{\text{DC}}}{mr_0^2} \quad (1.13)$$

Figure 1.3: Detailed zoom to the stability diagram near the a-q origin. Only pairs of a and q stability parameters that lie in the red bordered zone provide stable trapping conditions in both spacial directions. The fraction of U_{DC} and U_{RF} determines the gradient of the load line. With this selection, ions with (a,q) parameters that lie in the triangle above the load line are transmitted through the quadrupole mass filter.



and when using $\psi_0 = \frac{Z|e|U_{\text{RF}}^2}{4mr_0^2\Omega^2} = \frac{qU_{\text{RF}}}{8}$ the pseudo potential of the quadrupole mass filter can be written as:

$$\psi_{\text{Pseudo}}(x, y) = \psi_0 \frac{x^2 + y^2}{r_0^2} + \frac{U_{\text{DC}}}{2} \frac{x^2 - y^2}{r_0^2} \quad (1.14)$$

For fixed trap parameters r_0 and Ω the values of U_{DC} and U_{RF} can be used select the mass range of particles, that have bound trajectories in the x-y plane. The definition of the stability parameters allows the expression

$$\frac{a}{q} = \frac{2U_{\text{DC}}}{U_{\text{RF}}}$$

As shown in figure 1.3, the selection of U_{DC} and U_{RF} leads to a line through the origin with gradient $2U_{\text{DC}}/U_{\text{RF}}$. Every ion that has a charge-to-mass ration which brings it in the triangle above this load line is stable and thus transmitted through the quadrupole mass filter. In praxis, a suitable detector (e.g a Faraday cup or a secondary-electron multiplier) is used to detect ions that are transmitted by the analyzer. A choice of the pitch of the load line that brings it nearer to the apex ($a=0.23699$, $q=0.706$) of the triangle results in a higher resolution of the quadrupole mass analyzer.

The choice $U_{\text{DC}} = 0$ leads to a maximal transmitting quadrupole mass filter. This operating mode is known as the quadrupole ion-guide and it acts like a high-pass for masses. For $a = 0$, all positive q-parameters smaller than $q_{\text{max}} = 0.908$ lead to stable trajectories in the x-y-plane. For fixed r_0 and Ω , the RF-voltage on the quadrupole electrodes U_{RF} determines the minimal mass still stable. In praxis, this leads to a wide mass range that can be guided in z-direction. The secular frequencies in x-and y-direction are degenerated and the theoretical treatment of the adiabatic approximation is reduced to:

$$\text{secular frequency: } \omega_{\text{sec},x}^2 = \omega_{\text{sec},y}^2 = \omega_{\text{sec}}^2 = \frac{(Z|e|)^2 U_{\text{RF}}^2}{2m^2 r_0^4 \Omega^2} = \frac{(q\Omega)^2}{8} \quad (1.15)$$

$$\text{pseudo potential: } \psi_{\text{pseudo}}^{U_{\text{DC}}=0}(x, y) = \psi_0 \frac{x^2 + y^2}{r_0^2} \quad (1.16)$$

1.1.3 Doppler-cooling in a two and three level system

This section reviews the methods of Doppler laser-cooling [55] of trapped ions for the two and three level atomic ion case. The two experimental relevant examples of $^{24}\text{Mg}^+$ - and $^{138}\text{Ba}^+$ -ions are discussed. The theoretical framework will be developed for the case of a free particle. This treatment is justified when working outside the Lamb-Dicke regime, when the recoil energy of the absorbed photon is higher than the energy of the oscillation in the trap. Quantitatively, the Lamb-Dicke parameter η

$$\eta^2 = \frac{\hbar f_{\text{photon}}}{\hbar \omega_{\text{sec}}} = \frac{p_{\text{photon}}^2}{2m\hbar \omega_{\text{sec}}} = \frac{\hbar \omega_L^2}{2mc^2 \omega_{\text{sec}}} \quad (1.17)$$

has to be larger than one.

Two-level laser Doppler cooling The basic idea of radiation pressure cooling of a free particle is a time averaged non-vanishing energy difference between absorbed and emitted photons. A photon absorbed from a near resonant light field leads to a momentum kick $p_{\text{photon}} = \hbar \vec{k}_L$ in the direction of the laser beam. The Doppler-effect ensures that a red shifted frequency of the photon leads to an absorption of counter-propagating atoms only. Consequently, the particle is decelerated. The spontaneous emission decay of the excited state is isotropic. Averaged over many cycles, the momentum transfer caused by spontaneous emission of photons tends to zero and the radiation pressure force exerted on the atom will act on average only in the direction of the laser beam. The experimentally relevant limits of the lowest achievable temperatures with Doppler cooling schemes are due to the random nature of spontaneous decay of the excited state. Assuming a steady state, the width of the momentum distribution reaches a constant value. The Doppler cooling limit

$$T_{\text{Doppler}} = \frac{\hbar \Gamma}{2k_B}, \quad k_B = \text{Boltzmann constant}$$

is given by the linewidth Γ of the used transition and is near 1 mK for $^{24}\text{Mg}^+$ -ions and 0.4 mK for $^{138}\text{Ba}^+$ -ions.

The Liouville equation describes the time evolution of the density operator

$$\hat{\rho} = \sum_{i,j=1,2} \rho_{ij} |i\rangle \langle j| \quad (1.18)$$

The steady state solution of the resulting set of coupled differential equations known as the optical Bloch equations for the occupation of the excited state (assuming a two level system) is given by

$$\rho_{22} = \frac{\Omega^2}{4} \frac{1}{\Delta^2 + \left(\frac{\Gamma}{2}\right)^2 + \frac{\Omega^2}{2}} = \frac{S}{2} \frac{1}{\frac{4\Delta^2}{\Gamma^2} + S + 1} \quad (1.19)$$

where Δ is the detuning of the laser from the atomic resonance, Ω is the Rabi-frequency and $S = 2(\Omega/\Gamma)^2$ is the so-called saturation parameter defined as

$$S = \frac{I}{I_{sat}}, \quad I_{sat} = \frac{\pi\hbar c\Gamma}{3\lambda^3}$$

The optical force on an atom moving with the velocity \vec{v} is given by the momentum of the absorbed photon ($\hbar k_L$) times the photon scattering rate

$$\vec{F}(\vec{v}) = \hbar k_L \Gamma \rho_{22}(\vec{v}) = \frac{S\hbar k_L \Gamma}{2} \frac{1}{\frac{4(\Delta - k\vec{v})^2}{\Gamma^2} + S + 1}$$

For small \vec{v} the Taylor expansion of $\vec{F}(\vec{v}) = \vec{F}(0) + \vec{F}'(0)\vec{v} + O(\vec{v}^2)$ leads to a friction term

$$\vec{F}'(0) = \frac{4S\hbar k_L^2}{\Gamma} \frac{\Delta}{\left(\frac{4\Delta^2}{\Gamma^2} + S + 1\right)^2} \quad (1.20)$$

that is linear in velocity. The maximum is given by $\Delta = \sqrt{(S+1)\Gamma^2/12}$. An optimal cooling force is thus realized by using a simultaneous red detuning from the atomic resonance frequency of $\Delta \approx 0,37\Gamma$ and a laser intensity of $I = \frac{2}{3}I_{sat}$. The latter is normally used to minimize the effect of power broadening of the effective line width.

Figure 1.4 shows the relevant energy levels $3S_{1/2}$ and $3P_{3/2}$ that are used for the closed cycle cooling transition near 280 nm in singly ionized magnesium. The $3S_{1/2}$ state has a natural linewidth of $\approx 2\pi \cdot 43$ MHz and the resulting saturation intensity amounts to $I_{sat} = 253$ mW/cm². In the experiment only linear polarized light is used. This leads to induced transitions between states with same sign and absolute value of the magnetic quantum number m only. The additional spontaneous emitted circular polarized photons shift the saturation steady state of equal probability of spontaneous and induced emission. The experimental situation thus leads to a higher needed intensity to reach saturation. Dividing the saturation intensity with the squared Clebsch-Gordan coefficients of the involved transitions gives the experimental saturation intensity $I_{sat,exp} = 3I_{sat} \approx 760$ mW/cm².

Three-level laser Doppler cooling An effective two-level system is the easiest scheme to treat theoretically. The extension to a three-level Λ -system [56] interacting with two near-resonant laser fields (wavenumbers \vec{k}_1, \vec{k}_2) is conceptionally equivalent to the two-level treatment, if the third level, lying energetically between the two others, can be assumed to

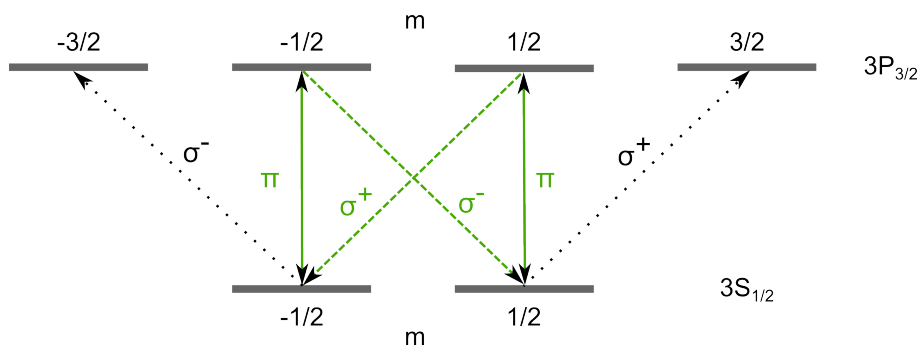


Figure 1.4: Degenerate fine structure manifold of the $3S_{1/2}$ and $3P_{3/2}$ states of $^{24}\text{Mg}^+$. The solid green arrows indicate the experimentally realized transitions using π -polarized light near 280 nm. Spontaneous decay of the $|m| = 1/2$ levels via σ^\pm -polarized photons is represented by the dashed green arrows. The dotted black arrows do not contribute to the experimental used scheme.

be metastable (rate of spontaneous emission Γ_3 tends to zero). The steady state solutions of the optical Bloch equations (ρ_{22}) determines the photon scattering rate and thus the optical force on the atom. If Γ_1 and Γ_2 denotes the spontaneous emission rate from the second to the first and third state respectively, the semi-classical force on a free particle can be written as:

$$\vec{F} = \hbar\rho_{22}(\vec{k}_1\Gamma_1 + \vec{k}_2\Gamma_2) \quad (1.21)$$

The friction term can be calculated similar to the two-level case.

However, the laser detunings Δ_1, Δ_2 to the respective Bohr-frequencies play an important role, when two different quasi-ground states are coherently coupled to a common upper level. For identical detunings, the population in the upper state vanishes. The effect of forming a coherent superposition of ground states is known as coherent population trapping [57]. In the case of laser cooling where the radiation pressure force depends on the population of the excited state one aims to avoid experimental parameters that would lead to a vanishing population ρ_{22} . In the presence of an external magnetic field, the three levels in the Λ -system may have diverse Zeeman sub-levels. The shift in energy is linear in the strength of the magnetic field

$$\Delta E = mg_j\mu_B|\vec{B}| \quad (1.22)$$

where the g_j are the Landé-factors of the particular level, m is the magnetic quantum number and μ_B the Bohr magneton. The population in the upper level will in this case tend to zero, if the two laser fields connect certain Zeeman sub-states of the ground and metastable state. Therefore, various so-called dark resonances can cause dips in the spontaneous fluorescence rate of a laser cooled atom depending on the detunings of the contributing laser frequencies.

Laser Doppler cooling of a three-level system is experimentally realized on $^{138}\text{Ba}^+$ -ions. In this case, the Λ -system is spanned by the $6S_{1/2}$, $6P_{1/2}$ and $5D_{3/2}$ levels. With a natural

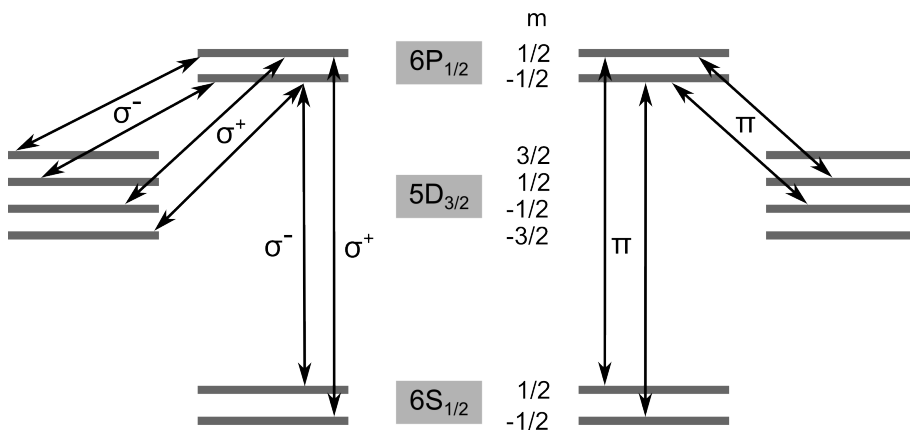


Figure 1.5: Fine structure level scheme of $^{138}\text{Ba}^+$ with Zeeman splitting in an external magnetic field. The scheme splits into two three-level systems that are only coupled by spontaneous decay. The allowed transitions labeled with the respective polarizations are indicated by arrows. σ^\pm photons can excite electronic transitions from all substrates in the $5D_{3/2}$ manifold and optical pumping into dark states is avoided.

linewidth of $4 \cdot 10^{-7}$ MHz the $5D_{3/2}$ level can be assumed to be metastable. The branching ratio of the decay into the ground state and into the metastable D state is approximately 3:1 [58]. Population, that decays into the intermediate D-level can be re-pumped by a laser near 650 nm. The laser that drives the $S_{1/2} \rightarrow P_{1/2}$ transition has a wavelength near 493 nm. If the quantization axis is given by the polarization direction of the laser radiation and thus allows only $\Delta m = 0$ transitions, states in the $D_{3/2}$ manifold with $|m| = 3/2$ are populated via spontaneous emission but cannot be de-populated. A weak magnetic field lifts the degeneracy of the contributing states and defines an external quantization axis. Now, light with a polarization direction that is perpendicular to the quantization axis (σ^\pm) can be scattered and the dark states can be re-pumped to the upper level. Under these conditions, the level scheme of $^{138}\text{Ba}^+$ splits into two Λ -systems, coupled only via spontaneous interactions (see figure 1.5) and no interruption of the nearly closed cooling transitions occurs. As a consequence of the applied magnetic field and its angle α with the polarization direction, a maximum number of eight dark resonances can be observed. At an angle $\alpha = 90^\circ$ the superposition of Zeeman sub-states leads to four dark resonances at detunings $\tilde{\Delta}$ [59]:

$$\tilde{\Delta} = \Delta_1 - \Delta_2 = \pm \frac{3\mu_B |\vec{B}|}{5\hbar}, \quad \pm \frac{11\mu_B |\vec{B}|}{5\hbar}$$

Crystalline structures If various ions, bound by a common trap potential, are cooled sufficiently a phase transition into an ordered crystalline structure occurs [40]. These Coulomb- or Wigner crystals have in contrast to solid state crystals a much higher inter-particle spacing (typically $\approx 10 \mu\text{m}$). Crystallization of singly charged particles was demonstrated for the first time in Penning-traps [52], due to the lack of RF-heating effects. The first observation of a phase transition of laser cooled ions in a Paul-trap has

N	$z_{i,0} [\mu\text{m}]$						
2			-3,31		3,31		
3		-5,66		0		5,66	
4		-7,54	-2,39		2,39	7,54	
5	-9,15		-4,32	0		4,32	9,15

Table 1.1: Steady state positions $z_{i,0}$ in μm for up to five $^{24}\text{Mg}^+$ -ions in a common trap potential with $\omega_{\text{sec},x}, \omega_{\text{sec},y} > \omega_z$. A fixed longitudinal frequency of $\omega_z = 2\pi \cdot 1 \text{ MHz}$ is used.

been reported in [37, 36]. If the position of the ion number j in the ensemble of trapped particles is given by $\vec{r}_j = (x_j, y_j, z_j)$ the potential combining the trap and the Coulomb repulsion of ions can be written in adiabatic approximation

$$V = \sum_{j=1}^N \frac{1}{2} m_j (\omega_{\text{sec},x}^2 x_j^2 + \omega_{\text{sec},y}^2 y_j^2 + \omega_z^2 z_j^2) + \sum_{j=1}^N \sum_{k=1}^N \frac{Z|e|^2}{4\pi\epsilon_0} \frac{1}{|\vec{r}_j - \vec{r}_k|} \quad (1.23)$$

and the steady state positions $\vec{r}_{j,0}$ can be calculated [41] by solving:

$$\frac{\partial V}{\partial \vec{r}_j} \Big|_{\vec{r}_j = \vec{r}_{j,0}} = 0 \quad (1.24)$$

For $N > 3$ the solution of 1.24 can be found using numerical methods. For a tightly bound system in radial direction ($\omega_{\text{sec},x}, \omega_{\text{sec},y} > \omega_z$) the steady state positions for up to five $^{24}\text{Mg}^+$ ions are given in table 1.1 for a fixed frequency of $\omega_z = 2\pi \cdot 1 \text{ MHz}$ in longitudinal direction.

A different approach to specify the phase transition of an ensemble of laser cooled trapped ions can be made by describing the ions by an infinite, homogeneous one component plasma (OCP). A OCP is a system of point like charges embedded into a charge neutralizing background given in the case of trapped ions by the trapping potential. It is convenient to introduce the so-called plasma parameter Π which is defined by the ratio of averaged, next-neighbor Coulomb energy and thermal energy.

$$\Pi = \frac{E_C}{E_{\text{kin}}} = \frac{mq\Omega^2}{12\pi k_B T} \quad (1.25)$$

The derivation of the plasma parameters dependence on the trap frequency Ω and the stability parameter q can be found for example in [60]. With the help of the plasma parameter, the transition from a chaotic to an ordered structure can be quantified. For three-dimensional structures Π has to be larger than 175 [60] for a crystalline order to form. The phase transition for one ($\Pi \approx 2$) and two dimensional ($\Pi \approx 125$) structures occurs for smaller plasma parameters. Figure 1.6 shows the typical crystalline structures that can be observed in a Paul-trap assuming a cylindrical symmetric focusing potential. For crystals in a linear trap as it is used in this thesis, a change in the type of structure at the borders

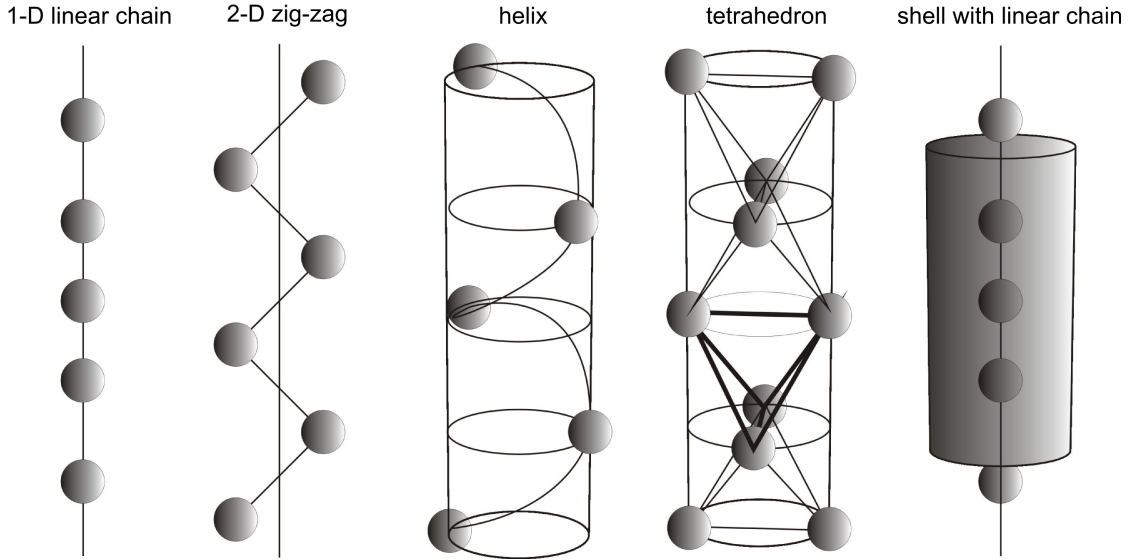


Figure 1.6: Schematic overview of the crystalline structures observed when various ions are trapped in a common potential with cylindrical symmetry.

of the z -potential must be taken into account. Going along z from the outskirts to the center of the trap, linear chains, two-dimensional zig-zag structures and three dimensional helical or tetrahedral structures are observed within the same ion crystal. In an ion-trap without longitudinal focusing, a dimensionless parameter λ , the so-called linear density, can be defined that determines the kind of structure in the trap. For a detailed treatment refer to [40].

sympathetic cooling Laser cooling of atoms and ions is a very powerful tool to reach low temperatures, but is restricted to particles that possess a closed cycling transition. Cooling schemes for molecules, for example, are complicated and often not practical because the amount of repumper lasers, needed to prevent optical pumping in dark states, increases dramatically with a richer ro-vibrational structure. In ion-traps, it is possible to commonly trap particles with different charge-to-mass ratios as long as the stability region is not left. The Coulomb repulsion of the ions can be used to damp out the motion of, for example, a molecular ion with the help of a laser-coolable ion. Before the phase transition to a crystalline state, part of the sympathetically cooled molecular ion's energy is mediated to the directly laser cooled ion via elastic collisions. Thermalization of the ensemble and sufficient cooling brings the cloud to a crystalline state. Now, the collective phononic motion couples the laser cooled ions with the molecular ions. Using Doppler cooling methods, temperatures of the sympathetically cooled ions in the millikelvin regime have been reported [61, 62]. The sympathetically cooled ion is often called a dark ion, because it scatters no photons and appears as a dark spot in fluorescence images. Nevertheless, it occupies a specific lattice site and its position can be detected via interpolation with the surrounding bright spots to an accuracy of $\approx 1 \mu\text{m}$, with the means used in this thesis. As quantum information protocols use phononic coupling to transfer information, a high probability for being in the motional ground state for the sympathetically and

directly laser-cooled ion is desired. Indeed, by exploiting sophisticated side band cooling schemes, sympathetic motional ground state cooling has been demonstrated [30]. Theoretically, the position accuracy is only limited by the size of the motional ground state wave-function of the ion. The technique of sympathetic cooling can be applied to a great variety of molecular ions. As stated above only the charge-to-mass ratio has to be compatible to the directly laser cooled ion. Even very heavy organic molecular ions have been treated by multiple charging [32]. Nevertheless, with greater mass discrepancy between the collectively trapped ions, the coupling is reduced because of a larger inter-ion spacing. Furthermore, the increased distance to the trap center for the heavier ion, leads to an increase in micro-motion. For a more detailed treatment of this point refer to chapter 6.

1.2 Elements of ultra-fast physics

This section gives a brief introduction to ultrashort electromagnetic pulses. For a more detailed treatment refer to [63]. The first part introduces a mathematical description of electromagnetic pulses and gives an introduction to their basic properties. The second part discusses the propagation of optical pulses in linear matter and provides a basic knowledge of the non-linear effects that are relevant for this thesis.

1.2.1 Description and properties of electromagnetic pulses

This section introduces the necessary notations and definitions to describe short light pulses as electromagnetic wave packets. The measurable pulse properties are characterized by the time- and space-dependent electric field $\vec{E}(\vec{r}, t)$. For the sake of simplicity, the vectorial character (direction of polarization) and the spatial dependence of the electric field is neglected and only the linearly polarized, time-dependent part $E(t)$ is considered.

In most practical cases, the spectral amplitude of the pulse is centered around a mean frequency ω_0 , also called the carrier frequency. In a frequency interval $\delta\omega$ that is small compared to the mean carrier frequency ($\delta\omega/\omega_0 \ll 1$) the complex representation of the electric field in the time-domain can be written as

$$\check{E}(t) = 1/2\check{\epsilon}(t)e^{i\omega_0 t}, \quad \check{\epsilon}(t) = \epsilon(t)e^{i\phi_0}e^{i\phi(t)} \quad (1.26)$$

where $\check{\epsilon}(t)$ ($\epsilon(t)$) is the time-dependent complex (real) field envelope function and $\phi(t)$ is the time-dependent phase. The description of electromagnetic pulses can be done either in the time- or in the frequency-domain. Both descriptions are equivalent, but specific experimental measurements can sometimes favor one of these domains. The conversion is done by complex Fourier transformation:

$$\check{E}(t) = \text{FT}^{-1} [\check{E}(\Omega)] = \frac{1}{2\pi} \int_{-\infty}^{\infty} \check{E}(\Omega)e^{i\Omega t} d\Omega \quad (1.27)$$

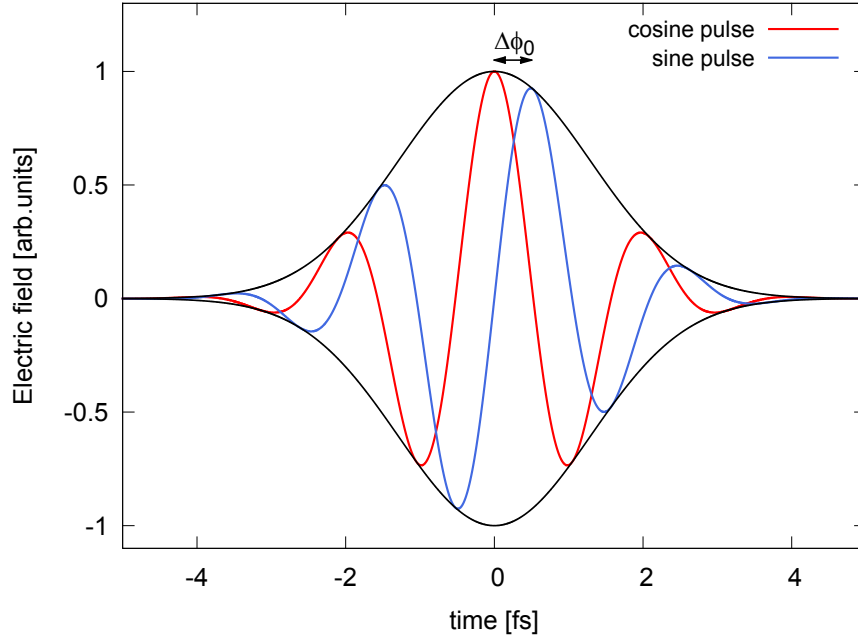


Figure 1.7: Two electromagnetic pulses with the same electric field envelope function, but an absolute carrier-to-envelope phase ϕ_0 that differs by $\pi/2$. Maximal field strength is achieved by the cosine pulse that by definition reaches its maximum at $t = 0$. The electric field of the corresponding sine waveform is zero at the time origin.

The constant phase term $e^{i\phi_0}$ in equation 1.26 describes the phase shift between the carrier frequency and the field envelope and is therefore often quoted as the carrier-to-envelope phase. The decomposition of the full phase term of the complex electric field into $e^{i\phi_0}$ and $e^{i\phi(t)}$ is not unique. The carrier frequency and the complex amplitude are required to remain invariant under a change of ϕ_0 . In order to minimize the temporal variation of $\phi(t)$ one of the most used definitions of ω_0 is the intensity weighted average frequency

$$\omega_0 = \frac{\int_{-\infty}^{\infty} |\check{\epsilon}(t)|^2 \omega(t) dt}{\int_{-\infty}^{\infty} |\check{\epsilon}(t)|^2 dt}, \quad \omega(t) = \omega_0 + \frac{d\phi(t)}{dt} \quad (1.28)$$

As a result of this definition, the time-dependent phase is slowly varying and thus has little variation over one optical cycle $T = 2\pi/\omega_0$. The time-dependent carrier frequency or instantaneous frequency $\omega(t)$ introduces a variation of the carrier frequency across the pulse. A non-constant first derivative of $\phi(t)$ leads to a carrier frequency that varies in time. The pulse is called frequency modulated or chirped. For a positive second derivative, the carrier frequency increases in time along the pulse. Such a pulse is referred to as up-chirped. On the other hand, a negative or down-chirped pulse is headed by high frequency components and the low frequencies are located within its trailing edge. As it will be discussed in the next section, the gradient of the refractive index of *normal* dispersive media increases with higher frequencies and thus introduces a positive chirp.

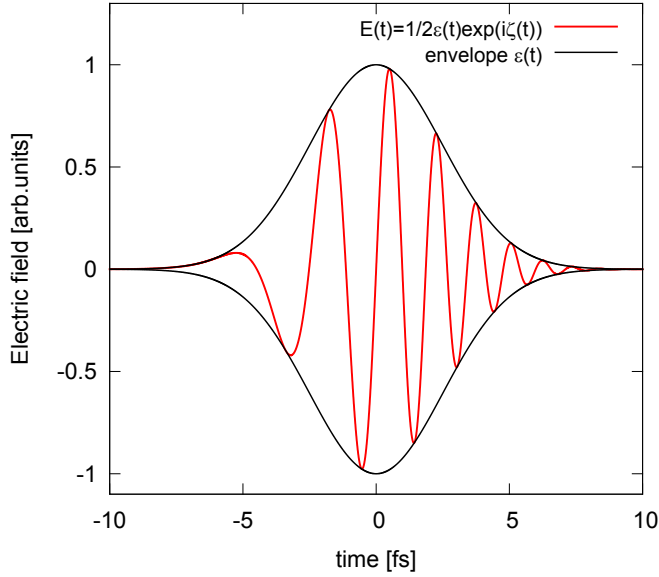


Figure 1.8: Electric field with the amplitude or pulse envelope function $\epsilon(t)$ and complete temporal phase $\zeta(t)$. The instantaneous frequency varies in time and the pulse has a linear positive chirp. The leading edge of the pulse contains lower frequencies than the trailing edge.

The most convenient definitions of the duration τ and the spectral width $\Delta\omega$ of a pulse is the full-width-at-half-maximum of the intensity profile $|\tilde{\epsilon}(t)|^2$ and the spectral intensity $|\text{FT}[\tilde{\epsilon}(t)]|^2$, respectively. Temporal pulse duration and spectral bandwidth are connected via Fourier transformation and the minimal pulse duration is given by the minimum time-bandwidth product [63]:

$$\Delta\omega \tau \geq 2\pi \cdot m$$

The numerical constant m depends on the shape of the pulse's field envelope (for a gaussian shaped pulse: $m = 2\ln 2/\pi$). The equality is true only for pulses without frequency modulation (unchirped pulses). A pulse with minimal duration at a given spectral width is called Fourier limited.

1.2.2 Pulse propagation and third order non-linear effects

This section, intended to give an overview of the terms and definitions relevant for the propagation and propagation effects of short optical pulses in matter is divided into two parts. The first part deals with the description of the propagation of electromagnetic pulses through linear matter. In this case, the field does not affect the response of the material. The second part provides the theoretical framework of non-linear effects, like harmonic generation or self-phase modulation.

The wave equation for the electric field $\vec{E}(\vec{r}, t)$ with full time and spacial dependence can be derived out of Maxwell's equations. In the following, external charges and currents are neglected. With the restriction to non-magnetic and uniform media the wave equation can be written as

$$(\nabla^2 - 1/c^2 \frac{\partial^2}{\partial t^2}) \vec{E}(\vec{r}, t) = \mu_0 \frac{\partial^2}{\partial t^2} \vec{P}(\vec{r}, t) \quad (1.29)$$

with the help of the magnetic permeability in vacuum μ_0 and the polarization \vec{P} of the medium. In equation 1.29, c denotes the speed of light. It is convenient to decompose the polarization that describes the influence and response of the medium on the field into a linear \vec{P}_L and a non-linear part \vec{P}_{NL} .

$$\vec{P} = \vec{P}_L + \vec{P}_{NL}$$

Assuming a linear polarized electric field, propagating in z-direction as a plane wave and neglecting non-linear polarization effects the wave equation 1.29 is solved in the spectral domain by

$$\check{E}(\Omega, z) = \check{E}(\Omega, 0) e^{-ik(\Omega)z} \quad (1.30)$$

The wave vector $k(\Omega)$ and the refractive index of the medium are related via the dispersion relation of linear optics.

$$k(\Omega) = \frac{\Omega n(\Omega)}{c} \quad (1.31)$$

The expansion in a Taylor-series around the carrier frequency ω_0 yields:

$$k(\Omega) = k_0(\omega_0) + k_1(\omega_0)(\Omega - \omega_0) + 1/2 k_2(\omega_0)(\Omega - \omega_0)^2 + \dots \quad (1.32)$$

The first coefficient k_0 corresponds to the oscillation of the phase of the propagating wave. It describes a trivial phase-shift of a propagating wave. With the help of the index of refraction $n(\omega_0)$, evaluated at the carrier frequency, k_0 can be related to the phase velocity $v_{phase} = \omega_0/k_0(\omega_0) = c/n(\omega_0)$. Similarly, the second coefficient k_1 can be related to the group velocity v_{group} . In a fixed frame of reference, the group velocity can be written as $v_{group} = 1/k_1(\omega_0)$. This results in a different propagation speed of the pulse envelope compared to the speed of the phase. The third term in equation 1.32 introduces a linear chirp in the frequency domain and the corresponding coefficient k_2 is called group velocity dispersion (GVD) conventionally in units of [fs²/μm]. In a material with well-known length through which the wave propagates, the GVD can be linked to the group delay dispersion (GDD) per unit length in units of [fs²]. The coefficient k_2 can be related ($k_2(\omega_0) = d(v_{group})^{-1}/d\Omega$) to the variation of the group velocity with frequency Ω . A positive GVD corresponds to a positive chirp.

For strong electric fields significant non-linear interactions with the material can take place. In particular, they are important in the case of short pulses since here the energy is concentrated in a short time-window and therefore high peak intensities can be reached.

Using the linear and non-linear part of the polarization in the wave equation 1.29 leads to the wave equation in a non-linear medium:

$$(\nabla^2 - n^2/c^2 \frac{\partial^2}{\partial t^2})E = \mu_0 \frac{\partial^2}{\partial t^2} P_{NL} \quad (1.33)$$

The induced polarization can be expressed as a power series in the strength of the electric field. In the following only third-order non-linear processes are considered ($P_{NL} \propto E^3$). The non-linear polarization consists of the following components:

$$P_{NL} \propto 1/8\epsilon^3 e^{3i\omega_0 t} + 3/8 |\epsilon|^2 \check{\epsilon} e^{i\omega_0 t} + c.c. \quad (1.34)$$

The first part describes the generation of the third harmonic that means radiation with tripled frequency. In the framework of this thesis, the third-harmonic conversion of short optical pulses in gaseous radially symmetric media (invariant under inversion transformation $\vec{r} \rightarrow -\vec{r}$) is used (see section 2.2.4). Due to the vanishing second order nonlinearity in those media, the lowest order nonlinear effect is of third order. As described in section 2.2.4 the phase matching between the different frequencies and thus the third-harmonic generation yield, is tuned via the pressure of the gas in the target. The phase mismatch has also been minimized by a minimal propagation length in the medium which in turn lowers the conversion efficiency.

The second term of 1.34 influences the fundamental frequency components and leads to a non-linear contribution of the refractive index. If I is the averaged intensity of the pulse, the intensity dependent refractive index can be expressed with the help of the third order nonlinear susceptibility χ_3 and the original refractive index n_0 :

$$n = n_0 + \frac{3\chi_3}{8n_0^2} \cdot I$$

The increase of n with increasing I is known as the optical Kerr effect. A consequence are the self-focusing properties of a beam with a spatial intensity profile, where the intensity in the center of the beam is higher than the intensity outside the center axis. This Kerr lensing is frequently used for passive mode-locking of pulsed lasers (see also section 2.2.3). The intensity dependent refractive index does also lead to a non-linear phase delay. For very short pulses, the variations of the time-dependent frequency can be greater than the spectral width of the pulse and thus leads to a significant spectral broadening. This effect called self-phase modulation (SPM) is used in the framework of this thesis to overcome the spectral limitations of the laser materials used in the oscillator and amplifier of section 2.2.3. A spectrally very broad supercontinuum is created via SPM in a neon gas filled hollow-core fiber. Self-phase modulation leads to additional frequency components and the amplitudes of the newly created components can interfere with the amplitudes that are already present in the pulse. In general, this interference can be constructive or destructive, depending mostly on the chirp of the pulse and the sign of $n_2 = 3\chi_3/8n_0^2$. Constructive interference leads to the desired spectral broadening, whereas destructive interference leads to a spectral narrowing. The spectrally broadened pulses after the fiber

are chirped and an additional chirped mirror compressor is used to compress the pulses to near the ultimate Fourier limit (for more information about the experimental details refer to section 2.2.3).

1.3 Dynamic quantum chemical calculation on $^{24}\text{MgH}^+$

A dynamic quantum chemical calculation on the diatomic molecular ion $^{24}\text{MgH}^+$ has been performed in order to treat the time-resolved pump-probe measurements discussed in chapter 3. A helping hand from theory was necessary to estimate the nature of the expected experimental signal, like the time-dependence, the contrast or the strength of the reaction in the initial stage of the experiment. Later, the theory did help significantly for example in trying to interpret the collected data. This section gives a rough summary of the theoretical work contributed by Markus Kowalewski¹ to this thesis.

In a first step, the eight energetically lowest lying singlet energy eigenstates, often referred to as potential energy curves (PEC) or potential energy surfaces (PES) in higher dimensional cases, are calculated as a function of the internuclear distance of the magnesium and the hydrogen atom. This calculation is performed with ab initio quantum chemical methods [64]. The time-dependent Schrödinger equation, using the molecular Hamiltonian $\hat{H}_{\text{MOL}} = \hat{T}_{\text{NUC}} + \hat{H}_{\text{EL}}$, can be separated because the nuclear kinetic energy operator \hat{T}_{NUC} has a negligible influence on the electronic wave-function. In this case, \hat{H}_{EL} combines the kinetic energy part of the electrons as well as the operators for the electron-electron, the nuclei-nuclei and the electron-nuclei interactions. The stationary molecular wave-function $\psi(r, R) = \psi_{\text{NUC}}(R) \cdot \psi_{\text{EL}}(r; R)$ can be separated into a nuclear and an electronic part, depending on the nuclear (R) and electronic (r) coordinates. The electronic wave-function depends only parametrically on the nuclear geometry, according to the Born-Oppenheimer approximation [65]. The potential energy curves as a function of the internuclear distance are calculated by solving the stationary electronic Schrödinger equation

$$\hat{H}_{\text{EL}}\psi_{\text{EL}}^n(r; R) = E_{\text{EL}}^n(R)\psi_{\text{EL}}^n(r; R) \quad (1.35)$$

together with the assigned eigen-energies $E_{\text{EL}}^n(R)$. The first $n=8$ states ($X[{}^1\Sigma^+]$, $A[{}^1\Sigma^+]$, $B[{}^1\Pi]$, $C[{}^1\Sigma^+]$, $D[{}^1\Sigma^+]$, $F[{}^1\Sigma^+]$, $E_{1,2}[{}^1\Delta]$) are calculated. The molecular term symbols given in brackets after the name assigned to the state, show that the total spin quantum number (superscript 1) vanishes for all involved states and that all wave-functions are symmetric with respect to a reflection on a plane containing the internuclear axis. The projection of the orbital angular momentum along the internuclear axis can be zero (Σ), one (Π) or two (Δ). The conventionally shown projection of the total angular momentum along the internuclear axis and the parity as a subscript are neglected. The result of the calculation is shown in figure 3.7 on page 76. The quantum chemistry program package MOLPRO [66] is used to calculate the solutions of equation 1.35. The program uses a configuration interaction expansion of eigen-states of \hat{H}_{EL} in a set of Slater-determinants

¹Group of Prof. Dr. R. de Vivie-Riedle, Chemistry Department, Ludwig-Maximilians-Universität München

(multi reference configuration interaction calculation [67, 68]), developed in a complete active space (CAS) calculation [69]. The CAS involves 12 electrons and 10 active orbitals and the atomic neutral orbital basis set by Roos [70], available in the MOLPRO basis library is used. After the calculation a consistency check on the potential energy curves is performed by comparing the molecular levels with the data provided in reference [71] and the atomic levels with the data in reference [72]. The vibrational energy levels are determined by solving the stationary nuclear Schrödinger equation in a very similar way.

The next step is the implementation of the quantum dynamics-calculation on the potential energy curves. For this purpose the time dependent Schrödinger equation

$$i\hbar \frac{d}{dt} \psi(r, t) = \left(\frac{\hbar}{2m} \frac{\partial^2}{\partial r^2} + \hat{V}(r) + \hat{H}_{int} \right) \psi(r, t) \quad (1.36)$$

for the nuclei under the influence of a pump-probe laser field has to be solved numerically. The potential energy operator $\hat{V}(r)$ includes the eight molecular states and the non-adiabatic terms, taking the couplings of the state C with D and of the state D with F into account. The diabatic couplings are introduced via hermitized derivative coupling matrix elements. The interaction term $\hat{H}_{int} = -\mu(r)\epsilon(t)$ of the Hamiltonian consists of the position dependent transition dipole matrix $\mu(r)$ and the pump-probe laser field $\epsilon(t)$. The coupling of the electronic states via the laser field is represented by an 8×8 dipole matrix accounting for the relevant transitions via 13 different transition dipole matrix elements. The ground state X can be coupled with the states A and B, the first excited state A can be coupled with the B, C, D, F, E_{1,2} states and the state B can be coupled with the C, D, F, E_{1,2} states. All the other matrix elements are set to zero. For the description of the laser field, gaussian shaped pulses (see also section 1.2) with a pulse delay time $\tau = \tilde{\tau} - t_0$ and the maximal electric field amplitude E_{max} are assumed:

$$\epsilon(t) = E_{max} (e^{-(t-t_0)^2/\sigma^2} \cos(\omega t - \omega t_0) + e^{-(t-\tau)^2/\sigma^2} \cos(\omega t - \omega \tilde{\tau})) \quad (1.37)$$

In equation 1.37, ω is the carrier frequency and σ is the width of the pulse. Additionally, the laser field can be modified by a frequency dependent phase to account for the chirp introduced by the used dielectric mirrors (refer to section 2.2.4). The phase function used in the simulation was provided by the manufacturer. In order to numerically solve the time-dependent Schrödinger equation 1.36, the potential is represented on a discretized finite spacial grid with 2048 points. It is assumed that before every interaction with the laser field, the molecular ion is in the electronic and vibrational ground state. The equations of motion are determined as the action of a propagator on the wave function. The propagator is approximated by a Chebychev polynomial expansion [73]. The time steps are chosen to 50 attoseconds (10^{-18} s). After every time step, the wave function is multiplied with a Butterworth function to remove the population. The propagation is stopped after the interaction with the laser field. The removed values of every time step are summed up over the whole propagation time. The population that remains in one of the dissociative states after the interaction with the pump and probe laser is over is added to the already removed population. With this, the dissociating fractions can be assigned to either a so called neutral channel (dissociation via C) or a charged

channels (all other dissociative states). The names are given to indicate the charge state of magnesium after the dissociation. With this method, the dissociation probability for given laser parameters such as spectrum, chirp, intensity or pulse duration, in the neutral channel can be calculated as a function of the pump-probe delay time τ . The assumption of the $X_{\nu=0}$ (ν denotes the vibrational quantum number) state as a fixed starting point for the interaction with the laser field is not valid in general when the same molecular ion can be excited many times by the laser without dissociating. In the special case of this thesis, this is exactly the case and vibrational heating within the molecular ion can occur and has to be taken into account by theory (see also section 3.2.1). A theoretical estimation which laser pulse repetition rate is acceptable to yield a sufficiently large modulation of the dissociation probability in dependence of the time delay had to be made to adjust the experimentally used repetition rate. The change in the vibrational distribution is simulated by a rate equation model with rate matrix W . The time evolution of the population vector p is given by $dp/dt = Wp$. For the initial value of p , all population is chosen to be in the $X_{\nu=0}$ state. The rate matrix W takes the lowest lying 20 vibrational states of the electronic X and A state into account. W is composed out of the vibrational and electronic decay rates of the A state, the excitation rates of a pulse sequence with given repetition rate and the two possible dissociation channels. The presented theoretical framework allows to simulate the steady-state distribution of the vibrational state population in the electronic ground state under laser cycles with different pulse repetition rates and therefore the point at which significant vibrational heating is expected. Several effective pulse repetition rates and their associated vibrational heating effects have been simulated. This gives a good figure of merit for the parameters that should be used in the experiment.

Chapter 2

Experimental setup

This chapter provides the basic knowledge of the setup used in the experiments on time-resolved spectroscopy of $^{24}\text{MgH}^+$ (see section 3.3), the implementation of a novel photoionization scheme for barium (see section 4.1 of chapter 4) and the realization of discrete kink solitons in ion traps (see chapter 5). The first section is dedicated to the mechanical hardware of the ion trap apparatus, whereas the second section discusses the used laser systems of this thesis. The last section presents the layout and first results of the newly developed Electro-Spray Ionization setup that plays an essential role in the attempt to extend the time-resolved measurements with single particles to larger molecular ions.

2.1 Apparatus

The section gives a summary of the operational technology and developed hardware of the ion trap setup used for time-resolved pump probe experiments on trapped single molecular ions, presented in chapter 3. The first part concentrates on the mechanical layout of the vacuum apparatus and on the frequently used inner-vacuum parts of the setup. A more detailed description can be found in [74, 75] and the related publication [76]. The second part describes the changes made to the apparatus to account for the needs of photoionization of neutral barium atoms and trapping and laser-cooling of singly charged $^{138}\text{Ba}^+$ -ions.

2.1.1 Mg trap apparatus

Figure 2.1 shows a top view of the main vacuum vessel that consists of three separately pumped chambers. The whole setup was carefully designed to be compatible with ultra-high vacuum conditions. The usage of materials other than stainless steel and oxygen-free copper was reduced to a minimum. Isolator parts are made out of MacorTM ceramics and all inner-vacuum screws are silver plated and vented either by shaft holes and/or complanated threads. After the assembly, a week of bake out with a maximum temperature of $\approx 180^\circ\text{C}$ followed. A slightly modified standard CF-160 cross is the central element of the first

chamber that is mainly designed for loading and preparation of atomic and molecular ions. A 5001/s turbomolecular pump¹ backed by a turbomolecular drag pumping station² maintains a total pressure in the low 10^{-10} mbar regime³ that can be monitored by a cold cathode gauge⁴. The central, second chamber consists of a standard vacuum CF-160 cube pumped by a 3001/s turbomolecular pump⁵ and serves mainly as an isolation between the first and the third chamber, but can be used for future implementations of, for example, more sophisticated cooling schemes for the internal degrees of freedom of the confined molecular ions (buffer gas [33] or optical cooling [35, 34]). Furthermore, an all-metal slider valve⁶ gives the possibility to connect another vacuum system, for example the femtosecond beamline. A base pressure of $2 \cdot 10^{-10}$ mbar is reached in the last chamber using a combined ion getter-titanium sublimation pump⁷ and can be measured and monitored with a nude Bayard-Alpert type ionization gauge tube⁸. The residual gas can be analyzed with a commercial quadrupole mass spectrometer⁹. Two electro-pneumatic valves¹⁰ protect the whole vacuum system from accidental venting that may be caused by power or pump failure.

An overview of the mechanical layout of the parts inside the vacuum chamber is presented in the computer drawing of figure 2.2. Four cylindrical, gold plated (thickness $\approx 2 \mu\text{m}$) copper rods of 2 mm diameter form a 48.5 cm long quadrupole ion guide, providing a two dimensional confinement for ions. The rod centers are arranged in a square with 3 mm edge length. The minimal distance between the guide center and the surface of the rods amounts to $r_0 = 1.12$ mm. The U-shaped ion-guide is bend twice by 90° with a radius of curvature of 35.5 mm. The two bends are used to enhance the pumping efficiency of gas that is injected into the vacuum system, required for the generation of molecular ions. Additionally, the bended structure can be used to guide and filter neutral polar molecules in a radio-frequency field (see also chapter 6) using the Stark effect [77]. With this arrangement it is possible to explore interactions with trapped molecular ions [78]. Radial confinement along the quadrupole is achieved by applying a RF-voltage on each pair of opposing electrodes with a mutual phase difference of π and a frequency of $\Omega = 2\pi \cdot 6.8$ MHz. The opposing pairs of the quadrupole are connected to the ends of a resonator coil (inductance $L=5.95 \mu\text{H}$, self-capacitance 7.4 pF) that is inductively coupled to a looped wire. This helical resonator is driven by a RF-voltage applied to the wire. To allow for ions with small charge-to-mass ratios Z/m , stable trapping conditions requires a high resonance frequency [54]. To achieve the highest resonance frequency possible, parasitic capacities, caused by e.g. dielectrics in proximity are reduced to a minimum by the chosen electrical layout. This leads to a total capacity of $C=92$ pF. Ohmic losses of the RF current are minimized in the setup by using massive contacting clamps and large

¹TMP 551, Varian

²701/s, TSU-071, Pfeiffer

³The monitoring gauge is in the under range regime $< 2 \cdot 10^{-9}$ mbar, but a similar lifetime of ions confined in the chambers 1 and 3 suggests a comparable pressure in the chambers.

⁴IKR261, Pfeiffer

⁵TMP 301, Varian

⁶48124-CE01-0001, VAT

⁷StarCell Plus 300, Varian

⁸274023, Granville-Phillips

⁹QMA200M, Pfeiffer

¹⁰AVC016/025PX, Pfeiffer

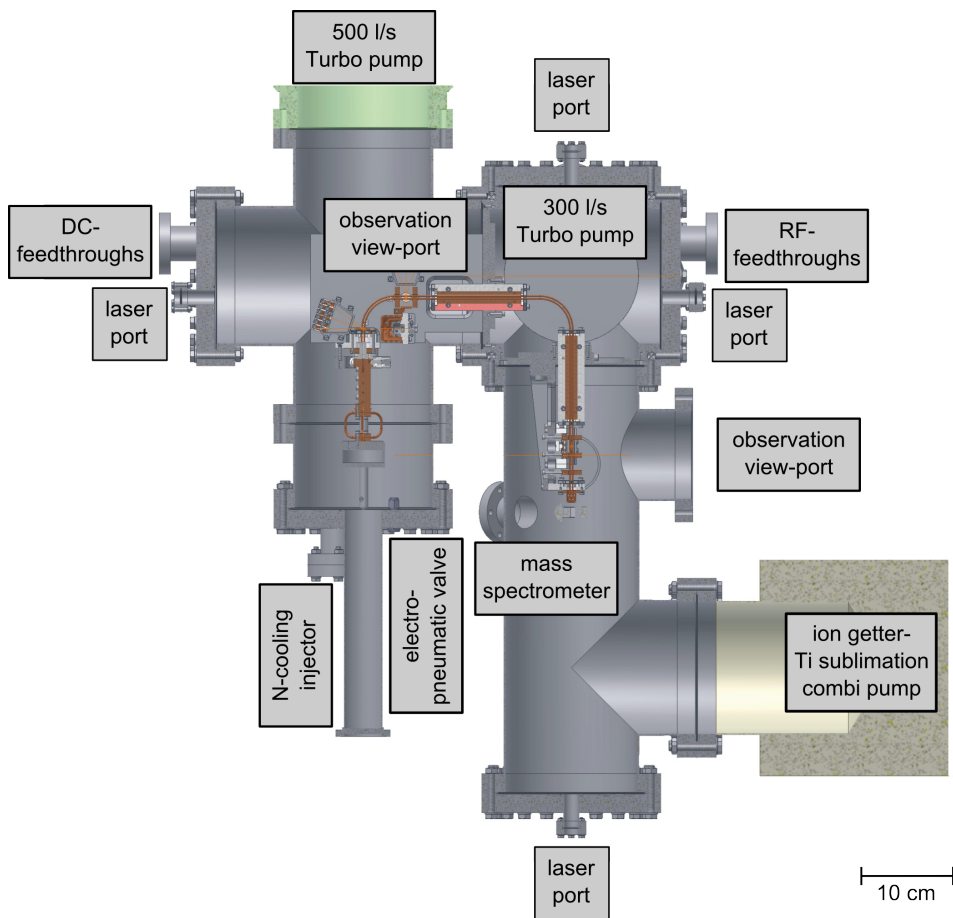


Figure 2.1: Top view of the vacuum chamber setup used for time-resolved pump probe experiments on trapped single molecular ions. The separation into three chambers with their particular pump designs, as well as the location of important mechanical parts is shown. A zoom into the guide structure inside the vacuum chamber gives figure 2.2.

surface contacting tapes. Additionally, the gold protection layer of the guide-rods prevents the formation of a inhomogeneous, poorly conducting oxide layer. A minimization of the ohmic losses lead to a high $Q=734$ (loaded) factor of the RF-resonator and thus supports the high voltages needed for a stiff confinement of (molecular-) ions with small Z/m (see chapter 6) and the envisioned experiments with neutral molecules.

As discussed in section 1.1.2 the quadrupole potential formed by the RF-electrodes confines the ions only in radial direction. In order to restrict the degree of freedom along the axial direction, pairs of 5 mm thick copper ring electrodes (outer diameter: 24 mm, inner diameter: 8 mm) have been placed around the guide, allowing for regions of three dimensional confinement. The ring electrodes can additionally serve as electrodes for the acceleration and controlled transfer of the ions (see section 3.1.2). The distance between the center of the two ring electrodes amounts to 20 mm. DC voltages on a pair of these electrodes lead to a nearly harmonic potential along the z -axis. This longitudinal potential superimposed with the potential created by the RF-electrodes forms the time-varying

potential of a linear Paul-trap, discussed in section 1.1.1. Mechanical stability, optical access and the shielding effects caused by the RF-electrodes have been the relevant design parameters for the ring electrodes. The ion trap, completed by the two ring electrodes after the first bend of the guide is labeled trap 1 in the following. This trap is mainly used for the preparation of molecular ions. At the end of the guide, three ring electrodes can create two trapping regions, named trap 2 and 3. The middle electrode is shared, resulting in a double well axial potential. Optionally, the traps can be combined to a larger one. All three Paul-traps have equal dimensions and similar trapping parameters. Typically, for $^{24}\text{Mg}^+$, the measured radial frequency in trap 2 amounts to $2\pi \cdot (410 - 540)$ kHz, which corresponds to a root-mean square RF-voltage on the electrodes of 34-46 V. The frequently used configuration of 210 V and 100 V on the two ring electrodes of trap 2 leads to a typical axial trap frequency of about $2\pi \cdot 30$ kHz.

Trap 1 and 2 can be selectively loaded with all stable isotopes of Mg^+ and Ba^+ ions. In both traps, a thermal beam of atoms can be ionized via an isotope-selective photoionization scheme for magnesium [79, 80] and barium [81]. The photoionization scheme and the used laser system for magnesium and barium are described in section 2.2.1 and section 2.2.2, respectively. The apparatus additionally offers the possibility to use electron-impact ionization to load trap 2. Due to the various advantages of photoionization (see chapter 4), the electron gun that produces the ionizing electron beam is used only as a backup system. A 0.8 mm thick Mg wire inside a tantalum tube that can be resistively heated (typical currents: 3.4-4.1 A) evaporates a beam of neutral magnesium into the trapping region. Three tantalum tubes¹¹ are combined in one atomic oven stack. The tubes extend into a housing that protects the traps from metal deposits. A 200 μm slit in the housing collimates the evaporated atomic beam in the radial direction of the guide. Except for the two atomic oven stacks that are used to load trap 1 and 2 an additional assembly is installed at the beginning of the guide. That way, the electron gun in chamber 1 can be tested. A zoom into the arrangement of trap 2 and 3 and the corresponding electron gun and atomic oven assembly can be seen in figure 2.2 B.

The fluorescence light of ions confined in the traps can be directed on a suitable detector. Two reentrant sapphire windows guarantee optical access to the two separated trapping regions along the ion guide (see figure 2.1). The imaging system of trap 1 consists of an air spaced two lens condenser¹² with 50 mm focal length followed by a photomultiplier tube¹³ or an electron-multiplying CCD camera¹⁴. A flip mirror changes the detector type suitable for the envisioned experiment. The EM-CCD camera is mainly used for applications that require an observation and spatial resolution of individual ions. The photomultiplier, in contrast, provides a spatially integrated fluorescence signal that serves well for a controlled loading the trap, for example. The magnification factor of the imaging system in chamber 1 was deduced to $M=12.3$. The magnification factor used to image ions in the second and third trap on the chip of the CCD camera can be chosen to be 9.8 or 50. A near diffraction limited four lens objective¹⁵ with 19.3 mm focal length is optimized

¹¹only one tube is filled with magnesium, the other two ovens are filled with barium

¹²01CMP119, Melles Griot

¹³H8259, Hamamatsu

¹⁴iXon DV885LC-VP, Andor

¹⁵custom design, Halle

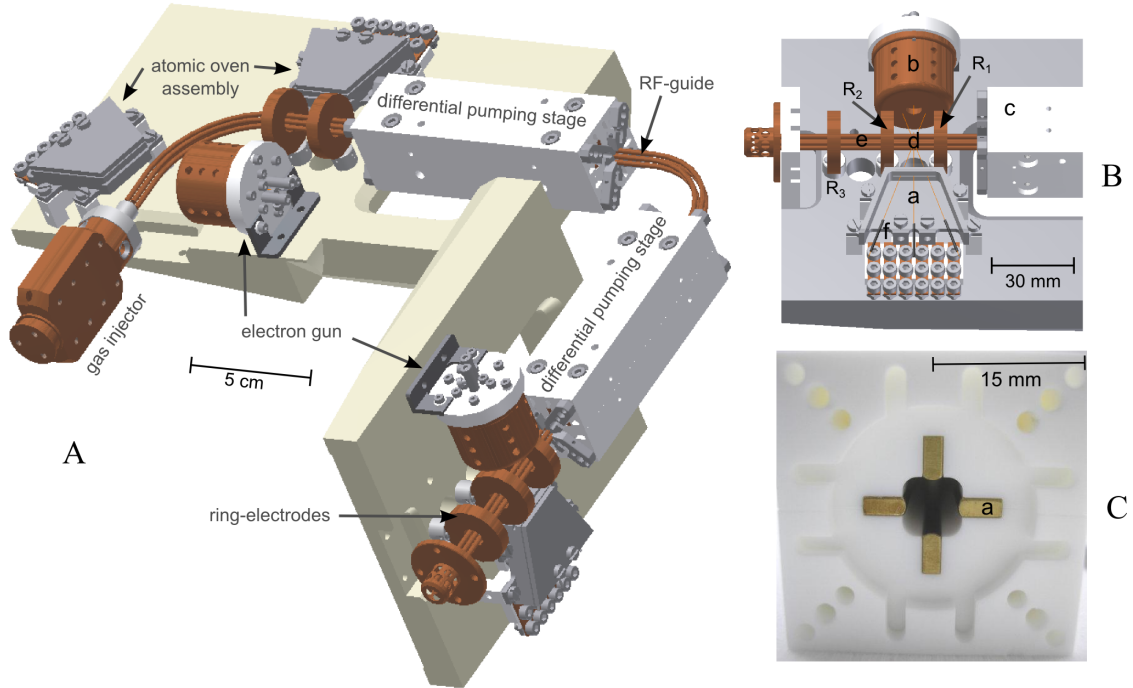


Figure 2.2: Overview computer drawing of the most important parts of the experimental setup inside vacuum. Most of the mounting parts have been removed for the demonstration and the sake of clarity. (A) shows the cryogenic gas injector and the double bended RF-guide. Two differential pumping stages separate three different chambers, that can be pumped individually. Five ring electrodes around the RF-guide form three optional trapping regions, where the confined particles can be observed by detecting the fluorescence light of laser cooled atomic ions. Three atomic oven stacks and two electron guns are positioned at selected sections of the guide. (B) gives a close up of trap 2 (d) and trap 3 (e). Neutral ^{24}Mg or ^{138}Ba atoms can be evaporated into the trap by heating the atomic ovens (f) in the assembly (a) and can be ionized either by photoionization or by electron bombardment ionization using the electron gun (b). (C) shows a close up on the front side of one of the two 10 cm long ceramic tubes, that serve as differential pumping stages. The clover leaf shaped profile leaves a 0.5 mm distance to the RF-electrodes and reduces the cross section between the different chambers to a minimum. Voltages on the four gold plated copper inlets (a) can either serve as compensation voltages or make up drift tubes for the guided ions. Additionally, they do not charge-up like the ceramics, that would potentially hinder a smooth transfer of the ions.

for imaging 280 nm light and used for the observation with high magnification. In this case, an area of $160\ \mu\text{m} \times 160\ \mu\text{m}$ is imaged on the 1002×1004 pixels of the detector. In order to completely observe ion crystals with a larger longitudinal extension, a three-lens condenser¹⁶ with $M=9.8$ is used. This results in a $800\ \mu\text{m} \times 800\ \mu\text{m}$ field of view on the detector and ion crystals of 50 to 60 ions using standard trap parameters can be imaged in total.

Aligned with the beginning of the guide in chamber 1, a cryogenic gas inlet system gives the possibility to inject gaseous molecules into the vacuum apparatus. The injected molecules can either be ionized via electron bombardment ionization inside the trapping or guiding region or induce photochemical reactions with already trapped atomic ions (see section 3.1.1). The design of the installed gas inlet stage follows closely the example of [77]. A gas reservoir with tunable pressure is connected to the vacuum chamber via a pulsed electro-pneumatic valve¹⁷. The gas pulses with an adjustable duration (typically a few ms) pass a meandering copper capillary, optimized for thermal contact to a liquid nitrogen bath, but can be additionally heated to evaporate a potential blockade. This additionally gives the possibility to carefully adjust the gas temperature needed for the envisioned experiment. After passing the copper injection tube, the molecules enter the chamber through a ceramic nozzle (inner diameter: 1.3 mm, length: 13.5 mm). A gap of 0.5 mm between the front surface of the quadrupole and the nozzle mitigates heat transfer. Between the end of the nozzle and the first bend of the quadrupole an electron gun (exact replica of the one described in [82]) ionizes the gas in the center part of the guide via electron bombardment. The whole injection system can be replaced by an Electro-Spray Ionization source (see section 2.3) based on soft protonation methods [83], which provides an additional, of advantage in some case, molecular ion preparation option.

The intrinsic need of gas injection for the production process of molecular ions is incompatible with the ultra high vacuum demands of the experiments with trapped and crystallized ions. The lifetime of ions in the trap benefits from minimized background reactions and minimized fatal collisions with residual gas particles. The described quadrupole ion guide permits to transfer ions from the preparation zone to a well isolated experimental zone. This concept allows for the comparatively high pressure ($10^{-3} - 10^{-6}$ mbar), related to the efficient creation of molecular ions or even buffer gas cooling to address the molecule's internal degrees of freedom and clean experimental conditions, simultaneously. Starting at the end of the gas injection system, the guide meanders through three chambers, that are separated by two 10 cm long differential pumping stages (see figure 2.2 A and C). A ceramic MacorTM-tube that adapts well to the size of the quadrupole, reduces the cross section of the throughput to a minimum (see figure 2.2 C). Care has been taken to avoid uncontrolled charge-ups, for example, on insulators near the guide. The generation of long living charges can cause time dependent residual fields near the guide that would change the transfer efficiency or even hinder the guiding of ions in the quadrupole completely. Therefore, the ceramic parts of the differential pumping stage that would remain in line of sight for the ions have been replaced by gold plated copper bars. These four electrodes inside a differential pumping stage can additionally serve as compensation electrodes or act as drift tubes for the transferred charged particles inside the guide. The

¹⁶SAASS2060, Sill

¹⁷Series 99 2-way, Parker Hannifin Corporation Pneutronics

isolating properties of the differential pumping stages are additionally enhanced by the possibility to pump each chamber individually. The pressure in the last chamber is in the few 10^{-10} mbar regime. The differential pumping stages allow to maintain a pressure difference of approximately 4 orders of magnitude between the first and the last chamber.

2.1.2 Ba trap apparatus

The experimental studies on trapping barium and heavier molecular ions (refer to chapter 4) are performed in the same vacuum and trap apparatus, that is used in the $^{24}\text{Mg}^+$ case. The apparatus was described in detail in section 2.1.1 and [74]. However, some changes had to be implemented in order to trap and laser cool $^{138}\text{Ba}^+$ and will be summarized in this section.

In the atomic oven stack that provides trap 2 with an atomic beam (see also figure 2.2 B), two out of three resistively heated tantalum tubes are filled with barium. Barium metal is highly reactive with oxygen and a clean barium surface will be covered with an oxidized layer within tens of seconds when exposed to normal atmosphere. Depending on the thickness of the oxide layer, the oven must be heated to very high temperatures to evaporate the layer. In a worst case scenario, the oxidization might be so severe that it completely excludes the atomic barium flux needed to ionize an adequate amount of atoms. Due to the comparably long time it took to assemble the trap apparatus, the barium oven technique described in [74] failed, because of exactly the described reason. A thin indium foil had been used to seal the tantalum tube. The sealing had been done under protection nitrogen atmosphere and the barium chips inside the tube should have been protected sufficiently against humidity and oxygen. Although, test runs using this technique turned out positive, the sealing properties of the indium foil did not sufficiently protect the metallic barium inside the tube when exposed to normal atmosphere for days. Another completely different technique is therefore applied in this work and it turned out to be successful. After flooding the vacuum chamber with dry nitrogen, the old atomic ovens were replaced by new, but empty tantalum tubes. The two oven tubes that enclose an angle of approximately $100 \pm 5^\circ$ and $80 \pm 5^\circ$ with the propagation axis of the laser beam have equal dimensions and completely follow the design described in [75]. The tube under 80° to the laser beam propagation direction is filled with a magnesium wire using the technique in [74, 84]. The other, non-perpendicular tube is filled with barium. The atomic oven under 90° to the laser propagation direction is designed in a completely different fashion. Here a tantalum wire is wound to a coil and a piece of barium is inserted into that coil. This technique allows to use a bigger chunk of barium that survives longer in oxygenic atmospheres. It has nevertheless the disadvantage that the heating of the windings is very local and that there is no housing of the metallic barium, collimating the atomic beam. This oven serves only as a back-up system, because of the enhanced risk of coating the trap with a layer of barium and the related formation of patch potentials.

The newly developed technique to fill one of the non-perpendicular tantalum tubes to the trap axis, will now be described briefly. The purchased barium rod is dipped in paraffin oil right after breaking the sealing of the shipping container that maintained a protection atmosphere. Diagonal pliers are used to cut the fairly soft rod into a 10 mm

long and 0.8 mm thick chunk. The paraffin oil seals the freshly cut surface immediately and protects it against oxidization. This technique allowed to produce a thin barium wire that fits into the tantalum tube in air, without the use of a complex protection atmosphere glove bag setup. Before inserting the barium chunks into the assembled atomic ovens, a three minute supersonic inhibitor-free diethyl ether bath cleans the wire from the paraffin oil. Under the protection atmosphere of the nitrogen flooded vacuum chamber, the 0.8 mm thin barium wires and the approximately 2 mm thick barium chunk are inserted into the two empty ovens of different design. Afterwards, the chamber is closed and pumped down immediately. Approximately one minute elapsed between the filling of the ovens and the coarse pump down of the chamber with a screw pump. This minimized the duration the unprotected barium chunk was exposed to the imperfect nitrogen atmosphere. After the final pumpdown, the success of the used oven concept was verified by two different techniques. On the one side, the resistively heated barium ovens caused a peak at mass 138 u in the mass spectrum of the residual gas analyzer in chamber 3. On the other side, a laser near 553 nm (refer to section 2.2.2 for details) drove the $^1S_0 \rightarrow ^1P_1$ transition in neutral barium and the fluorescence of the cloud evaporated into the trapping region was directly detected by the CCD camera.

As discussed in section 1.1.3, for the laser-cooling of singly ionized barium, a weak magnetic field has to be generated in the trapping region, in order to avoid optical pumping into the $m = \pm 3/2$ states of the $5^2D_{3/2}$ manifold. By applying an external magnetic field, the quantization axis is no longer defined by the electric field vector of the laser radiation and all states are coupled via σ^\pm -transitions. The linear polarization of the cooling beam, as well as the observation and the propagation direction are orientated perpendicular to the magnetic field axis in all presented experiments. The external magnetic field in chamber 3 is generated by two coils separated by $d=22$ cm. The coils have an averaged radius $R=65$ mm and $N=43$ windings. The resulting magnetic field B per amps can be estimated [85] with the help of:

$$B/I = 4\pi \cdot 10^{-3} NR^2 / (R^2 + d^2/4)^{3/2} \quad [\text{G/A}]$$

The experimental parameters result in $B/I \approx 1.1$ G/A. The estimated external magnetic field for a 5 A current through the coils of 5.5 gauss was experimentally verified on the $\pm 10\%$ level by a direct measurement using a flux-gate magnetometer.

The UV transparent and anti-reflection coated UG-5 filter in the imaging beam path that protects the CCD-chip from visible stray light when working with $^{24}\text{Mg}^+$ ions is replaced by a yellow fluorescent protein (YFP) excitation filter¹⁸ (see figure 2.3). The multiple dielectric layers deposited on a fused silica substrate provide a transmission of $>93\%$ for the desired 493 nm cooling laser light with a sharp cutoff on both spectral sides. The transmission of wavelengths outside of the transmission window are highly suppressed. This filter efficiently protects the detector from the normal laboratory illumination and from the stray and fluorescence light induced by the 650 nm repumper.

¹⁸MF497-16, Thorlabs

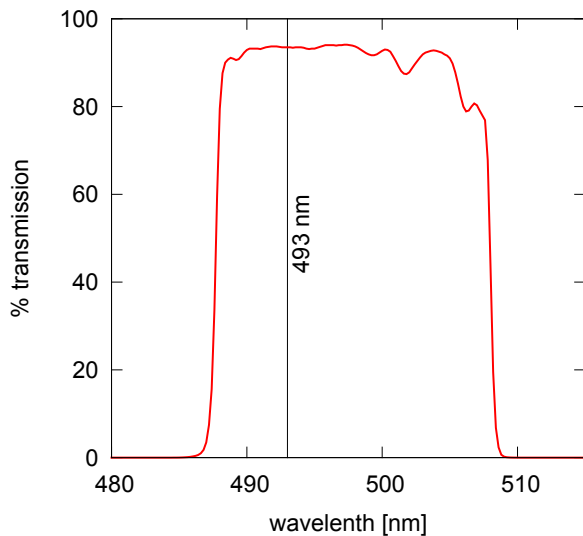


Figure 2.3: Transmission as a function of wavelength for the yellow fluorescent protein excitation filter used in the imaging beam path of chamber 3. The data is provided by the manufacturer. The filter features a high transmission ($>93\%$) at 493 nm, which is the fluorescence wavelength of the $S_{1/2} \leftrightarrow P_{1/2}$ transition used for $^{138}\text{Ba}^+$ Doppler cooling (refer to section 2.2.2 and 1.1.3). The transmission of the red repumper light is suppressed and effectively no 650 nm stray and fluorescence light is detected on the CCD-camera.

2.2 Laser systems

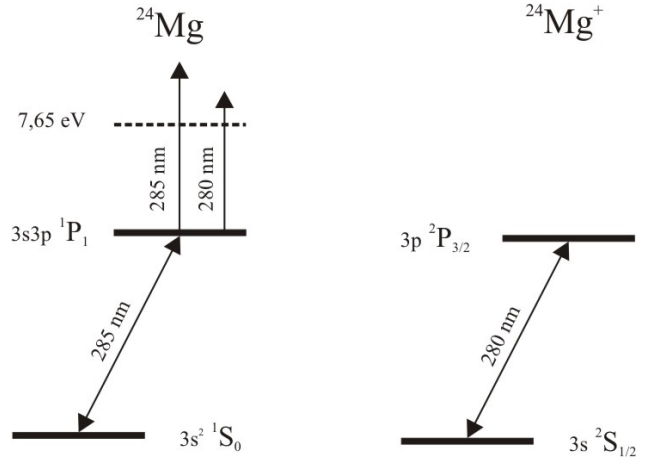
This section describes the lasers that were build up and are used in this thesis, starting with the two continuous wave (cw) systems needed to photoionize and laser-cool, both magnesium and barium. Following that, two sub-sections deal with the pulsed laser system used for the time-resolved pump-probe vibrational spectroscopy measurements on $^{24}\text{MgH}^+$. A more detailed description of the pulsed laser system can be found in [86, 87].

2.2.1 $^{24}\text{Mg}^+$ Doppler-cooling and photoionization

Figure 2.4 shows a schematic energy level diagram for the transitions used to photoionize neutral magnesium and to Doppler laser-cool the corresponding singly charged ion. The resonant two-photon process first demonstrated by [80] is used for photoionization. One photon with a wavelength near 285 nm excites the neutral magnesium atom from its ground state $3s^2S_0$ to the $3s3pP_1$ state. A second photon (285 nm) or a 280 nm photon of the Doppler cooling laser for $^{24}\text{Mg}^+$ is sufficient to reach the continuum. Since the first step towards ionization is realized by a resonant transition, this method provides a high isotope-selectivity. Additionally, it is more efficient than electron impact ionization. After the production, the singly charged magnesium is trapped and can then be Doppler laser cooled, in principle down to the Doppler limit (≈ 1 mK, see also section 1.1.3). The closed cooling cycle of $^{24}\text{Mg}^+$ consists of the $3sS_{1/2} \leftrightarrow 3pP_{3/2}$ transition with a natural linewidth of $\Gamma \approx 2\pi \cdot 42.7$ MHz [88]. A tunable, narrow linewidth all-solid-state laser system suitable for this kind of application has been demonstrated by [89] and will be used in the future. Within the framework of this thesis, the ultraviolet light at the required frequencies is created by frequency-doubled and long-term stabilized dye lasers.

A schematic summary of the laser setup for photoionization of neutral magnesium and laser

Figure 2.4: The relevant part of the energy level diagram of ^{24}Mg and $^{24}\text{Mg}^+$. For photoionization, a resonant two-photon process is realized. One photon near 285 nm excites the neutral magnesium atom from its ground state $3s^2\text{S}_0$ to the $3s3p\text{P}_1$ state. Another 285 nm photon or a 280 nm cooling light photon is sufficient to reach the continuum. The produced $^{24}\text{Mg}^+$ ions can then be Doppler laser cooled on the $3s\text{S}_{1/2} \leftrightarrow 3p\text{P}_{3/2}$ transition (see also figure 1.4).



Doppler-cooling of $^{24}\text{Mg}^+$ is shown in figure 2.5. Two cw dye ring lasers¹⁹ are pumped each by 3.5 W of a frequency-doubled Nd:YAG laser²⁰. For both lasers, the same dye solution (rohdamin 19 dissolved in ethylene glycol) is used. This laser system yields a typical output power of $\approx 500\text{ mW}$ at 570 nm and $\approx 250\text{ mW}$ at 560 nm. A regular maintenance period of three months for the exchange of the dye solution is sufficient. The degradation of the laser dye is most likely not the trigger for the service period, but rather a disadvantageous change in the dye viscosity, due to the exposure to air. Both dye lasers are long-term absolute frequency stabilized and locked using Doppler-free iodine spectroscopy. The cooling laser is stabilized using an absorption spectroscopy [90] setup with a 93 MHz double-pass acousto-optic modulator (AOM) in the pump beam. The 20 kHz modulation signal of a signal enhancing lock-in amplifier²¹ together with a voltage controlled oscillator drives the AOM. A typical Doppler-free iodine absorption spectroscopy signal obtained with this setup is shown in figure 2.6a. The stabilization of the photoionization laser is done without an AOM and signal enhancing techniques using polarization spectroscopy [91] (see figure 2.6b). Both spectroscopy setups are fiber coupled and Toptica's IodineSpec is used for the calibration of the frequency axis.

Two 70 m long, single-mode optical fibers connect the dye laser setup, that is located in a different laboratory, with the two second-harmonic generation (SHG) resonators [89] (see also figure 2.7) that share the same optical table with the vacuum apparatus. Both resonators are home-build, astigmatism-compensated SHG-external ring cavities based on a Brewster-cut β -barium borate (BBO) birefringent, non-linear crystal. The fundamental beam, exiting the fiber link, is mode-matched to the mode of the cavity by two spherical lenses. The full folding angle of the cavity is 27.4° to compensate the astigmatism induced by the BBO crystal. The exiting harmonic beam is projected into a Gaussian mode by a cylindrical telescope and collimated by a spherical telescope. Typical output powers of a few milli-Watts are easily achieved. The two UV-beams are finally overlapped on a polarizing beam splitter and focused into the vacuum chamber along the axis of the ion guide, using a $f=250\text{ mm}$ lens for the trap in chamber 1 and a $f=500\text{ mm}$ lens for

¹⁹the skeletal structure of the 699 and 899 model by Coherent is used, but various elements are upgraded

²⁰Millenia XP, Spectra Physics

²¹Model 116, Princeton Applied Research

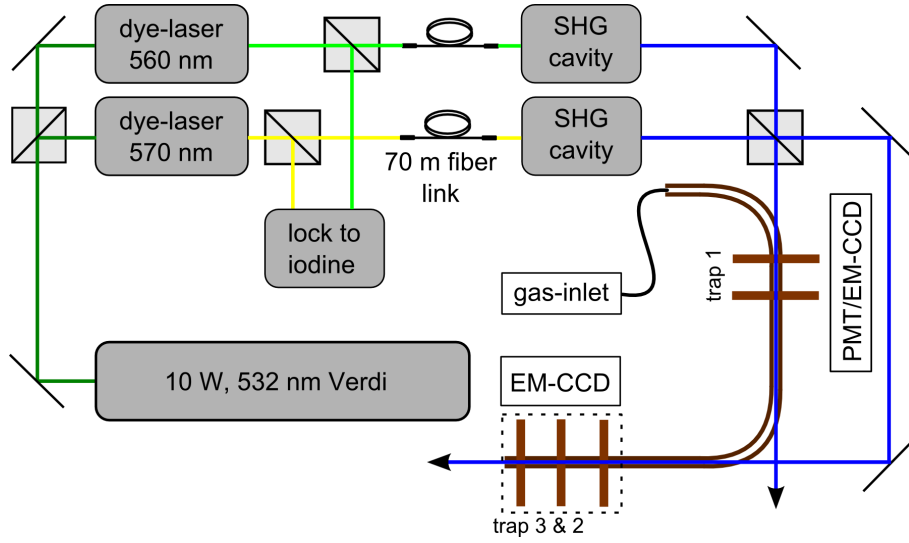
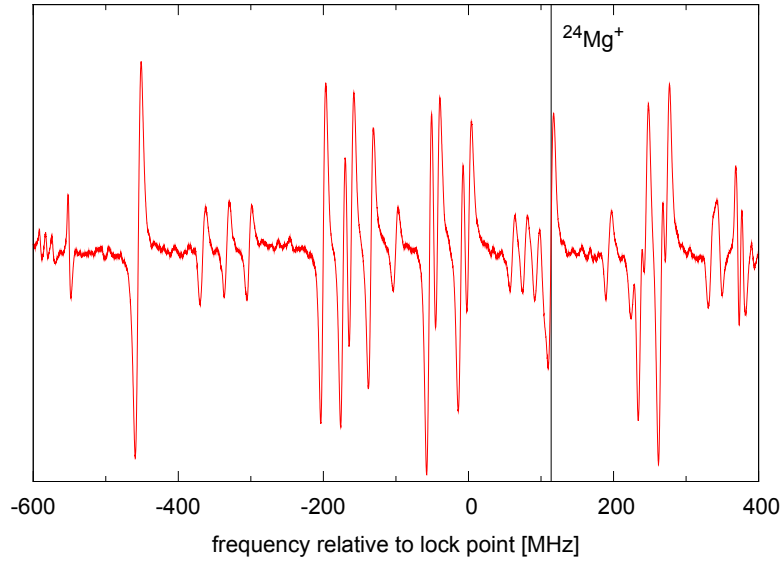


Figure 2.5: Schematic overview of the experimental setup, including the laser part for photoionization of neutral magnesium and Doppler-cooling of $^{24}\text{Mg}^+$. Two cw dye lasers pumped by a diode pumped solid state laser produce the two fundamental beams of the cooling (560 nm) and photoionization (570 nm) laser. These two lasers are long-term frequency stabilized and locked to iodine (see also figure 2.6). Two second-harmonic generation external ring-cavities (see also figure 2.7) frequency-double the output of the two dye lasers. The resulting 280 nm light for cooling of $^{24}\text{Mg}^+$ and the 285 nm light for photoionization of neutral magnesium are overlapped using a polarizing beam splitter and enter the quadrupole in the vacuum chamber along its symmetry axis via two laser ports (see also figure 2.1). The two beams are focused to a waist of $\omega \approx 80 \mu\text{m}$ at the position of the ions between the corresponding copper ring electrodes and propagate approximately along the symmetry axis of the trapped ion crystal.

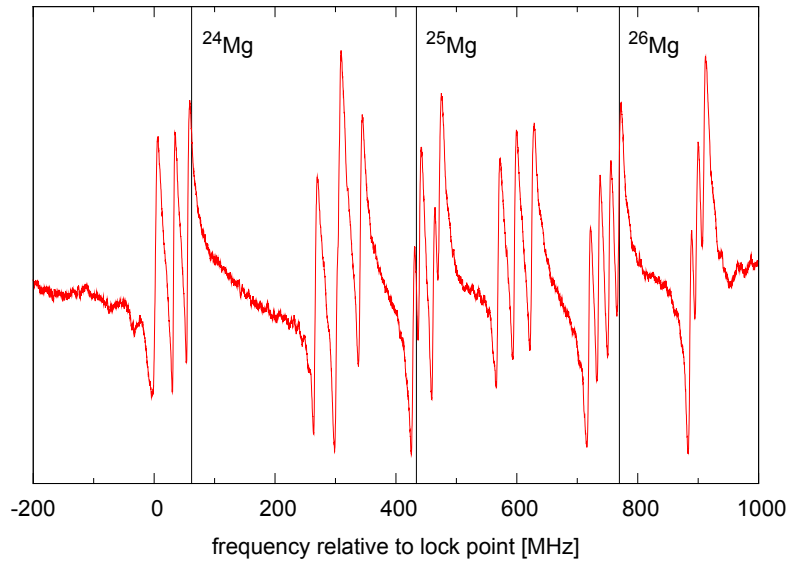
the traps in chamber 3. The orientation of the polarizing beam splitter guarantees, that the polarization axis of both beams is perpendicular to the imaging system, in order to enhance the collection efficiency of the objectives.

2.2.2 $^{138}\text{Ba}^+$ Doppler-cooling and photoionization

Four different cw lasers are used for photoionization of neutral barium and laser cooling of $^{138}\text{Ba}^+$. A schematic energy level diagram of the neutral atom and singly positively charged ion, including the used states and transitions is given in figure 4.1. Two different photoionization methods are exploited within this thesis and will be discussed in greater detail in 4.1. This section concentrates on the production of the two required lasers with wavelengths 553 nm and 413 nm for this purpose. As already discussed in 1.1.3 the simplest cooling scheme for $^{138}\text{Ba}^+$ requires two lasers. The main cooling transition couples the $6S_{1/2}$ ground state with the $6P_{1/2}$ state using a laser near 493 nm. The upper P-state decays with a 3:1 branching ratio into the ground and a metastable D-state [58]. The repumper laser near 650 nm avoids optical pumping into the $5D_{3/2}$ manifold. In this



(a) Absorption spectroscopy iodine spectrum near 560 nm. The frequency red-shift of the lock point to the absolute transition [92] labeled with $^{24}\text{Mg}^+$ is composed out of the double passed AOM in the pump beam and a natural linewidth red-shift (42 MHz) to achieve close to optimal cooling conditions.



(b) Polarization spectroscopy iodine spectrum near 570 nm. The marked frequencies [93] represent the atomic resonances of the three stable isotopes of magnesium. In order to enhance the isotope selectivity of the photoionization scheme in favor of ^{24}Mg , the lock point is shifted ≈ 62 MHz to the red.

Figure 2.6: Experimentally recorded iodine absorption and polarization spectrum, used to lock the frequency of the corresponding cooling and photoionization lasers for $^{24}\text{Mg}^+$ and ^{24}Mg . All values are given relative to the lock point used in the experiment.

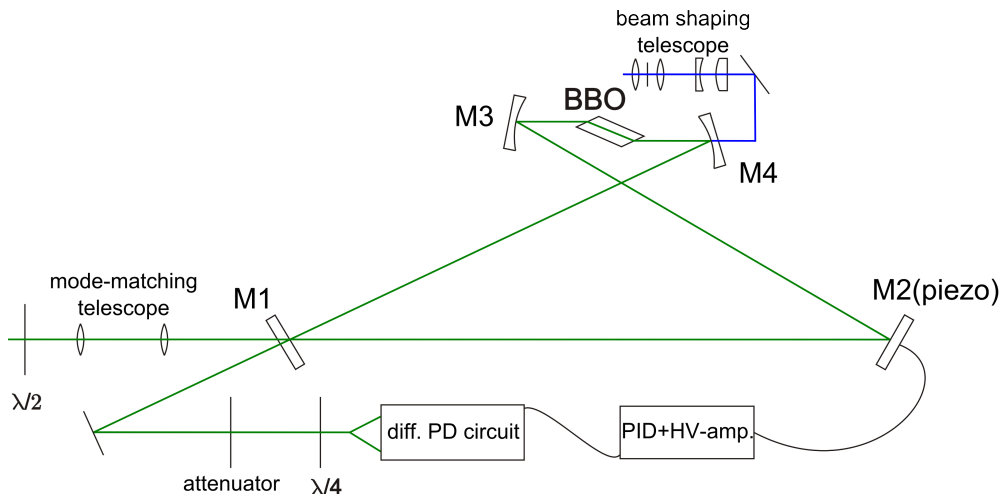


Figure 2.7: Schematic of the BBO bow-tie enhancement resonator and the Hänsch-Couillaud stabilization scheme [94]. The 470 mm long cavity is built around the 10 mm long non-linear crystal using the mirrors M1-M4. The second harmonic is produced in the crystal using critical type I phase matching. The in-coupling mirror M1 has a reflectivity of 98.4% for the fundamental beam to account for the losses inside the cavity. The folding mirror M2 has a reflectivity $>99.93\%$ and is mounted on a piezo. The two curved (ROC=50 mm) mirrors M3 and M4 create the optimal primary focus in the crystal. Additionally, M4 is used as an out-coupler with reflectivity $>99.8\%$ at 560 nm and transmission $>94\%$ at 280 nm. The part of the p-polarized fundamental beam that is reflected by the in-coupler overlaps with the part that travels through the cavity and is transmitted by the in-coupler. Because a change in the length of the cavity leads to a phase shift, these two beams form an elliptically polarized superposition, which is split into two orthogonal polarized components by a quarter wave plate and a Wollaston prism. A dispersive error signal for stabilizing the cavity length is created on a differential photodiode circuit. This signal passes a proportional-integral-derivative (PID) servo and a HV amplifier. The voltage created by the electronics is then applied to the piezo of the tweeter mirror M2.

section, the production of the two required wavelengths for the cooling scheme is discussed.

Figure 2.8 shows a schematic summary of the barium laser system. The three commercial narrow linewidth (typically 1 MHz), tunable diode lasers are operated in Littrow configuration. All diode laser systems consist of a diode laser head²², an adjustable anamorphic prism pair (AAP) to compensate the astigmatic ellipticity of the diode laser beam and a diode laser supply electronic rack²³. The supply rack provides the current through the laser diode, the grating scan voltage and the possibility to adjust the temperature of the diode. It additionally offers an input to add an external voltage to the offset of the scanning voltage of the piezo acting on the grating which can be used for remote control applications or active stabilization. A maximum of 100 mV are added directly to the backplane of the scan control plug-in module of the supply electronics. To fine tune the output frequency of

²²DL100, Toptica Photonics AG

²³Sys DC110, Toptica Photonics AG

the diode laser, a precision potentiometer adjusts this voltage to the required value. Right after the AAP a small fraction of each diode laser beam is coupled to a scanning Fabry-Perot-Interferometer (s-FPI) and a lambda-meter²⁴ with absolute accuracy of ± 0.3 GHz. The laser diode current, the offset voltage of the piezo actuator acting on the grating and the laser diode temperature are used to reach the desired wavelength range and single mode operation, simultaneously. To confirm that the laser oscillator runs single mode, the signal of the scanning Fabry-Perot Interferometer has to show equidistant fringes with the same amplitude. The 413 nm light for photoionization and the repumper light at 650 nm are directly produced by two of the diode lasers with 13 mW and 30 mW output power, respectively. The third diode laser produces 135 mW at 987 nm. To reach the desired 493 nm for Doppler cooling of $^{138}\text{Ba}^+$, this near-infrared beam is frequency doubled in a home-built second-harmonic generation cavity (see figure 2.9). The layout of this cavity is based on the technology already used in the production of the UV-beam for Doppler cooling of $^{24}\text{Mg}^+$. Non-critical phase matching in a 10 mm long, b-cut KNbO_3 biaxial, birefringent crystal is used to produce the second-harmonic at 493 nm. The crystal front surfaces are anti-reflection coated for the fundamental wavelength to minimize inter-cavity losses. The optimum temperature $T = 41.5^\circ$ of the crystal is maintained by a platinum heater and controlled by a temperature transducer and a temperature stabilization loop electronic. The bow-tie enhancement cavity around the crystal has a full folding angle of only 14° , limited by mechanical constraints. A small folding angle minimizes astigmatism induced by the tilted spherical mirrors. The output second-harmonic beam is walk-off free and the Gaussian mode profile is collimated with two spherical lenses. This beam is coupled into a single-mode optical fiber that is out-coupled on the optical table of the experiment. The second-harmonic generation setup is mounted on a separate breadboard to allow for a maximum in flexibility. After first optimization, this diode laser driven enhancement cavity produces 20 mW of output power at 493 nm. However, it turned out that the 30 dB optical Faraday-isolator that protects the laser head from back reflections, is not sufficient. Operation of the diode laser in scanning mode and a simultaneously stable locking of the enhancement cavity was not possible. Optical feedback into the laser head and the resulting spectral disturbances were minimized by tilting the doubling crystal out of the former orthogonal orientation to the resonator mode by a few degrees. The temperature of the crystal had to be readjusted to $T = 34.1^\circ$ and the output dropped to ≈ 5 mW. That way, a drawback in power allows a stable scanning operation and still enough power for laser cooling of $^{138}\text{Ba}^+$ ions is available after the fiber. For more information about the parameters of the second-harmonic generation enhancement resonator see figure 2.9 and for a more detailed treatment of the resonator design and the characteristics of the crystal, refer to [74].

The laser near 553 nm additionally needed for one of the ionization schemes is produced by the cw dye ring laser that also serves as the cooling laser for $^{24}\text{Mg}^+$. The wide tunability of this laser system permits to re-use it for the purpose of photoionization of neutral barium. Moreover, the same dye solution, consisting of rhodamine 19 diluted in ethylene glycol, is used and 50 mW of output power are easily produced on a daily basis. Although pyrromethene 556 with a peak power operating wavelength of 553 nm would be the optimal choice for the highest power output, the lasing dye solution is not changed

²⁴WA1000, Burleigh

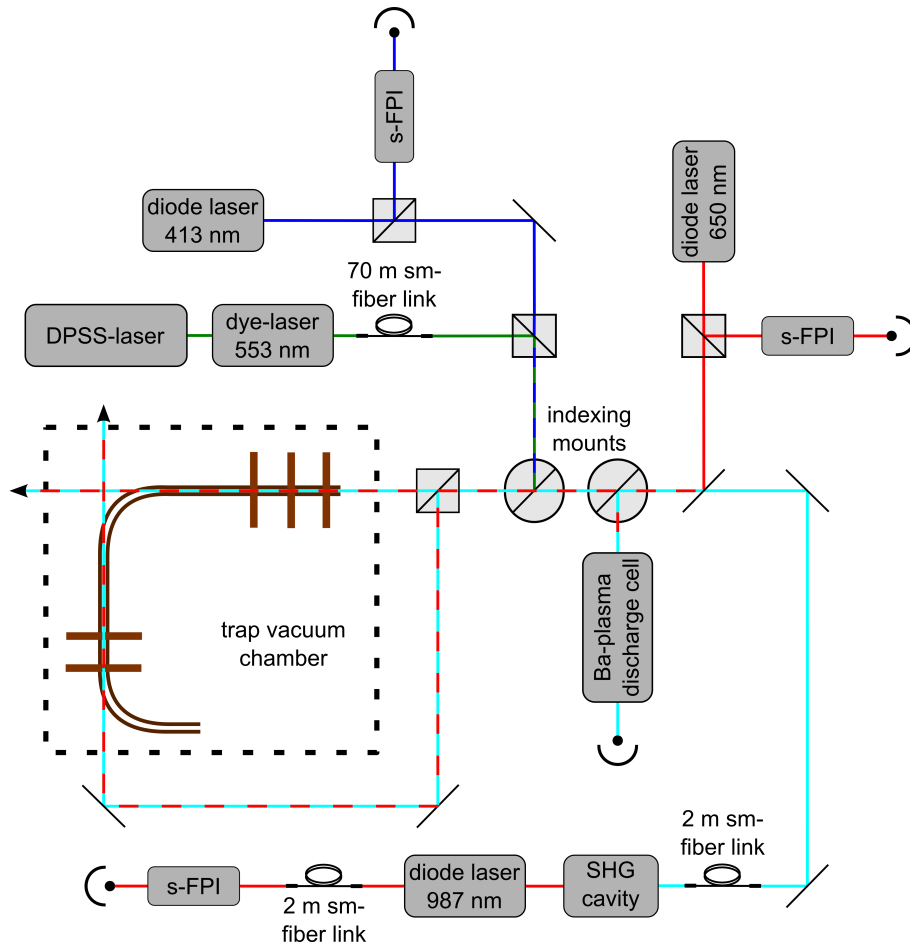


Figure 2.8: Schematic layout of the laser system for photoionization of neutral barium and laser cooling of $^{138}\text{Ba}^+$. The trap apparatus with the double-bended RF-guide and the three Paul traps is adumbrated in the dashed frame. Two lasers, one at 553 nm, provided by a fiber coupled dye-laser and one at 413 nm provided by a tunable external-cavity diode laser in Littrow configuration, are used for photoionization purposes. These two laser are polarization overlapped on a polarizing beam splitter and can illuminate the Paul traps in chamber 3 and chamber 1 by using a removable indexing mount and a beam splitter. The 650 nm repumper light for laser cooling is also directly produced by a diode laser. A frequency doubled IR-diode laser produces the main cooling wavelength at 493 nm. All diode lasers can be coupled into a wavemeter and a scanning Fabry-Perot Interferometer (s-FPI). The two cooling lasers are overlapped on a red reflector mirror (see also figure 2.10) and focused on the ions confined in the trap. After the overlap, another indexing mount can couple the two cooling lasers into a barium discharge cell. Absorption in the plasma is used to fine tune the absolute frequency to the ionic transitions (see also figure 2.11 and figure 2.12).

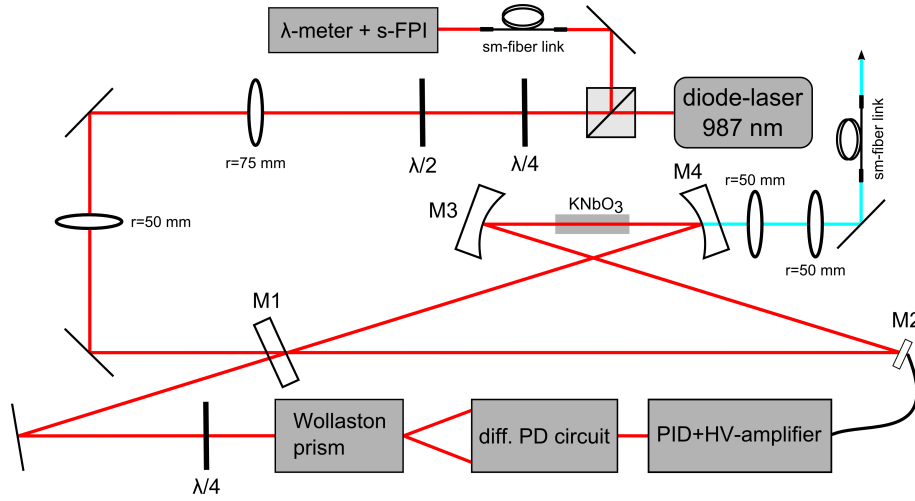


Figure 2.9: Basic layout of the SHG enhancement resonator used to produce light at 493 nm for $^{138}\text{Ba}^+$ Doppler-cooling. The fundamental beam is mode matched with the help of two spherical lenses to the mode of the resonator build by mirrors M1-4. KNbO_3 is used as a birefringent, non-linear crystal. The optimal focal beam waist in the middle of the crystal is approximately $16\ \mu\text{m}$. The distance between the two spherical (ROC=38 mm) mirrors M3 and M4 is 45 mm and the overall cavity length amounts to 535 mm. The in-coupling mirror M1 has reflectivity for the fundamental beam of 94 % to account for the losses inside the resonator. All other mirrors have a reflectivity higher than 99.5 % for the fundamental beam with an angle of incidence between 7° and 10° and are high transmittivity coated for 493 nm. The backside of the output coupler M4 is additionally anti-reflection coated for the harmonic. Similar to the case of figure 2.7 the cavity is stabilized using a Hänsch-Couillaud scheme. The harmonic beam is collimated and coupled into a single-mode optical fiber by two spherical lenses.

because of obvious compatibility reasons. Nevertheless, the rhodamine 19 solution is more than sufficient for the intended application. Since recently, a commercial, frequency doubled diode laser system operating at 553 nm is available with suitable output power and is planned to substitute the dye laser²⁵. With this, an easy to handle, all-solid-state laser system can be used for the very effective photoionization of neutral barium described in section 4.1.

To minimize reflection and transmission losses of the various laser beams with different frequencies, mirrors with a specially designed broad-band high reflectivity coating²⁶ and lenses with a broad-band anti-reflection coating²⁷ are used for beam steering and shaping in the setup. The only exclusions are two UV enhanced aluminum mirrors that build up a periscope to reach the trap height and the re-used two lenses that focused the UV beams for $^{24}\text{Mg}^+$ near the trap centers of chamber 1 and 2. By re-using these components for the barium laser setup, a maximum of compatibility is achieved. The overlap of the two cooling beams for barium is done on a red reflector mirror under 45° . These standard mirrors

²⁵Toptica Photonics AG

²⁶BBHR 400-660 nm, Laseroptik

²⁷BBAR 400-700 nm, Laseroptik

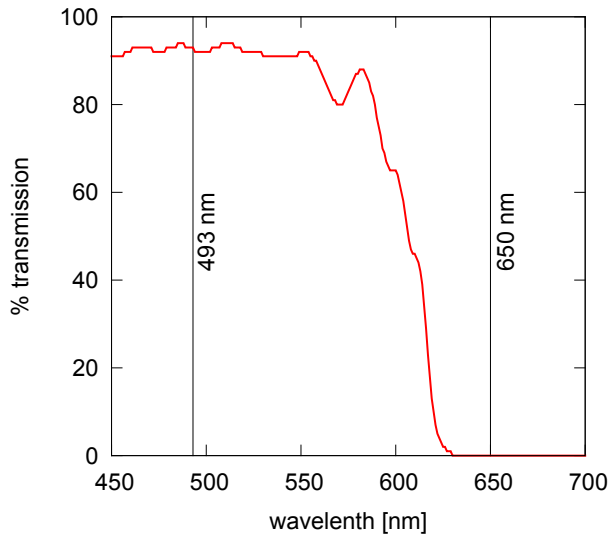


Figure 2.10: Transmission as a function of wavelength for the red reflector mirror used to overlap the two cooling beams for $^{138}\text{Ba}^+$. The data is provided by the manufacturer^a. The 493 nm light lies in the high transmission region of the spectrum, whereas the reflection of 650 nm light on this mirror is very high.

^aThorlabs GmbH

are typically used to block unwanted heat from a heat sensitive setup. Figure 2.10 reveals that they provide a rather steep slope between a high transmission region in the blue and a high reflectivity region in the red. As a matter of fact, the 493 nm light lies in the high transmission and the 650 nm light lies in the high reflectivity region. Consequently, this mirror is nearly perfectly suited to overlap the two beams, which otherwise would require a polarization dependent technique and might interfere with the polarization demands of the cooling scheme. However, due to the 1 mm thickness of the substrate, the beam profile of the reflected beam is not perfect anymore, but still good enough to serve as a repumper in the cooling scheme.

The two lasers for photoionization are polarization overlapped on a polarizing beam cube. These two beams can be directed and focused to the center of trap 2 in chamber 3 by using a removable indexing mount in the beam line of the cooling lasers. Mostly due to reflection losses on the periscope, build up by two aluminum mirrors and Fresnel-reflections on the focusing lens, approximately 5 mW maximum power of the 413 nm laser are available in front of the entrance laser port to the vacuum apparatus. In order to avoid too strong saturation effects, the power of the 553 nm laser is restricted to a maximum of 5 mW, although a factor of five more would be available with the present setup.

After coarse frequency adjustment using the wavemeter, the cooling beams are directed to a gas filled barium discharge cell with the help of an indexing mount. This cell is an opto-galvanic sensor²⁸ with a see through hollow barium cathode. The cathode and the ring-shaped anode are mounted inside a neon gas filled glass bulb with Brewster's angle input and output windows. A voltage of 350 V produces a discharge plasma at the hole of the cathode. Normally, this cell is used to observe a change in the electrical properties of the plasma when illuminated by resonant laser radiation. The change in conductivity of the discharge plasma irradiated by resonant light is known as the optogalvanic effect and the obtained optogalvanic signal can be used to measure the absolute wavelength of the incident laser. Optogalvanic sensors can also be applied for stabilization of the laser

²⁸Laser Galvatron Series L2783, Hamamatsu Photonics

radiation. In the framework of this thesis, the laser galvatron is used as an absorption cell. Photons out of a resonant laser beam, propagating through the plasma, can be absorbed by either neutral barium atoms or singly charged barium ions. The change in intensity of the laser beam propagating through the cell compared to a freely propagating reference beam is monitored using a differential photodiode²⁹ circuit. With this technique, it is possible to tune *all* lasers used for barium to the needed absolute frequency of the transition with a precision of approximately 100 MHz. On a daily basis, the tuning of the photoionization beams with the help of the wavemeter is sufficient, and only the 650 nm and 493 nm laser is tuned using the discharge cell. Figure 2.11 shows a typical signal of the discharge cell absorption setup, as seen on an oscilloscope. In this case, the 493 nm cooling laser scans approximately 1.6 GHz symmetrically around the resonance. The black curve is the standard TTL output signal from the scan control of the diode laser. It is used to synchronize the oscilloscope and to identify regions of up or down scan of the laser. The colored part of the two gray curves, in between the dashed lines, corresponds to one single frequency up scan. The green curve shows the photodiode signal after the disabled barium discharge cell. In contrast, the red curve corresponds to the photodiode signal with enabled discharge cell. The absorption dip of the $6S_{1/2} \rightarrow 6P_{1/2}$ transition in singly ionized barium is clearly visible. In addition to the lower time axis, the single up-scan region is frequency calibrated with the help of a Fizeau wavemeter³⁰ with 10^{-6} relative accuracy. The result is shown in the upper horizontal axis. The offset voltage of the piezo driving the grating is tuned to a value where the scan is symmetric around the resonance. By turning off the scan, the laser rests at the middle frequency of its former scan. This way, all lasers can be tuned to an absolute frequency value near the desired transition frequency with a precision sufficiently high for efficient cooling of trapped barium ions, using a cost-effective setup.

For the initial loading of barium ions, the repumper 650 nm laser is prepared exactly the way it is described above. With the help of the barium discharge cell, it's tuned close to resonance. After loading, the offset voltage of the piezo can be fine adjusted with the help of the precision-potentiometer by maximizing the fluorescence of the $^{138}\text{Ba}^+$ -ions in the trap. As described in section 1.1.3, the main cooling laser at 493 nm has to be about one natural linewidth red-detuned from resonance to achieve optimal cooling of an ensemble of ions. A blue-detuning from resonance would lead to a heating of the ions and cause a breakdown of the fluorescence. For this reason, the laser scan is adjusted with the help of the discharge cell to the red side of the resonance. Figure 2.12 shows a typical laser scan before loading. The resonance dip is far on the blue side of the scan. A slight scanning over the resonance is used to observe a pronounced blinking of the ions in the trap for the first daily loading attempts. After successful loading, the scan is turned off and the frequency of the laser is fixed in the middle of the scan interval, still far on the red side of the resonance. The offset voltage of the grating piezo is used to tune the laser more and more to higher frequencies, until optimal laser cooling is achieved. After this initial procedure, the two cooling lasers have to be slightly readjusted in frequency from time to time because of the lack of a direct long-term frequency stabilization. As already mentioned, an implementation of an active frequency stabilization of the barium

²⁹S5821-01, Hamamatsu Photonics

³⁰WS/6D, High Finesse

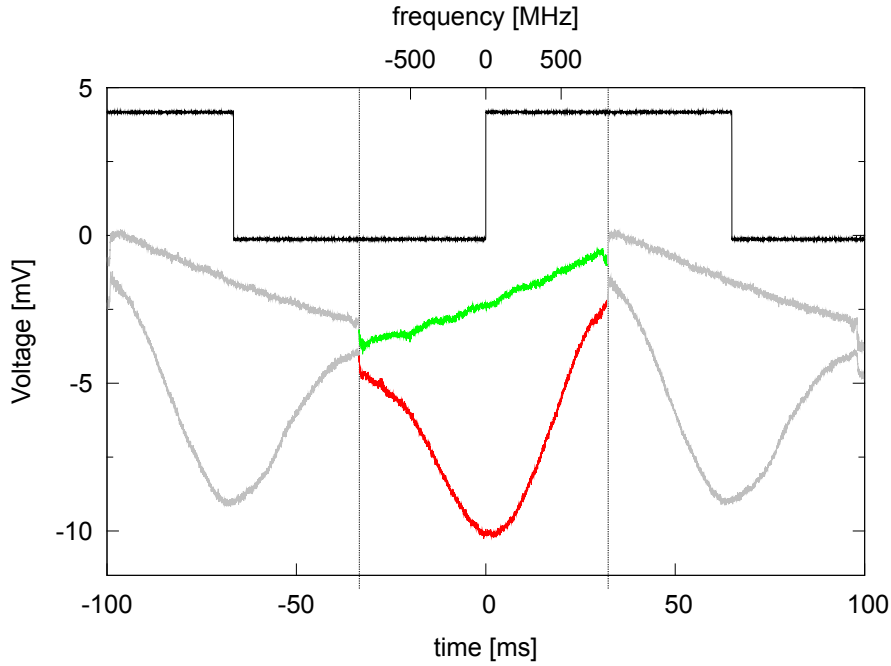


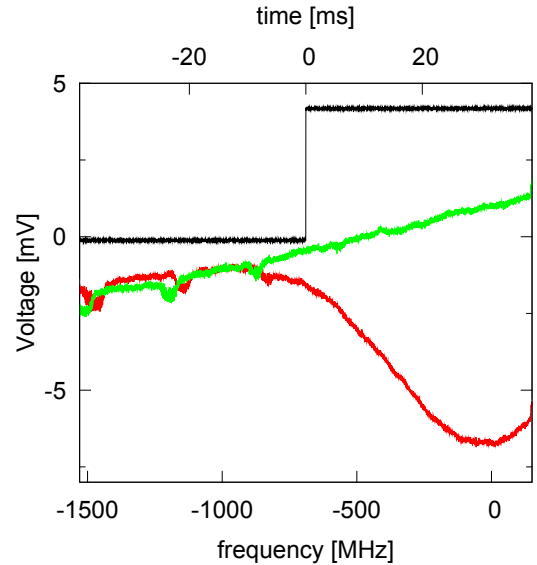
Figure 2.11: Signal of the differential photodiode circuit after the opto-galvanic sensor, illuminated with resonant 493 nm light. The black curve is the TTL monitor signal provided by the commercial diode laser driver electronics. The frequency of this signal corresponds to the scan frequency of the laser and is shown here to indicate regions of up- and down-scans of the laser. The two gray curves are the photodiode circuit output voltages for an activated and a disabled opto-galvanic sensor. The region of a single frequency up-scan is bordered by the two vertical dashed lines. In this region, the green curve is taken without a barium discharge plasma present. The red curve, in contrast, is the signal with an activated discharge cell. The small global vertical offset between these two curves is due to an illumination of the photodiodes by the plasma itself. In comparison to the green curve, the red curve shows a dominant ≈ 770 MHz (FWHM) broad absorption dip of the transition $6S_{1/2} \rightarrow 6P_{1/2}$ that is approximately centered with respect to the scan. The upper frequency axis corresponds only to the colored part of the gray curves and is calibrated by a high resolution Fizeau-wavemeter.

laser sources is one of the next, future steps. Nevertheless, the actual cooling laser setup is absolutely sufficient to perform experiments, where a long-term frequency control is not required, e.g. the experiments on photoionization of neutral barium presented in section 4.1.

2.2.3 Few-cycle NIR/VIS pulses

The shortest deep-ultraviolet laser pulses generated so far [95] have been used in this thesis to perform time-resolved experiments on single molecular ions. Intense, ultrashort laser pulses with a spectral range spanning from the visible (VIS) to the near infrared (NIR) are used to generate sub-4 fs UV-pulses in a non-linear, third-harmonic generation process.

Figure 2.12: Same situation as in figure 2.11, but only a single frequency up-scan of the 493 nm laser is shown. The laser scans slightly over resonance, visible as the absorption dip on the far blue side of the scan. Once ions are confined in the trap and the repumper laser is set properly (again with the help of the barium discharge cell) a dominant fluorescence blinking can be observed. Afterwards, the scan is turned off and the laser stops in the middle of the former scan interval, thus comparably far red detuned from resonance to avoid a heating of the ions. With the help of the offset voltage on the piezo, the frequency is fine tuned on the fluorescence of the confined $^{138}\text{Ba}^+$ -ions.



The second part of this section describes the generation of these UV-pulses in a noble gas target and the preparation of spectrally shaped pulse replica that serve as pump and probe beams for the experiment. The first part concentrates on the laser system that provides the fundamental few-cycle NIR/VIS pulses for the third-harmonic generation. For a more detailed treatment refer to [87].

A schematic summary of the NIR/VIS laser system is shown in figure 2.13. Pumped by 4.35 W of a solid state green cw laser³¹ at 532 nm, the Ti:Sapphire oscillator³² produces 4.6 nJ pulses with a duration of 6 fs and a repetition rate of approximately 71 MHz. These pulses seed the Chirped-Pulse-Amplifier (CPA) system³³ that consists of three stages. The stretcher, a piece of flint glass with normal dispersion, induces a positive chirp in the pulse. The duration is stretched to about 10 ps and the pulse peak power is severely reduced. The pulses are now amplified in a Brewster's angle cut Ti:Sapphire crystal that is cooled down to 193 K, without concern that the crystal might be damaged. A pulsed laser³⁴ at 532 nm with 20 W averaged power pumps the amplifier crystal and the seed pulses are boosted to 1.6 mJ after nine subsequent passes. After four passes, a Pockels cell, synchronized with the pump and the oscillator, picks pulses with a repetition rate of 3 kHz. After the amplification stage, a compressor reduces the pulse duration to about 22 fs. This stage consists of the main prism compressor and a subsequent chirped mirror compressor compensating the chirp induced in the bulk material of the last prism. Fully compressed pulses with a pulse energy of 1.25 mJ and a repetition rate of 3 kHz leave the Chirped-Pulse Amplifier system.

The spectral width of the pulses produced in the CPA does not support a few cycle duration in the corresponding spectral range. The spectrum is therefore additionally broadened via

³¹Verdi V10, Coherent

³²Femtosource Compact Pro, Femtolasers GmbH

³³modified Femtopower Compact Pro, Femtolasers GmbH

³⁴Photonics Industries

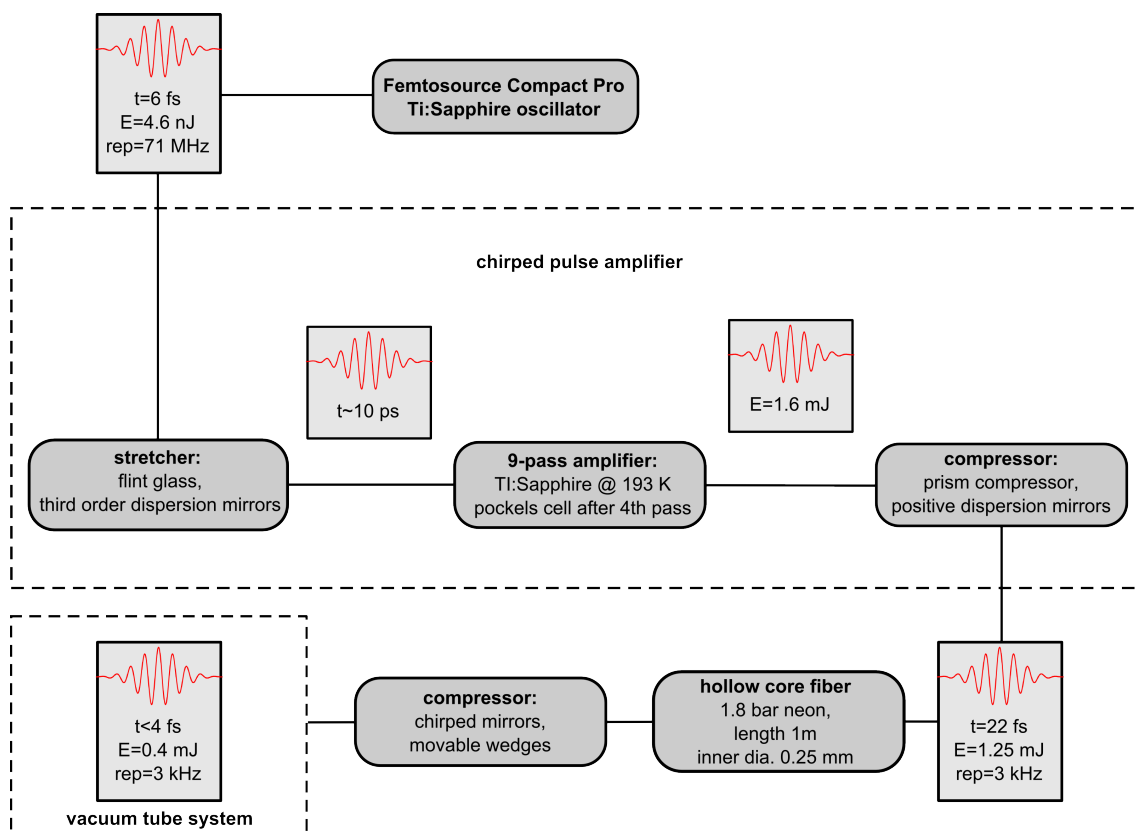


Figure 2.13: Schematic of the laser system that produces few-cycle NIR/VIS pulses used as the fundamental for the third-harmonic generation process described in 2.2.4. The pulse parameters (duration: t , energy: E and repetition rate: rep) after essential parts of the system are given in the boxes above the schematic beam line. After the oscillator, a Chirped-Pulse Amplifier system amplifies the stretched pulses and compresses them afterwards. Spectral broadening, due to self-phase modulation in a neon filled hollow-core fiber and subsequent compression in a chirped mirror compressor leads to sub-4 fs NIR/VIS pulses with $400 \mu\text{J}$ energy and 3 kHz repetition rate. To inhibit pulse broadening in the time domain due to dispersion in air, the pulses are coupled into a vacuum tube system right after the final compression.

self-phase modulation in a noble gas [96]. A beam stabilization setup ensures stable in-coupling of approximately 50% of the power into a 1 m long, fused silica hollow-core fiber with $250 \mu\text{m}$ inner diameter. Inside the fiber, a neon atmosphere at 1.8 bar pressure is maintained. The broadened spectrum after the hollow-core fiber consists of components ranging from the visible (500 nm) up to the near-infrared ($1 \mu\text{m}$) [97, 95]. A pair of moveable wedges are used to fine tune the amount of dispersion inducing glass in the laser beam, in order to precompensate part of the negative GDD induced by the following chirped mirror compressor. Six reflections on specially designed, high reflectivity chirped mirrors compress the pulses to sub-4 fs and leave pulse energies of 0.4 mJ.

Various parts of the presented NIR/VIS-laser system have been fine adjusted to enhance

the following third-harmonic generation process (see section 2.2.4) or change the spectrum in a way, suitable for the experiment (see section 3.2). Due to the complex interplay of the different fine tune parameters, this is an iterative process. The divergence and the spatial mode of the beam after the hollow-core fiber depends on the quality of the in-coupling. Because self-phase modulation is a non-linear process, the adjustment of the prism compressor affects the spectrum and the UV-generation process. Two other parameters that have been tuned during the measurements presented in 3.3 are the movable wedges and the pressure in the hollow-core fiber.

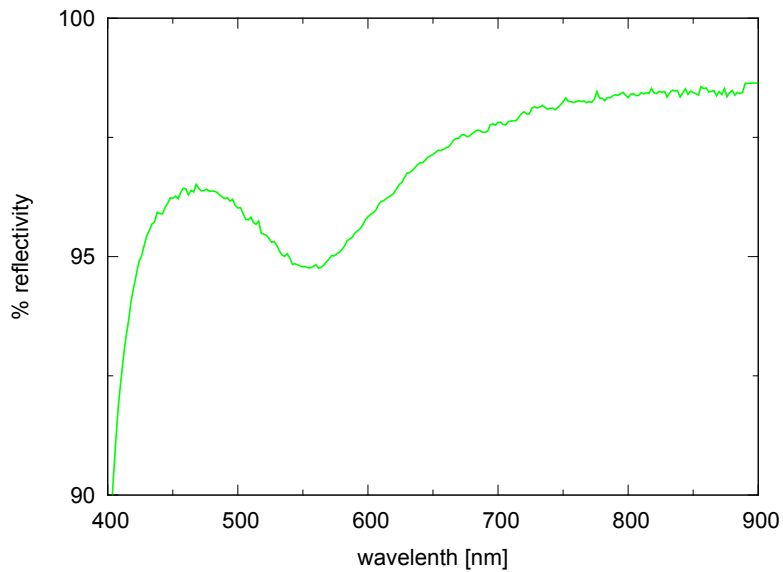
2.2.4 UV-pulse pair generation and connection to the trap

The few cycle NIR/VIS pulses, discussed in the last section, are very sensitive to pulse broadening, due to dispersion in air. Therefore, right after the final compression, the laser pulses are coupled into a vacuum tube system. A schematic of the following UV-laser beamline can be found in figure 2.15. After passing several vacuum chambers, used to steer the pulses to various other experiments, the beam enters the third-harmonic generation (THG) chamber. Four reflections on commercial silver mirrors (a reflectivity curve versus wavelength for the interesting part of the spectrum can be seen in figure 2.14a) steer the pulses to the THG. The beam path up to this point is approximately 15 m long. A 3-D technical drawing of the THG chamber shows figure 2.16a. Inside this chamber two planar Ag-mirrors direct the beam on a curved Ag mirror (ROC= 1.2 m) that focuses the beam to a waist of approximately 50 μm on the gas target. The laser drills the hole in a closed nickel tube ($\text{\O} 3 \text{ mm}$ squeezed to 1 mm inner width, 0.1 mm wall thickness) containing the noble gas at an adjustable pressure of up to 5 bar. The tube can be fine positioned in the focus of the fundamental laser beam by a xyz-manipulator. Although, this technique ensures minimal possible connection of the high pressure region of the target and the vacuum chamber, the gas load would be far too high to maintain an acceptable background pressure. The target is therefore placed in small target chamber that can be pumped separately by a screwpump³⁵, inside the actual vacuum chamber. The laser enters and exits the target chamber via two small exchangeable apertures ($\text{\O} 0.25\text{-}1 \text{ mm}$). Outside the target chamber a comparably low pressure (10^{-3} mbar) can be maintained by a turbomolecular pump³⁶. The generated harmonic beam propagates less than 4 cm in the high pressure region, due to the small dimensions of the target chamber. This reduces absorption of the harmonic photons to a minimum. In addition to the tuning parameters discussed in 2.2.3, the target position, the gas pressure and the laser intensity are used to enhance the third-harmonic production yield. A more detailed discussion of the mechanical layout of the third-harmonic generation chamber and the UV production process can be found in [86].

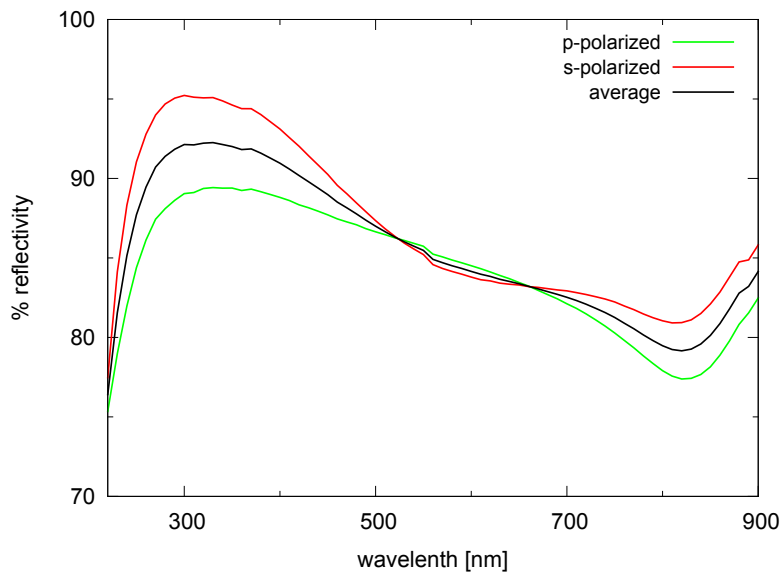
A periscope consisting of two UV-enhanced aluminum mirrors (for a reflectivity measurement refer to figure 2.14b) couple the nearly co-propagating UV and residual NIR/VIS beams into a differential pumping stage that separates the third-harmonic generation chamber from the following delay chamber. The differential pumping stage is pumped

³⁵ScrewLine SP250, pumping speed: 200 m^3/h , Leybold

³⁶TMP600C, pumping speed: 600 $1/\text{s}$, Oerlikon



(a) Reflectivity of metallic silver mirrors as a function of wavelength for 45° angle of incidence provided by the manufacturer.



(b) Reflectivity of the metallic UV-enhanced aluminum mirrors as a function of wavelength and angle of incidence provided by the manufacturer

Figure 2.14: Reflectivity measurements versus wavelength for the metallic mirrors used in the pulsed UV beamline. The Ag mirrors, due to their high reflectivity feature in the wavelength range 450-900 nm, are exclusively used in the NIR/VIS beamline. The UV-enhanced Al mirrors provide a reflectivity on the order of 90% for pulses with a spectral width of approximately 20 nm centered at 280 nm as used in the experiment.

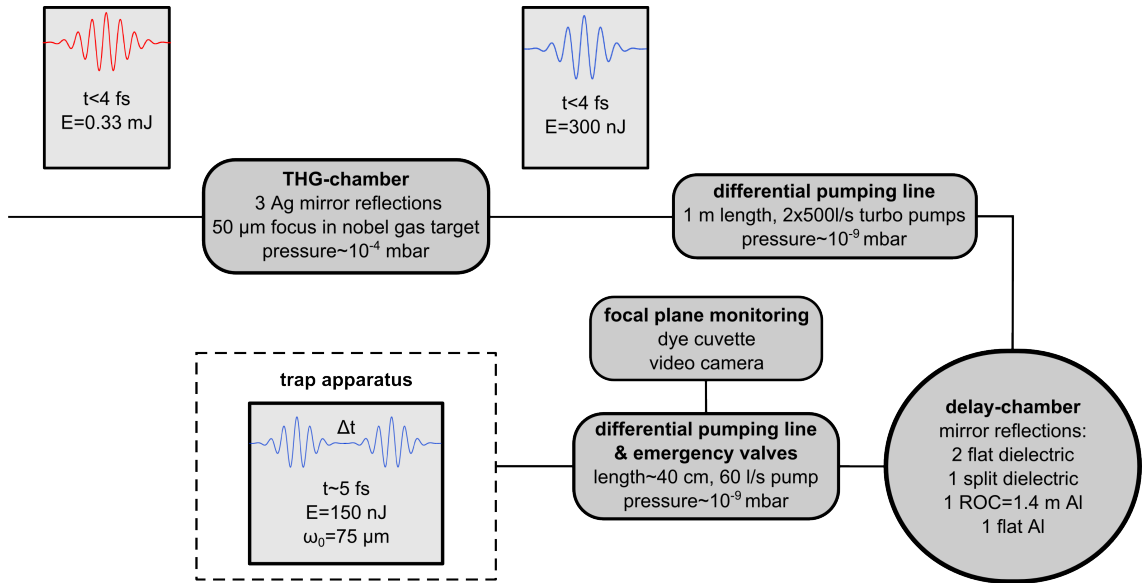


Figure 2.15: Schematic of the femtosecond UV-laser beamline. Two differential pumping lines separate the delay chamber from the third-harmonic generation chamber and the trap apparatus. Pulse parameters after important steps are given in the rectangular boxes.

by two turbomolecular pumps³⁷. The delay chamber is used to spectrally filter the UV beam, generate two time-delayed pulse replica and to steer them onto the ions in the trap apparatus. A turbomolecular pump³⁸ in combination with the isolation properties of the differential pumping stage maintains a low $1 \cdot 10^{-9}$ mbar pressure in the chamber. A view inside the delay chamber gives figure 2.16b. A comparison of the pulse parameters in figure 2.15 reveals that the residual NIR/VIS pulses are three orders of magnitude stronger than the UV pulses. The properties of the molecular ion used in the experiment (see section 3.2) call for a nearly complete suppression of the fundamental pulses and special spectral properties (suppression of the higher frequency part) of the UV-pulses. Both requirements are fulfilled by custom designed dielectric mirrors³⁹. A reflectivity measurement as a function of wavelength of these mirrors shows figure 2.17. The mirrors additionally provide a nearly flat spectral phase in the spectral region 265 nm-300 nm, resulting in a nearly linear-chirp free reflected pulse. Slightly different angles of incidence are used (refer to figure 2.17) to damp the oscillation amplitude on the higher frequency side of the high reflectivity interval and therefore achieve a better suppression.

After two reflections on flat dielectric mirrors (M1,M2), the last dielectric mirror M3 is hit by the pulses (refer to figure 2.16b). This one inch mirror consists of two half mirrors, where the upper half is mounted on a piezo driven translation stage⁴⁰ and can be shifted with respect to the lower half. The two half mirror setup splits the UV-beam into two nearly identical replica. The part of the pulse that hits the upper half mirror has a slightly

³⁷2x500l/s, Pfeiffer Vacuum

³⁸400l/s, Pfeiffer Vacuum

³⁹layertec

⁴⁰nanoSX400CAP, piezosystem jena

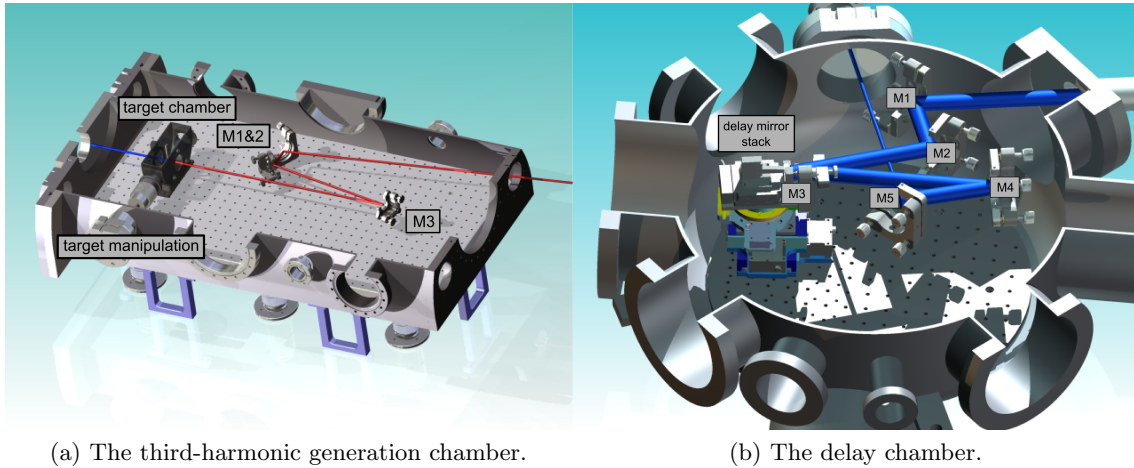


Figure 2.16: The two main chambers of the ultra-short pulse laser beamline with implied NIR/VIS (red) and UV (blue) beam path. In (a), parts of the third-harmonic generation main chamber and the small target chamber is shown. The flat Ag mirrors M1-2 direct the beam to the curved (ROC=1200 mm) Ag mirror M3. The beam is focused down on the gas target that can be precisely positioned (resolution $\approx 10 \mu\text{m}$) using a xyz-vacuum manipulator. The peak intensity of the pulses at the gas target is approximately $7 \cdot 10^{14} \text{ W/cm}^2$ [97]. Computer drawing (b) shows the delay chamber that is separated to the THG chamber by a differential pumping stage. The dielectric (see figure 2.17) mirrors M1-3 are used to significantly reduce the NIR/VIS pulse intensity and spectrally shape the UV pulses. The mirror M3 is split and the upper half can be translated with the help of a precision piezo. The two half mirrors are mounted on a positioning stack, consisting of two piezo driven translation stages and one rotation stage. The curved Al-mirror M4 focuses the two time-delayed replica of the UV-pulse on the trap center and the Al-mirror M5 is used to steer the beam inside the trap chamber in order to hit the ions.

different propagation length, adjustable by the piezo of the translation stage with a 1 nm resolution. The two pulse pairs arrive therefore with a specific time delay Δt at the target. To fine tune the position and the angle of the two half mirrors, the whole mirror setup is mounted on two orthogonal translation stages with a resolution of 100 nm and one rotation stage with a resolution of $24 \mu\text{rad}$ ⁴¹.

The following two reflections on aluminum mirrors align the two UV-pulse replica with the longitudinal axis of the trap. The spherical mirror M4 has a radius of curvature of 1.4 m and focuses the pulses to a beam waist of approximately $60 \mu\text{m}$ - $75 \mu\text{m}$ (see also figure 2.18). Care has been taken to minimize the reflection angle on the curved spherical mirror, in order to avoid astigmatism and coma. The mechanical layout restricts the angle of incidence to 6.5° . Under normal incidence a beam waist of $15 \mu\text{m}$ would have been possible. With the achieved beam waist, an estimated 5 fs pulse duration and a transmission through the apparatus downstream of the third harmonic gas target of approximately 50%, a conservative estimation of the peak intensity of the UV-pulses at the position of the

⁴¹nanomotion

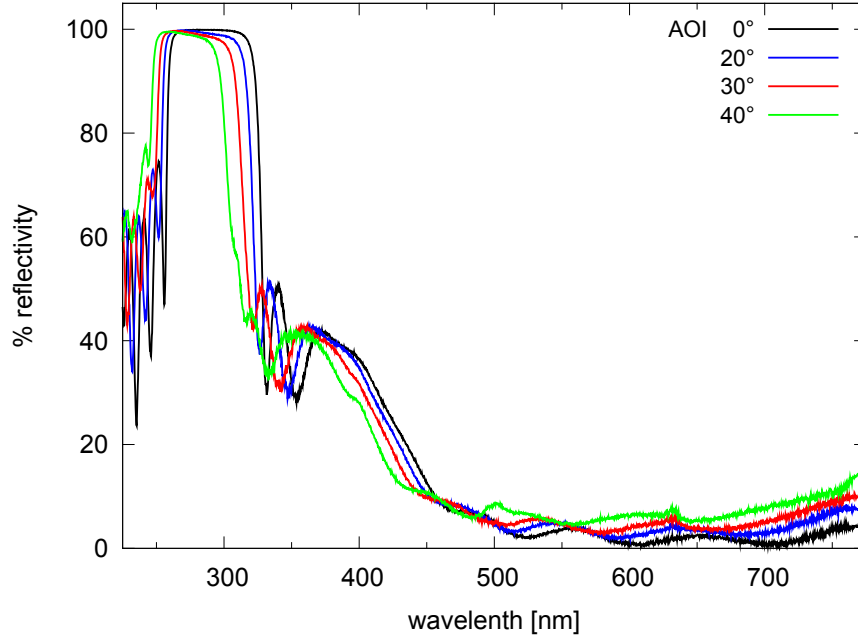


Figure 2.17: Reflectivity of the dielectric mirrors used in the delay chamber versus wavelength and for different angles of incidence (AOI), measured by a transmission spectrometer. In order of appearance in the beam path, different angles of incidence of 35° (M1), 30° (M2) and 16° (M3) are used (see figure 2.16b). The high reflectivity interval between 260 nm and 310 nm guarantees suppression on the blue side of the UV spectrum and otherwise a good transmission through the delay chamber. The suppression of $>90\%$ in the visible and near-infrared part of the spectrum gives the possibility to filter out the strong and nearly co-propagating fundamental NIR/VIS-pulses from the harmonic UV-pulses.

ions is 320 GW/cm^2 (assuming Gaussian profiles). The last, flat mirror M5 controls the overlap of the pulses leaving the delay chamber and the ions confined in trap 2 of the trap apparatus.

A 40 cm long differential pumping stage connects the output port of the delay chamber with the entrance port of chamber 2 of the trap apparatus that is installed in-line with the axis of trap 2 and 3 (see also section 2.1.1). This stage is pumped by a dry turbo pumping system⁴² with a pumping speed of 60 l/s. An all-metal gate valve⁴³ securely separates the ion trap apparatus from the beamline. Automatic protection against leaks or pump failure in the beam line is ensured by appropriate choice of the set points of the electronic operating an electro-pneumatic valve⁴⁴. Due to the good isolation properties of the differential pumping line separating chamber 2 and 3 in the ion trap apparatus and the additional differential pumping line connecting the delay chamber, a rise in background pressure when opening the valves to the beamline was not detected on the $2 \cdot 10^{-10}$ mbar

⁴²TPS compact, Varian

⁴³series 48124-CE01, VAT

⁴⁴series 01032-CE31, VAT

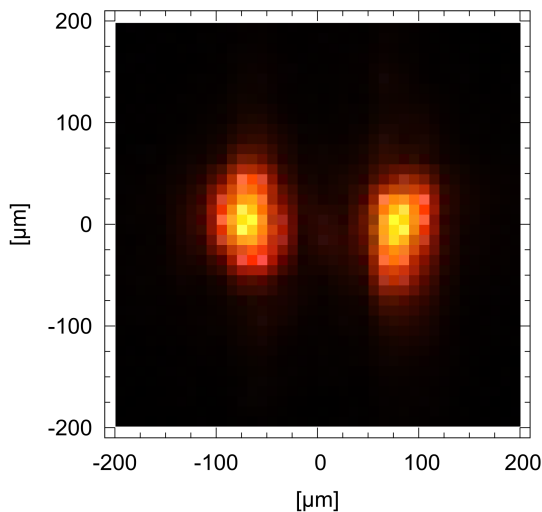


Figure 2.18: Picture of the dye cuvette, taken by the monitoring CCD camera with a $10\ \mu\text{m}$ pixel size. The two focused beams produced by the split mirror M3 are separated in the focal plane by the piezo driven actuators of the lower half mirror. This configuration is used to coarse tune the two beams to nearly equal intensity and beam waist.

level in chamber 3 of the trap apparatus.

In order to get a direct observation possibility of the focal plane of the UV-pulses, a $1\ \mu\text{m}$ Cytop⁴⁵ foil under 45° reflects 5% of the beam through a fused silica window. This monitoring beam exits the vacuum chamber in the middle of the differential pumping line. The Cytop pellicle induces only a marginal dispersion of $\approx 0.05\ \text{fs}^2$ and can therefore be permanently placed in the pulsed beam. A cuvette filled with a solution of sulforhodamin B is placed outside the vacuum at the same distance to the reflecting pellicle as the trapped ions. The dye absorbs in the ultraviolet and fluoresces in the visible. Thus, the focal plane can be permanently observed with a CCD digital video camera⁴⁶, without disturbing the carefully aligned overlap of the ions with the pulsed UV-beam. This setup is used to coarse tune the intensity distribution among the time-delayed pulse replica (see figure 2.18), as well as their spatial and temporal overlap (see figure 2.19 and figure 2.20). The saved picture of optimal alignment of the pulses with the ions serves as a good starting point to realign the setup from day to day.

To ensure a nearly equal intensity of the two pulse replica, the piezo driven actuator of the lower half mirror M3 is used to spatially separate the two beams on the dye cuvette as shown in figure 2.18. The mirrors M1 and M2 are used to bring the two beams to nearly equal waists and intensities. For this purpose, the two fluorescing spots on the camera observing the cuvette are tuned to approximately the same size and brightness, as far as it is possible with bare eye. This initial adjustment is afterwards checked for consistency on the equal response of the ions in the trap (see section 3.2.2) and it turned out that this rather simple tuning procedure is sufficient in accuracy. Another adjustment that has to be done from day to day is finding the voltage on the precision piezo translation stage of the upper half mirror that corresponds to a coincidence in time of the two pulses on the target. This time-zero of the pump-probe experiment is also adjusted with the help of the CCD-camera monitoring the dye cuvette. The actuators of the lower half mirror are

⁴⁵amorphous fluoropolymer type 602, Micro lithography inc.

⁴⁶Chameleon, Point Grey Research

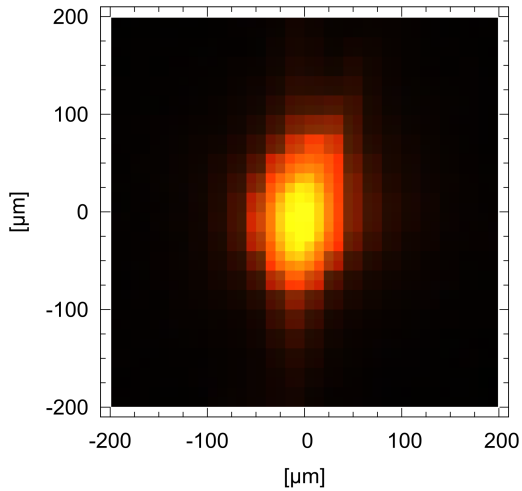


Figure 2.19: Coarse alignment of the spatial overlap. The two separated beams of picture 2.18 are overlapped with the help of the actuators of the lower half mirror. The voltage of the precision piezo that defines the position of the upper half mirror with respect to the lower half, is set to an arbitrary value. The two beams have no temporal overlap.

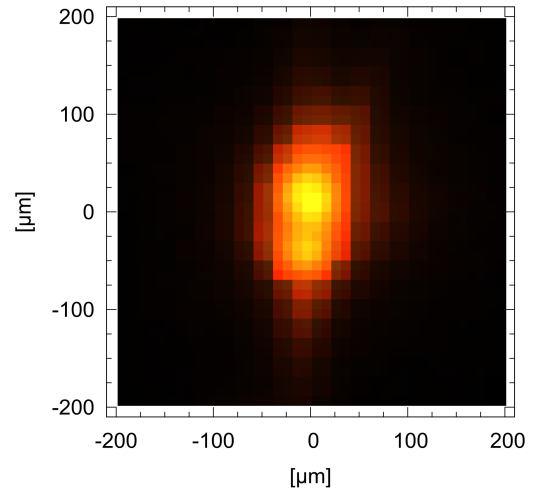


Figure 2.20: Same situation as in figure 2.19, but this time the translation stage of the upper half mirror is tuned such that the two spatially overlapping beams also coincide in time. A good value for the piezo-voltage needed to match the temporal overlap gives the shown interference structure on the dye cuvette.

used to overlap the two spots of now equal intensity. Setting the voltage of the precision piezo stage to a value that does not correspond to time-zero, the two spatially overlapped beams look like shown in figure 2.19. If the voltage of the piezo stage is tuned such that the pulses also coincide in time, interference fringes are observed as shown in figure 2.20. The two beam paths are not interferometrically stable and as a consequence the interference structure changes on a timescale <1 s. Thus, although the precision piezo stage has a resolution of 1 nm which would in principle allow to determine the time-zero with an accuracy far below one femtosecond, the temporal overlap of the two beams is accurate to ± 5 fs when using this method.

As already discussed in section 1.3 when working with targets that can be excited multiple times without dissociating (like in the case of ions confined in a Paul trap) vibrational heating can occur that reduces the modulation in the signal due to a higher probability to dissociate via higher lying electronic states. To account for these unwanted heating effects, only a few pulses should interact with the molecular ion followed by a time without irradiation, to allow for a sufficiently long radiative cooling duration. Therefore, the pulse trains of the UV-beam with a repetition rate of 3 kHz (defined by the Chirped-Pulse Amplifier) have to be chopped. For simplicity (the UV-beamline is evacuated) the fundamental laser before final compression passes through a mechanical chopper⁴⁷. Two relative orientation of two overlapping chopper wheels in combination with a mechanical

⁴⁷model 3501, New Focus

shutter was used to control the number of pulses which irradiate the ions in the trap and the time duration of no irradiation. The opening slit angle of the chopper wheel and the chopper speed was adjusted that way that with the given repetition rate of the laser the number of transmitted pulses (typically 6) and the number of blocked pulses (typically 122) in one chopper cycle always added up to 128. In other words the ions are irradiated with a 3 kHz repetition rate UV-laser for approximately 2 ms and afterwards a pause of approximately 41 ms allows for a radiative decay of vibrational excitations. This exposure cycle is repeated for the required irradiation time of the ions and the total amount of cycles is controlled by the mechanical shutter. The energy of the pump-probe pulse pairs after passing through the trap setup is measured with the help of a photo-diode. This way the pulse energy statistics of one exposure interval is recorded during an experiment.

2.3 Electro-Spray Ionization source

The efficient photoionization scheme for barium atoms presented in section 4.1 and the Electro-Spray ionization (ESI) source presented in this section are the main ingredients needed for an extension of the time-resolved measurements towards larger molecular ions (see also chapter 6). The ESI-source setup was designed, build and tested in a vacuum chamber different from the one presented in section 2.1.1. Nevertheless, the source for molecular ions in this apparatus, the gas inlet stage, can be replaced by the module of the ESI-apparatus.

2.3.1 Apparatus and concept

The concept and implementation of Electro-Spray ionization was pioneered in 1984 by the work of John Bennett Fenn [98] and awarded with the nobel prize in chemistry in 2002. This work was build on the ideas of Dole [99] and co-workers formulated in 1968, already. Today, ESI is one of the most versatile and widely used ionization techniques in mass spectrometry. In fact, the features of soft protonation and the possibility to ionize almost generic molecules out of solution, are the major criteria to choose an Electro-Spray Ionization source as an universal ionization device [83]. With this technique, the out-of-solution embedding of molecular ions into Coulomb crystals of laser cooled atomic ions is possible [62, 100]. Furthermore, protonation is a soft ionization method and fragmentation of chemical compounds is usually not observed. Together with the trapping and laser cooling of barium ions, discussed in section 4.2, ESI allows access of molecular ions with a wide range of charge-to-mass ratios.

Several reviews dealing with the ion formation in ESI, can be found in the literature. For a detailed description refer to [83]. Here, only a brief summary of the relevant aspects of the topic is given. Figure 2.21 shows a schematic illustration of the electrospray process. The solution of the analyte is pumped through a capillary, set to high (typically several kV) positive voltage. The electric field induces a charge separation in the solvent, due to electrostatic repulsion. The resulting force balances with the force of the surface tension of the solvent and a so called Taylor cone forms at the exit of the capillary. As the solution

emerges with a flow rate of typically 1-10 $\mu\text{l}/\text{min}$, the cone is drawn to a filament and highly (positively) charged droplets, with a typical initial diameter of several micrometer are sprayed into vacuum. While passing the potential and pressure gradient towards the counter electrode, evaporation of the solvent reduces the size of the droplets and its charge density on the surface rises. At the Rayleigh limit, the droplet Coulomb explodes into many smaller droplets. As long as the surface tension σ balances with the charge Q , a droplet is stable. The minimal stable radius r_{min} can be deduced from the Rayleigh equation.

$$r_{\text{min}} = \sqrt{Q^2/64\pi\epsilon_0\sigma} \quad \epsilon_0 : \text{dielectric constant in vacuum}$$

Two models are well established [101, 102], concerning the mechanisms that lead to the formation of single ions out of the multiple charged droplets. The first one is called charge-residue model or single-ion-in-droplet-theory and is illustrated in the upper path of figure 2.21. Evaporation of solvent and the resulting higher charge density leads to a continuous reduction of the droplet size. Collisions activate a further evaporation of the solvent until the desolvated single ion is produced. The second mechanism is based on the so-called ion-evaporation-model that assumes field emitted single ions from a comparably large, highly charged droplet. The charged part of the molecules penetrates the droplet surface and Coulomb repulsion with the charged surface ejects the entire molecular ion. The importance and occurrence of the two mechanisms depends on the actual experimental situation and remains topic of scientific discussions and research up to now. The ESI process produces desolvated ions in various charge states $[\text{M}+\text{nH}]^{\text{n}+}$ and even clusters. Therefore, the active filtering of the ion flux with a mass selecting element is recommended, when a stream of only one molecular ion species is required by the experiment.

The hardware of the ESI-source used in the framework of this thesis had to be composed out of refurbished parts, purchased from Finnigan. Figure 2.22 shows a schematic drawing of the essential parts. An infuse pump⁴⁸ with a Hamilton syringe⁴⁹ delivers a flow rate of typically 10 $\mu\text{l}/\text{min}$ of the solution. The chosen test solution is L-arginin hydrochlorid with 1 nmol/ μl molar concentration dissolved in equal parts of water and methanol plus 5% formic acid. The syringe is connected via the fused silica sample transfer line with the sample tube, a 30 cm long fused silica capillary with 100 μm inner diameter. The sample tube ends approximately 1 mm before the end of the stainless steel ESI-needle and is secured to the needle housing. A high positive⁵⁰ voltage of typically 8 kV is applied to the needle to produce the Taylor cone and the spray filament at its end. Tubes in the needle support allow a concentric nitrogen gas flow, that affects the mist of highly charged droplets generated at the end of the spray filament. This so called sheath gas stabilizes the spray, especially when using high flow rates and also affects the evaporation of the solvent. The sheath gas pressure tunes the flux of molecular ions (see section 2.3.2) and their charge distribution. A higher gas flow normally leads to higher charge states of the molecule. At the end of the atmospheric spraying chamber, the droplets enter a heated capillary, that begins 1 cm after the needle. Droplets, that enter this capillary shrink

⁴⁸Harvard Apparatus 22 dual syringes

⁴⁹MicroliterTM syringe 500 μl , Hamilton Bonaduz AG

⁵⁰If negatively charged molecules are required, the polarity of the high voltage can be switched.

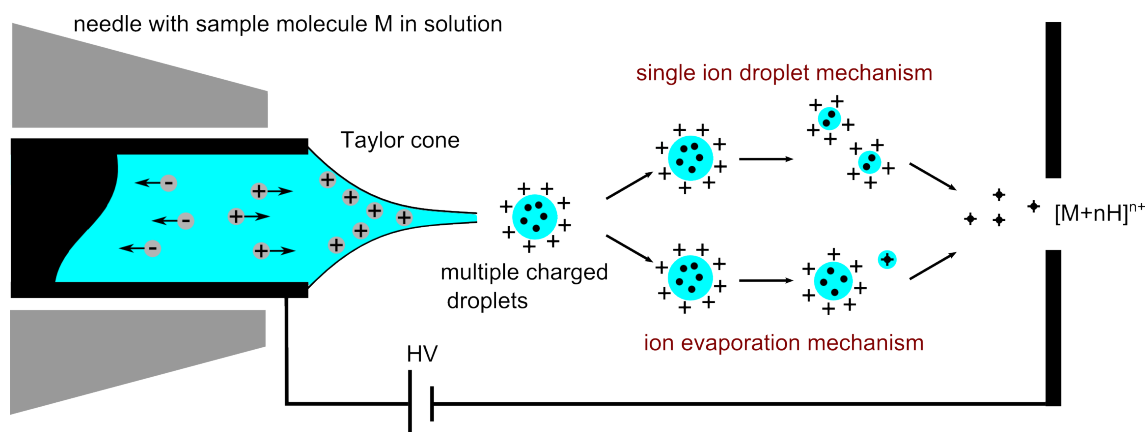


Figure 2.21: Schematic illustration of the Electro-Spray Ionization process. Molecules in solution pass a capillary at high potential. Highly charged droplets emerge from the tip of the Taylor cone, that forms at the exit of the capillary. Evaporation of the solvent reduces the size of the droplets until the high charge density leads to Coulomb explosion at the Rayleigh limit. Two mechanisms are proposed to lead to desolvated, eventually multiple charged ions. Continuous field emitted single ions from the charged droplets is the basic mechanism in the ion evaporation model. The alternative model is based on continuous reduction of the droplet size by fission resulting in a protonated single ion. Depending on the polarity of the applied high voltage, ESI can produce both, cations and anions.

in size, due to enhanced evaporation of the solvent and the charge density rises until at the Rayleigh limit, the droplet explodes. The heated capillary with an inner diameter of $250\ \mu\text{m}$ is also used as a differential pumping stage. The chamber following the capillary is pumped by a $28\ \text{m}^3/\text{h}$ oil sealed, two-stage sliding vane pump⁵¹ to a typical pressure of 1.6 mbar. The pump is equipped with an outlet oil mist filter and an oil recovery system. After the heated capillary, a cylindrical, electrostatic lens in conjunction with a skimmer focuses the produced ions into an octupole ion guide. The octupole works at a radio-frequency of approximately $2\pi \cdot 2.5\ \text{MHz}$ and transfers the ions with efficiency close to one to a mass selecting quadrupole. The skimmer separates the octupole chamber from the heated capillary chamber. A turbomolecular pump⁵² pre-pumped by a dry scroll vacuum pump⁵³ evacuates the octupole chamber to a pressure of $5 \cdot 10^{-4}$ mbar. The total ion current up to this stage of the experimental layout is measured, using a Faraday cup and a pico-amperemeter, in the experiments of section 2.3.2 that characterize the ESI-source.

As mentioned before, the ESI-source produces a large variety of eventually multiple charged molecules and clusters. In order to filter the required charge-to-mass ratio out of the total ion flux, a quadrupole mass filter is used after the octupole. The hardware and supply electronics are purchased from Extrel. The quadrupole electrodes have a diameter of 19 mm operating at a frequency of 1.2 MHz. Capacitive coupled pre-and postfilters advance the field profile at the beginning and at the end of the quadrupole and can be ad-

⁵¹model E2M28, EDWARDS GmbH

⁵²Pfeiffer Vacuum GmbH

⁵³model SH-100, Agilent Technologies/Varian Inc.

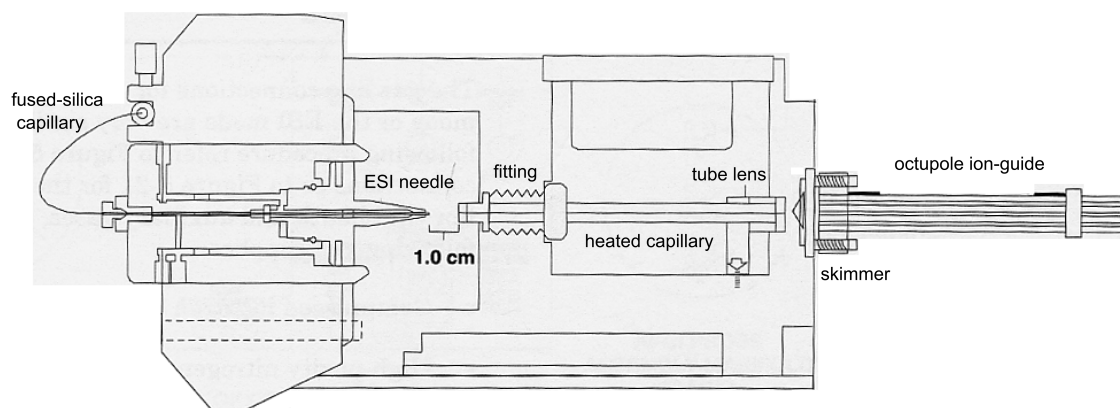


Figure 2.22: Computer drawing of the refurbished ESI hardware. A fused silica capillary enters the ESI setup through a fitting adapter and ends approximately 1 mm before the exit end of the electrospray needle. The chamber containing the needle is under atmospheric pressure. Tubes in the body of the needle support can be used to inject sheath and auxiliary gas (not used). 1 cm downstream, the heated capillary separates the spraying chamber from the next chamber pumped by a two stage rotary vane pump. After the heated capillary, a skimmer together with a cylinder forms an electrostatic lens, that focuses the ions into an RF-octupole. This octupole ion guide transfers the produced charged particles (including clusters) to the mass-selecting quadrupole. In addition, the skimmer assembly separates the second chamber from the third chamber, pumped by a turbomolecular pump, and a typical pressure of $5 \cdot 10^{-4}$ mbar is reached.

ditionally set to a common DC potential. Two electrostatic single electrode lenses control the in-coupling and out-coupling of ions to the quadrupole. The supported mass range is 1 to 500 atomic mass units (amu). The vacuum chamber containing the quadrupole is shown in figure 2.23. The octupole guiding the ions produced by the ESI-source ends at an electrostatic lens L1, that focuses the ions into the quadrupole. The two electrodes of this lens are labeled L1-1 and L1-2 in the following. The small open cross section of L1 is used as a differential pumping stage to separate the chambers before and after the mass filter. The quadrupole is mounted on axis with the octupole in a stainless steel cylinder, that is screwed in-between the two chambers. The mounting aperture is sealed with the help of an o-ring to the cylinder. The lens L1 fits tightly in this aperture and the only connection to the next chamber remaining is the small hole in the electrodes. A 3101/s magnetically levitated turbomolecular pump⁵⁴ maintains a $1.5 \cdot 10^{-6}$ mbar pressure in the chamber after the quadrupole, nearly two orders of magnitude lower compared to the previous chamber. As a pre-pump, a combination of a 181/s turbomolecular pump⁵⁵ and a dry scroll pump⁵⁶ are used. The pressure is monitored by a nude Bayard-Alpert type ionization gauge. After the mass filter, a two-stage microchannel plate (MCP) detector⁵⁷ is used to detect the

⁵⁴TPU 520M, Pfeiffer Vacuum GmbH

⁵⁵TPD 20, Pfeiffer Vacuum GmbH

⁵⁶model SH-100, Agilent Technologies/Varian Inc.

⁵⁷ChevronTM, Galileo/Scientific Instruments GmbH

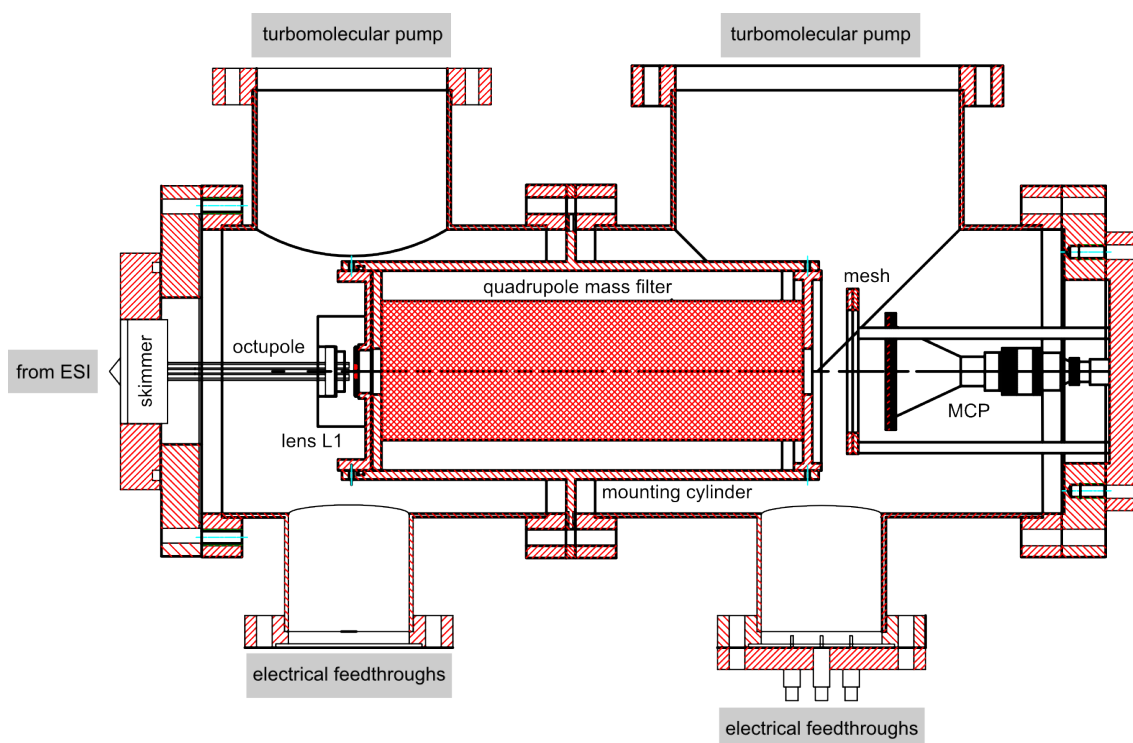


Figure 2.23: Computer drawing, showing the home-built quadrupole mass filter part of the experimental setup. Ions produced in the ESI-source (see figure 2.22) are guided along the octupole and focused by lens L1 into the mass selecting quadrupole. The hole in the electrodes of L1 is the only aperture between the chamber before and the chamber after the mass filter. This differential pumping stage improves the vacuum conditions by nearly two orders of magnitude. The commercial quadrupole features input and output electrostatic lenses and capacitive coupled pre-and post-poles. After passing the grounded mesh, the ions leaving the mass filter are detected by a two-stage MCP for calibration purposes⁵⁸. Two turbomolecular pumps are connected to the upper two flanges of the apparatus. The lower two flanges are used for the electrical feedthroughs and connections.

ions leaving the quadrupole. The two single MCP wafers are mounted in tandem with opposing channel bias angles (12°) to enhance the detector gain. A cone-shaped, 50 ohm impedance matched readout housing is used to avoid signal reflection. A voltage of -2 kV is applied to the input surface and -100 V to the output surface of the plate. The anode is grounded via a 50 ohm resistor. An additional mesh at ground potential is mounted before the MCP. The detector achieves a maximal gain of 10^7 .

Only the hardware of the ESI-source and the mass selecting quadrupole was purchased. All electronic signals required and send by the ESI/Quadrupole control module are produced and read-out by USB-based data acquisition modules⁵⁹ controlled by a in-house developed software. One USB1208LS module providing 8 analog inputs and 16 digital I/O connections and three USB3112 modules providing each 8 16-bit analog voltage out-

⁵⁹Plug In, Measurement Computing

Table 2.1: Summary of digital I/O and analog out voltages produced by the boards #0 (USB-3112) and #1 (USB-1208LS) for the control of the ESI-source electronic module. The function within the ESI setup is given in the last column.

module/board #	type	function
USB-1208LS/1	digital out	valve sheath gas
USB-1208LS/1	digital out	HV needle 'enable'
USB-3112/0	analog out	HV needle 'set'
USB-1208LS/1	digital out	HV needle 'on'
USB-3112/0	analog out	HV current 'set'
USB-1208LS/1	digital out	HV polarity
USB-3112/0	digital in	current limitation
USB-1208LS/1	digital out	capillary heater
USB-3112/0	analog out	DC volt. capillary
USB-3112/0	analog out	DC volt. cylinder
USB-3112/0	analog out	octupole RF 'set'
USB-3112/0	analog out	octupole DC 'set'
USB-1208LS/1	digital out	valve aux gas
USB-1208LS/1	digital out	7 channels for multipl. chip select, adress and out

puts and 8 digital I/O ports are used in total. Table 2.1 and table 2.2 give a summary of the digital and analog voltages processed by the modules and their functions for the ESI-source and the mass filter, respectively. Concerning the voltage supply of the quadrupole, all signals enter the commercial RF/DC power supply module⁶⁰ that produces the RF and DC voltages of the quadrupole except for five voltages (two voltages for the electrodes of L1, two voltages for the in- and output lenses and the common DC potential of the pre-and postfilters). These signals are amplified by a factor of 10 by five operational amplifiers⁶¹ and are afterwards directly fed to the corresponding electrodes. Computer control of the send and readback voltages for the ESI-source and the quadrupole is implemented by two graphical user interfaces (GUI). The software was developed using DELPHI 2005 and the basis-software kit of the USB1208LS and USB3112 modules, provided by the manufacturer. Figure 2.24 shows a screen-shot of the two GUI. All essential functions of the apparatus can be monitored and manipulated. The parameters of the previous session can be saved to a file and push-button loaded for the next session.

2.3.2 Characterization

Within the framework of this thesis the Electrospray Ionization source and the accompanied quadrupole mass filter have been assembled and tested fully functional. Two types of measurements have been performed. The intention of the first experiment is the implementation and characterization of the Electrospray Ionization source. The second measurement shows the combined ESI-quadrupole mass filter system working properly. In order to measure the total ion current, a Faraday Cup is placed directly after the guiding

⁶⁰150QC, Extrel

⁶¹PA93, Apex Microtechnology

module/board #	type	function
USB-3112/2	analog out	mass command
USB-3112/2	analog out	Δ Res
USB-3112/2	analog out	Δ M
USB-3112/2	analog out	Pole Bias
USB-3112/2	analog out	*DC volt. L1-1
USB-3112/2	analog out	*DC volt. L1-2
USB-3112/2	analog out	*DC volt. lensIn
USB-3112/2	analog out	*DC volt. lensOut
USB-3112/2	digital out	Res ON/OFF
USB-3112/2	digital out	DC poles reverse
USB-3112/3	analog out	*DC pre/postfiler
USB-1208LS/1	analog in	Pole Bias Readb.

Table 2.2: Summary of analog I/O and digital out voltages produced by the boards #2 (USB-3112) and #3 (USB-3112) for the control of the mass selective quadrupole. The respective function is given in the last column. Voltages labeled with * are post-amplified by operational amplifiers and directly fed to the corresponding electrodes.

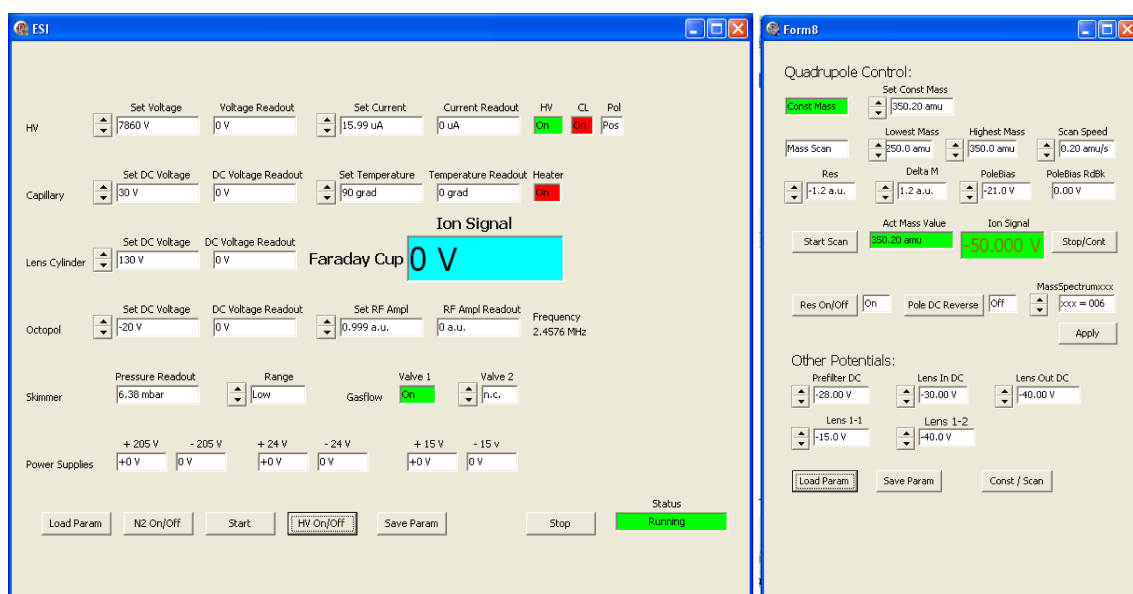


Figure 2.24: Screen-shot of the two graphical user interfaces for the control of the ESI-source and the quadrupole mass filter. All relevant parameters can be set, controlled and read out. Previous used parameters can be saved and reloaded.

constant parameters	ion current as a function of					
	HV on needle	N ₂ pressure	capillary voltage	capillary temperature	cylinder lens voltage	octopol voltage
HV needle [kV]	-	7.9	7.9	7.9	7.9	7.9
N ₂ pressure [psi]	55	-	55	55	55	55
cap. voltage [V]	30	20	-	17.1	17	30
cap. temp. [°C]	90	90	90	-	90	90
lens voltage [V]	130	130	90	150	-	130
octup. volt. [V]	-20	-20	-20	-20	-20	-

Table 2.3: Summary of the parameters chosen in the experiments presented in figure 2.25. A slightly different set of constant parameters is used for each of the six measurements of the total ion current out of the ESI-source as a function of the corresponding, varying parameter.

octupole of the ESI-source. To measure the ion current, that lies typically in the pA regime, a suitable ampere-meter⁶² is used. In order to collect the major part of the positively charged single molecules, fragments and clusters leaving the octupole, a potential of -30 V is applied to the cup. With this setup, it is possible to measure the total ion current of the ESI-source as a function of the six tuning parameters. Figure 2.25 shows the results of these measurements. The syringe pump flow rate of the L-arginin-hydrochlorid solution is kept constant at 10 µl/min throughout the measurements. A slightly different set of constant parameters is used in each measurement and table 2.3 gives a summary of the actually used values. The highest total ion current achieved so far amounts to approximately 30 pA, equivalent to $2 \cdot 10^8$ ions/sec. Using the results of these calibration measurements, a good performance of the ESI source is achieved by applying a voltage of 8 kV on the spraying needle, 55 psi nitrogen sheath gas pressure, a 30 V voltage on the capillary heated to 90° C, a 130 V voltage on the cylindrical lens and -20 V on the octupole.

The second experiment is performed to show the quadrupole mass filter after the ESI-source functional. In this case, the setup with the MCP as detector, as described above, is used. With the help of the graphical user interface of figure 2.24, all of the necessary tuning parameters of the quadrupole are accessible. Pole Bias applies a DC offset potential to the quadrupole electrodes (poles). The potential difference between the ion source and the Pole Bias offset voltage sets and controls the effective ion energy in the quadrupole. The typical energy range of ions that a quadrupole can resolve is 2 eV to 12 eV. Relatively slow ions spend more time in the filter volume and experience more cycles of the radio-frequency. This increases the filtering effect and allows higher resolution. However, if the velocity of the ions is too small, it is more difficult to focus them into the quadrupole and the overall transmission drops. The best trade-off, according to the manufacturer, are ion energies in the range of 5 eV to 10 eV. The parameters ΔM and Resolution (Res) define the resolution curve of the quadrupole. Res is controlled by a voltage ranging from -5 V to +5 V. A lower value decreases the resolution. The resolution needed, changes

⁶²Keithley Instruments Inc.

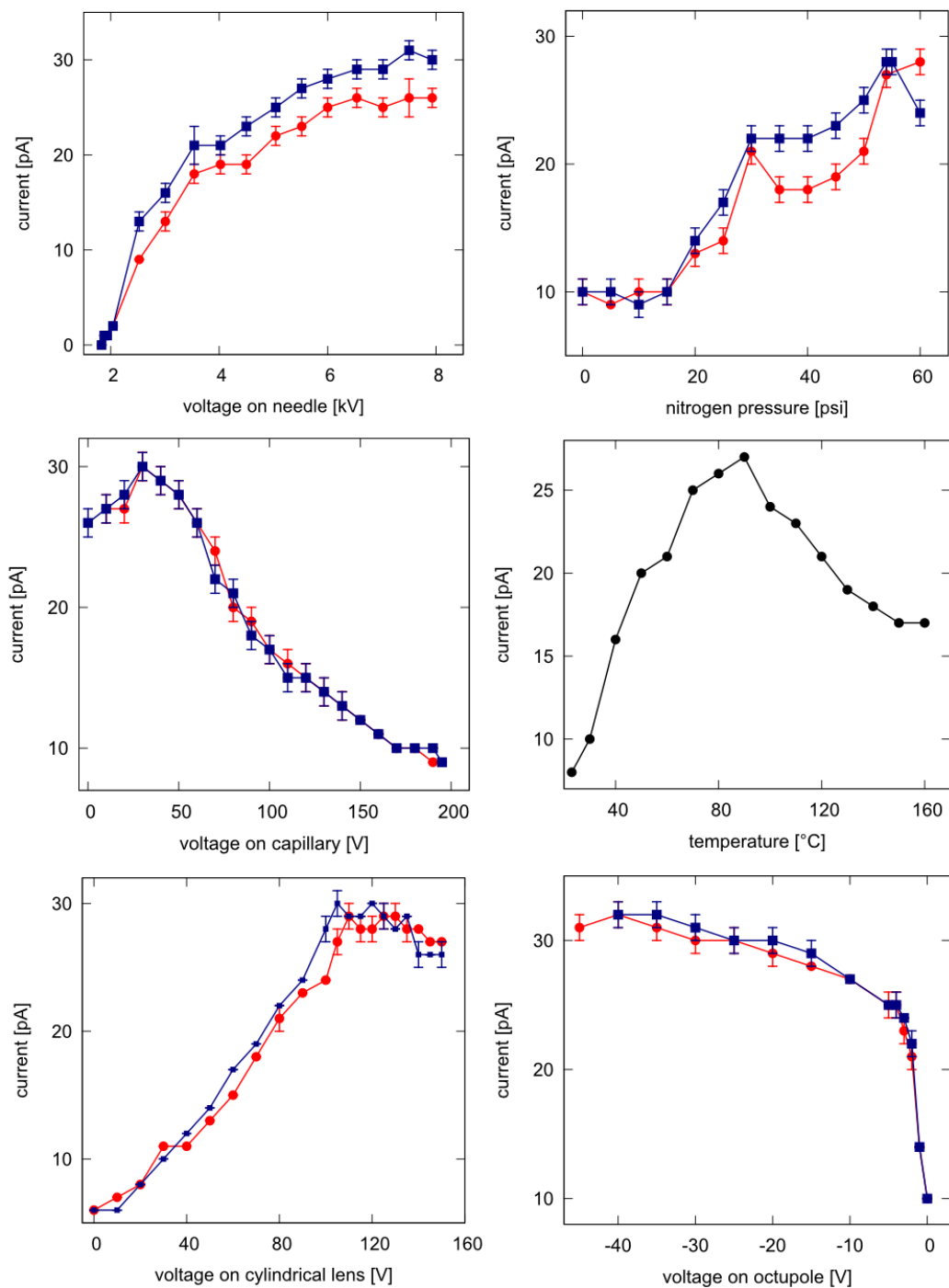


Figure 2.25: Measurements of the total ion current of the ESI-source as a function of the voltages on the spraying needle, the heated capillary, the cylindrical lens and the octupole, as well as the nitrogen sheath gas pressure and the temperature of the heated capillary. For each measurement a slightly different set of constant parameters according to table 2.3 is used. Except for the measurement of the total ion current as a function of temperature, all measurements have been performed twice and are plotted in blue and red respectively.

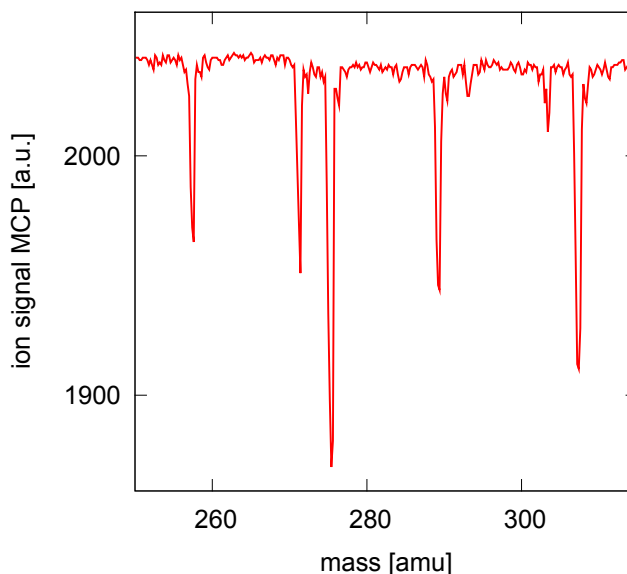


Figure 2.26: Inverted mass scan of the L-arginin Hydrochlorid test solution between 250 and 315 atomic mass units, assuming only singly charged ions. The voltages used on the quadrupole setup are briefly summarized in table 2.4.

with the mass, assuming singly charged ions. In order to increase the resolution for lower masses and decrease resolution for higher masses, the ΔM parameter changes the slope of the resolution curve. The other parameters tunable with the help of the GUI, like the voltages on the electrodes of lens L1, the voltages of the focusing lenses and the common DC voltage of the pre-and post filter, have been discussed above. Figure 2.26 shows a mass scan of the test solution between 250 and 315 atomic mass units, assuming singly charged ions. The parameters of the quadrupole used in this experiment are summarized in table 2.4. Several well separated signal fringes are resolved. The measurement is not intended to represent an accurate mass scan with a calibrated mass axis, but merely serves as an indication, that the mass filter option of the combined ESI/Quadrupole setup is working properly. Nevertheless, three mass differences of 18 u are clearly visible, which indicate a separation of H_2O out of clusters with water. In order to obtain a valuable mass spectrum the concentration of the solution can be lowered to avoid clusters that are eventually multiply charged.

With the presented experiments, the ESI-source is characterized and the mass selecting quadrupole is proven functional. The next step will be to connect the setup to the experimental apparatus described in 2.1.1. The ESI setup will replace the cryogenic gas inlet stage. Designs including detailed, mechanical computer drawings for the connection of the two setups are already available. An additional conical ion-guide could link the commercial quadrupole mass spectrometer with the quadrupole ion guide and finally with the three Paul-traps. Together with directly laser cooled and trapped $^{138}\text{Ba}^+$ ions, the protonated molecules out of the ESI-source cover a wide charge-to-mass range up to biologically relevant molecular ions. For a detailed analysis of this point, refer to [31] and chapter 6. The envisioned experiments (refer to the introduction to this thesis) using X-FEL laser pulses with 10^{13} coherent X-ray photons in each single pulse need a target that can be deterministically prepared with the repetition rate of the laser source. As an example, the current repetition rate of the Linac Coherent Light Source X-FEL amounts

parameter	value	[unit]
Mass	300.00	[amu]
Lowest Mass	250.00	[amu]
Highest Mass	350.00	[amu]
Scan Speed	0.20	[amu/s]
Res	-1.20	[a.u.]
ΔM	1.20	[a.u.]
PoleBias	-21.00	[V]
L1-1DC	-15.00	[V]
L1-2DC	-40.00	[V]
LensInDC	-30.00	[V]
LensOutDC	-40.00	[V]
PrefilterDC	-28.00	[V]

Table 2.4: The experimental parameters applied to the quadrupole setup, with the help of the GUI shown in figure 2.24. For explanation of the used abbreviations see the main text.

to 120 Hz. Taking the newly developed, efficient photoionization scheme for barium atoms (see chapter 4) into account, the source for the cooling agents is estimated to be effective enough. As stated in this section, the ESI-source operated with the test solution, even not optimized for a high production rate, yields a rate of $2 \cdot 10^8$ ions/sec before the filtering stage. The rate at which ions with the right charge-to-mass ratio emerge from the quadrupole, depends on the used solution and the coupling efficiency of ions from the octupole to the quadrupole. As shown in [85], 10% coupling efficiency is a conservative estimation and a rate of $2 \cdot 10^4$ ions/sec is a typical value. Therefore, the rate at which suitable molecular ions can be delivered, lies still in the several hundred kHz regime and is thus estimated to be more than sufficient.

Chapter 3

Time-resolved spectroscopy on single molecular $^{24}\text{MgH}^+$ -ions

3.1 Ion trapping and transfer

In this section, the successful implementation of loading, trapping and cooling of atomic $^{24}\text{Mg}^+$ and molecular $^{24}\text{MgH}^+$ -ions is described. After the loading routine and direct laser-cooling of magnesium ions, the used preparation methods for molecular $^{24}\text{MgH}^+$ -ions and their integration and sympathetic cooling in the crystalline structure of the cold trapped atomic ions is discussed. The second part of this section concentrates on the deterministic transfer of the molecular ion into an isolated region after its creation. For a single ion the efficiency of this transfer process is close to unity and fast ($\ll \text{ms}$). For the transfer of many individual molecular and atomic ions, three schemes suited for different applications are described. The deterministic delivery of a selectable number of externally cold molecular ions, allowing for repetition rates up to kHz is presented and an accuracy for spatial positioning of a micrometer is demonstrated.

3.1.1 Ion trapping and molecular ion preparation

The essential initial step for experiments with single or few molecular ions embedded into a Coulomb crystal of laser-cooled $^{24}\text{Mg}^+$ -ions is the reliable, isotope-pure preparation of the atomic ion ensemble confined in the trap. Other magnesium isotopes ($^{25}\text{Mg}^+$, $^{26}\text{Mg}^+$) and accidentally ionized residual gas particles appear as dark lattice sites within the crystal and are not directly distinguishable from the molecular ions by evaluating fluorescence images only. Other methods to identify contaminant ions, like increasing its kinetic energy above the trap depth by resonantly driving its radial secular motion [54, 103], have mostly a destructive nature. Thus, the isotope-selective resonant two-photon photoionization loading scheme, discussed in section 2.2.1 of chapter 2 is used to load a pure $^{24}\text{Mg}^+$ -crystal with negligible contamination. The isotope shift in the intermediate resonance is larger than the resonant linewidth of the atom and a fairly good isotope purity can be guaranteed using this method [80, 79]. If the experiment does not require a fast or

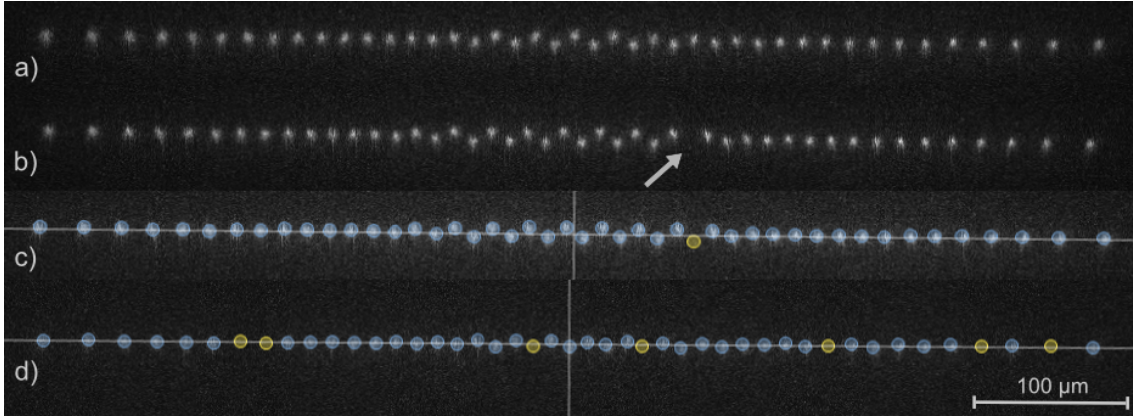


Figure 3.1: Two-dimensional fluorescence CCD images of crystalline ion structures confined in trap 2 (see figure 2.2 B). The objective with ten times magnification to image the whole ion crystal is used. Crystal a) contains only $^{24}\text{Mg}^+$ -ions and is referred to as a pure crystal. Crystal b) contains exactly one molecular $^{24}\text{MgH}^+$ -ion indicated by the arrow. In c) the output of the image analysis software (for details refer to [74]) is superimposed over the fluorescence image b). Non-fluorescing, molecular ions are marked with yellow circles and bright ions are marked with blue circles. The software identifies bright spots and exploits the inherent symmetry of Coulomb crystals (the horizontal and vertical symmetry axis of the crystal is given by white lines) to determine the position of non-fluorescing molecular ions. The ion crystal d) demonstrates the preparation of 7 molecular ions. The number of sympathetically coolable molecular ions is determined by the cooling forces of the atomic ions [104, 100, 105]. It depends on the ratio of cooling agent ions to sympathetically cooled ions and on the mutual distance. One cooling ion can be sufficient to sympathetically cool and crystallize > 10 molecular ions.

even continuous reloading, an optional cleaning of the ion-crystal by resonant heating can be implemented. The amplitude modulated beat signal, created by the sum of the well-resolved radial secular frequencies ($\propto U_{\text{RF}} \cdot Z/m$) of particles with masses $m=25$ u ($2\pi \cdot 480$ kHz) and $m=26$ u ($2\pi \cdot 462$ kHz) is provided by an arbitrary waveform generator and applied to a copper wire parallel to the axis of trap 1. A standard cleaning cycle, used in the experiment, consists of a typically 2 s long resonant excitation with a sufficiently high voltage (typically 250 mV). The probability to obtain a pure crystal after one cleaning cycle without simultaneous laser-cooling of the $^{24}\text{Mg}^+$ -ions is close to unity, but suffers from a severe fraction ($\approx 30\%$) of additionally lost $^{24}\text{Mg}^+$ -ions. Multiple cleaning cycles with simultaneous moderate laser cooling is the method of choice that has been proven functional for the applications presented in this section. After three excitation cycles, the all contaminant ions are lost out of the trap. The $^{24}\text{Mg}^+$ -ions have a survival probability of $>95\%$. A pure $^{24}\text{Mg}^+$ -ion crystal, after successful isotope-selective loading, is shown in figure 3.1a). The linear density λ in the center part of the crystal is sufficiently high to cause a two-dimensional zig-zag structure as discussed theoretically in section 1.1.3. Towards the end of the crystal, λ decreases and a phase transition of second order from the zig-zag structure to a one-dimensional string occurs.

The apparatus offers three different schemes to create a single or up to a few hundred

molecular ions and embed them on lattice sites of an atomic ion crystal (see also section 2.1.1). The electron gun, located right after the ceramic nozzle of the cryogenic gas inlet stage can be used for electron bombardment ionization of neutral molecules out of an effusive beam. Molecular ions, covering a wide mass range, can be produced using this method. Nevertheless, the molecule even if originally internally cold, will end up in a highly excited, dissociative state or the electron-impact might lead to an immediate dissociation [106]. Additionally, the bombarding electrons might ionize unwanted atomic or molecular species, present in the background gas and this results in the need for a resonant cleaning process of the crystal after the embedding. In section 2.3, the implementation, characterization and first tests of an Electro-Spray Ionization (ESI) source are presented. Optionally, this setup can substitute the gas inlet stage and serve as a soft ionization device for larger molecules of selectable charge-to-mass ratios, where fragmentation of chemical compounds is usually not observed. The mass-selective quadrupole after the ESI-source ensures a tremendously reduced embedding of unwanted masses into the crystal compared to electron-impact ionization. The third production method is based on the photochemical reaction [61]



A collisions of an electronically excited ${}^{24}\text{Mg}^+$ -ion with a hydrogen molecule leads to the formation of a magnesiumhydrid ion and an hydrogen atom. Within this section the photochemical production of ${}^{24}\text{MgH}^+$ is the method of choice, because this diatomic molecular ion is best suited as a test candidate for the envisioned scheme of time-resolved X-ray diffraction on single particles. It is well treatable by theory [107, 31, 71], yields sufficiently fast vibrational dynamics on the few-femtosecond timescale and the required ultra-short UV-laser pulses for a pump-probe experiment, exploring its vibrational wavepacket dynamics [108], can be generated in a normal scale laboratory. The ${}^{24}\text{MgH}^+$ -ion serves as a model system to calibrate the setup for most generic molecular ion species having a suitable charge-to-mass ratio and is used, for example, to demonstrate the control and transfer capabilities of the experiment.

After the preparation of a pure atomic ${}^{24}\text{Mg}^+$ -crystal by isotope-selective photoionization, small amounts of hydrogen gas are injected into chamber 1. The pulsed valve in the gas inlet stage closes the hydrogen reservoir under a pressure of ≈ 0.3 mbar. The partial H_2 pressure in the vacuum chamber can be controlled by the opening times of the valve, which can operate in the milliseconds regime. Simultaneously, the atomic ${}^{24}\text{Mg}^+$ -ions are exposed to ≈ 1.5 mW of near resonant, 280 nm cooling light. The laser is about half a linewidth red detuned from the atomic resonance and focused down to a waist of approximately 80 μm . This leads to a significant population of the $3p \text{P}_{3/2}$ state and therefore to approximately 4 eV of additional energy allowing for the photochemical reaction 3.1. This provides a controlled transformation of a selectable amount of ions in the crystal to the molecular ion model system ${}^{24}\text{MgH}^+$. Opening times of 5-15 ms of the pulsed valve yields a conversion of nearly 50 % of the ${}^{24}\text{Mg}^+$ -ions into ${}^{24}\text{MgH}^+$. Under these conditions, the degradation of the vacuum conditions in chamber 1 is still tolerable and limits the pressure rise to a few 10^{-9} mbar for a period lasting less than 2 seconds. Figure 3.2 shows the count rate of the photomultiplier, detecting the fluorescence light of ions in trap 1 and

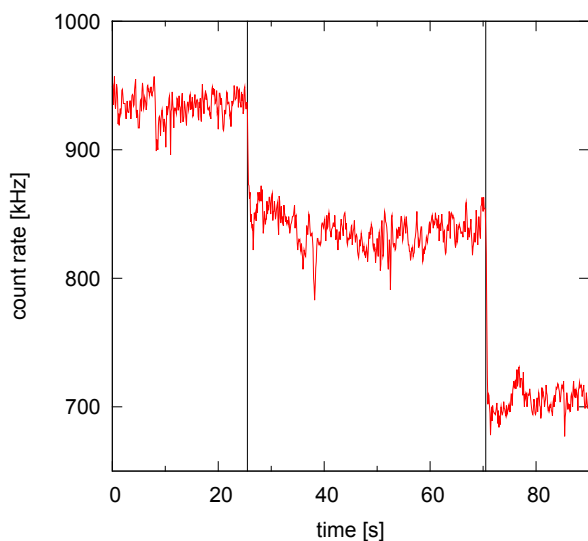


Figure 3.2: Count rate of the photomultiplier, detecting the fluorescence photons emitted from $^{24}\text{Mg}^+$ -ions in trap 1. The breeding of molecular ions via the photochemical reaction 3.1 is observed. Hydrogen is injected at the indicated instants by vertical lines. The count rate drops when $15 \pm 3\%$ and $25 \pm 3\%$ of the atomic ions are converted into $^{24}\text{MgH}^+$. The stray light induced background count rate (no ions in the trap) amounts to 320 kHz. Each data point represents an accumulation time of 100 ms.

its change during H_2 injection. The fluorescence rate drops suddenly by approximately 20 % at the indicated instants of opening the valve, due to a conversion of $^{24}\text{Mg}^+$ -ions into non-fluorescing $^{24}\text{MgH}^+$ molecular ions. After about 250 milliseconds the reactions cease indicating fast pumping of the injected hydrogen gas. The amount of molecular ions in the crystal, ranging from a single to a few hundred can be controlled by the opening times of the valve. Typical bi-crystals, bred as described above, are shown in figure 3.1b-d). In c) and d) the home-made image analysis software of the experiment is applied to the raw fluorescence CCD image. This software marks the positions of bright ions with blue circles and the position non-fluorescing ions with yellow circles. The analysis is a two-step process described in detail in reference [74]. In a first step the software applies a suitable algorithm employing the à trous wavelet transform to identify bright spots and in a second step the inherent symmetry of a Coulomb-crystal is exploited to identify the positions of the dark ions. The image analysis software is of great importance when numerous fluorescence images have to be evaluated, as it is the case in the experiments presented in this section.

As pointed out in [61], the $^{24}\text{MgH}^+$ model system shows cooling laser induced reactions that lead to a dissociation of the molecular ion. Exactly this dissociation is used as a signal in the time-resolved pump probe experiment of this chapter (a detailed description follows in 3.2). For such an experiment, it is crucial to know whether cooling laser induced dissociation is negligible on the time scale of the experiment or not. The study of long term laser-induced reactions on the $^{24}\text{MgH}^+$ model system shows also the need to separate the production region of the molecular ion from the precision experimental region. The composition of four two-component ion crystals with different fractions of $^{24}\text{Mg}^+$ and $^{24}\text{MgH}^+$ are observed over an extended period of time (up to 3 hours). Figure 3.3 shows the experimental results. The time-dependent amount of atomic and molecular ions in the crystals are recorded by evaluation fluorescence images snapshots. The rates of the reaction 3.1 are proportional to the population of the excited state $3pP_{3/2}$. In order to minimize the rate of reactions, the power of the cooling laser is set just high enough to sustain the crystalline structure. In addition, the experiments are performed

under ultra-high vacuum conditions. A rate equation model is used to describe the time evolution of the atomic (n_{atom}) and molecular (n_{mol}) fraction. Three light induced types of reactions are considered and reaction rate coefficients κ_1 , κ_2 and κ_3 were assigned to each process. κ_1 is the reaction constant of an $^{24}\text{Mg}^+$ -ion converted into $^{24}\text{MgH}^+$, as in reaction 3.1. The other two considered reactions are $^{24}\text{MgH}^+ \rightarrow ^{24}\text{Mg}^+ + \text{H}$ and $^{24}\text{MgH}^+ \rightarrow ^{24}\text{Mg} + \text{H}^+$. The reaction constants κ_2 and κ_3 are assigned to these processes respectively. A single set of rates $\kappa_1 = 0.13 \text{ h}^{-1}$, $\kappa_2 = 0.79 \text{ h}^{-1}$, $\kappa_3 = 0.10 \text{ h}^{-1}$ reproduces the measured time dependent composition of the four experiments. The time scale for the relevant reactions is consistent with results reported in [35]. This experiment is intended to give only a rough estimation of the time scales rather than a precision evaluation of the reaction constants, because it is performed on the few ion level and thus, the statistics is limited. The resulting statistical errors are quite high ($\pm 20\%$) and do not allow for an accurate, precision measurement. To conclude, experiments even on the reactive molecular ion $^{24}\text{MgH}^+$ are possible when performed in ultra-high vacuum. All investigated reaction occur on the many minute time scale and thus, concerning the time-resolved experiments of this section, laser induced reaction events are negligible on the typical time scale of the pump-probe experiment (1 to 4 minutes). The required ultra-high vacuum conditions are difficult to maintain, simultaneously to an efficient and fast production of molecular ions. A deterministic transfer of few molecular ions from the production region to a well isolated experimental ultra-high vacuum region is highly recommended, especially when the production of generic molecular ions has to be done fast or has to be achieved in a continuous way, for example by Electrospray Ionization.

3.1.2 Deterministic ion-transfer protocol

As discussed in the last section, atomic and molecular ions produced in chamber 1 and trapped by trap 1 should be transferred as fast as possible to a chamber that provides a nearly background free, ultra-high vacuum environment. In addition, the implementation of a buffer gas cooling stage [33] to address the molecular ions internal degrees of freedom or if a fast replacement of molecular ions is required [76], a fast transfer is desired. For the purpose of demonstrating the deterministic transfer scheme, a molecular ion is prepared and confined in trap 1. The ion is accelerated and the quadrupole guides it through chamber 2 and the two differential pumping stages, described in section 2.1.1 of chapter 2. The quadrupole ends in the third chamber of the experimental apparatus, that maintains UHV conditions. The four copper bars along the full length of each of the differential pumping stages can serve as drift tubes [109] for the transferred ion, although it turned out that for the confinement parameters used in the experiments described in this section, the transfer is efficient, reliably and fast enough. Thus, the copper bars are simply grounded in the following. The transferred ion is decelerated and subsequently trapped by the Paul traps 2 and/or 3, located at the end of the guide. The three ring electrodes, that form the axial confining potential for these two traps are referred to as R_1 , R_2 and R_3 in the following (refer to figure 2.2). A grounding of the ring-electrode of trap 1 facing the differential pumping stage leads to a release of the molecular ion out of the axial confinement (see figure 3.4). The grounding or switching of the voltages applied to the ring-electrodes takes currently less than $1 \mu\text{s}$ by fast MOS-FET transistors. The ion is

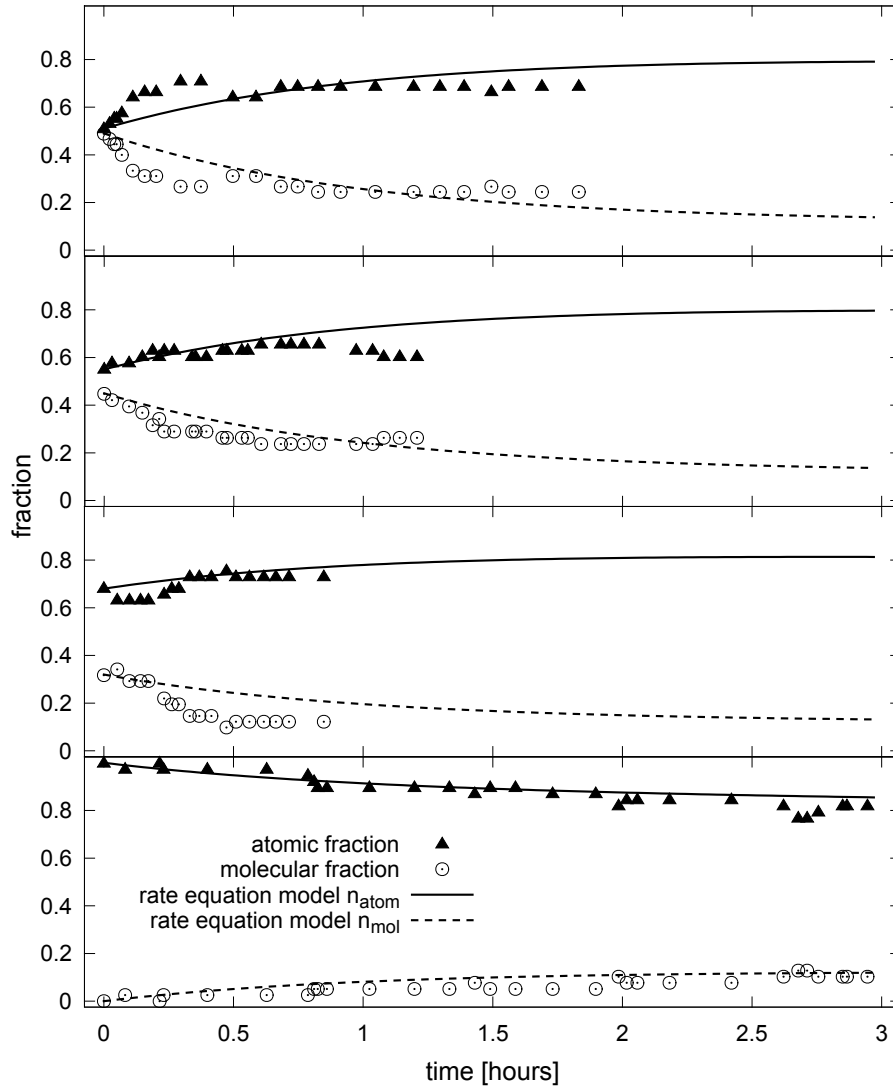
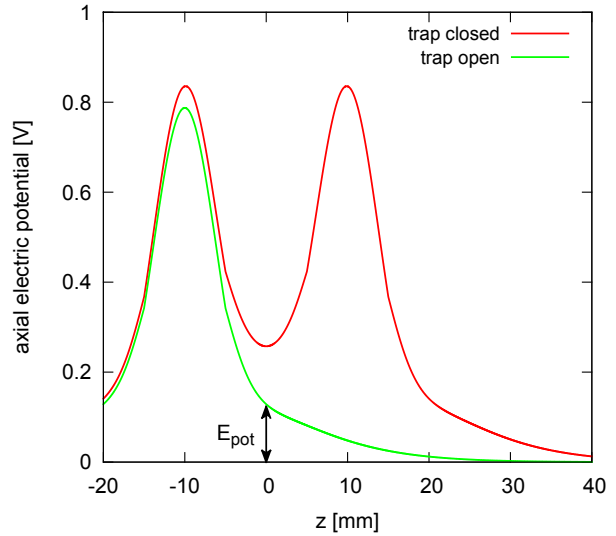


Figure 3.3: Atomic $^{24}\text{Mg}^+$ and molecular $^{24}\text{MgH}^+$ -ion composition of four Coulomb crystals observed over an extended period of time. The fraction is plotted in dependence of the storage duration in trap 2. The atomic fraction of the initial crystal increases stepwise from 50% to 100% in the experiments presented from top to bottom. The compositions are derived out of fluorescence images, taken by the EM-CCD camera observing trap 2. The laser power was chosen sufficient to sustain the crystalline state of the ions in the trap ($\approx 150 \text{ mW/cm}^2$ intensity and about one natural linewidth detuning). According to a nude Bayard-Alpert type ionization gauge (calibrated on N_2), the total pressure of the vacuum chamber amounts to approximately $2 \cdot 10^{-10}$ mbar. The results of a rate equation model describing the time evolution of the atomic-molecular fraction are presented as solid and dashed lines. The evolution of all four ion-crystals is described with a single set of rates. No counting error in the evaluation of the fluorescence images is assumed, therefore the composition of each crystal can be given exactly.

Figure 3.4: Results of a simulation of the axial electric potential provided by voltages applied to the ring electrodes of trap 1 taking the shielding effect of the rf-electrodes into account. The result of the simulation when a voltage of 250 V is applied to both electrodes is depicted by the red line. The trap is opened axially by switching one of the ring electrodes to electrical ground (green line). The ions are accelerated along the RF-guide by the potential gradient and their excess potential energy E_{pot} is converted into axial kinetic energy.



accelerated along the residual potential gradient, caused by the applied voltage of 250 V to the first ring-electrode of trap 1. The electric potential at the trap center defines the ions initial potential energy E_{pot} that is converted into axial kinetic energy of the ion. The quadrupole electrodes cause a substantial shielding effect on the electric field generated by the ring-electrodes. A Charged Particle Optics simulation¹ reveals a reduced electric axial potential at the trap center by approximately a factor of thousand. Simulating an applied voltage of 250 V on both ring electrodes results in an excess potential energy of 130 meV that can be converted into axial kinetic energy of the ion. Time of flight measurements reveal an average ion velocity of 1850 ms^{-1} , indicating that the voltages applied on micro-motion compensation wires near trap 1 contributed to the acceleration. Additionally, an incorrect simulation of the shielding effect due to deformations of the quadrupole electrodes can contribute to this discrepancy. The molecular ion accelerated out of trap 1 arrives at the Paul traps 2 and 3 after a propagation of approximately $190 \mu\text{s}$ without axial confinement. Approaching the position of the axial electric field minimum of trap 2, the voltages applied to the two ring-electrodes (R_1 and R_2) are grounded and the transferred ion can enter the trapping volume of trap 2. Re-applying the voltages on the two ring electrodes confines the transferred ion again in three dimensions (see figure 3.5). For a single molecular ion, this transfer can be processed with nearly 100% efficiency, because the radial confining RF field provides a deep trapping potential (typical 1 eV) rendering radial losses of ions negligible. Figure 3.6a) shows the result of simulations of the particle dynamics in the time-depending potentials of the transfer process by numerically solving Newton's equation of motion. Applying the protocol and parameters described above, a single ion can be trapped reliably when the voltages on the ring-electrodes are switched in a $5 \mu\text{s}$ time window.

The discussed scheme is not limited to a single ion. Moreover, if required the transfer of tens to hundreds of individual ions is possible at once with the discussed scheme. However, the transfer efficiency suffers for an increased number of ions. An ensemble of ions expands

¹Charged Particle Optics programs, CPO Ltd

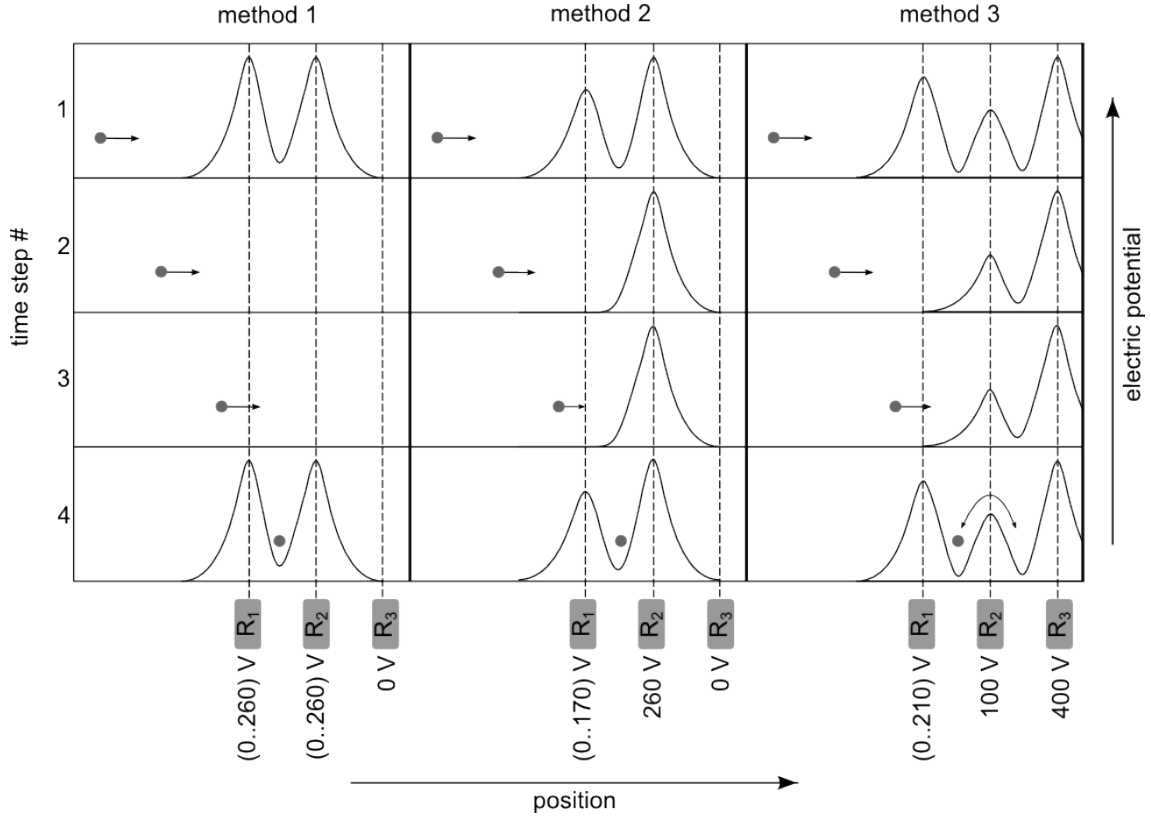


Figure 3.5: Schematic overview of the three different methods used to decelerate and trap various number of ions at the end of the transfer process. Different timings and amplitudes of voltages on the ring-electrodes R_1 , R_2 and R_3 provide the switching axial electric potential along the radial confining RF-guide. The dot and arrow represent a single or a bunch of ions and their average velocity, respectively. The position relative to the switching axial potential wells is shown for different time steps. The voltage range of the switching is given in brackets under the schematic of the corresponding ring-electrode.

in the axial direction during propagation, due to mutual Coulomb repulsion. The maximal number of ions that can be decelerated and trapped, depends on the distance between the ring-electrodes, the average time of flight and the parameters for axial confinement in trap 1. Stiffer axial confinement is related to a higher potential energy that is converted into kinetic energy and thus leads to a shorter time of flight. A shorter time of flight corresponds to a shorter time, the ensemble can spread. On the other hand, a stiffer axial confinement in trap 1 is related to a reduced the inter-ion spacing that leads to an initially increased Coulomb repulsion and hence to a faster spreading of the ensemble. Within the chosen range of parameters the influence of the shorter time of flight dominates and the increased Coulomb repulsion has only an influence on the order of a few percent on the maximal number of ions that can be trapped in total.

Figure 3.5 shows a schematic illustration of three different methods that have been developed to enhance the transfer efficiency for an increasing initial number of ions (N) in trap 1. Method 1 is closely related to the single ion transfer scheme discussed above except

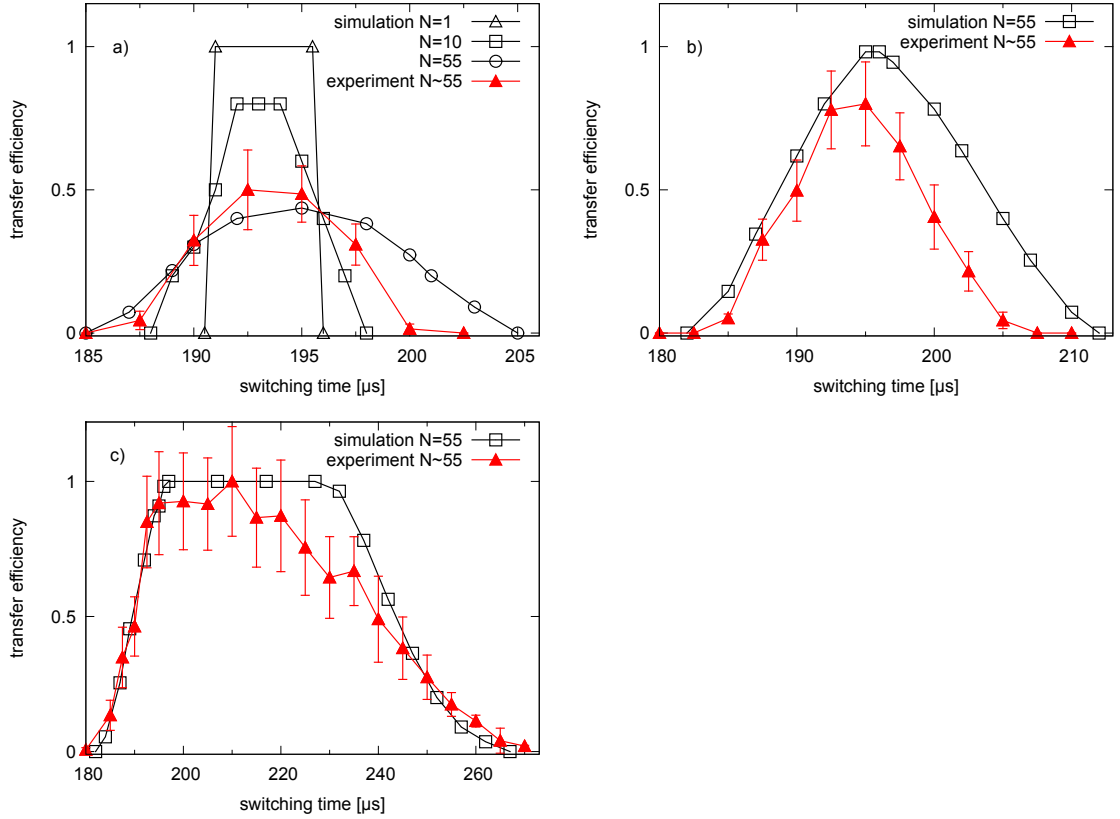


Figure 3.6: Measured and numerically simulated transfer efficiencies of an ensemble of ions from trap 1 over a distance of 39 cm to trap 2 in dependence of the delay of switching the involved ring-electrodes (time of flight of the ensemble). Figure a) shows the result of simulations of the transfer efficiency using method 1 for different initial particle numbers. The measurements were performed under conditions comparable to those assumed in the $N=55$ simulation. Figure b) and figure c) compare the experimental deduced data with the numerical simulation results for 55 ions using transfer method 2 and 3, respectively. The presented error bars take the uncertainties of the initial number of ions in trap 1 and the statistical errors into account. The fluorescence count rate of the photomultiplier in chamber 1, used to load initial crystals with similar particle numbers, yields an estimated uncertainty of $\pm 15\%$ for the absolute scale of the measurements. Furthermore, discrepancies between simulation and experiment are due to uncertainties about the exact shape of the axial electric potential of the traps 1 and 2. Additional voltages on the micro-motion compensation electrodes cause deviations from the axial potential solely generated by the ring-electrodes. Nevertheless, trends of the simulation, the different durations of successful re-capture and the different absolute efficiencies are in agreement with the experimental results.

that now a comparably large ion crystal consisting of atomic $^{24}\text{Mg}^+$ and sympathetically cooled molecular $^{24}\text{MgH}^+$ -ions is released out of trap 1. The ring-electrode R_3 is grounded and R_1 and R_2 are switched simultaneously between 0 V to 260 V. The switching is synchronized with the release of the crystal from trap 1, in order to close trap 2 when the maximal fraction of ions can be enclosed. When the electrodes are switched, all ions of the transferred ensemble that are not in the trapping section are cut off. Due to the effects that lead to a spread of an ion ensemble discussed above, the transfer efficiency of method 1 for an ion crystal that contains 10 ions, is reduced to 80%. If the released ion crystal consists of approximately 50 ions, the transfer efficiency even drops to 50%. Figure 3.6a) shows the results of simulations for $N=1, 10, 55$ and of a measurement on the transfer efficiency dependence on the time delay between launching of the ions and switching of the electrodes R_1 and R_2 . The experimental datapoints in figure 3.6a) correspond to conditions comparable to those assumed in the simulation ($N \approx 50 - 55$ ions). Experimentally, the initial number of ions in trap 1 is derived from the averaged photon count rate of the photomultiplier. The absolute number of ions and the measurement of the absolute transfer efficiency are estimated to be accurate to $\pm 15\%$. To increase the accuracy, a second CCD camera, substituting the photomultiplier, is necessary.

The maximum number of ions that can be re-trapped in total increases by switching only the ring-electrode R_1 from ground to 170 V and leave the voltage on R_2 and the grounding of R_3 constant (method 2). The sustained voltage on R_2 decelerates the transferred ensemble and finally reflects it. This leads to a double-pass of the trap volume and a collective bunching of the ensemble in the trapping region. Both effects increase the ion density in the trap and lead to an extended time window for trapping compared to method 1. The black simulation curve in figure 3.6b) shows that the largest ion crystal, that can be theoretically recaptured without losses contains approximately 55 ions. In the figure, the simulated transfer efficiency is compared with the results of the performed experiment (red datapoints). Experimentally, a transfer efficiency of 80% is deduced although the simulation predicts an efficiency close to 100% for an ion ensemble with $N=55$ ions. In addition to the uncertainties discussed above, the discrepancy between simulation and experiment might be due to a lack of knowledge about the exact shape of the axial electric potential of the traps 1 and 2 generated by the ring-electrodes and/or due to deviations in the axial potential caused by the voltages on the compensation electrodes used to minimize micro-motion. Nevertheless, a pronounced improvement in the total transfer efficiency compared to method 1 is observed.

The third method to enhance the transfer efficiency for large number of ions uses the ring-electrode R_3 as an additional reflector for ions, having a kinetic energy allowing to surpass R_2 . The voltages on R_2 and R_3 are set to 100 V and 400 V, respectively and kept constant during the whole transfer procedure. The ring-electrode R_1 is switched from 0 V to 210 V. The asymmetry between the voltages on R_1 and R_3 provides an axial positioning of the ions where micro-motion compensation is optimal. Sufficiently fast ions overcome the potential hill generated by the middle ring-electrode R_2 and are reflected by the potential of the ring-electrode R_3 . The voltage on R_1 is sufficiently high to prevent reflected ions from escaping in backward direction and therefore, an oscillation of ions between the two potential minima takes place. However, after a certain time (typically a few seconds), the cooling laser reduces the kinetic energy of the $^{24}\text{Mg}^+$ part of the

oscillating ions and the oscillation of ion-exchange between the two Paul traps eases, reaching a stationary state with a crystalline ion ensemble in both traps. The duration required to re-crystallize the ensemble of atomic and molecular ions critically depends on the laser intensity, the detuning from the atomic resonance and sufficient access of all motional degrees of freedom. A laser beam that has a red-detuning at optimum for an already crystallized ensemble, is far off-resonant for ions at velocities $\gg 1$ m/s due to the Doppler shift. To shrink the time interval it takes to re-crystallize the ion ensemble to its minimum, an additional far red-detuned laser beam has to be used. Additionally, in the present setup the cooling beam propagates nearly along the axis of the trap. The very small (few degrees) residual tilt of the cooling laser with respect to the traps' longitudinal axis, barely addresses the radial degree of freedom. Therefore, mainly the normal modes of the crystal at a linear density allowing for zigzag and higher dimensional structures sufficiently couple the longitudinal and radial motion. Figure 3.6c) shows the transfer efficiency into trap 2 as a function of the time delay for switching R_1 using method 3. The simulation for $N=55$ ions predicts a time window of approximately $30 \mu\text{s}$ with 100% re-capture probability. The corresponding experimental data (in red) qualitatively confirms this duration for maximizing the probability for re-capture and the asymmetric shape of the simulation curve.

Using the transfer method 3, the traps 2 and 3 are populated with ions. In the absence of a cooling laser beam the population of the two traps is nearly equal. However, a different spatial overlap of the cooling beam with the centers of trap 2 and 3, leads to different number of ions in the two traps. The ions will preferably gather in the trap with the better beam overlap. An interchange of the ions between the traps can be performed by switching the voltage on the middle ring-electrode R_2 with an efficiency close to 100%. Since R_2 is shared by the two traps, the tight axial confinement is preserved for all ions during the switching. A grounding of R_2 for $25 \mu\text{s}$ leads to an oscillation of the two ensembles centered at the new potential minimum. In order to analyze the potential interaction of, or exchange between the two initial ensembles, a distinguishable composition of molecular and atomic ions were prepared in trap 2 and 3. If the duration ($25 \mu\text{s}$) of the grounding of R_2 coincides with half the oscillation period of the two ion ensembles, a complete exchange of trap 2 and 3 is observed without any exchange of ions between the ensembles. No change in the fluorescence rate on the CCD camera was detected when interchanging the ensembles of ions, indicating a unit efficiency of the transfer and that the crystalline structure is preserved during the oscillation (if unlikely a melting did occur, the re-crystallization happened too fast to be detected by the CCD with a 100 ms exposure time). A redistribution of the total amount and composition ratio of ions in the two traps is achieved by using a grounding duration different from $25 \mu\text{s}$. For example, a random distribution of the ions is achieved by reducing the grounding duration and a gathering of $\approx 90\%$ of the ions into one of the trap is achieved by increasing the grounding duration.

3.2 Experimental concepts and procedure

This section is intended to give an overview of the concepts of the time-resolved pump-probe experiment on single molecular $^{24}\text{MgH}^+$ -ions and to explain the experimental pro-

cedure used to generate the results on this topic presented in section 3.3. The technical aspects, in particular the used laser systems and the used apparatus have already been described in chapter 2. In the first part of this section, the basic physical mechanisms of an ultra-short UV pump-probe pulse pair interacting with a single $^{24}\text{MgH}^+$ -ion are explained. The second part concentrates on the experimental realization and discusses the procedure that was used to obtain the results.

3.2.1 A pump-probe experiment on single $^{24}\text{MgH}^+$ -ions

Figure 3.7 shows the eight lowest lying potential energy curves of the diatomic molecular ion $^{24}\text{MgH}^+$ as a function of the intermolecular distance calculated by ab initio state-of-the-art quantum chemical models described in section 1.3 of chapter 1. A deterministically positioned (refer to section 3.1.1), single $^{24}\text{MgH}^+$ -ion is prepared in the vibrational and electronic ground state $X_{\nu=0}$. A fluorescence image of the adjacent, directly laser cooled $^{24}\text{Mg}^+$ atomic ions is shown in the lowest inset. The white circle indicated by the white arrow shows the spatial position of the localized $^{24}\text{MgH}^+$ -ion. The mechanism of the time-resolved pump-probe experiment is illustrated in the figure via the blue arrows and vertical gaussian beam profiles. As shown, the UV pump-pulse with about 4 fs duration, excites the molecular ion from the electronic and vibrational ground state to the first excited electronic state A. The equilibrium positions of these two electronic states yield a significant offset in the internuclear distance. The spectrally broad (~ 27 nm at a center wavelength of 280 nm) pump-pulse coherently excites a vibrational wave packet oscillating in the bound electronic potential of state A. The oscillation period T is approximately 30 fs. After the first excitation, an identical replica of the pump-pulse interacts with the molecular ion after the delay time τ , adjustable in the experiment. This probe-pulse can further excite part of the population in A to the dissociative electronic state C. When the molecular ion dissociates in C, the breaking of the chemical bond is signaled by the disappearance of the dark, non-fluorescing spot within the crystalline structure of the adjacent $^{24}\text{Mg}^+$ -ions. A schematic illustration of the experimentally observed indication is given by the fluorescence image associated with the C-state. The fragments of the dissociated molecular ion are a neutral magnesium atom and essentially a proton that is not supported by the stability region of the trap. Hence, both fragments are no longer confined and leave the trap. The equilibrium positions of the remaining fluorescent ions in the trapping potential change and the dark lattice site disappears. The dissociation of a single molecular ion in state C, referred to as the neutral channel in the following, is experimentally detected with an efficiency of 100%. Nearly the same argumentation applies in the case of a dissociation in one of the so called charged channels, where the magnesium fragment of the dissociated molecular $^{24}\text{MgH}^+$ -ion is charged. In this case, the resulting $^{24}\text{Mg}^+$ -ion is resonant with the cooling laser light. A dark, non-fluorescing lattice site turns into a fluorescing site, as indicated by the schematic fluorescence images associated with the states B, D, F and $E_{1,2}$. The same remarkable detection efficiency is achieved experimentally.

Due to the slope of the potential energy curve of state C, the probability for the dissociation induced by the probe-pulse depends on the position of the vibrational wave packet in state A created by the pump-pulse. The stretching motion of the molecular ion in state

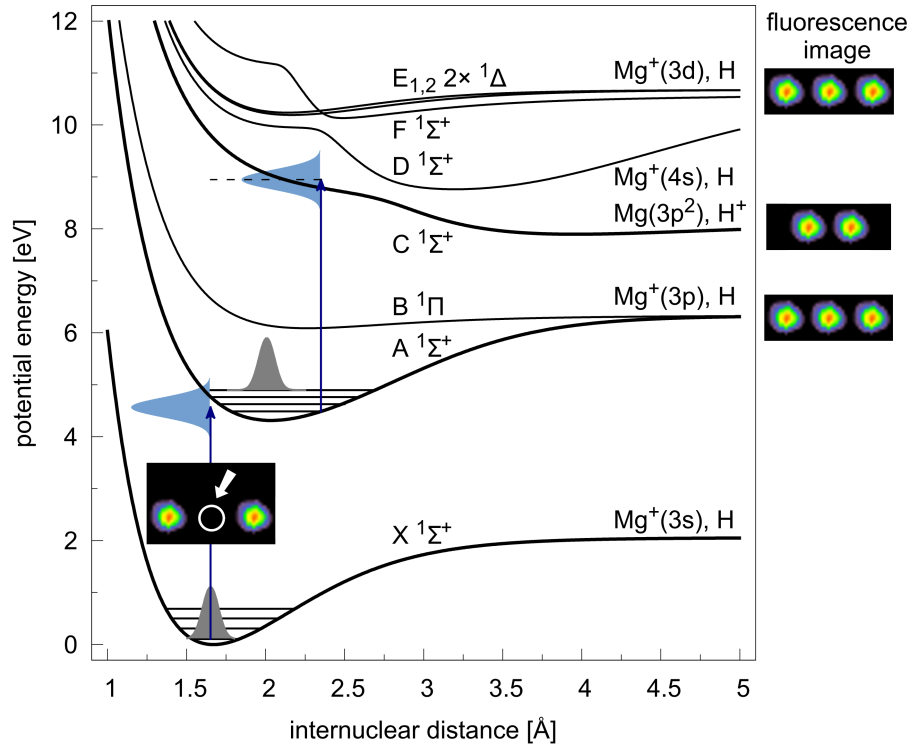


Figure 3.7: Schematic illustration of the basic mechanisms of the interaction of an ultra-short UV-pulse pair with $^{24}\text{MgH}^+$. The figure shows the eight lowest lying electronic potential energy curves of the molecular ion $^{24}\text{MgH}^+$ calculated with ab initio quantum chemical models (see section 1.3). The pump-probe experiment uses UV-pulse pairs with a spectrum around 285 nm and a duration of approximately 4 fs and is performed on a deterministically positioned single molecular ion. The molecular ion $^{24}\text{MgH}^+$ is prepared in the vibrational and electronic ground state $X_{\nu=0}$ symbolized by the gray gaussian wave packet. Experimentally, the ion can be observed as a non-fluorescing lattice site sympathetically cooled by the adjacent, directly laser cooled atomic $^{24}\text{Mg}^+$ -ions. The $^{24}\text{MgH}^+$ -ion is indicated by the white circle in the lowest of the four insets depicting fluorescence images of atomic ions. Arrows and vertical Gaussian profiles (symbolizing the spectral width of approximately 27 nm) indicate the identical ultraviolet pump and probe pulses. The spectrally broad pump pulse creates a vibrational wave packet oscillating with a period of 30 fs in the electronically excited state A (symbolized by a gray gaussian profile). Its motion is mapped onto the probability for the probe-pulse to excite the molecular ion in a second step to the repulsive state C. Dissociation via C results in loss of both product particles (Mg and H^+). The fluorescence images on the right assigned to the different dissociative channels indicate how the different charge state of the magnesium fragment can be observed experimentally (see also main text).

A modulates the dissociation probability in C with the period T. The position of the wave packet at the time instant when the interaction with the probe-pulse takes place depends on the time delay of the two pulses. That way, a periodical modulation of the dissociation probability via state C as a function of the pump-probe delay can be observed experimentally. In a simplified way, this mechanism can be described by a photon energy picture (the mean photon energy is symbolized by vertical blue arrows in figure 3.7). In one instant of time, the mean photon energy of the probe-pulse overlaps well with the dissociative state C and mismatches half an oscillation period later. The energy difference between the states A and C at approximately 1.6 \AA , which corresponds to the inner turning point of the oscillation of the wave packet is larger than the mean photon energy of the probe pulse and a dissociation is suppressed. At the outer turning point (approximately 2.5 \AA) the energy difference of the involved electronic states coincides better with the mean photon energy and the dissociation probability in C is higher compared to the inner turning point case.

Experimentally, the maximal used delay time between the pump and the probe pulse is $\tau_{\text{max}}=80 \text{ fs}$. The probability of a spontaneous decay from the first excited electronic state A into the ground state X during τ_{max} is very small because the radiative lifetime of A is on the order of 10 ns. Additionally, the assumption made in the theoretical description of section 1.3 that the molecular ion starts every pump-probe sequence in the electronic ground state is also valid because the used laser pulse repetition rate of 3 kHz is four orders of magnitude smaller than the electronic decay rate of 100 MHz. The marginal condition of the performed experiment implies a non-vanishing probability to excite the same molecular ion several times by the laser without a dissociation event. As already discussed in section 1.3, this will lead to vibrational heating within the molecular ion. The electronic configuration in the excited state A leads to a shift of approximately 0.35 \AA of the equilibrium position of the nuclei compared to the equilibrium position in the ground state. The nuclear motion is very slow compared to electronic transitions and therefore, a minimal change in the nuclear coordinates is favored. This Franck-Condon principle leads to a mixing of vibrational states and a multiple excitation of the same molecular ion without radiative cooling leads to a broad distribution in the population of vibrational states of the electronic ground state. The increasing vibrational radiative decay rates in state X balance this heating effect and a steady-state is formed. The probability of a population of the states D and E and a subsequent dissociation rises with a vibrational highly excited molecular ion. A dissociation via those states follows a charged channel which shows no pronounced dependence on the pump-probe delay time and should thus be suppressed in the experiment. Additionally, the same argument applies for a dissociation via the B or A state. A high energetic photon in conjunction with a severe occupation of higher vibrational states in the ground state can lead to this unwanted dissociation event.

3.2.2 Experimental routine

This part describes the main steps performed during the experimental procedure. Among the tasks that have to be mastered on a day-to-day basis are the tuning of the two UV-pulse replica to equal intensity and the finding of the time-zero of the pump-probe experiment that is to be performed. The experimental procedures for both steps have already been

described in section 2.2.4 on page 46. As a next step, the overlap of both, the pump and the probe beam, with the ions in the trap has to be found. The marked beam position on the fluorescence image of the CCD-camera observing the dye cuvette is not sufficient in accuracy for that purpose but serves as a good starting point of the alignment procedure. With the help of the piezo actuators of the lower half of mirror M3, the two beams can be spatially separated at the position of the ions. Therefore, it is possible to find the optimal position of the two beams independently. The response (dissociation either in the charged or the neutral channel) of the molecular ions in the trap to the laser field is used for optimization. First one of the beams is scanned vertically to the position that corresponds to a maximum observed reaction rate. The time it takes for all of the molecular ions in a heterogeneous Coulomb-crystal to be dissociated is minimized. This measurement is of course limited in statistics (typically, the measurement was repeated 3-4 times), but turned out to be sufficient in accuracy. Afterwards, the procedure is repeated in the horizontal direction. The optimized beam position of the first beam is marked using the fluorescence spot in the monitoring cuvette, and the same alignment procedure is repeated with the other beam. Finally, the correct positioning of both beams is cross-checked by observing the quadratic dependence on intensity of the dissociation rate.

An experimental sequence starts with the preparation of a heterogeneous Coulomb-crystal, consisting of a suitable fraction of $^{24}\text{Mg}^+$ - and $^{24}\text{MgH}^+$ -ions. Up to the point where the mechanical shutter of the pulsed beam line is deactivated to start an experiment, the performed steps are automatized with the help of a home-made experiment control software. First, the atomic oven used to load a $^{24}\text{Mg}^+$ ion-crystal in trap 1 is pre-heated for 40-60 seconds with a typical heating current of 3.3 A. Both, the photoionization and the cooling laser beams for magnesium illuminate the trap. After this adjustable pre-heating time elapsed, the photoionization laser beam is blocked and the cooling laser beam is attenuated by a slide-in neutral density (ND) filter. The software activates the photomultiplier tube that measures the averaged fluorescence rate of ions in trap 1 and checks if the rate of the already loaded ions exceeds a pre-set value. This value is adjusted for an optimal size (the crystal completely fills the observable region of the trap) of the transferred ion crystal in trap 2, taking the measurements on the transfer efficiency of larger Coulomb-crystals using transfer method 3 of section 3.1.2 into account. If the set value is reached, the experiment control software sets the heating current of the atomic oven to zero, otherwise the loading is continued by activating the photoionization laser beam again and sliding the ND filter out of the cooling laser beam path. This control loop is repeated after pre-set time steps (typically a few seconds) until the desired fluorescence rate value is reached. After successful loading, a sequence of three cleaning cycles is performed with the help of an arbitrary waveform generator that produces the sum of the radial secular frequencies of particles with masses $m=25$ u and $m=26$ u and applies this amplitude modulated beat signal to the micro-motion compensation electrode of trap 1. As already stated in section 3.1.1, this procedure ensures an even higher probability for an isotopically clean $^{24}\text{Mg}^+$ -crystal compared to solely relying on the used isotope-selective photoionization scheme. Molecular $^{24}\text{MgH}^+$ -ions are produced in trap 1 and transferred to trap 2 the way described in section 3.1.2 using transfer method 3. The typically used opening time of the pulsed valve amounts to 10 ms. Before the transfer, the main power of the cooling laser is distributed to trap 2 in order to minimize the time it takes to re-

crystallize the transferred ensemble. After successful crystallization and a quick check on the suitable size and molecular-to-atomic ion ratio of the crystal, the cooling laser power distributed to trap 2 is reduced to $\approx 50 \mu\text{W}$ to minimize the laser-induced reactions (refer to figure 3.3). Right after deactivation of the mechanical shutter, starting the pump-probe experiment, the automated loading routine is re-started to save experimental dead time.

Before the mechanical shutter allows an exposure of the ions with the chopped pulse trains (refer to section 2.2.4) of the UV-femtosecond beamline, a fluorescence image documents the initial ion crystal configuration. As described in section 3.1.1, this fluorescence image reveals the amount and position of both, the molecular and atomic fraction of the crystal with the help of the developed image analysis software. Provided that the fluorescence image is unambiguous (no flipping of the zig-zag structure during the exposure time) and of good enough quality, the counting error made by the software is negligible. The heterogeneous Coulomb-crystal is irradiated by the UV pump-probe pulses for an exposure interval that leads to a dissociated fraction of the molecular part of the crystal of 10-30%. The length of this exposure depends on the available pulse energy, the adjusted spectrum and the pulse delay settings. Another fluorescence image documents the state of the crystal after this interval. The experimental sequence of irradiation and taking a fluorescence image after the exposure is repeated until about 90% of the molecular ions are dissociated out of the crystal. After such an experimental run, trap 2 is emptied by grounding the ring-electrodes R_2 and R_3 for a sufficiently long time. As mentioned before, in an ideal situation the re-started automated loading routine should be finished up to this point and a fresh initial crystal can be transferred to trap 2 on time. This procedure is repeated with different time-delay settings as often as required for an experimental dataset with suitable statistics.

The overlap of the pulses with the ions in the trap, the energy and spectrum of the UV pulses are checked in regular intervals in order to balance drifts in the femtosecond laser system. Giving the fact that the beamline extends over separate tables with own supports, the long propagation length of pulses in this system (17 m) and that there is no active beam stabilization system after the hollow core fiber, it is astonishing, that the overlap with target is lost only every 3 hours on average.

3.3 Measurements on the time-resolved dissociation of single molecular ions

Two main experimental results are presented in this section. The vibrational heating effect of single molecular ions that can be electronically excited multiple times by the laser is studied in the first part. The second part presents the time-resolved measurement on $^{24}\text{MgH}^+$ discussed in section 3.2.1 for two different central wavelengths of the laser pulses. The main results and conclusions of the experiment on vibrational heating are taken into account for setting the right parameters of the time-resolved pump-probe vibrational spectroscopy experiment.

The basic mechanisms behind the occupation of higher excited vibrational states of a single molecular ion repeatedly exposed to the exciting laser pulses without a dissociation event

was discussed in detail in section 3.2.1. The theoretical treatment of this concrete experimental situation is described in section 1.3. The experimental signature of a dissociation event in the neutral channel C (the magnesium fragment of the dissociation is not charged) is different from the one in one of the charged channels A, B, D, F, E_{1,2} (the magnesium fragment is charged). After the dissociation of a single molecular ion observed in the trap, the experimental signal allows to decide with nearly 100% significance in which channel the dissociation happened. The ratio of dissociation events in the charged and the neutral channel after accumulating many fragmentations of $^{24}\text{MgH}^+$ indicates the vibrational population distribution in the steady state. The dependence of this ratio on the repetition rate of the laser for different central wavelengths reveals the "temperature" (the vibrational state population is not strictly a thermal distribution) of the molecular ions in the time-resolved pump-probe experiment that is to follow. For this purpose, the mechanical chopper discussed in section 2.2.4 is used to excite the molecular ion with an adjustable train of pulses and afterwards create a time interval for radiative cooling by blocking a suitable amount of pulses. This procedure is assumed to be equivalent to an effective pulse repetition rate of the laser calculated by multiplying the ratio $n_{\text{trans}}/(n_{\text{trans}} + n_{\text{blocked}})$ to the repetition rate of 3 kHz of the pulsed UV-laser system. Here n_{trans} is the number of transmitted pulses and n_{blocked} is the number of blocked pulses in one chopper cycle. These two numbers add up to 128 for the chopper wheel configuration that is used in this experiment. By analyzing the pulse statistic recorded by the photodiode in the UV beam path after passing the trap setup (refer to section 2.2.4 for details), n_{trans} is determined experimentally. Figure 3.8 shows the experimental results for five different chopper settings and the unchopped full repetition rate of the laser system. The ratio of dissociation events in the charged and neutral channel is evaluated for a central wavelength of approximately 280 nm and 260 nm. Both datasets show a linear dependence on the effective pulse repetition rate. The linear fit of the data points corresponding to 260 nm central wavelength lies significantly above the one for 280 nm central wavelength. This clearly verifies the theoretical hypothesis that a higher photon energy leads to higher vibrational distribution in the electronic ground state after relaxation and the corresponding higher probability to dissociate either in the higher lying electronic states or to pass the dissociation threshold in state A or B with a single high energetic photon. Both curves show that the increase in time for radiative cooling and the decrease of excitations leads to a decrease of vibrational heating. The 280 nm fit-curve passes through the origin. This reveals that in the limit of lowest effective repetition rates the probability for events in the charged channel goes to zero. This result is crucial for the decision which experimental parameters to use in the time-resolved experiment that critically relies on a dissociation in the neutral channel C. The non-vanishing intercept of the 260 nm curve (at a ratio of approximately 0.07) shows a different behavior in the case of a blue shifted spectrum of the laser pulses. The associated pulse energy is high enough to allow for a certain fraction of the molecular ions, even in the vibrational ground state, to dissociate in one of the charged channels. These measurements on the vibrational heating mechanism of repeatedly excited, single molecular ions reveals that a low effective repetition rate and a suppression of the blue side of the spectrum should be used to obtain a high enough signal with good contrast in the time-resolved measurement.

The pump-probe experiment on single molecular $^{24}\text{MgH}^+$ -ions is based on the experimen-

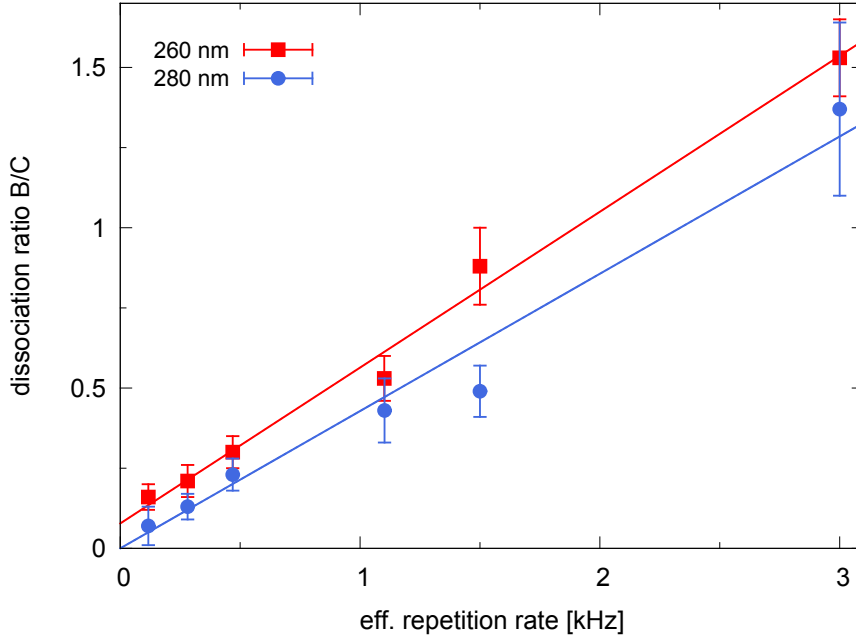


Figure 3.8: Measurement on the vibrational heating mechanism of single molecular ions that are multiple excited. The ratio of dissociation events according to $^{24}\text{MgH}^+ \rightarrow ^{24}\text{Mg}^+ + \text{H}$ and $^{24}\text{MgH}^+ \rightarrow ^{24}\text{Mg} + \text{H}^+$ are measured in dependence of the effective UV-laser pulse repetition rate. With the effective repetition rate, the interacting pulses of a chopper cycle are equally distributed in time (see main text). The pulse delay time τ was set to zero and the measurements are performed with two different central wavelengths of the pulses (approximately 260 nm and 280 nm). The ratio is expected by theory to increase linearly with the effective pulse repetition rate because vibrational heating increases (see section 3.2.1) and excitations followed by a dissociation in the higher lying electronic states D, E or the dissociation in state A, B become more probable. The linear dependency is confirmed with both central wavelengths of the pulses. The ratio corresponding to 260 nm pulses is always bigger than at 280 nm and its linear regression line reveals a non-vanishing intercept with the ordinate. For an explanation refer to the main text.

tal results of the measurement on the vibrational heating mechanism. The settings of the mechanical chopper were chosen such that on average approximately 5 pulses illuminate the ions followed by a radial cooling period of 123 pulses. This corresponds to an effective pulse repetition rate of approximately 117 Hz. The simulated steady state distribution of the vibrational state population in X for this effective pulse repetition rate reveals a population of $>80\%$ of the vibrational ground state. The states $\nu = 1$ and $\nu = 2$ have a population of $\sim 10\%$ and $\sim 5\%$, respectively. Higher vibrational states have a population of significantly less than 5%. The measurements in figure 3.8 reveal a ratio of the charged and neutral channel of 0.07 for these settings. As already described in 3.2.2 the experimental sequence of irradiation and taking a fluorescence image allows to fit a decay curve on the residual molecular ions versus time. From this, the statistically weighted exponential

half-life decay time $t_{1/2}$ is deduced for every pump-probe delay time τ . From $t_{1/2}$ the mean dissociation probability per pulse can be calculated. For a detailed description of the data analysis refer to [74]. Figure 3.9 shows the experimental result on the dissociation probability per pulse as a function of τ for a central wavelength of 280 nm of the pump-probe pulse pairs. Exactly 2477 individual molecular ions contribute approximately equally to 26 data points in the delay time range -2 fs to +75 fs. This range covers more than 2 oscillation periods. The almost full recovery of the amplitude after one period shows the long coherence times of this type of measurement due to minimal environmental disturbances. At zero delay, standard measurement procedures normally conceal the immediate response of the target due to overlapping and interfering pump-probe pulses. This coherence artifact or coherence spike [110, 111] usually excludes measurements in this regime. The measurements presented in figure 3.9, in contrast, are limited only by the pulse duration. The given statistical errorbars are deduced from the statistical average of the number of observed dissociation events corresponding to a specific pump-probe delay time. The theoretical prediction using the ab initio quantum chemical models of section 1.3 are depicted in the figure as a solid line. The modulation period of approximately 30 fs and the absolute amplitude are in good agreement with the theoretical curve. A temporal shift of approximately -7 fs is included in the fit of the theoretical prediction to the data points to account for the relatively coarse experimental adjustment of the temporal overlap of the pulses as stated in section 2.2.4. The same is done for the experimentally not well known pulse intensity on the ions. The scaling of the dissociation probability per pulse suggested by the theory, taking the random spatial orientation of the molecular ions into account, leads to an intensity of 180 GW/cm² which is in good agreement with the conservative estimation of the intensity in section 2.2.4. An additional time-independent offset has been used in the fit of the theory curve to account for the experimental contrast being smaller than expected. Several uncertainties can lead to a decrease of the experimental contrast in comparison to theory. The most severe ones are the absolute energy and the slope of the electronic state C considered by the simulation and the experimental uncertainty in the equal intensity of the pump- and the probe-pulse. Additionally, time-independent dissociation events induced by the cooling laser (refer to section 3.1.1) and the induced chirp of the pulses contribute. Both of the latter contributions are considered to have a minor influence because the probability for a time-independent dissociation event during a typical experiment time is low as shown in figure 3.3 and the main contribution to the chirp (the dielectric mirrors) has been taken into account by the simulation.

Systematic errors in the measurement are reduced to a minimum by several precautions. Long term drifts in the energy of the UV-pulses are corrected in regular intervals by adjusting the third-harmonic generation yield to account for a constant energy. Short term energy drifts are treated by recording the energy of the applied pulses on a photodiode during the experiment and correct the data points with these measurements. The overlap of both beams with the ions was checked by regularly performing a reference measurement at $\tau = 0$. If a deviation was found, the recorded data since the last reference measurement was omitted and the overlap was re-adjusted by the means described in section 3.2.2. Although the contribution of the charged channel is reduced to a minimum by the used mechanical chopper setting, events in such a channel were taken into account in the data evaluation. The same is done when a creation of a molecular ion via reaction 3.1 is

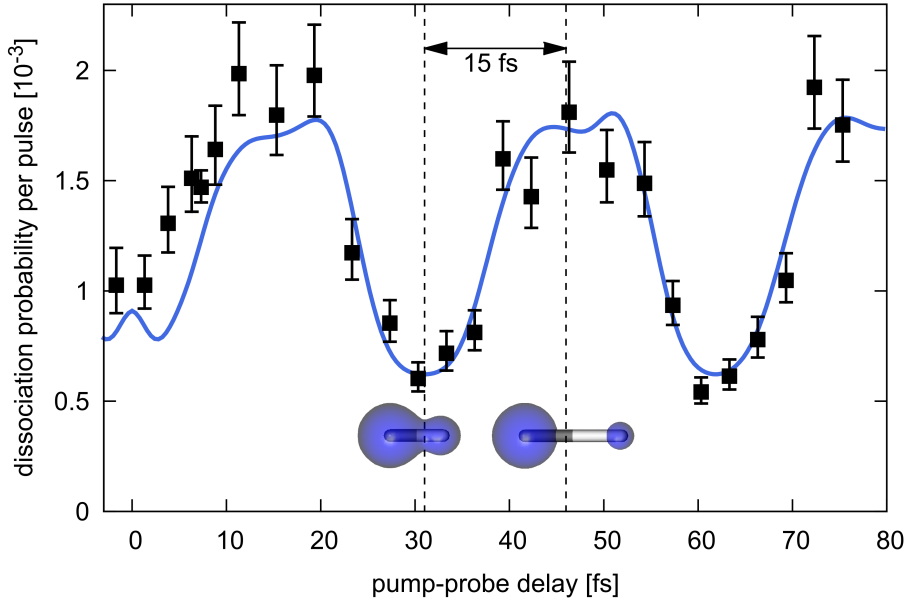


Figure 3.9: Vibrational motion of molecules derived from the dissociation of single $^{24}\text{MgH}^+$ -ions as a function of pump-probe delay for UV-laser pulses with a center wavelength of approximately 280 nm and duration of approximately 4 fs. The dissociation probability per pulse in channel C (see figure 3.7) is modulated with a period of ≈ 30 fs. An illustration of the two related electronic probability densities of $^{24}\text{MgH}^+$ at the classical turning points is given. Each data point corresponds to the statistical average ($\pm 1\sigma$) of experiments with in total between 50 and 108 molecular ions. The solid line represents the result of the theoretical model (see section 1.3) for the experimental parameters described in the text. The simulation is scaled along the ordinate to account for the experimentally not well known pulse intensity at the position of the ions. An additional temporal shift along the pump-probe delay axis and an additional time-independent offset of the simulation are introduced in order to match the experimental data (see main text). Note the almost full recovery of the amplitude after the first oscillation period and the little deviations from the simulation near zero pump-probe delay.

observed. In both cases, it is assumed that the event happened after half of the exposure interval. For a detailed description of the data evaluation and the treatment of the short-term energy drifts or the contributions of other reaction channels refer to [74].

The time-resolved measurement as described above was repeated using a spectrum of the pump-probe pulses that is shifted to the blue side. Figure 3.10 shows the main result of this measurement using a pulse spectrum with a center wavelength of 260 nm. As expected by the theoretical simulation as well as the experimental measurements on the vibrational heating mechanism, the signal of the dissociation probability per pulse in the electronic excited state C looks different compared to the 280 nm case. The, in first order, sinusoidal oscillation of the dissociation probability in state C with the pump-probe delay time in the case of 280 nm pulses is substituted by a decreased time-dependent signal up to the 20 fs delay regime, followed by a pronounced dip at 30 fs. Additionally, the contrast of the

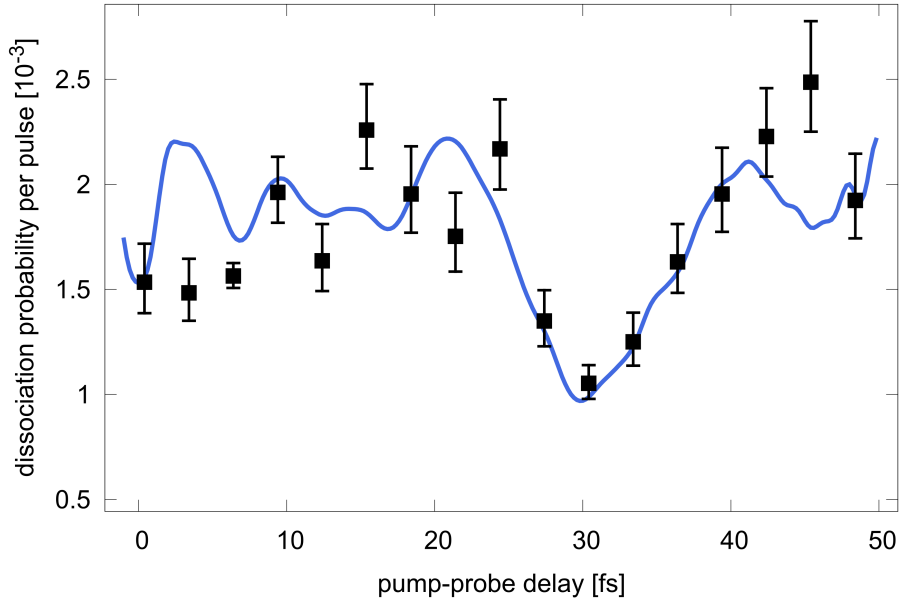


Figure 3.10: Dissociation probability per pulse in dependence of the delay time for pulses with approximately 260 nm central wavelength and an estimated pulse duration of 5 fs. The dissociation probability in channel C (see figure 3.7) is less modulated and less harmonic compared to the 280 nm case presented in figure 3.9. A pronounced dip in the dissociation probability per pulse is observed at approximately 30 fs. The presented error bars correspond to the statistical error within one standard deviation ($\pm 1\sigma$). The solid line represents the theoretical model for the used experimental parameters. The simulation result is scaled along the ordinate to account for the experimentally not precisely known intensity of the pulses at the spatial position of the ions. Additionally, a temporal shift of 6.4 fs is introduced because the temporal overlap of the pump- and the probe-pulse can experimentally only coarse adjusted. No additional time-independent offset is introduced in this case.

signal is significantly reduced. The solid line in the figure corresponds to the theoretical simulation performed taking the change of the center wavelength into account. Like in the 280 nm case, a temporal shift (6.4 fs) is introduced to account for the temporal overlap of the pulses that can be adjusted only coarsely with other experimental means. Likewise, the simulation is scaled along the ordinate to adjust the experimentally used intensity of the pulses at the spatial position of the ions. Different to the 280 nm case, no additional time-independent offset had to be used to match the simulation with the data points. This indicates that the estimated pulse parameters (chirp, temporal duration) done by the theory is valid and that the calculated potential energy curves are correct even concerning their absolute value. The experimental signal of the 260 nm case can be interpreted by taking into consideration that higher averaged pulse energies lead to a more position (of the vibrational wavepacket in the excited electronic state A) independent dissociation probability in C, as explained in section 3.2.1.

Chapter 4

Experimental studies towards heavier atomic and molecular ions

This chapter describes the first steps towards the attempt to broaden the mass range of molecular ions that can be investigated with the current apparatus. Using trapped barium ions with almost six times bigger mass than magnesium gives the possibility to escalate the mass range of sympathetically cooled molecular ions [54]. The first section concentrates on a novel, highly effective and isotope selective photoionization scheme for barium atoms, experimentally demonstrated for the first time in the framework of this thesis. The new scheme is compared to an established one [112] in terms of efficiency. A theoretical model is developed to reproduce the dependencies of the achieved loading rate into a linear Paul trap on the detuning of the laser source from the peak loading rate and on the laser power. The second section is dedicated to the demonstration of trapping and laser Doppler-cooling of $^{138}\text{Ba}^+$ ions and to the experimental routine to achieve the latter. The third section demonstrates the successful preparation of light, diatomic molecular ions and shows the embedding of those into the crystalline structure of $^{138}\text{Ba}^+$ ion crystals. The molecular ions are identified using a destructive, resonant excitation scheme of their radial secular motion [103].

4.1 Photoionization of neutral Barium

Loading a Paul trap via photoionization of neutral atoms inside the trapping region has recently substituted the electron beam bombardment technique. The main reasons are a higher efficiency and the isotope selectivity of most of the photoionization schemes presented so far [113]. Additionally, photoionization has a lot of other beneficial effects, like strongly reduced static charging of dielectrics [114], lower motional heating rates due to the suppression of patch potentials [115] and easier loading of surface-electrode traps with a substantially restricted trap depth [116].

In section 2.2.1 a resonant two-photon ionization scheme for neutral magnesium atoms has been described which was first demonstrated in reference [80]. This isotope selec-

tive scheme has been successfully implemented within the framework of this thesis and $^{24}\text{Mg}^+$ ions have been loaded (see section 3.1.1) into a linear Paul trap. In this section, two efficient and isotope-selective resonant two-photon ionization schemes for loading barium ions into linear Paul traps are demonstrated. The novel technique of using the strong dipole-allowed transition $6s^2\ ^1\text{S}_0 \rightarrow 6s6p\ ^1\text{P}_1$ at $\lambda = 553\text{ nm}$ as a first step towards ionization is compared to the established technique of using a weak intercombination line [112] ($6s^2\ ^1\text{S}_0 \rightarrow 5d6p\ ^3\text{D}_1$, $\lambda = 413\text{ nm}$). An increase of two orders of magnitude in the ionization efficiency is found favoring the transition at 553 nm. This technique can be implemented using commercial all-solid-state laser systems¹ and is expected to be advantageous compared to other narrowband photoionization schemes of barium in cases where highest efficiency, isotope-selectivity or a fast, controlled and minimal invasive reloading of the trap is required [76].

Figure 4.1a) gives a summary of the relevant transitions of neutral barium used by the two different, resonant two-step excitations from the ground state $6s^2\ ^1\text{S}_0$ to the continuum. In both cases, the first excitation step is realized by a resonant transition and the isotope shifts are large compared to the laser linewidth and the Doppler and power broadening of the transition. For example, the isotope shifts for the $6s^2\ ^1\text{S}_0 \rightarrow 6s6p\ ^1\text{P}_1$ transition relative to ^{138}Ba are: ^{137}Ba : $2\pi \cdot 215\text{ MHz}$; ^{136}Ba : $2\pi \cdot 128\text{ MHz}$; ^{135}Ba : $2\pi \cdot 259\text{ MHz}$; ^{134}Ba : $2\pi \cdot 143\text{ MHz}$ [117]. Therefore, both schemes provide a high probability to load an isotope clean crystal which is of uttermost importance in many experiments. Only relying on the natural abundance of ^{138}Ba (71.7%), the probability to load an isotopically clean ion crystal consisting of 20 $^{138}\text{Ba}^+$ ions for example amounts to $0.717^{20} \approx 0.1\%$. The probability for the given example in the case of the used isotope selective photoionization schemes is estimated to be much higher than 90% and can even be enhanced by detuning the first step photoionization laser towards lower frequency, because ^{138}Ba has the lowest frequency of all stable isotopes. The impact of quality of the isotope selectivity is even higher when the experiment relies on rare isotopes [118].

The first, established scheme requires two photons at 413 nm and is resonant in the first step towards ionization with the intercombination line of the $6s^2\ ^1\text{S}_0 \rightarrow 5d6p\ ^3\text{D}_1$ transition. It was first demonstrated in [112] and will be labeled scheme A in the following. This scheme benefits from the fact that light at only one frequency has to be provided and that it can be generated by commercial and robust diode lasers. A drawback is the weak transition strength and the fact that the atoms are optically pumped (wavy line in 4.1a)) to the metastable states $6s5d\ ^3\text{D}_{1,2}$, because the spontaneous emission rate is larger than that to the ground state. Within the framework of this thesis, this scheme has been realized for comparison. As described in section 2.2.2 the 413 nm laser propagates on axis through the trap setup and is focused by the $f=500\text{ mm}$ lens re-used from the magnesium setup. The measured beam waist at the trap center (see Fig.4.2b) amounts to $w_{413} \approx 440\ \mu\text{m}$ ($1/e^2$ of intensity).

The strong dipole allowed $6s^2\ ^1\text{S}_0 \rightarrow 6s6p\ ^1\text{P}_1$ transition at 553 nm [120] is used as the first excitation step in the second scheme, labeled scheme B in the following. The laser light required for this first step is generated using a dye laser ($\sim 500\text{ kHz}$ linewidth) pumped by a frequency-doubled Nd:YAG laser. For a detailed description refer to section 2.2.2.

¹Toptica Photonics AG

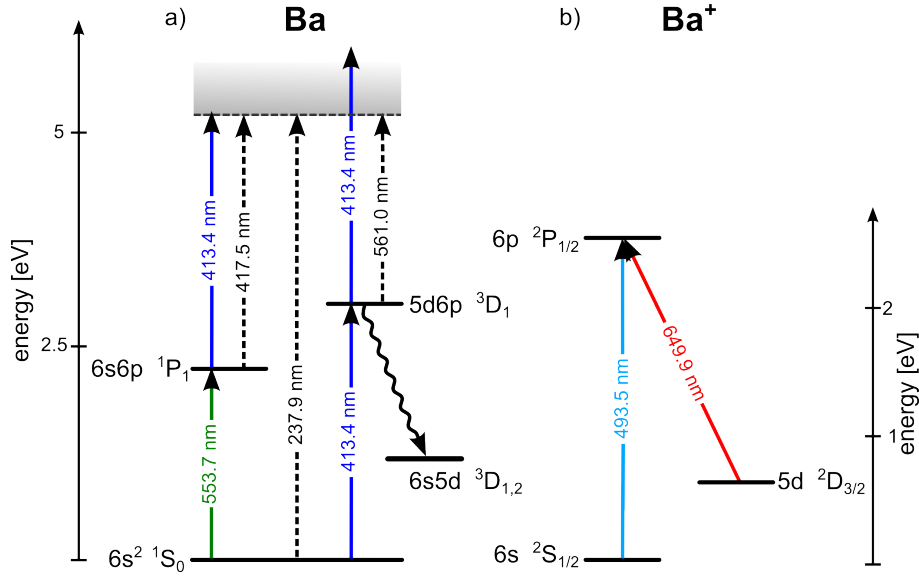


Figure 4.1: Energy level scheme of a) neutral and b) singly ionized barium. Only the relevant levels and transitions are shown. Solid lines indicate experimentally realized transition, whereas dashed lines are only given for comparison. For coarse orientation, an energy scale is given for both cases. Photoionization of neutral barium is experimentally realized using two different schemes, that both use one initial resonant excitation followed by a non-resonant excitation into the continuum. In scheme B, a 553.7 nm photon excites the 1P_1 state of $2\pi \cdot 18.9$ MHz natural linewidth, corresponding to 8.4 ns lifetime [119]. An additional photon at 413 nm excites the atom above the ionization threshold at 5.21 eV. The other ionization scheme (scheme A) requires two photons at 413 nm. The first photon resonantly couples the ground state with the $5d6p \ ^3D_1$ level. The second photon excites the electron deeply into the continuum. Note that in scheme A, the atoms are optically pumped (wavy line) to metastable states because the spontaneous emission rate to the states $6s5d \ ^3D_{1,2}$ ($3.8 \cdot 10^7 \text{ s}^{-1}$ to 3D_1 , $1.9 \cdot 10^7 \text{ s}^{-1}$ to 3D_2) is larger than that to the ground state ($1.5 \cdot 10^6 \text{ s}^{-1}$). Laser cooling of the singly charged ion is done on the Λ -system spanned by the $^2S_{1/2}$, $^2P_{1/2}$ and $^2D_{3/2}$ levels, using lasers near 493 nm and near 650 nm.

The second step from the 1P_1 state to the continuum requires a wavelength <418 nm. Therefore, a 413 nm photon is sufficient to reach the continuum and the laser of scheme A can be re-used. The 553 nm laser is focused to a beam waist of approximately $230 \mu\text{m}$ (see Fig.4.2a) and overlapped with the 413 nm laser. Both lasers, again, propagate on axis through the trap.

A thermal beam evaporated by resistively heating the barium filled tantalum tube of the atom oven assembly in chamber 3 provides neutral barium atoms in the trapping region (see section 2.1.2). A 3.15 A heating current corresponds to an oven temperature of approximately 600 K. The atomic barium beam has an angle of approximately $100 \pm 5^\circ$ with the laser propagation direction. The observed transition frequencies are thus red-shifted. The atomic beam is collimated by a $200 \mu\text{m}$ slit aperture at a distance of 4 cm from the trap axis in the direction perpendicular to the laser to ensure a minimal contamination of the

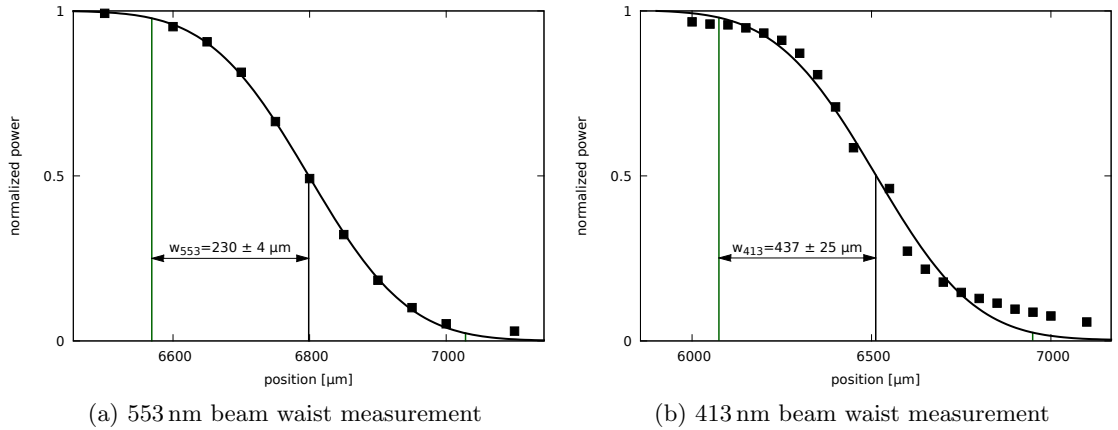


Figure 4.2: Measurement of the beam waist at the position of the potential minimum of the trap. Figure 4.2a and figure 4.2b show the results for the 553 nm laser and the 413 nm laser, respectively. A razor blade is moved across the beam and the power that still passes the blade is recorded for several positions within the beam. The power blocked by the razor blade $P(x)$ can be described by an error-function assuming a gaussian beam: $P(x) = P/2 \cdot (\text{erf}(\sqrt{2}(x_0 - x)/w) + 1)$. P is the power of the unblocked beam, x_0 the position value in unit length at which the power drops to 50% and w is the beam waist ($1/e^2$ of intensity). This function is fitted with P , x_0 and w and the results are plotted as solid lines in the figure. The datapoints in 4.2a fit better than in 4.2b, because the 553 nm laser is fiber coupled to the optical table and therefore very near to a perfect gaussian beam. The 413 nm light, in contrast, is produced via a diode laser and its elliptical beam profile is compressed in one spatial direction using an anamorphic prism pair. Still the fit shows that the measured beam profile can be assumed, within a good approximation, to be gaussian.

trap electrodes with barium. However, if an ultimately high grade of isotope selectivity is required, a collimated atomic beam orientated perpendicular to the propagation direction of the photoionization lasers should be used. This minimizes Doppler-broadening and avoids overall Doppler-shifts.

After ionization, the $^{138}\text{Ba}^+$ ions are laser-cooled on the $^2\text{S}_{1/2} \rightarrow ^2\text{P}_{1/2}$ transition at 493 nm. Figure 4.1b) shows the relevant electronic levels and transitions of singly ionized barium. The upper state decays with a branching ratio of approximately 3:1 to the ground and to a metastable $^2\text{D}_{3/2}$ state [58]. The population in the D state is re-pumped to the P state by an additional laser at 650 nm to approach a closed cycling transition for laser cooling. In addition, a weak magnetic field (0.5 mT, see also section 2.1.2) perpendicular to the linear laser polarization is used to prevent dark states in the Zeeman manifold of the metastable state. Both, cooling laser and repumper are overlapped and propagate approximately along the axis of the linear trap. With the cooling laser tuned in frequency to be resonant with the desired barium isotope ($^{138}\text{Ba}^+$), the number of fluorescing ions in a Coulomb crystal can be determined with 100% accuracy [76]. Throughout this section loading rates of ions are determined by the evaluation of fluorescence images of ions

confined in the Paul trap after a certain loading duration.

In Fig. 4.3, the experimentally determined ion loading rates are shown as a function of the detuning of the laser from the overall shifted atomic resonance coupling the ground and the intermediate state (first step laser). Figure 4.3a and figure 4.3b show the results for scheme A and B, respectively. From now on, all frequency values in this section are given divided by 2π . In both cases, the power of the first step laser and the power of the second step laser, coupling the intermediate state and the continuum, are equal and set to 1 mW. The zero of the horizontal frequency detuning axis is calibrated by fitting the maximum loading rate. As discussed above, the atoms have a velocity component along the propagation direction of the lasers in the present setup. The maximum loading rate is thus Doppler-shifted towards lower frequencies and the spectral line is Doppler-broadened. The center of the unshifted atomic resonance is indicated by an arrow in the figure. The solid lines represent the results of a fit using a theoretical model that will be described in detail in the following. The Doppler broadening of the spectral lines is caused not only by the temperature T of the atomic ensemble but also by the angle θ between the atomic beam and the ionization laser beams. Figure 4.3a reveals an experimentally observed 110 MHz full-width-at-half-maximum (FWHM) of the spectral line of scheme A. The FWHM achieved via scheme B should amount to 82 MHz for the same experimental setup, if this effect was caused by Doppler-broadening at the given angle θ only. The experimental result in figure 4.3b, however, shows a larger broadening of approximately 105 MHz. This additional broadening is supposed to be caused by power-broadening, because in scheme B the transition dipole moment μ is much higher than in scheme A. The following theoretical model explains the broadening of the spectral lines for the used geometrical layout of the atomic oven and ionization laser beams and the estimated temperature of the Maxwell-Boltzmann distribution of a thermal atomic beam. That means, a consistent description of the experimental situation and all measurements presented in this section is done with a set of three parameters (θ , T , detuning from the resonance frequency of an atom at rest).

For convenience, Cartesian coordinates (x, y, z) are used. The laser beams and the atomic oven are placed in the $x - z$ plane. The origin of the coordinate system is chosen at the atomic oven. The laser beams propagate along the z -axis and their center has the transverse coordinates $x = X_0$ and $y = 0$. The ion loading rate η at a specific position (x, y, z) is assumed to be proportional to the atom population at the intermediate state ($6s6p^1P_1$) and to the intensity of the second laser beam transferring the population from the intermediate state to the continuum. The population of the intermediate state ρ depends on the intensity of the first laser beam driving the transition from the ground to the intermediate state.

The transverse intensity distribution of the laser beam is assumed to be gaussian:

$I_i e^{-2[(x-X_0)^2+y^2]/w_i^2}$ ($i = 1$ (2) for the first (second) step laser). I_i represents the intensity at the center of the laser beam with a beam waist w_i . The ionization probability for an atom leaving the oven at $t = 0$ with velocity (v_x, v_y, v_z) is given by

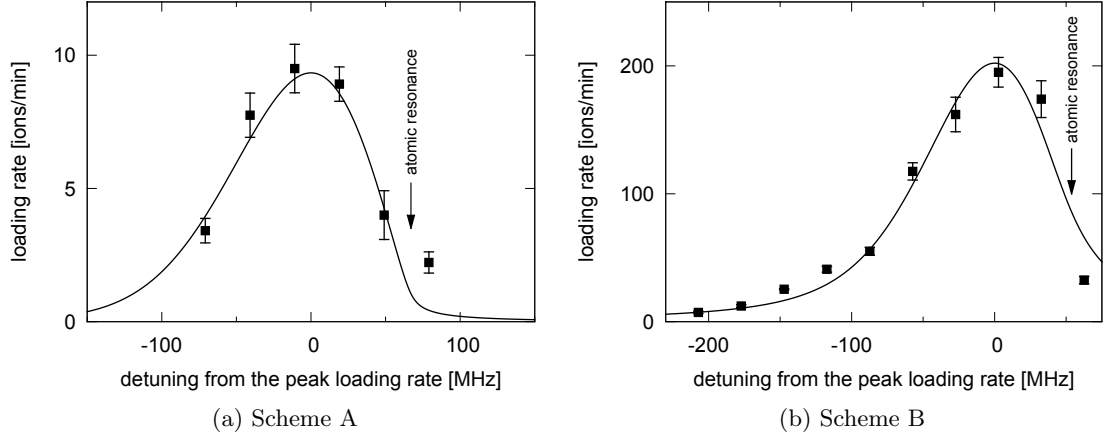


Figure 4.3: Loading rate of $^{138}\text{Ba}^+$ ions into the linear Paul trap as a function of the detuning of the laser used in the first ionization step to the peak loading rate. In 4.3a and 4.3b the results for scheme A and B are shown respectively. In both cases, the laser powers are set to 1 mW. In the present setup, the atoms have a velocity component along the propagation direction of the laser and therefore, the peak of the loading rate is redshifted with respect to the atomic resonance (indicated by an arrow). Note the asymmetry of the fitted model curve (black solid lines) in both photoionization schemes which is also due to the non-perpendicular orientation of the laser beam and atomic oven. The given errorbars represent statistical errors only.

$$\eta(v_x, v_y, v_z) = \alpha \int_0^\infty I_2 e^{\Delta} \rho(v_x t - X_0, v_y t, v_z t) dt, \quad (4.1)$$

$$\Delta = -\frac{2 \left[(v_x t - X_0)^2 + (v_y t)^2 \right]}{w_2^2}$$

where α is a constant of proportionality (see also caption of Fig. 4.4). The peak intensity is related to the laser power P_i by $I_i = 2P_i / (\pi w_i^2)$.

The population ρ of an atom in the intermediate state is assumed to be stationary. The lifetime in the intermediate state (inverse of the natural linewidth Γ) is much shorter than the typical transit time of the atom across the laser beam. For example, assuming a Maxwell-Boltzmann distribution for $T = 600$ K, the most probable speed of barium atoms is about 200 m/s. The corresponding transit time through the laser beam ($2w_1 = 460 \mu\text{m}$) amounts to $2.3 \mu\text{s}$, which is much longer than the lifetime of the $6s6p^1P_1$ state (8 ns). Therefore, ρ can be expressed as [55],

$$\rho = \frac{1}{4} \frac{\Omega_0 (v_x t, v_y t)^2}{(\delta - kv_z)^2 + \frac{\Gamma^2}{4} + \frac{\Omega_0 (v_x, v_y)^2}{2}}, \quad (4.2)$$

where δ is the detuning of the laser from the atomic resonance frequency at rest, k is the wavenumber of the laser beam driving the transition. The Rabi frequency Ω_0 is a function of the spatial coordinates:

$$\Omega_0(x, y)^2 = \frac{2\mu^2}{\hbar^2 \varepsilon_0 c} I_1 \exp \left\{ -\frac{2}{w_1^2} \left[(x - X_0)^2 + y^2 \right] \right\}. \quad (4.3)$$

In Eq. (4.3), \hbar is the reduced Planck constant, ε_0 is the electric constant and c is the speed of light in vacuum.

By integrating over the atomic velocity for an appropriate velocity distribution function $f(v_r, v_y)$, the total ion loading rate η_0 can be obtained:

$$\eta_0 = \int_0^\infty v_r dv_r \int_{-\infty}^\infty dv_y \int_{\theta-\delta\theta}^{\theta+\delta\theta} d\theta f(v_r, v_y) \eta(v_r \sin \theta, v_y, v_r \cos \theta). \quad (4.4)$$

The coordinates r and θ , defined as $x = r \sin \theta$ and $z = r \cos \theta$, are introduced and v_x and v_z are replaced by $v_r \sin \theta$ and $v_r \cos \theta$, respectively. The azimuthal angle θ is the angle included by the direction of the atomic and the laser beam. For a thermal beam of atoms with mass M , a Maxwell-Boltzmann distribution can be assumed:

$$f(v_r, v_y) = \frac{1}{N} \exp \left(-M \frac{v_r^2 + v_y^2}{2k_B T} \right), \quad (4.5)$$

where k_B is the Boltzmann constant, and N is a normalization factor. In the present experimental setup, the slit aperture collimates the beam in the y-direction. However, the diverging angle of the atomic beam in the x-z-plane is negligible compared to the velocity distribution of atoms in a thermal beam. Therefore, the divergence $\delta\theta$ in Eq. (4.4) approaches zero and θ is assumed to be at one value in the following.

Up to this point, the theoretical model is developed for the case of scheme B where the assumption that the population ρ is stationary is valid. Concerning the case of scheme A the spontaneous emission from the intermediate state ($5d6p^3D_1$) mainly leads to metastable states such as $6s5d^3D_{1,2}$. The maximal spontaneous emission rate from $5d6p^3D_1$ to the ground state ($6s^2^1S_0$) amounts to $1.5 \cdot 10^6 \text{ s}^{-1}$, whereas that to $6s5d^3D_1$ is $3.8 \cdot 10^7 \text{ s}^{-1}$ and that to $6s5d^3D_2$ is $1.9 \cdot 10^7 \text{ s}^{-1}$ [88]. Therefore, the atoms are optically pumped to the metastable states, and the stationary value of ρ approaches zero. By changing the definition of ρ to be the transition probability from the ground state to the intermediate state, it is possible to use the same formulae as in Eqs. (4.1-4.5), except for the value of the constant of proportionality α . Thus, applying the present model does not allow for comparing the absolute value of the loading rates achieved via the two schemes.

By substituting Eqs. (4.1-4.3) and (4.5) into Eq. (4.4), the theoretical curves in Fig. 4.3 are obtained. In the case of scheme A, the temperature of the atomic beam is assumed to be $T=600 \text{ K}$, the spontaneous emission rate is $5.85 \cdot 10^7 \text{ s}^{-1}$, and the parameters of the laser providing the first and the second step of ionization are identical. For scheme

B, the temperature is also assumed to be $T=600\text{ K}$, but the spontaneous emission rate is $1.2 \cdot 10^8\text{ s}^{-1}$, and the parameters of the first and second step lasers have to be set independently. In the calculation, the parameters θ , α , and the center frequency of the resonance are left as fitting parameters for the data presented in Fig. 4.3a and $\theta = 98.3$ degrees is deduced. The center of the resonance is indicated by an arrow in the figure. In Fig. 4.3b, θ is fixed to the obtained value, and only the center frequency of the resonance and α remain as fitting parameters.

The experimentally derived loading rates of the two schemes (A: blue circles and B: red squares) are shown in dependence of the laser power in Fig. 4.4. The datapoints corresponding to scheme A show in principle a dependency on the square of the laser power at 413 nm, as to be expected in a process requiring two photons. The same argument applies in the case of scheme B, where a dependency on the product of the laser powers at 413 nm and 553 nm is expected. In scheme B, the laser power of the second laser (413 nm) is kept equal to that of the first laser (553 nm) and the two schemes are comparable in terms of power. This is justified, because scheme B does in principle not require a separate laser system at 413 nm as chosen in the current experiment for simplicity, having the laser source of scheme A available. As shown in [121, 122], the transition into the continuum does not have to be of narrow bandwidth (different to the first step in scheme A and B) and can be replaced by an incoherent light source. For the given parameters, the loading rate of scheme B is already about 40 times larger than that of the scheme A. As already mentioned, the beam waists of the two lasers used in scheme B differ considerably at the trap center. The lifetime of the excited state is much shorter than the typical transit time of the atom through the beam. Therefore atoms can only be ionized when both required beams overlap. Taking the currently not contributing power within the 413 nm beam into account, a lower bound for the additionally increase in ionization efficiency can be derived. For the comparison of the two schemes, a homogeneous atom density in the trap volume and an equal probability to trap an ionized atom is assumed. Implying a flat top profile for both beams of different waists would lead to an underestimation of scheme B in the comparison of efficiencies by a factor of $(w_{553}/w_{413})^2 \approx 4$. Considering, more realistically, gaussian beams and assuming a concentric overlap, the measured ionization rate achieved via scheme B has to be multiplied at least with a factor of 2.5 for comparison with scheme A. This allows to derive an increase of the total efficiency via scheme B by two orders of magnitude. The lines in figure 4.4 are the results of the calculations based on the discussed model. For the red dashed curve, the detuning was set to the frequency at which the loading rate is at its maximum, the temperature of the atom oven is assumed to be 600 K and the angle between the atom beam and the laser beam is set to $\theta = 98.3^\circ$ which was extracted from the measurements presented in figure 4.3. The only fitting parameter is the total efficiency α . The data points corresponding to low power values ($<1.5\text{ mW}$) seem to show a systematic lower loading rate than expected by the model. This might be due to a drift of the laser frequency away from the maximum loading rate. As described in 2.2.2 the lasers used for photoionization of neutral barium and Doppler-cooling of $^{138}\text{Ba}^+$ are not long-term stabilized and a drift in frequency during the measurements is possible. Such a drift would cause the discrepancies with the model in the low power region. The additional red solid curve in figure 4.4 is the result of the fit with the model when a detuning of +75 MHz from the peak loading rate is assumed.

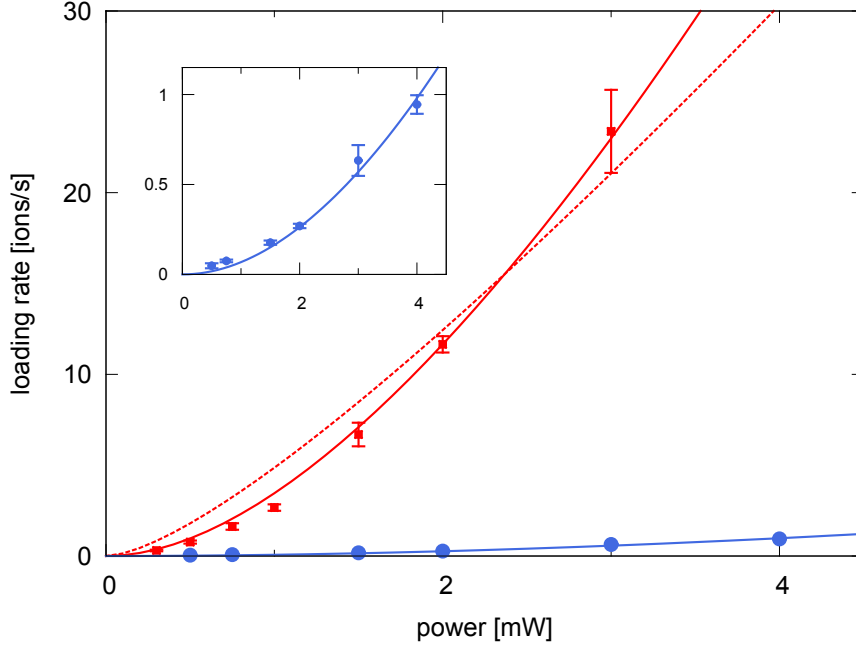


Figure 4.4: Loading rate achieved with scheme A (blue circles) and B (red squares) as a function of the laser power used in the first step towards ionization. The power of the 553 nm and the 413 nm laser are kept equal for scheme B. The dashed and solid curves represent the results of a calculation, assuming an atomic oven temperature of $T=600$ K. For the dashed red curve, the detuning of the first step laser is set to the frequency at which the loading rate is at its maximum and the angle θ between the laser and the atomic oven is taken to 98.3° . The remaining fitting parameter is the total efficiency α (see main text). The additional solid red curve shows the result of the fit with the model for scheme B when a detuning of $+75$ MHz from the peak loading rate is assumed. This might explain the discrepancy of the results from the model at low powers. The experimental data show that the ion loading rate in the experiment following scheme B is already about 40 times larger than following scheme A. Due to different beam waists used to realize scheme B, an additional increase of the efficiency by a factor of approximately 2.5 has to be considered, leading to a total enhancement of the efficiency by approximately two orders of magnitude compared to scheme A (for details see main text). The inset shows a close-up of the experimental data derived following scheme A and the corresponding curve fitted according to the model with the laser frequency set to the value where the loading rate is maximal.

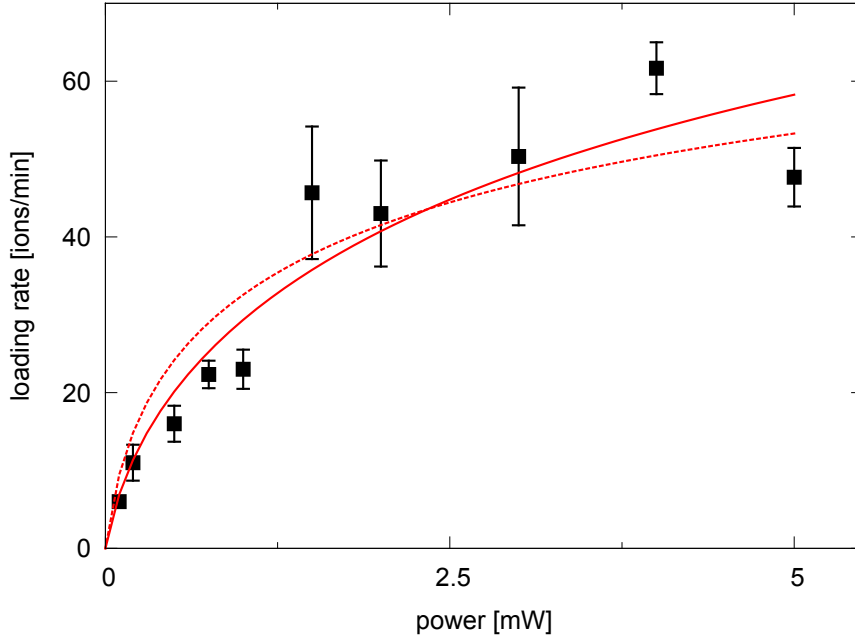


Figure 4.5: Loading rate achieved via scheme B as a function of the laser power used in the first ionization step. The power of the laser driving the second ionization step into the continuum is kept constant at 1 mW, and the temperature of the atomic oven is assumed to be 550 K for the calculation. The different assumed temperature accounts for a reduced heating current of the atomic oven used in this experiment, compared to the one chosen to obtain the results presented in the figures 4.3 and 4.4. The red dashed curve is the result of fitting the model with parameter α and the frequency set at the maximum loading rate. The additional red solid line is the result of the fit with α when a detuning of -50 MHz from the frequency corresponding to the maximum loading rate is assumed (see main text).

Fig. 4.5 shows the dependence of the loading rate on the power of the first laser in scheme B when the power of the second laser is kept constant at 1 mW. Deviations from a linear dependency of the laser power at 553 nm as one would expect are mostly due to saturation effects. The power dependence is similar to that described in reference [121] (Fig.6) and follows in principle a dependency on the square root of the power, as to be expected for an increased saturation of the transition. The red dashed curve was derived from the model by fitting the total efficiency α and setting the detuning to the frequency at which the loading rate is at its maximum. However, deviations of the experimental results from this curve are prominent, especially at low laser power. After scrutinizing the experimental data, it turned out that the laser frequency has drifted a few tens of megahertz to the red of the frequency for the peak loading rate, for the same reason described above. Assuming a detuning of -50 MHz from the frequency of maximal loading rate, the result of the model (red solid line) is in better agreement with the experimental findings.

In conclusion, a novel, isotope-selective resonant two-photon photoionization scheme for barium has been demonstrated and the loading rates into a linear Paul trap was compared to an established scheme. An increase in efficiency by two orders of magnitude

was found. This allows to enhance the advantages of photoionization for barium like minimal charge build-up on insulators compared to electron bombardment ionization or patch potentials caused by a contamination of the trap electrodes. Reducing these effects might have a great impact in experiments that rely on high efficiency such as in cavity quantum-electrodynamics with ion coulomb crystals [123], one-dimensional surface traps for quantum information processing [116], two-dimensional trapping arrays for quantum simulations [124, 125] or the recently realized optical trapping of ions [126]. The direct, efficient photoionization of an optically trapped barium atom reduces detrimental charging effects, followed by a loss of the ion out of the shallow (compared to RF-potentials) optical potential. This might allow, for example, to study cold-chemistry processes [127] and to simultaneously avoid micro-motion that normally occurs in conventional ion traps [128]. In addition, providing loading rates of 10^4 ions/s are required to allow for experiments at repetition rates of the order of 0.1-1 kHz, for example, exploring controlled molecular ions that are sympathetically cooled via directly laser cooled ions, as discussed in chapter 3. An experiment like the envisioned one will substantially depend on the sufficient efficiency of the barium ion source.

The presented technique can be further advanced by exploiting the tuneability of the 413 nm laser and its proximity to the ionization threshold. An increase in efficiency is expected by tuning the laser on resonance with a transition to either a field ionized Rydberg state [114] or with an autoionization resonance [129, 130]. The presented technique can be simplified because the dye laser used to generate the 553 nm light can be substituted by a low maintenance, all-solid-state laser system. Very recently, a commercial frequency-doubled diode laser system with the required wavelength and power became available. Since the second ionization step does not require a laser of narrow linewidth, substituting the 413 nm laser by an incoherent light source is possible [121, 122] and the presented highly efficient photoionization scheme could thus be implemented with modest effort and a robust setup.

4.2 Trapping and laser cooling of $^{138}\text{Ba}^+$ -ions

Trapping and Doppler laser cooling of barium ions was achieved in the framework of this thesis. The changes made to the trap apparatus used to trap and Doppler-cool magnesium ions to make it suitable for trapping the new ion specie is described in detail in section 2.1.2. An elaboration of the used laser system can be found in section 2.2.2. After loading of $^{138}\text{Ba}^+$ -ions by exploiting one of the photoionization schemes described in the last section the cooling lasers for barium are prepared for initial trapping. The frequency of the 650 nm repumper-laser is tuned close to resonance with the help of the absorption signal generated by the barium discharge cell. The 493 nm cooling-laser is slightly frequency scanned over the resonance (see also Fig.2.12 on page 44) in order to observe a pronounced blinking of the ions on the CCD-camera for the initial daily loading attempts. After successful loading, the scan is turned off and both lasers can be fine adjusted by changing the offset voltage of the grating piezo to maximal fluorescence of the ions in the trap.

As discussed theoretically in section 1.1.3 crystalline ion structures with cylindrical symmetry form in ion traps. Figure 4.6 shows a selection of fluorescence images of $^{138}\text{Ba}^+$ Coulomb-

Table 4.1: The experimental DC-parameters applied to the electrodes of trap 2 for trapping of barium ions. The definitions of the ring electrodes R_{1-3} are given in section 3.1.2. The atomic oven housing and the location of the compensation wire for trap 2 are described in detail in 2.1.1.

electrode	value [V]
R_1	+210
R_2	+170
R_3	+408
atomic oven housing	0
compensation wire trap 2	+65

crystals observed with the CCD-camera. All of the presented crystals have been loaded exploiting the photoionization scheme B with the frequency of the laser that resonantly drives the transition from the ground to the intermediate state tuned to optimal loading of $^{138}\text{Ba}^+$. Therefore, the loaded Coulomb crystals have a high probability to be isotopically pure and an observation of a dark ion directly after loading (most probable other barium isotopes) is very seldom. A variety of $^{138}\text{Ba}^+$ Coulomb-crystals with different linear density λ of ions in trap have been produced. The crystals presented in 4.6 a)-c) are trapped using identical trap parameters, summarized in table 4.1 but different number of ions in the trap. Figure 4.6a) shows an example of a linear chain consisting of 20 barium ions and in b) the linear density in the middle of the crystal is sufficiently high for the phase transition into a zig-zag structure to occur. In Fig. 4.6 c) only a fraction of a larger Coulomb-crystal is shown and the transitions from a linear, via a zig zag towards higher (helical) structures are observed (left to right). The secular frequency of $^{138}\text{Ba}^+$ and thus the RF-voltage (U_{RF}) applied to the quadrupole electrodes is measured by resonantly driving the ions radial secular motion. A voltage applied to the micro-motion compensation wire next to trap 2 (refer to 2.1.1), with a frequency that is resonant with the secular motion leads to an radial excitation of the components of the ion crystal [103]. In a linear chain this can be recognized by a radial smeared fluorescence image of the ions. Having a zig-zag structure, the radial excitation leads to an additional flipping of the crystal between two zig-zag configurations. A value of $\omega_{\text{sec},\text{Ba}^+} = 2\pi \cdot 470 \text{ kHz}$ is deduced for $^{138}\text{Ba}^+$. As shown in section 1.1.1, the stability parameter q can be calculated in the adiabatic approximation and in the absence of a direct current voltage on the RF-electrodes ($U_{\text{DC}} = 0$) via $q = \sqrt{8}\omega_{\text{sec}}/\Omega = 0.195$. Here the trap frequency $\Omega = 2\pi \cdot 6.8 \text{ MHz}$ is used. With the help of the relation

$$U_{\text{RF}} = \frac{qm\Omega^2 r_0^2}{2|e|Z}$$

where r_0 is the minimal distance from the center of the trap to the surface of the quadrupole electrodes and Z/m defines the charge-to-mass ratio of the trapped particle, it is possible to derive the amplitude of the RF-voltage on the quadrupole electrodes to $U_{\text{RF}} = 320 \text{ V}$.

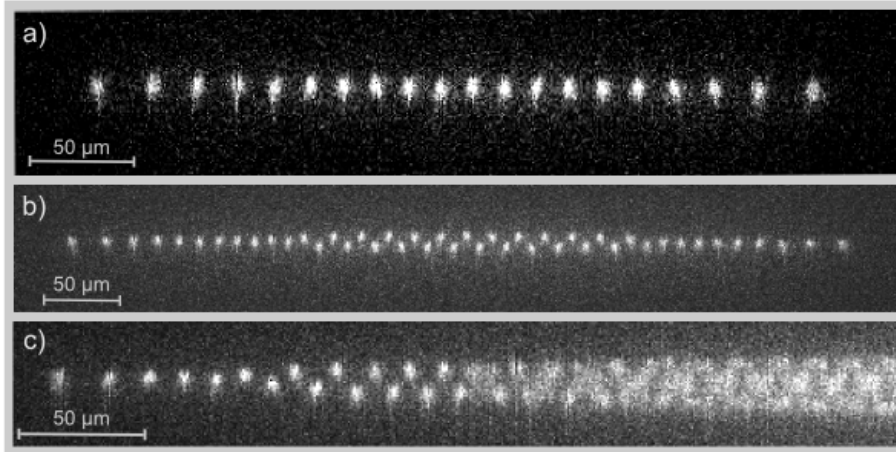


Figure 4.6: Two-dimensional fluorescence images of three isotopically pure $^{138}\text{Ba}^+$ Coulomb-crystals are shown. In all cases, identical trapping parameters have been used, but different total number of ions are confined in the trap. In a) the linear density λ of ions in the trap leads to a minimal energy configuration of the crystal that looks like a linear chain. The Coulomb crystal shown in the fluorescence image b) is an example of a zig-zag configuration. Due to the restricted size of the CCD-chip of the camera, only a part of a larger Coulomb-crystal is presented in c), whose linear density towards its center rises sufficiently high to allow a higher (helical and tetrahedral) structure to form.

4.3 Sympathetic cooling of molecular ions with $^{138}\text{Ba}^+$

In principle, the apparatus allows to produce molecular ions via electron bombardment ionization of gaseous neutral molecules injected into the guide by the cryogenic gas inlet stage. An implementation of these molecular ions into an existing Coulomb-crystal of laser cooled barium ions as well as the photoionization of neutral barium atoms in the trap afterwards is possible [85, 81]. With the help of the ESI-source described in section 2.3 a large charge-to-mass variety of sympathetically cooled molecular ions is accessible. In addition, the molecules are protonated, fragmentation of chemical compounds is usually not observed and generic molecules out of solution can be used. The implementation of laser-cooled $^{138}\text{Ba}^+$ -ions gives access to molecular ions, ranging from diatomic to biologically relevant organic molecules such as lysozyme (≈ 14300 amu) close to its natural charge state $Z = +8$ or cytochrome c (≈ 12390 amu) at a charge state $+12$ [31]. In this section the first steps towards heavier molecular ions is described with the help of the production and identification of the diatomic molecule BaO^+ . Like in the case of magnesium, the molecular ion is currently produced via a collision with a background gas particle. Figure 4.7 a) shows the final state of a isotopically pure $^{138}\text{Ba}^+$ Coulomb-crystal containing 16 ions that was trapped over an extended period of time (approximately 10 min). Two lattice sites marked by white circles and indicated with arrows are now occupied by particles that are no longer resonant with the cooling light, illuminating the crystal. The initial purity guarantees that the dark ions are not other isotopes of barium that are accidentally loaded and that the creation of the dark spots is due to a chemical reaction. Such background reactions have been studied intensively in reference [100]. Having in mind, the

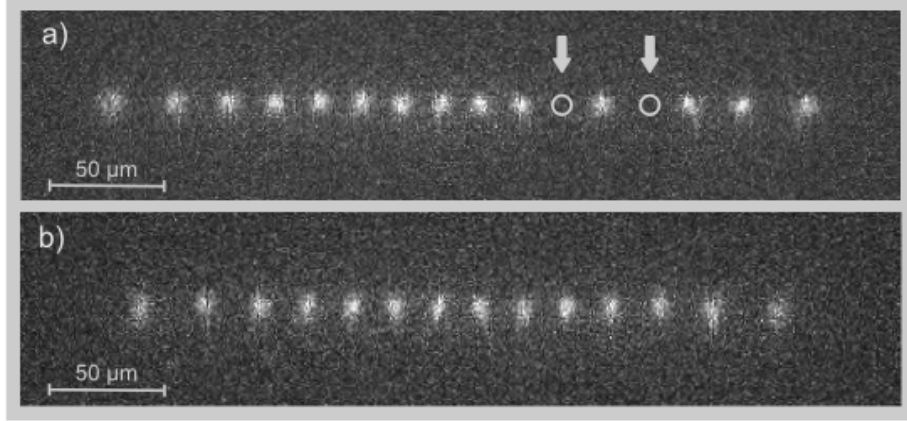


Figure 4.7: Two-dimensional fluorescence images of Coulomb-crystals in a linear chain configuration. The image in a) was taken several minutes after a pure $^{138}\text{Ba}^+$ crystal containing 16 ions was loaded into the trap via isotope selective photoionization. The formation of the two dark ions marked by circles and indicated by arrows is due to a chemical reaction with the background gas. After applying a heating frequency that is resonant with the radial motion of particles with mass 154 the dark ions have left the trap and the pure 14 ion $^{138}\text{Ba}^+$ crystal shown in fluorescence image b) is left. This destructively identifies the non-fluorescing ions as BaO^+ , created via reaction 4.6.

strong reactions of barium metal exposed to air (see also section 2.1.2) a chemical reaction with dioxygen seems reasonable, although the partial pressure of O_2 in the backed vacuum chamber is very low and additionally, the pumping speed for molecular oxygen of the used Ti-sublimation pump is quite high compared to H_2 for example. Nevertheless, it has been shown in [131, 100] that even when the $^{138}\text{Ba}^+$ -ion is optically excited, the reaction is endotherm and does not occur under the experimental conditions. For the same reason, a reaction with an H_2 background gas like in the case of magnesium is excluded. Most of the chemical reactions of barium ions observed in Paul traps are exothermic reactions with background CO_2 gas [132, 133]:



A direct identification of BaO^+ is possible because its secular frequency lies approximately 10% lower than the secular frequency of $^{138}\text{Ba}^+$ and a radial excitation of the interloper components of the ion crystal can be done without affecting the rest of the crystal. A voltage with a frequency that is resonant with the secular motion of an BaO^+ -ion is again applied to the micro-motion compensation electrode. The resonance frequency $\omega_{\text{sec},\text{BaO}^+}$ can be calculated from the measured resonance frequency $\omega_{\text{sec},\text{Ba}^+}$ of $^{138}\text{Ba}^+$:

$$\omega_{\text{sec},\text{BaO}^+} = m(\text{Ba}^+)/m(\text{BaO}^+) \cdot \omega_{\text{sec},\text{Ba}^+}$$

Figure 4.7 b) shows the Coulomb-crystal in fluorescence image a) after applying a resonant heating frequency of $\omega_{\text{sec},\text{BaO}^+} = 420 \text{ kHz}$ for a few seconds. The cooling lasers are

simultaneously blocked to make the heating process more efficient, due to the absence of sympathetic cooling. The result is a pure $^{138}\text{Ba}^+$ Coulomb-crystal that contains 14 ions. The two dark ions have been destructively identified as the expected BaO^+ .

Chapter 5

Discrete Kink Solitons in Ion-traps

In this chapter, the first-time observation of local, metastable deformations of the zig-zag structure of ions confined in a linear Paul-trap is demonstrated. The first section gives an introduction to discrete topological defects, commonly referred to as kinks, and a short motivation to study such configurations in linear ion-traps. The second section presents the experimental observation of so-called extended and localized kinks and the comparison to a numerical simulation of those defects. The first attempts towards a measurement of the dispersion relation of solitonic internal modes are presented in the last section.

5.1 Introduction and motivation

As cited in section 1.1.3, the first observation of a crystalline structure of laser cooled ions in a Paul-trap has been reported in 1987 by the groups of Walther and Wineland [36, 37]. Since then, the structure of cold ions in a Paul-trap has been studied intensively, both experimentally [60, 134, 135, 29, 100] and theoretically [40, 39, 38, 136]. Very recently, it was proposed to observe topologically protected localized distortions, so-called "kinks" of the "normal" two-dimensional zig-zag structure in an ion-trap (see also section 1.1.3) already with a moderate number of ions ($N \sim 20$) [42, 43]. The proposal claims that these kinks were metastable (stable over many oscillation cycles of the trap frequency) and should withstand collective motion and vibration of the entire crystal and thermal fluctuations of up to 15 times the Doppler-limit temperature of the ions (15×1 mK in the case of $^{24}\text{Mg}^+$). According to the proposal, it should be feasible to observe kinks in conventional linear and ring-shaped ion-traps using established laser-cooling techniques. However, the experimental observation of these topological defects has not been reported so far. In section 5.2, the first-time experimental observation of kinks in an ion-crystal, confined in a linear Paul-trap, is presented.

The experimental and theoretical investigations of ion structures in a harmonic confining potential revealed that depending on the number of ions in the trap, a quench of the transverse or axial trapping frequency leads to a transition from a linear chain of ions to a zig-zag configuration [38, 136]. When lowering the radial confinement (or increasing

the axial confinement) the potential crosses a critical value and the structure of a linear ion chain changes to a two-dimensional zig-zag structure. This structural transition is a continuous phase transition [38, 137, 138]. The assigned order parameter is the displacement of the ions in the crystal from the trap axis, departing from or tending to zero in a continuous way [51]. It has been predicted theoretically that a topological defect can form during such a linear to zig-zag structural phase transition [42, 43, 51]. In a simplified picture, during the transition, domains of zig-zag structures with opposite orientations or "phase"¹ form at different locations and can meet in the crystal, revealing a long-lived soliton like topological defect. Figure 5.1 shows a schematic illustration of how such topological defects in planar two-dimensional crystals look like (5.1b-c)) in comparison to the "normal" zig-zag configuration 5.1a).

Solitons can be defined as localized, non-perturbative solutions of non-linear systems that are topologically protected [139] and in this sense, the defects in an ion-crystal confined in a Paul-trap, indeed posses solitonic properties² [42]. In contrast to extended periodic solutions of the system (phonons), a topological soliton also referred to as a "kink", is a non-dispersive solution with a localized, exponentially decreasing spatial energy profile [140]. The soliton essentially depends on the non-linearity of the system (non-perturbative) and cannot be destroyed by any continuous transformation (topologically protected). In the simple picture of a spin chain, a spin pointing in the other direction than the rest of the chain ($\cdots \uparrow \uparrow \uparrow \downarrow \uparrow \uparrow \cdots$) would be a local defect but since the spin can easily flip without disturbing the others, this defect is not topologically protected. An example of a topologically protected defect in an infinitely long spin chain system would be ($\cdots \uparrow \uparrow \downarrow \downarrow \cdots$). Flipping a spin at the conjunction of two domains, pointing collectively up and down, does energetically not change the system. Solitons are often found in classical systems and have been studied intensively in the literature [140, 141, 139, 142]. Topological solitons are solutions, for example of the Frenkel-Kontorova (FK) model [143] that describes the dynamics of a chain of particles interacting with their nearest neighbors in an external periodic non-linear substrate potential. Under certain conditions, a kink soliton is the absolute minimum ground state configuration. The classical kink configurations observed in an ion-trap without any additional external potential are very similar to the minimum energy configuration of non-massive kinks in the two dimensional extension of the FK-model (zigzag model), where the point particles are allowed to move in two degrees of freedom [144, 145].

Investigations on topological defects are not restricted to the aspects of classical physics discussed above. Solitons have localized internal vibrational modes shared by the core particles. These internal modes can be canonically quantized around a specific, stable minimum of the potential energy. For a detailed treatment refer to [146]. The results are quantum internal oscillation modes around the classical kink particle configuration. Quantum mechanical properties and quantum dynamics of solitons have been studied experimentally in various systems, like for example in Josephson junctions [147], waveguides [148], in optical systems [149, 141] and Bose-Einstein-condensates [150]. The quantized internal modes of solitons in an ion-trap, give the possibility to study quantum mechanical effects with solitons in a system with unprecedented control. An example would be

¹one orientation is referred to as a zig-zag, the other as a zag-zig structure

²topologically protected strictly holds in a ring-shaped trap only

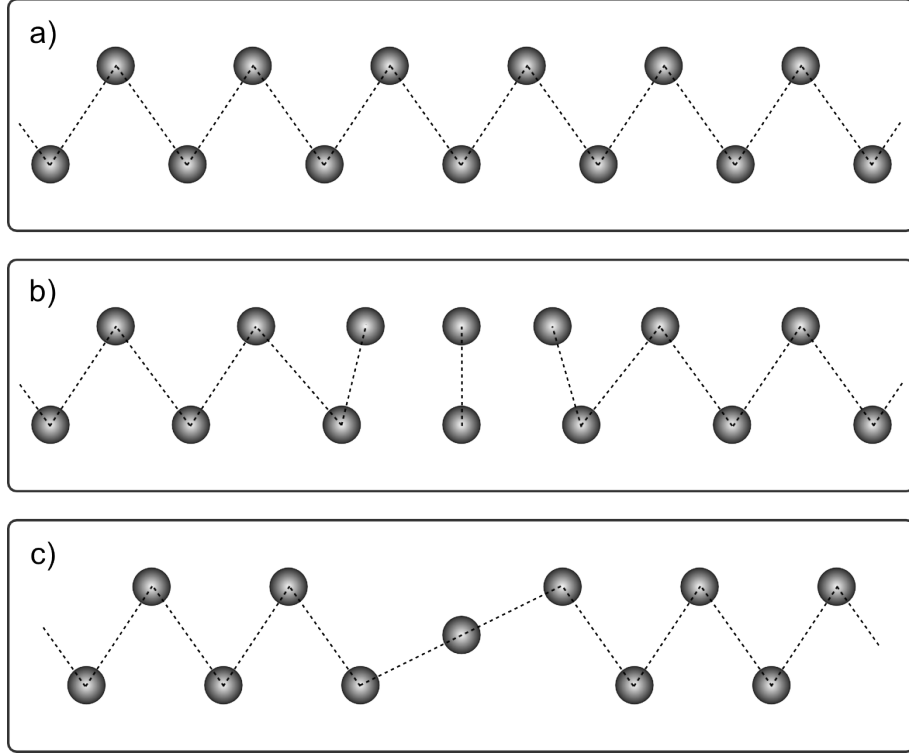


Figure 5.1: Schematic illustration of the zig-zag structure and different types of topological defects in a planar, two-dimensional crystal, confined in a ring-trap or in the center part of a crystal confined in a linear Paul-trap (neglecting edge effects). In a) the "normal" two dimensional zig-zag structure of the ions is shown. For a particular choice of trapping parameters and for a certain number of ions in the trap, this configuration (or the zag-zig configuration with opposite phase) is the minimum energy configuration of the combined potential of Coulomb-repulsion and the confining, harmonic background trapping potential. The ion configurations b) and c) show so-called extended and localized kink configuration, respectively. Both are metastable deformations of the zig-zag structure and exhibit solitonic properties. Theoretical calculations suggest that these kinks are long-lived (many oscillation cycles of the trapping frequency) already with a moderate number of ions ($N \sim 20$) and established Doppler laser-cooling [42]. In the case of the extended kink, the longitudinal ion distance decreases towards the kink core while the transverse ion distance stays more or less constant. The two ions at the core are nearly "above" each other. The localized kink, in contrast, involves mainly one center ion and its direct neighbors. Outside this kink core, the zig-zag structure is nearly undisturbed.

the observation of the coherent quantum time evolution of the internal modes [146] and a first direct measurement of the coherence time of solitons. Moreover, solitonic internal modes are predicted [42] to be suitable as a carrier for quantum information in ion-traps [151, 152, 153, 154]. Using internal modes of trapped ion solitons for an implementation of quantum information processing has the advantage that the high frequency of those modes is theoretically predicted to be separated by a gap from the rest of the phonon band and that this property is scale independent. When scaling the number of particles in the trap, existing quantum information schemes are very sensitive to the spectral resolution of the mode that couples the electronic states of the individual ions. The predicted applications of topological defects in ion-traps, like their contributions to quantum information processing or the experimental implementation of the inhomogeneous Kibble-Zurek mechanism that might allow new insights into the physics of topological defect nucleation in the laboratory and even in cosmological systems, will be further discussed in the outlook.

5.2 Experimental observation of static extended and discrete kinks

In this section the first-time observation of discrete static kink solitons in an ion-trap is presented. The experimental observation of kink solitons in a linear trap was achieved only a few months after the defects were theoretically predicted [42]. The experimental observation in this thesis will be presented along with theoretical studies of the observed structures. The numerical simulation of the ion positions in the kink structures and the corresponding dispersion relations (linearized frequency spectrum of the normal-modes) are the work of H. Landa and B. Reznik³, who also contributed to the comparison of theoretical prediction and experimental realization of kink solitons in the ion-trap of this thesis.

The experiments were conducted in trap 2 (refer to section 2.1.1) which contained the single molecular ion target for the time-resolved vibrational spectroscopy measurements presented in chapter 3. In contrast to the mentioned experiment, no molecular ions have to be produced and thus, a transfer of an ion ensemble from trap 1 to trap 2 is not necessary. The realization of topological defects in an ion crystal is performed using exclusively $^{24}\text{Mg}^+$ -ions. The tantalum tube of the atomic oven assembly in chamber 3 that contains the magnesium wire (see figure 2.2 and section 2.1.1) is resistively heated and used as an atomic beam source. $^{24}\text{Mg}^+$ -ions are directly loaded into trap 2 by isotope-selective photoionization. The laser sources used for the experiments of this chapter were already described in section 2.2.1 of chapter 2. The trap parameters for a given number of ions are adjusted to favor a kink structure as minimal energy configuration of ions in the trap. At an axial frequency of $\omega_z \approx 2\pi \cdot 50$ kHz and a ratio $\kappa = \omega_{\text{sec}}/\omega_z$ of radial secular frequency ω_{sec} to axial frequency ω_z of approximately 5 turned out to be a good starting point for the observation of extended, as well as localized kinks. Figure 5.2 depicts two fluorescence images of 34 $^{24}\text{Mg}^+$ -ions confined in trap 2. The trap parameters used in the two images are identical. In 5.2a), the ion crystal is in the "normal" zig-zag configuration. In con-

³School of Physics and Astronomy, Tel-Aviv University, Israel

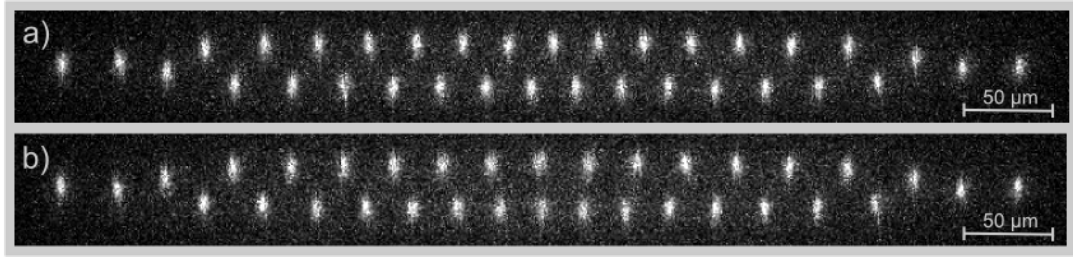


Figure 5.2: Fluorescence images of pure $^{24}\text{Mg}^+$ -ion crystals confined in trap two (refer to section 2.1). The ion crystal in fluorescence image a) is in the "normal" zig-zag configuration like in the illustration of figure 5.1a). The ion crystal in b) shows an extended topological defect similar to the one illustrated in figure 5.1b). The two crystals contain exactly 34 $^{24}\text{Mg}^+$ -ions and the two images were obtained with identical trap parameters. The extended kink in b) is easiest recognized by observing that the 17th and 18th ion counted from the left hand side appear approximately above each other.

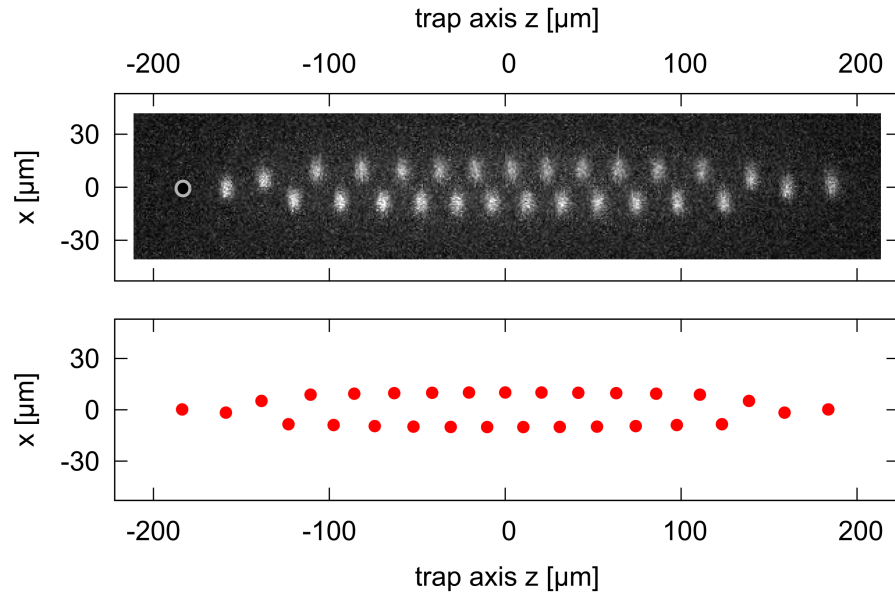
trast, the fluorescence image b) reveals an extended kink (similar to the one illustrated in figure 5.1b)). In the center of the crystal two ions appear approximately above each other. Although the theoretical treatment suggests a fast quench of the axial or radial confining potential causing a linear to two-dimensional structural transition to produce metastable kink defects, this was not necessary in the current experimental situation. The kinks shown in this section are exclusively produced by spontaneous formation, most likely by a sudden melting and re-crystallization of the ion ensemble. However, the crystallization process seems to imply similar boundary conditions as the quench. Although not expected by theory, this method turned out to be the most convenient one with the current experimental setup. The melting of the crystal might be due to heating effects in the trap, most probable collisions with background gas molecules. The typical timescales between structural changes, no matter if in kink or zig-zag configuration, are on average of order of a few seconds at the current experimental conditions. The structural lifetime of the kink is thus currently limited to this timescale. The heating rates in the current trap setup have to be lowered, in order to measure the maximal structural lifetime of a kink configuration in comparison to a zig-zag configuration. For a deeper discussion of this aspect and first experimental attempts to increase the structural lifetime in the trap, refer to section 5.3.

The ion-crystal shown in figure 5.3, allows to test the compatibility of the numerical simulations and the experiment. For a detailed description of the concepts used in the calculations refer to [146]. The fluorescence images are recorded with the CCD-camera, using an exposure time of 100 ms. The presented ensemble contains 28 $^{24}\text{Mg}^+$ ions and one non-fluorescing, dark ion, most probable a $^{24}\text{MgH}^+$ molecular ion or a different magnesium isotope. The position of this ion within the crystalline structure is indicated in the figure by a gray circle. The change in position of the dark ion reveals that the ion-crystal has actually changed its configuration in the time interval during the shot of the fluorescence images presented in figure 5.3a) and figure 5.3b). Without a dark ion embedded in the crystalline structure, this fact would be hard to observe with the experimental means used in this thesis. However, certain structural changes, for example, from zig-zag to zag-zig can be observed even with a pure crystal. In figure 5.3a) the crystal is in the original zig-

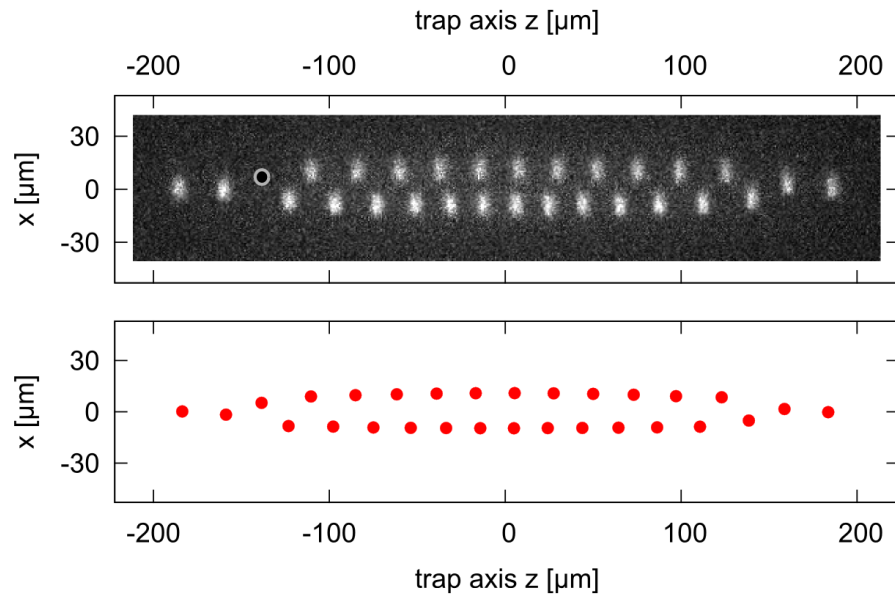
zag configuration. In the lower plot of figure 5.3a), the theoretically calculated equilibrium positions of the ions are indicated by the red circles. With the help of the x-and z-axis labeling of the fluorescence image, a good agreement with the theory is confirmed. In the theoretical treatment, an axial frequency of $\omega_z = 2\pi \cdot 52$ kHz, a frequency ratio to the radial secular frequency of $\kappa = 5$ and a pure $^{24}\text{Mg}^+$ -crystal containing 29 ions that are uniformly and continuously laser cooled is assumed. The fact that in the experiment one ion has a slightly lower charge-to-mass ratio and is not directly but only sympathetically laser cooled, has no substantial impact on the numerical simulation. A simulation that takes the dark ion into account shows negligible changes in the equilibrium positions of the other ions, independent of its location within the crystal. The theoretically expected, discrete frequency spectrum of the linearized normal modes is presented in figure 5.4 by the black points. It reveals that in the zig-zag configuration, the lowest mode has a frequency in units of ω_z of exactly one and corresponds to the center-of-mass (COM) motion of the whole crystal. No pronounced energy gap is found on top of this spectrum.

In contrast to figure 5.3a), figure 5.3b) shows the ion-crystal in an extended kink configuration. Two ions near $z=0$ μm appear almost above each other and the lower "row" of the radial extension contains one ion more than the upper "row". Again, the theoretical prediction of the minimal energy configuration of the ion-positions within the crystal is shown by the red circles in the lower plot and a comparison with the fluorescence image reveals good agreement. The calculated vibrational frequency spectrum corresponding to the extended kink configuration is shown in figure 5.4 in red. The frequency, in units of the axial frequency ω_z , of the energetically lowest mode lies below 1 and is no longer corresponding to the COM-motion of the crystal. An axial sliding motion of the upper "row" of the structure against the lower "row" can be assigned to this mode. The second lowest frequency mode of the extended kink configuration corresponds again to the COM-motion. At the high frequency end of the spectrum of the linearized normal modes, a more pronounced splitting of modes that lie on top of the rest is observed compared to the zig-zag configuration. This high-frequency gap, already discussed in the introductory part in section 5.1, is even more pronounced in the case of a localized kink.

As mentioned before, the isolated vibrational modes of the linearized normal mode spectrum which are sufficiently separated from the frequency of other modes and the localization to a few ions make kink solitons in ion-traps particularly well suited for quantum information processing and other applications [42]. While the first requirement might be partially fulfilled in the case of an extended kink, the latter is not. An extended kink configuration of ions in a linear trap has to involve numerous ions as theoretically shown in [42] (see also figures 5.2 and 5.3). In its localized configuration, in contrast, the kink consists mainly of three core ions. Such localized kinks can also be observed in the same parameter regime as used for the extended kinks. In figure 5.5 such an experimentally observed localized kink is compared to theoretical calculations. The fluorescence image a) in figure 5.5 shows an ion crystal confined in trap 2, consisting of 45 $^{24}\text{Mg}^+$ -ions and one non-fluorescing "dark" ion. The dark ion is embedded into the crystalline structure of the fluorescing ions for the same reason already described above. The position of this ion is again marked by a gray circle, superimposed over the fluorescence image. At $z \approx +100$ μm , figure 5.5 shows a localized kink (as illustrated in figure 5.1c)). The kink core is highlighted by a gray arrow. The image clearly shows that the kink structure is localized



(a) Observed zig-zag configuration compared to theory.



(b) Observed extended kink configuration compared to theory.

Figure 5.3: Comparison between experimentally observed ion structures and the predictions based on numerical simulations for the used trap parameters and number of ions in the trap. In (a), the ion crystal containing 29 ions is in the "normal" zig-zag configuration. In (b), an extended kink is observed. The two ions near $z=0 \mu\text{m}$ appear nearly above each other. The lower "row" of the structure that extends into the radial direction contains one ion more than the upper "row". In both cases, one of the 29 ions is a dark one, indicated by a gray circle, not affecting the structure or the type of kink.

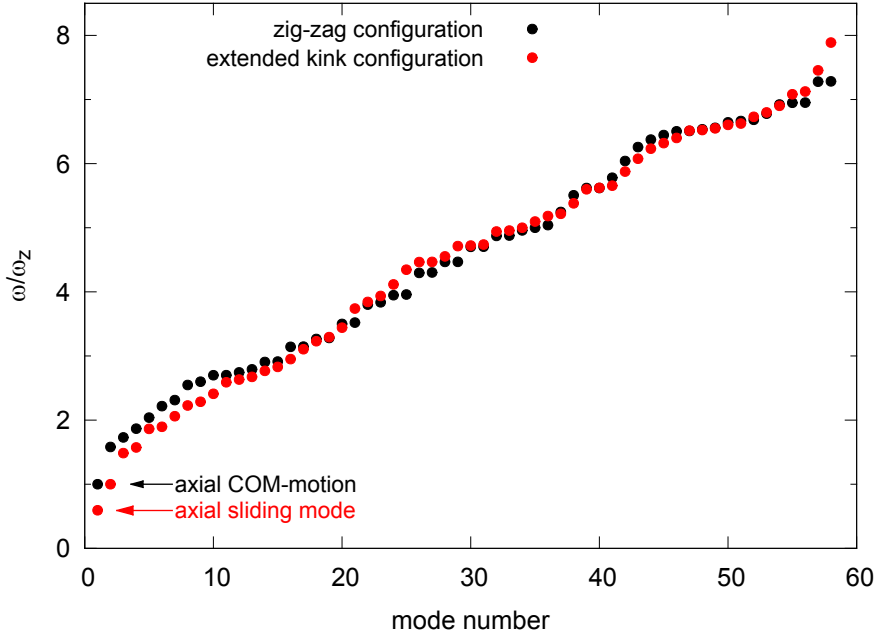


Figure 5.4: Theoretical frequency spectrum of linearized normal modes. The ordinate of the plot gives the frequency of the mode in units of the axial frequency ω_z . The black points correspond to a theoretical treatment of the normal zig-zag configuration of the ion crystal presented in figure 5.3a). The lowest mode has a frequency in units of ω_z of exactly 1 and can be assigned to the COM-motion of the crystal. No pronounced energy gap is found on top of this spectrum. The red points correspond to the extended kink configuration of the ion crystal presented in figure 5.3b). The second mode of this configuration again corresponds to the COM-motion, but the lowest mode in frequency is assigned to the sliding motion of the kink (refer to the main text). In terms of axial frequency, the frequency of this mode is smaller than 1. The energy gap found on top of the spectrum is more pronounced compared to the zig-zag configuration.

to the three core ions. A first attempt to simulate the observed localized kink for the parameters used in the experiment ($\kappa \approx 8, \omega_z = 2\pi \cdot 35 \text{ kHz}, N = 46$) failed. For $\kappa = 8$ an initially localized kink even with very strong cooling dissolves in an extended kink in the simulation. However, the simulation of the "normal" zig-zag structure, corresponding to 46 $^{24}\text{Mg}^+$ -ions assuming an axial trapping frequency of $\omega_z = 2\pi \cdot 35 \text{ kHz}$ and $\kappa \approx 8$ resembled the experimentally observed crystal concerning both, shape and absolute length. It turned out that localized kinks, according to the numerical simulation, should only show up for a value of κ bigger than 11.4. The successful simulation of a localized kink for $\kappa = 11.4$ is presented in figure 5.5b). This fact might be attributed to the anisotropy of the trap in the experiment that is not considered by the theory. Such an anisotropy could be caused for example by local patch potentials. A first attempt to theoretically describe the experimental anisotropy of the trap is made by implementing a slightly higher transverse trapping confinement localized to a small region in the trap. Figure 5.5c) shows the theoretical result for $\kappa = 8, \omega_z = 2\pi \cdot 35 \text{ kHz}$ and a 10% stronger confinement in a region

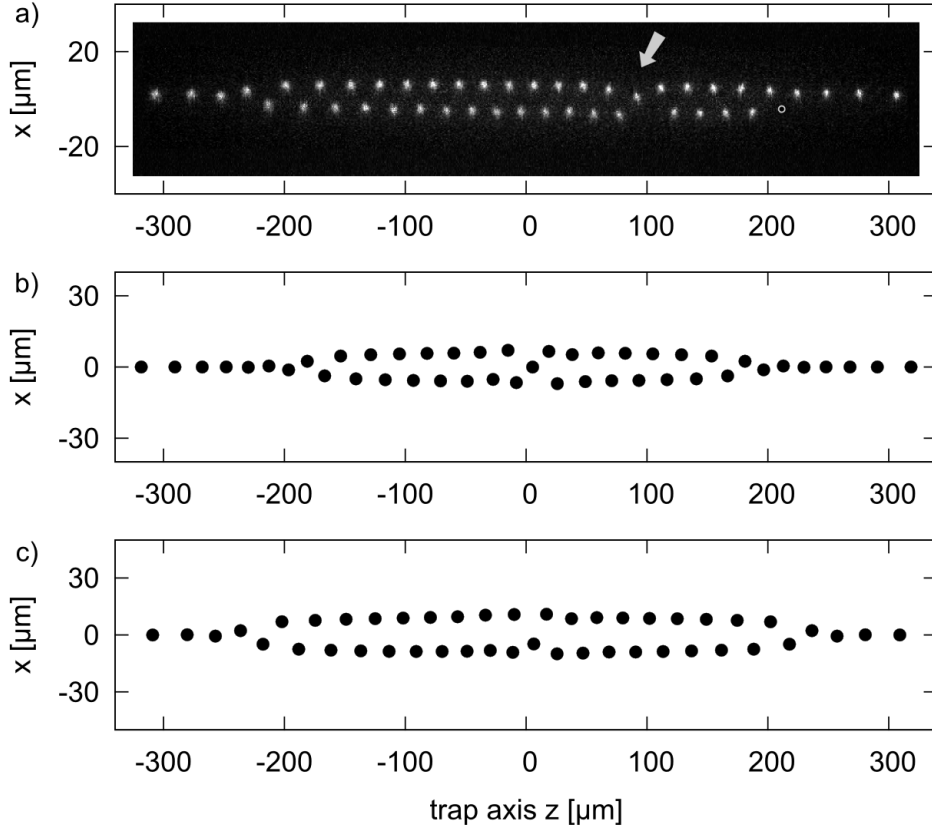


Figure 5.5: An experimentally observed localized kink and the first attempt of a comparison to theory. The fluorescence image a) shows an observed localized kink in a magnesium crystal consisting of 46 ions at $z=100 \mu\text{m}$ further indicated by a gray arrow. The first attempts to simulate the experimental results are presented in b) and c). In b), a localized kink is numerically simulated for an axial trapping frequency that corresponds to the one used in the experiment, but a different ratio to the radial secular frequency of $\kappa = 11.4$. The theoretical treatment revealed that at $\kappa = 8$ which would correspond to the situation in a) a localized kink should not be stable. The figure in c) shows the theoretical result for these parameters and an additional slightly higher transverse trapping confinement (approximately 10%) localized to a small region in the trap center. This is assumed to account for the experimental anisotropy of the trap. Indeed, a localized kink is stable with these assumptions. The not ideal match to a) calls for a further theoretical investigation.

in the center whose width is smaller than the inter-ion distance in the trap. With this modified parameters, localized kinks for $\kappa \approx 8$ are shown to be stable in the simulations. The non-perfect match to the situation in the experiment indicates that the anisotropy is not the only experimental boundary condition that has to be considered and a further improved theoretical description has to be developed in the future.

Figure 5.6 shows the theoretical linearized normal mode spectrum of the calculated localized kink solitons presented in figure 5.5b) and c). The kink spectrum for $\kappa = 8.06$ and

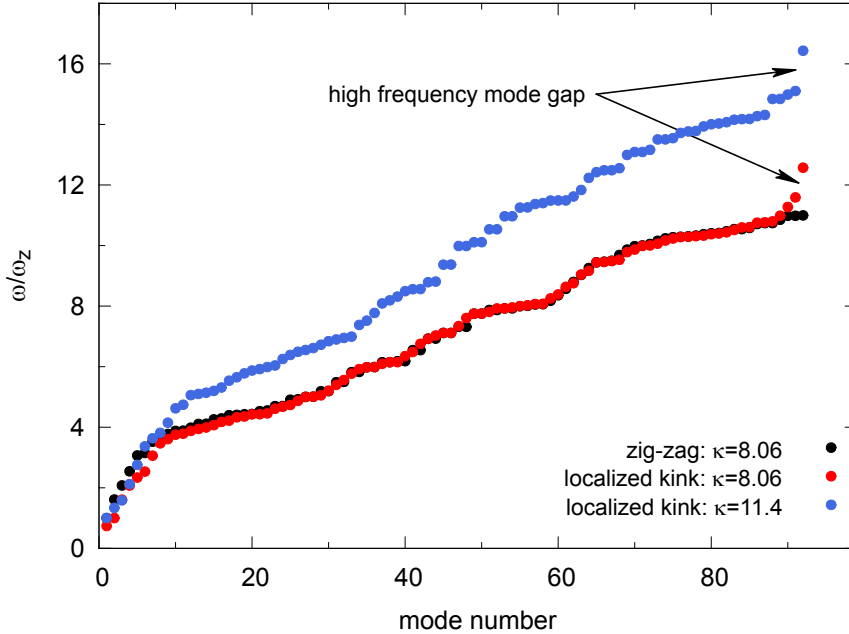


Figure 5.6: Frequency spectrum of linearized normal modes for the zig-zag and localized kink configuration. The black dots corresponds to a numerical simulation of the "normal" zig-zag configuration of a $^{24}\text{Mg}^+$ -crystal, consisting of 46 ions, confined in a trap with parameters $\omega_z = 2\pi \cdot 35$ kHz and $\kappa \approx 8$. This corresponds to the trapping parameters used to obtain the fluorescence image a) in figure 5.5. No energy gap is found at the top of the spectrum. The two other curves, indeed, reveal such a high frequency mode gap. The blue and red dots represent a simulation of a localized kink for $\kappa = 8.06$ (with anisotropy simulation, see also the main text) and $\kappa = 11.4$, respectively. The minimal energy position of the ions in the trap corresponding to these frequency spectra are given in part c) and b) of figure 5.5.

$\kappa = 11.4$ is presented with blue and red dots, respectively. For comparison, the spectrum for the "normal" zig-zag configuration for $\kappa = 8.06$ is also given. In contrast to the zig-zag, both kink configurations reveal a pronounced energy gap between the high frequency modes which could be used, in principle, for applications in quantum information processing. A possible experiment revealing either the low frequency extended kink or the high frequency localized kink modes is discussed in the next section.

5.3 Towards a measurement of the dispersion relation of kinks in ion-crystals

The first part of this section discusses the already mentioned experimental attempts to increase the average timescale between structural changes of a crystal in the trap. Experiments indicate that a kink soliton in the trap currently seems to be stable on a similar timescale as a zig-zag structure until it reforms, for example to a zag-zig configuration

and an increase in structural lifetime would allow both, maximize the available time to perform a measurement on a kink and the direct measurement of the metastability of the soliton. The second part gives a summary of the current ideas aiming for a measurement on an extended and on a localized kink confined in a linear Paul-trap.

Two different routes have been followed to extend the structural lifetime of the observed crystalline structure in the trap. As already stated in section 3.1.2, the cooling laser beam includes a small angle (a few degrees at most) with the trap axis only and thus, with the longitudinal axis of the crystal. Nevertheless, in the current experimental situation, the normal modes of the crystal couple the longitudinal and radial motion sufficiently to allow for a cooling of the ions in a crystalline state. A further optimized cooling is essential to balance the heating effects in the trap and to avoid too large transition rates of the crystalline state into a hot cloud of ions. Experimentally, it is observed that for the trapping parameters of section 3.1 a number of ions in the trap exceeding approximately 8 is necessary to allow for sufficient coupling such that the heating, leading to micro-motion, is not directly observable on fluorescence images taken by the CCD-camera. For a smaller amount of ions in the trap, a transverse smearing of the ions is observed, indicating micro-motion and a not sufficiently cooled motion in the radial direction. For a larger number of ions and particularly in the case when the string structure bifurcates into a two-dimensional zig-zag structure the coupling of the degrees of freedom is sufficient and a smearing is no longer observed. Nevertheless, an insufficient coupling in the case of a small amount of ions in the trap might indicate that the heating rates in the case of a two-dimensional structure can be better compensated when an additional direct cooling of the transverse degrees of freedom is implemented. For this purpose, a second cooling laser beam was set up, additionally illuminating the trap from the transverse direction. Figure 5.7 shows the result obtained with the additional transverse laser beam. The two fluorescence images on the left hand side show one $^{24}\text{Mg}^+$ -ion and a linear chain of three $^{24}\text{Mg}^+$ -ions, respectively, confined in trap 2. In both cases, the ions are cooled only by the laser beam propagating nearly along the trap axis. The discussed radial heating and the related smearing in the radial direction is clearly visible. It is hard to derive a temperature from the amplitude of the excitation of the ions, since it is partially driven by the RF-voltage. For that reason the smearing is only used as an optimization parameter and not for an attribution of a temperature. The two fluorescence images on the right hand side show the same ions, but with an additional cooling in the transverse direction. The single ion in the upper fluorescence image, as well as the linear chain in the lower image look significantly better localized in the radial imaging plane which can be attributed to a more efficient cooling of the radial degrees of freedom. This demonstrates a clear improvement in cooling the ions, at least for a single ion and small ion crystals. Nevertheless, it turned out that the larger two-dimensional ion crystals, whether in zig-zag or kink configuration, seemed to be unaffected by the additional cooling beam in terms of structural lifetime and no significant change of the rates of "diffusion" of ions through the crystal, flipping from zig-zag to zag-zig and complete melting of the whole crystal are observed.

This observation suggests that a better micro-motion compensation in conjunction with the newly developed technique for radial cooling might be key for the envisioned longer structural lifetimes. As discussed in section 2.1 the RF-voltage for radial confinement is applied to two opposite pairs of the quadrupole electrodes with a mutual phase difference

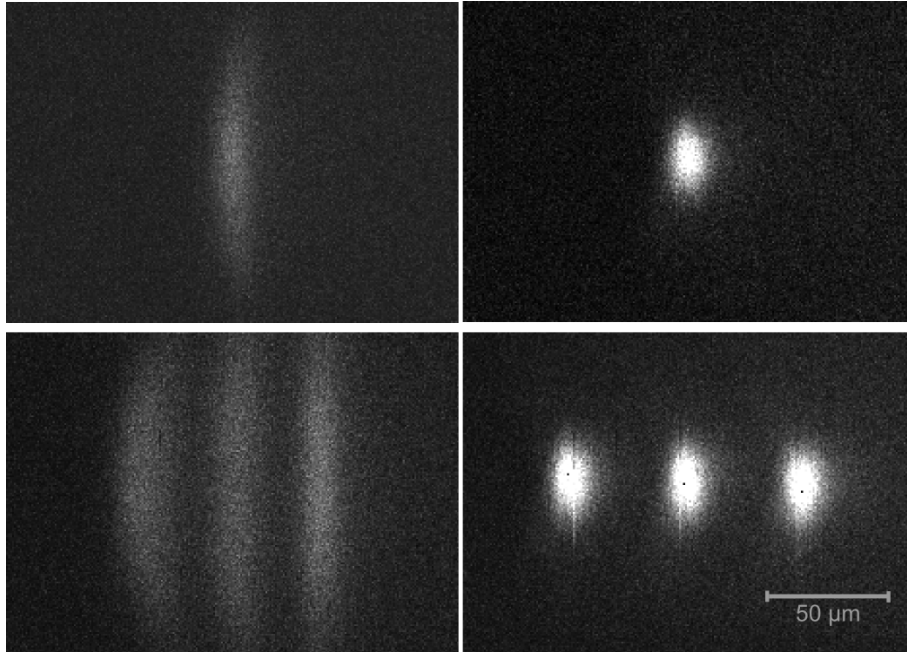


Figure 5.7: Experimental results achieved with a laser beam cooling the ions confined in trap 2 from the radial direction, in addition to the laser beam illuminating the trap along its axis. The upper two fluorescence images show the situation for a single ion in the trap. On the left, only the axial laser beam is used for cooling. A pronounced radial smearing, indicating a hot ion in this direction, is observed. The fluorescence image on the right, in contrast, shows the situation using both laser beams. No smearing is observed and all of the motional degrees of freedom of a single ion are sufficiently cooled. The lower fluorescence image pair shows the situation with the same parameters as described above, but in the case of a small linear ion chain consisting of three $^{24}\text{Mg}^+$ -ions.

of π . This arrangement is called the symmetric case. In such a case, it is convenient to compensate micro-motion with additional voltages on compensation electrodes which are not directly part of the trap. This is done, because an additional DC-voltage on the electrodes which can also compensate micro-motion is rather difficult to apply without severely reducing the Q-factor of the RF-enhancement resonator. The compensation has to be done in two independent directions with the help of voltages on two different compensation electrodes. Until now, the compensation of micro-motion in trap 2 was performed using a suitable voltage on an additional wire along the trap axis (refer to section 2.1) and a voltage applied to the housing of the atomic oven stack, providing the beam of neutral atoms for trap 2. The housing, however, is far away from the trap center (approximately 2 cm) and in conjunction with the strong shielding effect (refer to section 3.1.2) of the trap electrodes, a high voltage had to be used. In most of the cases, the highest applicable voltage (limited by the maximum voltage on the vacuum-feedthrough) was not sufficient to compensate micro-motion to a degree as it would be necessary for the experiments presented in this section. For this reason, a new enhancement resonator was designed that allows for a so-called asymmetric supply of the RF-voltage on the trap electrodes. In this

case, one opposing pair of the quadrupole electrodes is permanently RF-grounded with respect to the RF-voltage. On the other pair, the RF-voltage is applied. This gives the possibility to rather easily apply an additional DC-voltage on the grounded RF-electrodes and to use the control of its amplitude for compensation of micro-motion in one direction. The other direction is compensated with the voltage applied to the micro-motion compensation wire mounted along the trap axis. Although the degrees of freedom are coupled with this arrangement, a much better micro-motion compensation in any axial position of the ions along the trap axis is achieved. As a consequence, a single or few $^{24}\text{Mg}^+$ -ions can be confined in the trap without the formally observed smearing even in the case when laser cooling is only applied along the trap axis. Nevertheless, these positive effects on a small number of ions did again not affect the structural lifetime of a two-dimensional structure.

The conjunction of the two improvements on one or a few $^{24}\text{Mg}^+$ -ions in the trap is considered to have no or only a minor effect on the structural lifetime of a larger Coulomb-crystal. In order to test this assumption, measurements on the lifetime of larger (approximately 20-30 ions) ion-crystals that show a zig-zag configuration in a different trap setup have been performed. For a more detailed information about this setup, refer to [124] and [84]. The setup provides a cooling laser beam that couples the longitudinal and radial degrees of freedom and the micro-motion compensation of a single ion has been carefully adjusted [84, 155]. In addition, the influence of a far red-detuned (10-11 natural linewidths, $\approx 440\text{MHz}$) laser beam can be measured. Performed measurements in this setup reveal that also the conjunction of the two mentioned features does not lead to a pronounced longer structural lifetime. The far red-detuned laser beam does not have a pronounced effect concerning this particular problem. The measured structural lifetimes of approximately 10 seconds are only a factor of 2-3 better than the ones measured in the trap described in section 2.1. This improvement can be attributed to better vacuum conditions of also approximately a factor of 2. Supported by the literature [135], this strongly indicates that the structural lifetime of a zig-zag and kink structure in the trap described in this section is limited by the background pressure. The attempts to increase the structural lifetime will be continued in the future. Meanwhile, the many seconds timescale is considered to be sufficient for first experiments on kink solitons in ion-traps.

As already mentioned in section 5.1, the pronounced energy gap on top of the linearized normal mode spectrum of a localized kink in an ion-trap is a key ingredient for applications in quantum information processing schemes. With the first-time observation of a localized kink soliton in an ion-trap, a first experimental verification and measurement of this energy gap is possible. Since a zig-zag configuration and a localized kink configuration can be realized in the trap with identical parameters, the difference in the mode spectra of these structures can be measured. For this purpose it is proposed to use a time-varying voltage on some of the electrodes which, depending on the symmetry of the mode, could be the micro-motion compensation wire-electrode of trap 2 or the ring-electrodes, similar to the case described in section 3.1.1 where such a voltage is used to resonantly heat a particle with a specific charge-to-mass ratio in the trap. If the applied frequency coincides with a frequency of one of the modes of the crystal, this should be visible by a smearing of the ions on the CCD-camera images. One possible way to measure the energy gap could thus be to observe the correlated destruction of a localized kink with the application of

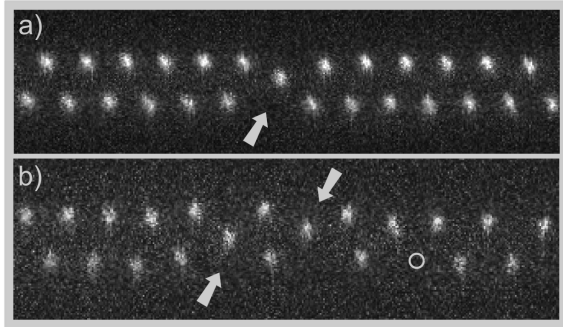


Figure 5.8: The fluorescence image a) shows a localized defect with opposite topological charge compared to the one presented in figure 5.5. The different defects can be referred to a kink and the corresponding antikink. One connects a zig-zag to a zag-zig and the other vice versa. A kink and an antikink in the same crystal is presented in b). The two defects are direct neighbors and are indicated by two gray arrows. The position of one non-fluorescing ion in b) is indicated by a gray circle. For the sake of clarity, only a part of a larger crystal containing ≈ 45 ions is shown.

a certain frequency to the micro-motion compensation wire. If this frequency is found to have no effect on a zig-zag structure, the difference in frequency to the highest lying mode in the spectrum of a zig-zag could be deduced experimentally. In a very similar way, the difference in frequency of the lowest lying center-of-mass mode of a zig-zag structure to the frequency that excites the sliding motion of an extended kink could be measured.

In addition to the measurements of the energy gap of kinks in comparison to "normal" zig-zag structures, other experiments were proposed (for a more comprehensive treatment refer to the outlook section 6.2). In the framework of this thesis, not only single localized kinks and antikinks (one connects a zig-zag to a zag-zig and the other vice versa) are observed, but also the existence of two solitonic structures in one ion crystal is demonstrated. The fluorescence image shown in figure 5.8a) reveals that the localized defect indicated by the gray arrow has an opposite topological charge as, for example the localized kink shown in figure 5.5. In figure 5.8b) a localized kink and a localized antikink as a direct neighbor (both are indicated by a gray arrow) in the same crystal is presented. It is proposed that the static kink can be translated [146] in the crystal, resulting in the transformation into a moving kink (by for example suitable tickle voltages or the variation of the light pressure force). Together with the already demonstrated creation of two kinks with equal or different topological charge in one ion crystal, it should be possible to observe and explore kink-kink and antikink-antikink collisions or kink and antikink annihilation in the future.

Chapter 6

Conclusion and outlook

6.1 Time-resolved measurement on a single molecular target

Motivated by the envisioned applications in structural determination on the atomic scale with ultra-short free-electron X-ray laser pulses [15], a proof-of-method experiment on the diatomic molecular ion $^{24}\text{MgH}^+$ has been performed. The trap apparatus in conjunction with a continuous wave (cw) dye-laser system based on home-build second harmonic generation stages allows to trap and laser-cool atomic $^{24}\text{Mg}^+$ -ions with a spatial resolution and control currently limited by the resolution of the objective to approximately $1\ \mu\text{m}$. The implemented photoionization scheme for magnesium atoms ensures a high efficiency in isotope selectivity when initially loading a $^{24}\text{Mg}^+$ Coulomb-crystal. The molecular ion $^{24}\text{MgH}^+$ is produced via a photochemical reaction [61] of the electronically excited magnesium ion with injected hydrogen gas. The produced molecular ions have been sympathetically cooled by the adjacent $^{24}\text{Mg}^+$ -ions. The design of the apparatus allows to deterministically transfer the resulting heterogeneous Coulomb crystal over a distance of 49 cm to a trapping region along the ion-guide that is isolated from the production region by differential pumping stages. It has been shown that this isolation is necessary to perform a high precision experiment with $^{24}\text{MgH}^+$. Transfer schemes suitable for different applications have been developed and experimentally implemented [76]. The ultra-high vacuum apparatus was linked to a source of ultra-short ultraviolet pulses, provided by collaborators within the Munich-Center for Advanced Photonics (MAP) cluster of excellence. An extension of the existing pulsed UV-beamline, based on the third gas-harmonic of few cycle laser pulses in the visible and near-infrared [97], suitable for the pump-probe experiment on $^{24}\text{MgH}^+$ has been realized. The third-harmonic generation yield, the effective repetition rate, the spectrum and the intensity of the pulses have been optimized for the experiment. The few femtoseconds long UV-pulse has been split into two nearly identical replica that serve as pump- and probe-beam for the experiment. The temporal overlap of the pulses, as well as the overlap of the pulses with the molecular ions in the trap has been controlled by appropriate experimental methods.

The result of the pump-probe experiment on individual molecular ions represents the first

experimental demonstration of the combination of the field of trapped ions and ultra-short laser pulses. A fast oscillation of the vibrational wavepacket, with a period of approximately 30 femtoseconds, was created in the first excited state of individual $^{24}\text{MgH}^+$ -ions and observed experimentally. The experimental results required an involved theoretical model developed in collaboration with the theoretical femto-chemistry group¹ within MAP. The experiment indicated effects, such as vibrational heating, caused by sequential excitation, long coherence times and the absence of the coherence spike dominant for targets in solution near zero pump-probe delay.

The first experimental steps towards an extension of the method to biologically relevant molecules have been already implemented in the framework of this thesis. For the production of nearly generic molecular ions, an Electrospray-Ionization (ESI) source was set-up, characterized and tested fully functional. With this device, working with soft protonation methods, it is possible to produce molecular ions covering a wide range of charge-to-mass ratios out of solution. Working with molecular ions of smaller Z/m required adapting values of the cooling agents. Because of their approximately six times bigger mass, using barium ions instead of magnesium ions allows to sympathetically cool much heavier molecular ions. A novel scheme for isotope-selective photoionization of barium atoms has been developed and implemented [81]. In the framework of this thesis the most striking feature of this scheme is its increased efficiency by two orders of magnitude for $^{138}\text{Ba}^+$ -ions compared to established schemes. In addition, this scheme might be relevant for experiments that are highly sensitive to disturbances, enhanced by less efficient loading techniques, such as in cavity quantum-electrodynamics [123, 156], one-dimensional RF-surface traps for quantum information processing [116] and two-dimensional trapping arrays for experimental quantum simulations [124] or applications for the recently realized optical trapping of ions [126]. A cw laser system for Doppler-cooling of barium ions has been designed and build. $^{138}\text{Ba}^+$ -ions, produced via photoionization, have been confined in the traps of the apparatus and Doppler-cooled to form a Coulomb-crystal. As a first test molecular ion, barium oxide has been successfully produced, identified and embedded into the crystalline structure of the barium cooling agents.

The following paragraph discusses further applications and developments concerning the extension of the method to molecular ions with smaller charge-to-mass ratios that are planned to be implemented in the future.

Applications and extension to biologically relevant molecular ions Fundamental steps towards an extension of the presented scheme aiming for structural analysis on the atomic scale of biologically relevant molecular ions in the long run, have been already implemented in this thesis. The Electrospray-Ionization source can substitute the current cryogenic gas inlet stage of the apparatus. The ionization of biologically relevant molecules out of solution and the embedding of the produced, eventually multiply charged ions, into the crystalline structure of directly laser-cooled and confined barium ions afterwards will be the next step. The ESI-source in combination with the demonstrated effective photoionization scheme for barium atoms is capable of providing targets embedded into

¹group of Prof. Dr. R. de Vivie-Riedle

their sympathetic cooling environment at the repetition rate of the laser source. Radio-frequency traps have recently been shown to be capable to store sympathetically cooled molecular ions exceeding 10^4 atomic mass units with a charge-to-mass ratio of $1/1000$ [32]. However, this approach already reveals the drawback of large ensembles of sympathetically cooled bio-functional molecules for providing precisely positioned individual targets. The coupling to the heat sink is substantially reduced due to the weak confinement and large space charge, increasing the mutual distance to $\sim 70 \mu\text{m}$. The apparatus presented in this work allows a sufficiently close focusing of the different species to achieve mutual distances of $\sim 10 \mu\text{m}$ and the related enhanced coupling for efficient sympathetic cooling of small ensembles. A 1 kV RF-voltage on the quadrupole electrodes would result, for example, in a radial secular frequency of $2\pi \cdot 1.5 \text{ MHz}$ for $^{138}\text{Ba}^+$ and $2\pi \cdot 200 \text{ kHz}$ for the protein cytochrome c ($m \sim 12400 \text{ amu}$) at a charge state $Z = 12$. By choosing a weaker axial confinement, for example $2\pi \cdot 150 \text{ kHz}$ for cytochrome c, results in $2\pi \cdot 400 \text{ kHz}$ for the $^{138}\text{Ba}^+$ -ions and both species will be forced to the axis of the trap. The equilibrium positions in the trap can be calculated numerically [41] and reveal a mutual distance for the mentioned parameters of the order of $10 \mu\text{m}$. The motional amplitudes of both particles are on the order of 100 nm even in the case of an equilibrium temperature of as high as 20 times the Doppler cooling limit of the barium ions. This should allow for a precise positioning and individual resolving of molecular ions.

For experiments where molecular ions of a further extended charge-to-mass ratio of $>1/10^4$ have to be investigated, for example for molecules in the mass range of 10^5 amu at a charge stage $Z \approx 10$, an adjoined tighter trapping section is required, similar to the one already implemented in [28, 124]. A trap like this, with a set of trapping parameters of ($U_{\text{RF}} = 3 \text{ kV}$, $r_0 = 100 \mu\text{m}$, $\Omega = 2\pi \cdot 150 \text{ MHz}$) will lead to a positioning within the 100 nm scale and mutual distances on the order of $5 \mu\text{m}$ that is expected to allow for a sufficient coupling. In addition the segmented Paul-trap in [28] allows for the deterministic separation of single molecular ions from a larger Coulomb-crystal and to reliably position and overlap the target in the interaction region with the X-ray pulses.

A cooling scheme for the internal degrees of freedom of the confined ions that relies on radiative cooling is already implemented. If faster, more efficient cooling schemes are required, the apparatus is suitable for an implementation of a buffer gas [33] or an optical cooling stage [35, 34]. In addition, techniques that address the orientation of the molecular ions, like laser field-free alignment [157] can be implemented.

It is expected that the combined features and extensions of the presented scheme, might allow to deterministically deliver and accurately position biologically relevant molecular ions into intense, ultra-short X-ray pulses, allowing for time-resolved structural information of single molecules on the atomic scale. The potential impact is best concluded in reference [15]: "[...] ultrashort, high-intensity X-ray pulses [...], in combination with container-free sample handling methods based on spraying techniques, will provide a new approach to structural determination with X-rays." "Should this new femtosecond window in imaging provide a path to high-resolution structural information without the need for macroscopic crystals, its impact on structural biology would be tremendous."

6.2 Discrete kink solitons in ion-traps

Motivated by the experimental findings and recent theoretical work about the possible experimental implementation of metastable topological defects in two-dimensional Coulomb-crystals confined in an ion-trap, a nearly independent research attempt to the pump-probe experiment on $^{24}\text{MgH}^+$ was explored. Discrete kink solitons in ion-traps are presented for the first time. The theoretical predicted extended kink as well as the localized kink have been experimentally observed. These structures have been compared to theory, taking the experimentally used parameters into account. In addition, first attempts to maximize the structural lifetime of the kink solitons in the trap, used in this thesis, have been implemented. Both, the additionally applied radial cooling and the improved micro-motion compensation of the crystals had positive effects on their own and have been discussed concerning their relevancy. After the experimental demonstration of topological defects in the ion-trap system of this thesis, several experiments and extensions are possible.

Following the conclusions of the first attempts to increase the structural lifetime of crystals, an improvement can be achieved by either lowering the pressure in the vacuum chamber or by realizing kink structures with a heavier ion, for example $^{138}\text{Ba}^+$. If successful, this could lead to a measurement of structural lifetime for both, the extended and the localized kink in comparison with the zig-zag structure. In addition, the influence on the structural lifetime of kinks with additional species of higher or smaller charge-to-mass ratio within the crystal and the dependence whether these species are directly laser-cooled or not, can be examined. The first experimental verification of kink-dynamics, for example the controlled displacing transfer within the crystal, is within reach. A first, preliminary indication of a moving kink has been observed in the laboratory. This, together with the already successful implementation of two topological defects in one ion crystal can lead to investigations on interactions, for example the collision or annihilation of kinks. General investigations on topological defect structures in ion-traps is not restricted to two-dimensional zig-zag structures. A deeper insight into kink structures and formation processes in the three-dimensional case would be desirable. First experimental data that indicate a three-dimensional kink has been already collected. The verification and theoretical description is subject of current investigations.

For quantum information processing applications, the manipulation by laser beams of each individual ion in the trap whose internal states serve as a qubit for quantum computation is essential. In addition, the coupling of the electronic levels of two ions in the trap is a prerequisite for two-qubit gates. Typically, one or several modes of motion of a string of ions in a linear trap is used to couple the electronic states of the individual ions. When scaling the number of particles in the trap, these quantum information schemes reveal conflicting requirements on the trap frequency. The spectral resolution has to be increased with the increasing number of ions. Due to the Heisenberg uncertainty relation, this requires longer interaction periods in conflict with the required short gate operations to outrun de-coherence effects. To ensure spectral resolution of individual modes, the trapping frequency should be as high as possible. On the other hand, trapping more ions in a chain requires lowering of the trapping frequency to avoid two-dimensional structures and to preserve the individual addressability. In contrast, the properties of localized kink solitons in the ion-trap system does not depend on the number of ions. Moreover, as

pointed out in detail in [42], the internal modes of the kink are typically well separated from the rest of the phonon modes by an energy gap. With this concept, a single addressing of ions in the trap is predicted when scaling the number of ions without degradation of the frequency gap separation or the gate-speed. In addition, the transportation of quantum information is envisioned by the authors of reference [42] by a translation of the soliton in the ion-trap.

Another feature of topological defects in ion-traps is related to the continuous phase transition during a linear quench of the transverse or axial trapping frequency. As stated before, the phase transition from a linear ion chain to a two-dimensional zig-zag configuration is of second order. The homogeneous Kibble-Zurek mechanism (KZM) [44, 45] applies to infinite systems with a continuous phase transition that is described by Landau theory [158]. This mechanism is expected to account for the formation of cosmic strings in the early universe. The KZM predicts that the time scale of dynamical relaxation of the crystal diverges at the critical point of mechanical instability [43, 51]. The adiabaticity of a transition at the critical point is thus not directly related to the rate of change of the transverse trapping frequency. The transition does not remain adiabatic at the critical point no matter how slowly the transition parameter is changed [51]. After the adiabatic evolution fails at a certain distance from the critical point, the dynamic is frozen out until the evolution becomes adiabatic again [159]. In a quasi-infinite system like a ring-trap where the inter-ion distances are uniform throughout the whole ensemble, the homogeneous KZM applies for the formation of structural defects and predicts also the scaling of the density of defects after the quench [43]. This density scales with the inverse of the characteristic length over which the order parameter (displacement of the ions in the crystal from the trap axis) is correlated. The homogeneous KZM accounts for a variety of phenomena in the laboratory like the vortex formation in superfluid helium during neutron absorption [47, 48], defect production in a nematic liquid crystal [49] or defects in a light intensity pattern in a non-linear optical system [50]. Studies of topological defects in those laboratory systems have potential applications, for example the possibility to simulate the formation of cosmic strings in the early universe [46]. The lab-scale system is ideally suited to study the difficult to access cosmic phenomena.

In the case of a linear anisotropic ion trap, the inter-ion distances are inhomogeneous and the charge density in the center of a confined ion-crystal is higher than close to its ends. The dynamics of the phase transition thus becomes inhomogeneous, as the critical point is first crossed in the center of the trap and the front of the mechanical instability moves from the center to the edges of the linear chain. The velocity at which the front of the linear to zig-zag transition propagates along the trap axis depends on the rate of the quench of the transverse or axial trapping frequency. If this velocity is smaller than the velocity of sound, the dynamics evolve adiabatically and no defects are produced. However, in the other case, topological defects can be produced, even though their nucleation is suppressed compared to the homogeneous case. Thus, in the inhomogeneous case, a different scaling of the density of defects with the quenching rate is predicted [43, 51]. The inhomogeneous extension of the Kibble-Zurek mechanism (IKZM) has been studied theoretically [160, 159, 43, 51], however no experimental implementation has been realized up to now. The first observation of topological defects using ion-crystals in a linear Paul-trap is a promising starting point to verify the predicted scaling law of

the IKZM and might lead to new insights into cosmological systems.

6.3 Guiding of neutral polar molecules with electric fields in the radio-frequency regime

The extraction of a high-density beam of slow polar molecules with static or alternating electric fields in the few kHz regime is a field of intense research with widespread applications on its own [161, 77, 162, 163]. The interaction of the permanent electric dipole moment of a polar molecule, yielding an asymmetric charge distribution, with an electric field has been already demonstrated and used as a reliable tool to confine and guide molecules in a low-field seeking state in two-dimensions. Guiding molecules of small kinetic energies only, allows to start with a thermal distribution and to end with a fraction of molecules with a severely reduced spread of the kinetic energies. Assigning the mean velocity of the fraction to a corresponding thermal distribution, the related temperatures lie between 1 K and several 100 mK [164]. This technique is known as velocity filtering [165]. An extension of this method into the radio-frequency regime is desired because interactions of velocity selected, externally and internally cold polar molecules with cold atomic ions or even sympathetically cooled molecular ions could be investigated. Promising results have been already reported by connecting two separate setups, one guiding neutral molecules and one storing atomic ions [166, 167]. The apparatus build in the framework of this thesis has been designed to propel this field of research. The quadrupole is bend twice by 90° to allow for the longitudinal velocity filtering. The helical resonator, used to apply an RF-voltage on pairs of the quadrupole electrodes with a mutual phase difference of π and the whole setup is designed for a maximal Q-factor. This allows for the high voltages needed for sufficient depth of the time averaged Stark-potential, providing the radial confinement for the neutral molecules. An RF-voltage in the regime of several kV is estimated to account for the comparatively weak interaction of the neutral molecule with an electric field due to the Stark-effect and a simultaneous trapping of heavy atomic and molecular ions. A cryogenic nozzle can inject neutral molecules with a thermal velocity distribution into the guide and a commercial quadrupole mass spectrometer at the end can be used as a detector for guided neutral, polar molecules with RF-fields. An additional challenge will be to account for the zero-crossings of the electric field that occur every half an oscillation period in the radio-frequency regime (several MHz) and that might lead to fatal Majorana transitions from a low-field to a high-field seeking state of the molecule. If the investigation on efficient guiding of polar molecules is successful for a RF-guide, a variety of experiments and applications are proposed. For example, molecular ions could be stored on axis of the guide while simultaneously guiding cold polar molecules. This gives the possibility to study their mutual, cold collisions. Collision energies of $E_{\text{coll.}}/k_B \approx 1$ K for atomic ion - neutral molecule collisions have been already demonstrated [166] using a DC-filtering guide for polar molecules and an appendant ion-trap. A further reduction of the collision energy is possible with the proposed setup. This might lead into the field of cold chemistry and might allow the study of ultra-cold collisions where quantum effects play an important role.

Appendix A

Publications

- A.1 Deterministic delivery of externally cold and precisely positioned single molecular ions. *Submitted to Appl. Phys. B, ArXiv:1110.4254*

Deterministic delivery of externally cold and precisely positioned single molecular ions

G. Leschhorn · S. Kahra · T. Schaetz

Abstract We present the preparation and deterministic delivery of a selectable number of externally cold molecular ions. A laser cooled ensemble of $^{24}\text{Mg}^+$ ions subsequently confined in several linear Paul traps interconnected via a quadrupole guide serves as a cold bath for a single or up to a few hundred molecular ions. Sympathetic cooling embeds the molecular ions in the crystalline structure. $^{24}\text{MgH}^+$ ions, that serve as a model system for a large variety of other possible molecular ions, are cooled down close to the Doppler limit and are positioned with an accuracy of one micrometer. After the production process, severely compromising the vacuum conditions, the molecular ion is efficiently transferred into nearly background-free environment. The transfer of a molecular ion between different traps as well as the control of the molecular ions in the traps is demonstrated. Schemes, optimized for the transfer of a specific number of ions, are realized and their efficiencies are evaluated. This versatile source applicable for broad charge-to-mass ratios of externally cold and precisely positioned molecular ions can serve as a container-free target preparation device well suited for diffraction or spectroscopic measurements on individual molecular ions at high repetition rates (kHz).

1 Introduction

Following different approaches, sources of cold molecules have substantially advanced in recent years. Trapping [1] [2], deceleration [3] and filtering [4] of molecules and molecular ions are only a few examples. The huge amount of vibrational and rotational states and the related effort required to realize closed transitions hinders the effective use of direct laser cooling. Alternative approaches, for example sympathetic cooling of molecular ions within heterogeneous Coulomb crystals, have been demonstrated [5] [6]. Ranging from fundamental physics to a large variety of applications in physics and chemistry, trapped molecular ions are nearly ideal objects to study interactions of single, well prepared and localized particles.

One application requiring single, precisely positioned molecular ions is coherent hard X-ray diffraction for structural determination with atomic resolution and time-resolved pump-probe experiments using short X-ray pulses [7,8]. The weak interaction of X-rays with matter requires the Bragg diffraction from a solid state crystalline sample to achieve a sufficient signal gain [9]. Currently, the prerequisite of crystallization is the most severe constraint of these techniques, because many biological molecules are difficult or impossible to crystallize [10]. The proposal [7] of diffracting the short pulses of a free-electron laser on single molecules eliminates the mentioned constraints and even proposes a solution to the problem that the huge radiation dose alters the nuclear skeleton or even destroys the sample-molecule. However, the required amount of photons to image a single molecule (10^{13} per pulse) has to be bunched within a sufficiently short exposure allowing to record useful structural information before the radiation degrades the sample-molecule detrimentally. In order to reach this high photon flux a focus of ap-

G. Leschhorn · S. Kahra · T. Schaetz
Max-Planck-Institut for Quantum Optics
Hans-Kopfermann-Str.1
85748 Garching, Germany
Tel.: +49 89-32905-199
Fax: +49 89-32905-200
E-mail: tobias.schaetz@mpq.mpg.de

T. Schaetz
Albert-Ludwigs-Universität Freiburg
Hermann-Herder-Str. 3a
79104 Freiburg, Germany

proximately 100 nm diameter is required [7,11]. The realization of a micrometer sized beam of X-rays has already been reported [12]. Identically initialized, single trapped molecular ions provide the required localization and represent a container-free target at minimal background. Trapped ions provide excellent control over the external degrees of freedom down to the motional ground state within the confining potential [13]. A manipulation of the internal degrees can be achieved with state-of-the-art methods like buffer gas cooling [14]. Replacing of the target with the pulse repetition rate of the X-ray source on the 0.1-1 kHz level should be feasible. This work reports on a source for generic molecular ions, represented by $^{24}\text{MgH}^+$, sympathetically cooled into a Coulomb crystal of directly laser cooled atomic $^{24}\text{Mg}^+$ -ions and transferred into ultra-high vacuum with an efficiency close to unity.

2 Experimental setup

An overview of the mechanical layout is presented in figure 1. The ultra-high vacuum (UHV) chamber contains a linear quadrupole guide [15] providing a two dimensional confinement for ions. Direct current (DC) voltages on ring-electrodes enclosing the guide can either be used to accelerate and decelerate ions along the guide axis or allow for additional axial confinement required to turn three sections of the quadrupole into linear Paul-traps. Four cylindrical, gold plated copper rods of 2 mm diameter are arranged in quadrupole configuration, such that the minimal distance between the guide center and the surface of the rods amounts to $r_0 = 1.12$ mm. The 49 cm long guide is bent twice by 90° with a radius of curvature of 35.5 mm for a different application. This will allow to investigate the efficiency of the guide to transfer cold neutral polar molecules using the Stark effect [4] in a radio-frequency (RF) field and to explore their interactions with trapped molecular ions [16]. Concerning the experiments presented in this paper, the double bend enhances the efficiency of extracting the injected gas, required for the generation of the molecular ions. Radial confinement along the quadrupole is achieved by applying a RF-voltage on each pair of opposing electrodes with a mutual phase difference of π and a frequency of $\Omega_{\text{RF}} = 2\pi \cdot 6.8$ MHz. To allow for ions with small charge-to-mass ratios (Z/m), stable trapping conditions require a high resonance frequency of the used helical RF-enhancement resonator. Therefore, parasitic capacities, caused by e.g. dielectrics, are reduced to a minimum by the chosen electrical layout. Due to the skin effect, the RF-current flows only in a thin surface layer in copper of approximately 25 μm . A 3 μm thick gold coating protects the surface of the

copper electrodes from oxidation during the assembly and large contacting clamps maximize the electric and thermal contact. This leads to a high enhancement factor for RF-voltages of $Q=730$ (loaded) and thus supports the high voltages needed for a stiff confinement of (molecular-) ions with small Z/m and the envisioned experiments with neutral molecules.

Pairs of 5 mm thick copper ring electrodes (outer diameter: 24 mm, inner diameter: 8 mm), centered along the axis of the guide, create regions of 3D confinement (refer to figure 1) and additionally serve as electrodes for the acceleration and controlled transfer of the ions. A DC-voltage applied to each pair of these electrodes, spaced by 15 mm, generates a nearly harmonic potential in the central trapping region leading to static confinement along the guide axis. The ring electrodes have been carefully designed to account for mechanical stability, optical access to the axis of the guide and the shielding effects caused by the RF electrodes (see also figure 6). The ion trap, completed by the two ring electrodes after the first bend of the guide, is labeled trap 1 in the following. At the end of the guide, three ring electrodes can create two trapping regions, named trap 2 and 3. The middle electrode is shared, resulting in a double well axial potential. Optionally, the traps can be combined to a larger one. In total, up to three traps can be used. Typically, for $^{24}\text{Mg}^+$, the measured radial frequency in trap 2 amounts to 410-540 kHz, which corresponds to a root-mean square RF-voltage on the electrodes of 34-46 V. The frequently used configuration of 210 V and 100 V on the two ring electrodes of trap 2 leads to a typical axial trap frequency of about $2\pi \cdot 30$ kHz. The asymmetry of the applied voltages leads to a trap minimum at an axial position where micromotion [15] can be compensated best.

Trap 1 and 2 can be selectively loaded with all stable isotopes of Mg^+ and Ba^+ ions by applying photoionization schemes [17–19] on atoms out of a thermal beam, evaporated into the trapping region by heating one of three 0.8 mm thick metal wires inside tantalum tubes. One of the housed stacks of three atomic ovens (f) can be seen without cover in figure 1 B labeled (a). Photoionization is far more efficient and less disturbing compared to electron-impact ionization [20]. A smaller temperature of the resistively heated atomic ovens is required. As a consequence, the deposition of magnesium or barium on the trap electrodes and the influence of the related contact potentials is reduced. The smooth transfer of molecular ions along the guide and its efficiency is enhanced. Furthermore, charging of dielectrics by the electron gun is avoided. For photoionization of magnesium a resonant two-photon process is used. One photon with a wavelength near 285 nm excites the neu-

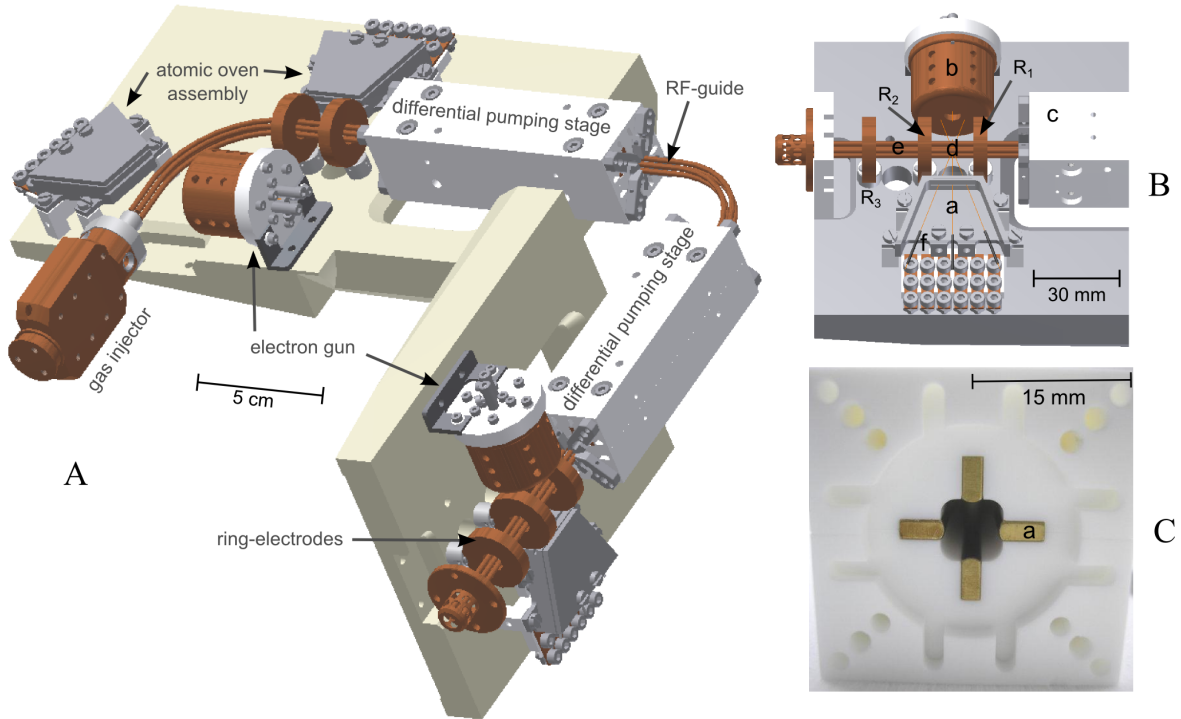


Fig. 1 Overview of the most important parts of the guide for (molecular) ions and optional traps. Various elements have been removed for the sake of clarity. (A) shows the cryogenic gas injector and the double bent RF-guide. Two differential pumping stages separate three different chambers, that can be pumped individually. Five ring electrodes allow to form three trapping regions, where the confined particles can be observed by detecting the fluorescence light of laser cooled $^{24}\text{Mg}^+$ or $^{138}\text{Ba}^+$ (see figure 3). Three assemblies of atomic ovens and two electron guns are positioned along the guide. (B) gives a close-up of the traps 2 (d) and 3 (e) at the end of the guide. Neutral ^{24}Mg atoms can be evaporated into the trap by resistively heating one of the Mg-filled tantalum tubes (f) of the atomic oven assembly (a) and can be ionized either by photoionization or by electron bombardment ionization using electron gun (b). (C) shows a close-up on the front side of one of the 10 cm long ceramic tubes, that serve as differential pumping stages. The clover leaf shaped profile leaves a 0.5 mm gap to the RF-electrodes and minimizes the open cross section between the different chambers. Voltages on the four gold plated copper inlets (a) can either serve as compensation voltages to counteract stray fields or form drift tubes to bunch the accelerated and guided ions. Additionally, they do not charge up like ceramics, that would hinder a smooth transfer of ions.

tral magnesium atom from its ground state $3s^2 S_0$ to the $3s3p P_1$ state. A second photon (285 nm) or a 280 nm photon of the Doppler cooling laser for $^{24}\text{Mg}^+$ (see figure 2) is sufficient to reach the continuum. All translational degrees of freedom of the $^{24}\text{Mg}^+$ ions can be laser cooled down to the Doppler limit (≈ 1 mK) driving the $3s S_{1/2} \leftrightarrow 3p P_{3/2}$ transition with a natural linewidth of $\Gamma \approx 2\pi \cdot 43$ MHz. If the kinetic energy of the ions at a given density falls below a critical value, a phase transition into a crystalline structure, known as a Coulomb- or Wigner crystal, occurs [21][22]. The lattice parameter of such a crystal is of the order of a few μm . The localization of an ion cooled to the ground-state of the quantized harmonic trapping potential is ultimately limited by the width of the ground state wavefunction (≈ 20 nm for $^{24}\text{Mg}^+$ at $\omega_{sec} \approx 2\pi \cdot 500$ kHz). Typically, a Doppler cooled ion can be localized to better than $1 \mu\text{m}$, currently limited by the imaging properties of the used objective.

The laser setup for photoionization of neutral magnesium and laser cooling of $^{24}\text{Mg}^+$ is shown in figure 2. Two dye-lasers are pumped each by 3.5 W of a frequency doubled Nd:YAG laser and provide a typical output power of 500 mW at 570 nm and 250 mW at 560 nm. UV-light at the required frequencies for laser cooling and photoionization is created by two external second-harmonic generation (SHG) ring resonators incorporating non-linear BBO crystals [23]. The enhancement cavities and the trap apparatus share the same optical table. The connection to the lasers, that are located in a different laboratory, is achieved using two 70 m long single mode optical fibers. The dye-lasers are frequency locked to suitable iodine transitions, using two different Doppler-free spectroscopy setups (Absorption spectroscopy [24] for the 560 nm and polarization spectroscopy [25] for the 570 nm light). A much more compact setup can be implemented using an all solid state turn key laser system described in [23].

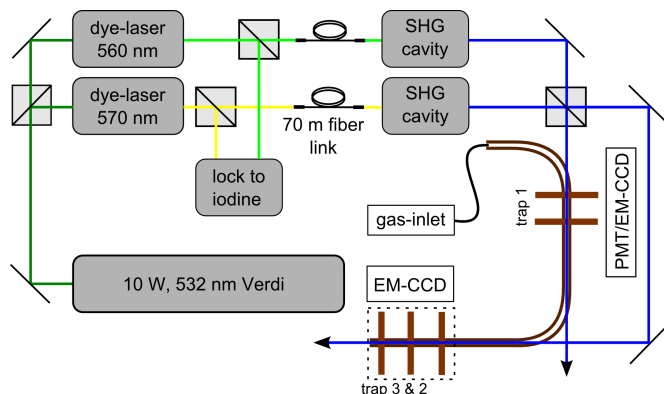


Fig. 2 Schematic overview of the experimental setup including the laser part for photoionization of neutral magnesium and Doppler cooling of $^{24}\text{Mg}^+$. Two second harmonic generation ring cavities are used for frequency doubling the output frequencies of two dye-lasers, which are stabilized and locked to two Doppler-free iodine spectroscopy setups. The resulting 280 nm light for cooling of $^{24}\text{Mg}^+$ and the 285 nm light for photoionization of neutral magnesium are overlapped using a polarizing beam splitter and enter the quadrupole (see figure 1) in the vacuum chamber along its symmetry axis via two laser ports. Ring electrodes form three trapping regions, where the confined particles can be observed by detecting the fluorescence light of laser cooled $^{24}\text{Mg}^+$. The observation in trap 1 is achieved by a photo-multiplier tube or a UV sensitive electron multiplying CCD camera, respectively. Ions in trap 2 and 3 can be imaged on a CCD camera.

The fluorescence light of ions confined in trap 1 can either be observed by an imaging system consisting of an air-spaced, two lens condenser (magnification: $10\times$) followed by an electron multiplying CCD camera or by a photomultiplier (see figure 2). The camera is used for applications, that require spatial resolution of individual ions while the photomultiplier provides a spatially integrated fluorescence signal, sufficient for a controlled loading of the trap. The magnification factor of the imaging system shared by trap 2 and 3 can be chosen to be 10 by using a three lens condenser or 50 by using a four lens near diffraction limited objective. Fluorescence light from these traps can be observed with a EM-CCD camera.

The apparatus offers several options for the creation of molecular ions of choice, discussed in greater detail in section 3.1. A cryogenic inlet, similar to the one in [4], can inject gas into the vacuum vessel via a pulsed valve. The gas pulses (few ms duration) pass a copper capillary, optimized for thermal contact to a liquid nitrogen bath, allowing for internally cold molecules, but can be additionally heated to evaporate a potential blockage and to carefully adjust the temperature of the gas, if required. After passing the copper-injection tube the molecules enter the chamber through a ceramic nozzle. A gap of 0.5 mm between the front surface of the quadrupole and the nozzle mitigates the heat trans-

fer. Right behind the injection system, an electron gun can ionize the neutral molecules in the center of the guide. The whole injection system can be replaced by an Electrospray Ionization source (ESI), based on soft protonation methods [26].

Ultra-high vacuum of the order of 10^{-10} mbar is required for experiments relying on trapped and crystallized ions, to minimize reactions and collisions with the background gas. As described in reference [27], the concept of using a quadrupole guide to transfer ions from the preparation zone to a spatially separated experimental zone allows for the required UHV, despite the comparatively high pressure ($\sim 10^{-3} - 10^{-6}$ mbar), related to the efficient creation of molecular ions. Additionally, a buffer gas cooling stage [14], to address the molecule's internal degrees of freedom, can be implemented if required by the experiment. Currently, the quadrupole, starting at the gas inlet nozzle, guides the ions through three chambers, that are separated by two 10 cm long ceramic tubes serving as differential pumping stages with an open cross section, that adapts to the quadrupole (see figure 1 C). Care has been taken to avoid uncontrolled charge ups, for example, on insulators near the guide, severely reducing the efficiency or even hindering the guiding of ions along the quadrupole. Therefore the ceramic parts of the tubes, that would remain in line of sight for the ions, have been replaced by gold plated copper bars. A voltage can be applied to these bars to enhance the transfer process. For the experiments presented in the next section, the copper bars are grounded. The differential pumping stages between individually pumped chambers allows to maintain a pressure difference of 4 orders of magnitude between the first and the last chamber, typically kept in the few 10^{-10} mbar regime.

3 Results

In this section, deterministic delivery and preparation methods for molecular ions and their integration and sympathetic cooling embedded in the crystalline structure of directly laser cooled atomic ions are described. After its creation, the molecular ion is transferred into an isolated region. For a single ion the efficiency of the transfer process is close to unity and fast (\ll ms). For the transfer of many individual molecular and atomic ions, three schemes suited for different applications are described. The deterministic delivery of a selectable number of externally cold molecular ions, allowing for repetition rates up to kHz, is persecuted and an accuracy for spatial positioning of a micrometer is demonstrated.

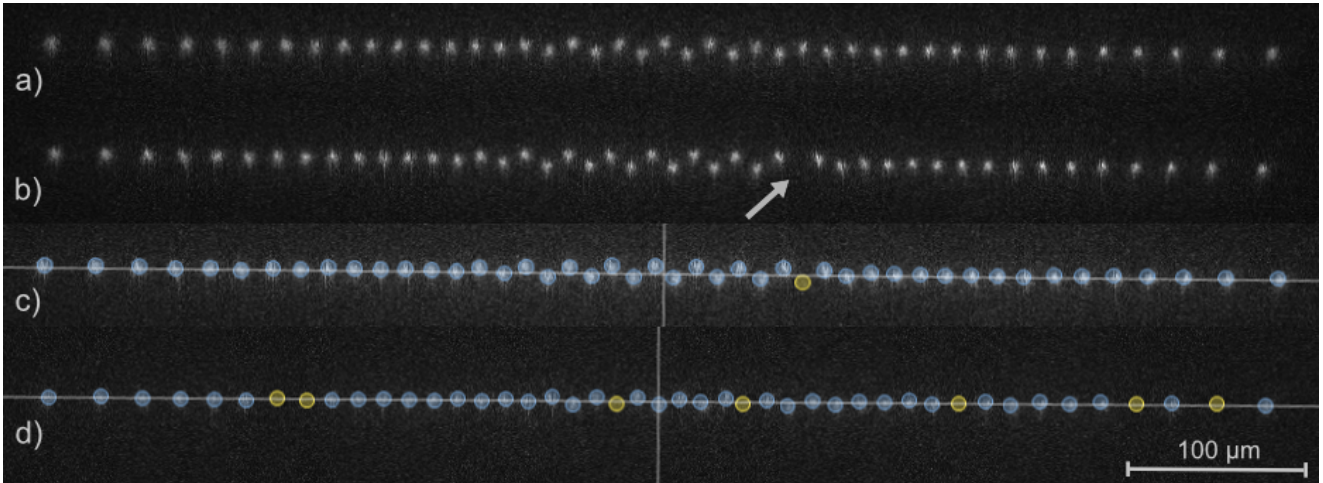
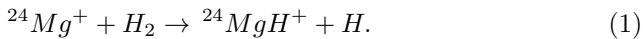


Fig. 3 Two-dimensional fluorescence CCD images of crystalline ion structures confined in trap 2 (see fig. 1 B) under UHV conditions, using ten times magnification to image the whole ion crystal. Crystal a) contains only $^{24}\text{Mg}^+$ ions and is referred to as a pure crystal. Crystal b) contains exactly one molecular $^{24}\text{MgH}^+$ ion indicated by the arrow. In c) the horizontal axis and the vertical symmetry axis of the crystal in b) is given by white lines. After the identification of the bright spots, the position of the atomic $^{24}\text{Mg}^+$ -ions is marked by blue circles. The symmetry of the Coulomb crystal is exploited to identify the position of the non-fluorescing molecular ion ($^{24}\text{MgH}^+$) marked by a yellow circle with an accuracy of approximately one micrometer. The ion crystal d) demonstrates the preparation of 7 molecular ions. The number of sympathetically coolable and crystallizable molecular ions is determined by the cooling rates mediated via the atomic ions. One cooling ion can be sufficient to sympathetically cool and crystallize ~ 10 molecular ions.

3.1 Production

The apparatus offers several schemes to create a molecular ion (see also section 2) and to embed it on a lattice site of an ion crystal. Electron bombardment ionization of neutral molecules out of an effusive beam is possible using the electron gun, that is located behind the cryogenic gas inlet (see figure 1 (A)). On the one hand, a wide mass range of molecular ions can be produced using this method. On the other hand, the molecule, even if originally internally cold, will end up in a highly excited, dissociative state or the electron-impact might lead to an immediate dissociation. Optionally, an already realized post-filtered ESI setup can substitute the gas inlet stage and serve as a soft ionization device for larger molecules of selectable charge-to-mass ratio. To investigate the control and transfer capabilities of the setup, the production of the molecular ions is realized by the photochemical reaction [5]



A collision of an electronically excited $^{24}\text{Mg}^+$ ion with a hydrogen molecule leads to the formation of an magnesiumhydrid ion and an hydrogen atom. The $^{24}\text{MgH}^+$ ion serves as a model system to calibrate the setup for almost generic molecular ion species having a suitable charge-to-mass ratio such that they can be sympathetically cooled exploiting directly a laser cooled $^{24}\text{Mg}^+$ or $^{138}\text{Ba}^+$ crystal as a heat sink [28].

A reliable preparation of an isotopically clean (here $^{24}\text{Mg}^+$) atomic crystal is the initial step. Different magnesium isotopes ($^{25}\text{Mg}^+$, $^{26}\text{Mg}^+$), as well as accidentally ionized residual gas particles, appear as dark lattice sites within the crystal (see figure 3 b) and c)) and are not distinguishable from the molecular ions. To keep the contamination negligible, the isotope selective two photon photoionization loading scheme, discussed in section 2, is sufficient for the current needs. If the experiment does not require a fast or even continuous reloading, an optional cleaning of the ion crystal can be implemented. The contaminant ion's kinetic energy can be increased above the trap depth, by resonantly driving its specific secular motion [29]. An arbitrary waveform generator produces the sum of the radial secular frequencies ($\propto U_{\text{RF}} \cdot Z/m$) of particles with masses $m=25 \text{ u}$ ($2\pi \cdot 480 \text{ kHz}$) and $m=26 \text{ u}$ ($2\pi \cdot 462 \text{ kHz}$) and the resulting beat signal is applied to a copper wire parallel to the axis of trap 1. After three cleaning cycles of typically 2 seconds, all dark ions are lost out of the trap. The $^{24}\text{Mg}^+$ ions have a survival probability of $>95\%$. A pure $^{24}\text{Mg}^+$ ion crystal after successful isotope selective loading is shown in figure 3 a).

After the preparation of a pure atomic $^{24}\text{Mg}^+$ crystal, small amounts of hydrogen gas are injected into chamber 1. Simultaneously, the atomic ions are exposed to 1.5 mW of the near resonant (about $\Gamma/2$ red detuned) cooling light, focused down to 80 μm beam waist, leading to a significant population of the $3p \text{ P}_{3/2}$ state and

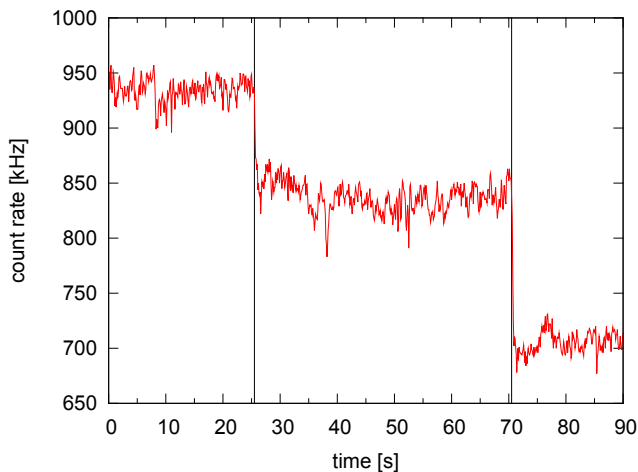


Fig. 4 Breeding of molecular ions via the photochemical reaction (1): The count rate, detected by a photomultiplier tube is proportional to the amount of $^{24}\text{Mg}^+$ ions in trap 1. Hydrogen injection was started at the indicated instants (vertical lines). The count rate drops twice when $15 \pm 3\%$ and $25 \pm 3\%$ of the atomic ions are converted into $^{24}\text{MgH}^+$. The background count rate (no ions in the trap) amounts to 320 kHz. Each data point represents an accumulation time of 100 ms.

therefore to approximately 4 eV of additional energy allowing for the photo-chemical reaction (see equation 1). This provides a controlled transformation of a selectable amount of ions in the crystal to the molecular ion model system $^{24}\text{MgH}^+$. Opening the pulsed valve for 5-15 ms with the hydrogen reservoir at a pressure of ≈ 0.3 mbar, rising the pressure to a few 10^{-9} mbar for a period of less than 2 seconds, yields a conversion of nearly 50 % of the $^{24}\text{Mg}^+$ ions into $^{24}\text{MgH}^+$. Figure 4 shows the count rate of the PMT, detecting the fluorescence light of atomic ions in trap 1 and its change due to two injections of hydrogen. After opening the valve, the rate drops by 20% due to the intended conversion of a fraction of the $^{24}\text{Mg}^+$ ions into non-fluorescing molecular ions. After about 250 milliseconds the reactions cease indicating fast pumping of the injected hydrogen gas. A typical bi-crystal, bred as described above is shown in figure 3 d).

In order to investigate the requirement to separate the region for production and the precision experiment in the setup, the rates of laser-induced reactions of the $^{24}\text{MgH}^+$ model system have been studied, similar to reference [5]. In figure 5, the time dependent composition of two-component ion crystals with different fractions of $^{24}\text{Mg}^+$ and $^{24}\text{MgH}^+$ are presented. The experiment was performed under UHV conditions over an extended period of time (up to 3 hours). The rates of the reaction of photodissociation described in equation (1) are proportional to the population of the excited state $3p P_{3/2}$. Thus, in order to minimize the rate of reactions in this

study, the laser power of the cooling beam was set to just sustain the crystalline structure. A rate equation model was developed to describe the time evolution of the fraction of atomic to molecular ions. Three light induced reactions are considered and reaction rate coefficients κ_1 , κ_2 and κ_3 were fitted to each process. One is the photochemical reaction described in equation 1 ($\kappa_1 = 0.13 \text{ h}^{-1}$) and the other two are the dissociation reactions $^{24}\text{MgH}^+ \rightarrow ^{24}\text{Mg}^+ + \text{H}$ ($\kappa_2 = 0.79 \text{ h}^{-1}$) and $^{24}\text{MgH}^+ \rightarrow ^{24}\text{Mg} + \text{H}^+$ ($\kappa_3 = 0.10 \text{ h}^{-1}$). This set of rates reproduces the measured time dependent composition of the four experiments and the time scale for the relevant reactions is consistent with results reported in [30]. The limited statistics gained within the experiments can not provide an accurate measurement of the reaction rates, however, it yields a rough estimate of the relevant time scales for the specific partial pressure of the reactional gases within chamber number 3. To conclude, stable conditions for Coulomb-crystals that allow for precise control of the position of individual ions require ultra-high vacuum conditions ($< 10^{-10}$ mbar). Experiments with molecular ions, even with the reactive molecular ion $^{24}\text{MgH}^+$, are possible on the time scale of minutes when performed in the UHV. These conditions are difficult to provide, if the production and delivery rate of the molecular ion and its surrounding Coulomb-crystal exceeds 1/s or has to be achieved in a continuous way for example by Electrospray Ionization. For these applications, a deterministic transfer of individual molecular ions from the production to a well isolated experimental region is required and becomes a powerful tool. For example, the transfer schemes presented in the next section are advantageous when an implementation of buffer gas cooling of the molecular ions or a deterministic initialization and a fast replacement of single molecular ions is required.

3.2 Deterministic transfer

For the purpose of demonstrating the deterministic transfer scheme, a molecular ion is prepared and confined in trap 1. The ion is accelerated and the quadrupole guides it through chamber 2 and the two differential pumping stages, described in section 2. The quadrupole ends in the third chamber of the experimental apparatus, that maintains UHV conditions. The transferred ion is then decelerated and subsequently trapped by the Paul traps 2 and/or 3 located at the end of the guide. The three ring electrodes, that form the axial confining potential for these two traps are referred to as R_1 , R_2 and R_3 in the following (see figure 1B).

The molecular ion is released out of the axial confinement of trap 1 by grounding the ring electrode fac-

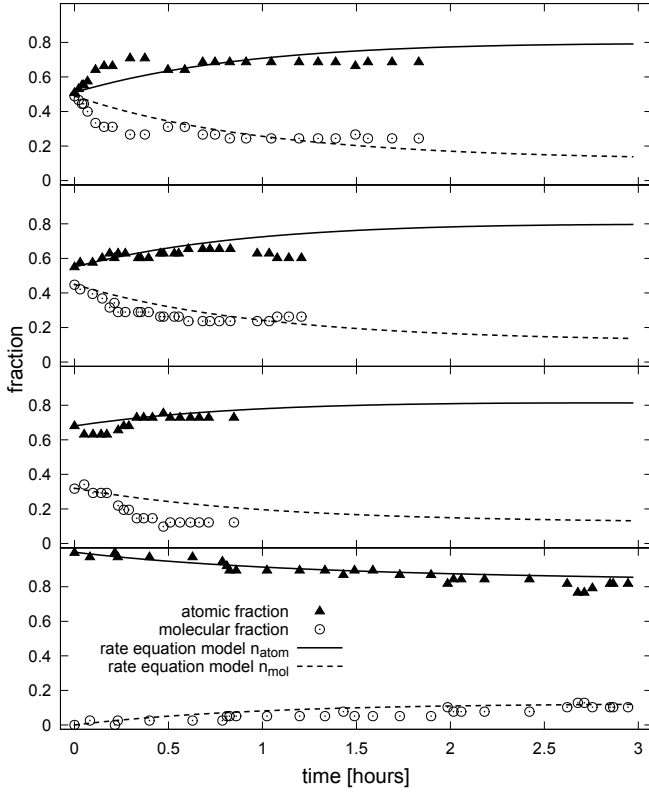


Fig. 5 Atomic $^{24}\text{Mg}^+$ and molecular $^{24}\text{MgH}^+$ ion composition of four Coulomb crystals in dependence of the storage duration in trap 2. The atomic fraction of the initial crystal increases from 50% to 100% for the experiments from top to bottom. The compositions are derived out of fluorescence images, taken by the EM-CCD camera. The laser power was chosen sufficient to sustain the crystalline state of the ions in the trap ($\approx 150 \text{ mW/cm}^2$ intensity and about one natural linewidth detuning). According to a nude Bayard-Alpert type ionization gauge (calibrated on N_2), the total pressure of the vacuum chamber amounts to approximately $2 \cdot 10^{-10}$ mbar. The results derived with a rate equation model of the time evolution of the atomic and molecular fraction are shown as solid and dashed lines. The evolution of all four ion-crystals is described with a single set of rates (see main text). No counting error in the evaluation of fluorescence images is assumed, therefore the composition of each of the observed crystals can be given exactly.

ing the differential pumping stage (see figure 1A). Switching of the voltages by MOS-FET transistors takes currently less than $1 \mu\text{s}$. The ion is accelerated along the axis of the guide by applying 250 V to the first ring-electrode of trap 1 (see figure 6). A CPO¹ simulation reveals a substantial shielding effect caused by the quadrupole electrodes, related to a reduced electric axial potential at the trap center by approximately three orders of magnitude. The remaining excess potential energy of 130 meV is converted into axial kinetic energy of the ion. Time of flight measurements reveal an average ion

¹ Charged Particle Optics programs, CPO Ltd

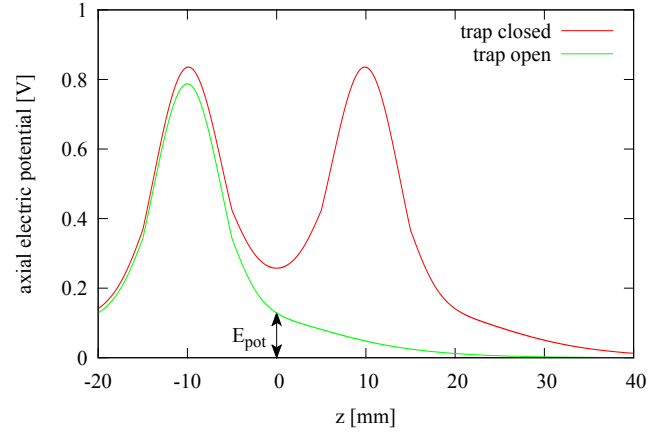


Fig. 6 Results of a simulation of the axial electric potential provided by voltages applied to the ring electrodes of trap 1 taking the shielding effect of the rf-electrodes into account. The result achieved for applying 250 V to both ring-electrodes is depicted by the red line. The trap is opened axially by switching one of the ring-electrodes to electrical ground (green line). The ions are accelerated along the RF-guide by the potential gradient and their excess potential energy E_{pot} is converted into kinetic energy.

velocity of 1850 ms^{-1} , indicating that the voltages applied on micro-motion compensation wires near trap 1 contributed to the acceleration. After approximately $190 \mu\text{s}$ of propagation without axial confinement, the molecular ion arrives at the optional Paul traps 2 and 3. Approaching the center position between the two ring electrodes R_1 and R_2 , the voltages are applied and the guided, transferred ion is trapped. For a single molecular ion, this transfer can be processed with nearly 100% efficiency, because the radial confining RF field provides a deep trapping potential (typical 1 eV) rendering radial losses of ions negligible. Simulations of the axial dynamic of the particle in the time-depending potentials of the transfer process by numerically solving Newton's equation of motion predict a $5 \mu\text{s}$ (see figure 8 a)) time window, where a single ion can be trapped reliably using the protocol and parameters described above.

If required, the transfer of tens to hundreds of individual ions is possible at once with the discussed scheme. However, the efficiency suffers for an increased number of ions. The mutual Coulomb repulsion in an ensemble, launched out of trap 1, causes an axial spreading of the ensemble during propagation. The maximal number of ions that can be decelerated and trapped, depends on the distance between the ring-electrodes, the average time of flight and the parameters for axial confinement in trap 1. Stiffer axial confinement is related to a higher potential energy, that is converted into kinetic energy and thus leads to a shorter time of flight. On the other hand, the related reduced inter-ion spacing in trap 1

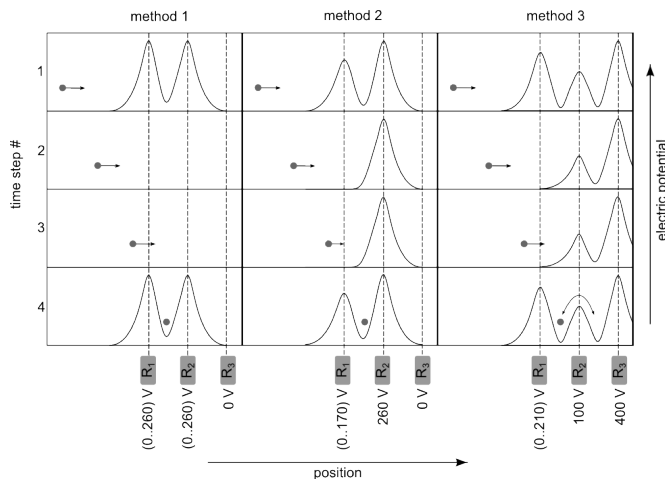


Fig. 7 Schematic overview of three different methods used to decelerate and trap various numbers of ions at the end of the transfer process. Different timings and amplitudes of voltages on the ring-electrodes R_1 , R_2 and R_3 (see figure 1) provide the switching of the axial electric potential along the radially confining RF-guide. The dot and arrow represent a single or the center of mass of a bunch of ions and their average velocity, respectively. The position relative to the switching axial potential wells is shown for different time steps.

leads to an initially increased Coulomb repulsion and hence to a faster spreading of the ensemble during the flight. Within the chosen range of parameters the influence of the shorter time of flight dominates and the increased Coulomb repulsion has only an influence on the order of a few percent on the maximal number of ions that can be trapped in total.

To enhance the transfer efficiency for an increasing number of ions, three different methods (see figure 7) have been developed. The first method is closely related to the single ion transfer scheme discussed above. The ring electrode R_3 is grounded and R_1 and R_2 are switched simultaneously between 0 V and 260 V. The switching is synchronized with the release of the crystal from trap 1, in order to close trap 2 when the maximal fraction of ions can be enclosed. The transfer efficiency of method 1 for an ion crystal, that contains 10 ions, is reduced to 80%, for 50 ions it drops to 50%. Figure 8 a) shows the result of simulations and of a measurement on the transfer efficiency in dependence of the time delay between launching the ions and switching of electrodes R_1 and R_2 . Experimentally, the initial number of ions in trap 1 is derived from the averaged photon count rate of the photomultiplier. The absolute number of ions and the measurement of the absolute transfer efficiency are accurate to $\pm 15\%$. To increase the accuracy, a second CCD camera is necessary.

A higher efficiency to decelerate and trap a spreading ion ensemble can be achieved via method 2 by switching only the ring electrode R_1 from ground to 170 V

leaving the voltage on R_2 and R_3 constant. The voltage applied to R_2 decelerates the ensemble and finally reflects it. This leads to a double-pass and a bunching of the ensemble in the trapping region, increasing the ion density and thus extending the time window for trapping compared to method 1. For the given parameters, the largest ion crystal, that can be theoretically recaptured without losses contains 55 ions. Figure 8 b) compares the simulated transfer efficiency for initially 55 ions with the results of the performed experiments. While method 1 allowed 50% transfer efficiency, 80% is reached using method 2.

The third method uses the ring electrode R_3 as an additional reflector for ions having a kinetic energy allowing to surpass R_2 . The potential generated by R_1 is raised sufficiently high to prevent reflected ions from escaping in backward direction. The voltages on R_2 and R_3 were set to 100 V and 400 V, respectively and kept constant during the whole transfer procedure. R_1 is switched from 0 V to 210 V. The asymmetry between the voltages on R_1 and R_3 provides an axial positioning of the ions where micro-motion compensation is optimal. The fraction of the ensemble that overcomes the potential hill generated by the middle ring electrode starts oscillating between the two potential minima. However, laser cooling reduces the kinetic energy of the $^{24}\text{Mg}^+$ -ions and the exchange between the two Paul traps ceases on time scales of typically a few seconds. The duration required to re-crystallize the ensemble of atomic and molecular ions critically depends on the laser intensity, the detuning from the atomic resonance and sufficient access of all motional degrees of freedom. Currently, one axial cooling beam enclosing only a small (few degrees) angle with the guide axis, barely addresses the radial degree of freedom. Therefore, mainly the normal modes of the crystal at a linear density allowing for zigzag and higher dimensional structures sufficiently couple the longitudinal and radial motion. A laser beam, that is red-detuned by about a natural linewidth of the atomic transition, as it is required to reach low temperatures for a crystal, is far off-resonant due to the Doppler shift for ions moving at velocities $\gg 1$ m/s. A different spatial overlap of the cooling beam with the ion crystals in trap 2 and 3 due to an imperfect matching of the two axis, leads to different final distributions of ions in the two traps. Figure 8 c) shows the transfer efficiency into trap 2 as a function of the time delay for switching R_1 using method 3. The experiment qualitatively confirms the duration for maximizing the probability for recapture and the asymmetric shape for long and short switching times predicted by the simulation.

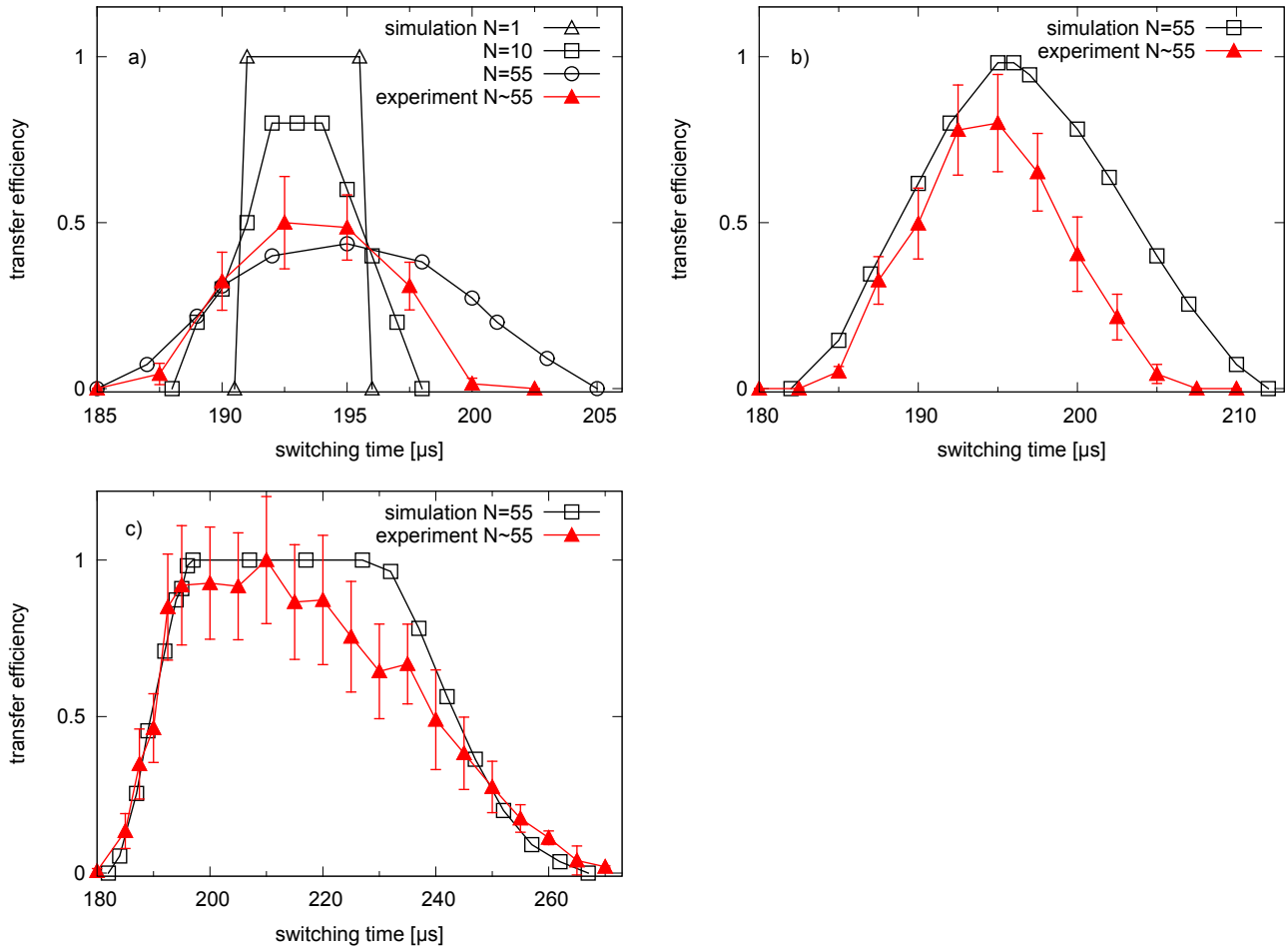


Fig. 8 Measured and numerically simulated transfer efficiencies of an ensemble of ions from trap 1 over a distance of 39 cm to trap 2 in dependence of the delay of switching the involved ring electrodes (time of flight of the ensemble). Figure a) shows the results of simulations of the transfer efficiency of method 1 for different initial particle numbers. The measurements were performed under conditions comparable to those assumed in the N=55 simulation. Figure b) and figure c) compare the experimental deduced data with the simulation results for 55 ions achieved following transfer method 2 and 3, respectively. The presented error bars take the uncertainties of the initial number of ions in trap 1 into account. The fluorescence count rate of the photomultiplier in chamber 1, used to load initial crystals with similar particle numbers, yields an estimated uncertainty of $\pm 15\%$ for the absolute scale of the measurements. Furthermore, discrepancies between simulation and experiment are due to uncertainties about the exact shape of the axial electric potential of the traps 1 and 2. Additional voltages on the micro-motion compensation electrodes cause deviations from the idealized axial potential solely generated by the ring-electrodes. Nevertheless, trends of the simulation, the different durations of successful re-capture and the different absolute efficiencies are in agreement with the experimental results.

Using the transfer method 3, the traps 2 and 3 get both populated with ions. An interchange of the ions between the traps can be performed at an efficiency close to 100%. The two traps share the electrode R_2 and the tight axial confinement is preserved for all times. Switching electrode R_2 to electrical ground for $25\ \mu\text{s}$ leads to an oscillation of the two ensembles centered at the new potential minimum. No change in the fluorescence rate on the CCD camera was detected when interchanging the ensembles of ions, indicating a unit efficiency of the transfer and that the crystalline structure is preserved during the oscillation (if unlikely a

melting did occur, the re-crystallization happened too fast to be detected by the CCD with a 100 ms exposure time). In order to analyze the potential interaction of, or exchange between the two initial ensembles, a distinguishable composition of molecular and atomic ions were prepared in trap 2 and 3. If the duration ($25\ \mu\text{s}$) of grounding R_2 coincides with half the oscillation period of the ions, a complete exchange of the ensembles between trap 2 and 3 is observed. A redistribution of the total amount and composition ratio of ions in the two traps is achieved by using a grounding duration different from the $25\ \mu\text{s}$. For example, a random distribution

of the ions is achieved by reducing the grounding duration and a gathering of $\approx 90\%$ of the ions into one of the trap is achieved by increasing the grounding duration.

4 Conclusions and outlook

We have shown the deterministic preparation of a selectable amount of externally cold and well localized molecular ions down to a single molecular ion. A pure $^{24}\text{Mg}^+$ ion crystal was loaded into a trap at the front end of a quadrupole ion guide. The model system $^{24}\text{MgH}^+$ was produced by the photochemical reaction of $^{24}\text{Mg}^+$ with hydrogen gas. The resulting molecular ion can be transferred along the ion guide and re-trapped by the second or third Paul trap at the end of the guide with unit efficiency. Three different transfer schemes for a mixed atomic and molecular ion ensemble and its corresponding transfer efficiencies have been investigated. The demonstrated highly efficient exchange of ion ensembles trapped in two separated traps can be used to load an ion trap with a transferred ion ensemble serving as a reservoir.

The method presented in this paper can be extended to other molecular ions using electron bombardment ionization or the already implemented Electrospray Ionization source (ESI) [26] combined with an additional charge-to-mass ratio filtering stage. Together with directly laser cooled $^{138}\text{Ba}^+$ ions (already implemented in the presented setup) [19], protonated molecules out of the ESI-source cover a wide range of charge-to-mass up to biologically relevant molecular ions. The presented transfer schemes can be enhanced in efficiency by using the electrodes inside the differential pumping stages as drift tubes to additionally bunch an ensemble during transfer [31] or to even realize a transfer where the crystalline structure of the ions is sustained [32], significantly improving the re-cooling times in the destination trap. An additional cooling of the internal degrees of freedom of the molecular ions by lasers [30,33] or by buffer gas [14] is realizable for example in chamber 1 or 2. The cooling light pressure, that acts on atomic ions only, can be used to separate the molecular from the atomic fraction of the crystal. Extending the setup by an additional segmented trap will give the possibility to cut single molecular ions out of a heterogeneous crystal and will be continuously loaded by exploiting the presented exchange of ensembles between two traps. The separation of individual molecular ions out of a two component crystal has already been demonstrated by our group, using a different segmented Paul-trap setup [34]. The presented production and control scheme for cold molecular ions can serve as a source for container-free molecular targets, in principle coolable to the mo-

tional ground state [13], for imaging or spectroscopic analysis [35].

Acknowledgements The authors would like to thank W. Schmid, T. Hasegawa, J. Bayerl, C. Kerzl and T. Dou for their contributions and W. Fuss for fruitful discussions and his encouragement. Financial support is gratefully acknowledged by the Deutsche Forschungsgemeinschaft, the DFG cluster of Excellence: Munich Center for Advanced Photonics, the International Max Planck Research School on Advanced Photon Science (IMPRS-APS) and the EU research project PICC: The Physics of Ion Coulomb Crystals, funded under the European Communitys 7th Framework Programme.

References

1. H. L. Bethlem, *et al.*, *Nature* **406**, 491 (2000).
2. T. Junglen, T. Rieger, S. A. Rangwala, P. W. H. Pinkse, G. Rempe, *Phys. Rev. Lett.* **92**, 223001 (2004).
3. H. L. Bethlem, G. Berden, G. Meijer, *Phys. Rev. Lett.* **83**, 1558 (1999).
4. S. A. Rangwala, T. Junglen, T. Rieger, P. W. H. Pinkse, G. Rempe, *Phys. Rev. A* **67**, 043406 (2003).
5. K. Mølhave, M. Drewsen, *Phys. Rev. A* **62**, 011401 (2000).
6. B. Roth, A. Ostendorf, H. Wenz, S. Schiller, *Journal of Physics B: Atomic, Molecular and Optical Physics* **38**, 3673 (2005).
7. R. Neutze, R. Wouts, D. van der Spoel, E. Weckert, J. Hajdu, *Nature* **406**, 752 (2000).
8. H. N. Chapman, *et al.*, *Nature Physics* **2**, 839 (2006).
9. G. Webster, R. Hilgenfeld, *Single Molecules* **3**, 63 (2002).
10. R. Henderson, *Quarterly Reviews of Biophysics* **28**, 171 (1995).
11. L. Young, *et al.*, *Nature* **466**, 56 (2010).
12. M. Seibert, *et al.*, *Nature* **470**, 78 (2011).
13. M. D. Barrett, *et al.*, *Phys. Rev. A* **68**, 042302 (2003).
14. D. Gerlich, G. Borodi, *Faraday Discussions* **142**, 57 (2009).
15. W. Paul, *Rev. Mod. Phys.* **62**, 531 (1990).
16. S. Willitsch, M. T. Bell, A. D. Gingell, S. R. Procter, T. P. Softley, *Physical Review Letters* **100**, 043203 (2008).
17. N. Kjaergaard, L. Hornekaer, A. Thommesen, Z. Videsen, M. Drewsen, *Applied Physics B: Lasers and Optics* **71**, 207 (2000).
18. D. Rotter, Quantum feedback and quantum correlation measurements with a single barium ion, Ph.D. thesis (2008).
19. G. Leschhorn, T. Hasegawa, T. Schaetz, *ArXiv e-prints:1110.4040* (2011).
20. D. N. Madsen, *et al.*, *Journal of Physics B: Atomic, Molecular and Optical Physics* **33**, 4981 (2000).
21. F. Diedrich, E. Peik, J. M. Chen, W. Quint, H. Walther, *Physical Review Letters* **59**, 2931 (1987).
22. D. J. Wineland, J. C. Bergquist, W. M. Itano, J. J. Bollinger, C. H. Manney, *Physical Review Letters* **59**, 2935 (1987).
23. A. Friedenauer, *et al.*, *Applied Physics B: Lasers and Optics* **84**, 371 (2006).
24. P. W. Smith, T. W. Hänsch, *Phys. Rev. Lett.* **26**, 740 (1971).
25. C. Wieman, T. W. Hänsch, *Phys. Rev. Lett.* **36**, 1170 (1976).

26. J. B. Fenn, M. Mann, C. K. Meng, S. F. Wong, C. M. Whitehouse, *Science* **246**, 64 (1989).
27. A. Ostendorf, *et al.*, *Physical Review Letters* **97**, 243005 (2006).
28. D. J. Larson, J. C. Bergquist, J. J. Bollinger, W. M. Itano, D. J. Wineland, *Phys. Rev. Lett.* **57**, 70 (1986).
29. M. Drewsen, A. Mortensen, R. Martinussen, P. Sta anum, J. L. Sørensen, *Phys. Rev. Lett.* **93**, 243201 (2004).
30. P. F. Sta anum, K. Hojbjerg, P. S. Skyt, A. K. Hansen, M. Drewsen, *Nature Physics* **6**, 271 (2010).
31. U. Schramm, T. Schaetz, D. Habs, *Phys. Rev. Lett.* **87**, 184801 (2001).
32. U. Schramm, T. Schaetz, D. Habs, *Phys. Rev. E* **66**, 036501 (2002).
33. T. Schneider, B. Roth, H. Duncker, I. Ernsting, S. Schiller, *Nature Physics* **6**, 275 (2010).
34. T. Schaetz, A. Friedenauer, H. Schmitz, L. Petersen, S. Kahra, *Journal of Modern Optics* **54**, 2317 (2007).
35. S. Kahra, G. Leschhorn. Controlled delivery of single molecules into ultra-short laser pulses: a molecular conveyor belt, (submitted 2011).

A.2 Controlled delivery of single molecules into ultra-short laser pulses: A molecular conveyor belt. *Accepted for publication in Nature Physics*

Controlled delivery of single molecules into ultra-short laser pulses: a molecular conveyor belt

Steffen Kahra^{1†}, Günther Leschhorn^{1†}, Markus Kowalewski³, Agustin Schiffrin¹, Elisabeth Bothschafter^{1,4}, Werner Fuß¹, Regina de Vivie-Riedle³, Ralph Ernstorfer^{1,4,5}, Ferenc Krausz^{1,3}, Reinhard Kienberger^{1,4}, Tobias Schaetz^{1,2}

¹Max-Planck-Institut für Quantenoptik, Hans-Kopfermann-Str.1, 85748 Garching, Germany

²Albert-Ludwigs-Universität Freiburg, Hermann-Herder-Str.3a, 79104 Freiburg, Germany

³Ludwig-Maximilians-Universität München, 81377 München, Germany

⁴Fakultät für Physik, Technische Universität München, 85748 Garching, Germany

⁵Fritz-Haber-Institut der Max-Planck-Gesellschaft, Faradayweg 4-6, 14195 Berlin, Germany

[†]These authors contributed equally to this work.

Trapping and laser cooling in atomic physics permits controlling single particles and their dynamics at the quantum mechanical level in background-free environment. The field of ultra-short and intense laser pulses provides the ultimate control of electromagnetic fields allowing the imaging of matter and its dynamics on atomic scales, in principle down to a single molecule or virus[1]. However, current methods fall short in efficiency to overlap each target with a pulse of comparable spatial extension. Here we combine the two areas of research by demonstrating a deterministic molecular conveyor belt. It is formed of electric trapping potentials that deliver individual diatomic molecular ions at millikelvin temperatures and sub-micrometer positioning into few-femtosecond ultraviolet laser pulses. We initiate and probe the femtosecond dynamics in a single molecule by two subsequent pulses of variable delay and finally detect the molecule and its response with 100% efficiency. This experiment might become key for investigations of individual molecular ions requiring the ultimate control and efficiency. For example, the new generation of few-femtosecond X-ray laser sources is predicted to permit imaging of single molecules with atomic resolution since the pulses are sufficiently short to outrun the radiation damage[1, 2]. To provide the molecule with the required amount of X-ray photons, the pulse must be focused down to (sub-)micrometer extension and still hit the target. Our scheme may overlap each pulse with its molecule of choice which can be prepared and replaced at the repetition rate of the laser source. This is predicted to establish a new approach to structural determination by scattering X-rays.

To achieve sufficient gain of the coherent scattering signal, state-of-the-art techniques using low-intensity X-ray sources require myriads of identical molecules crystallized to a macroscopic probe[2]. Currently, the prerequisite of crystallization is the major shortfall of these techniques[3]. This is mainly because many biological molecules, such as most of the membrane proteins, are difficult or impossible to crystallize. In addition, a lot of samples are one-of-a-kind, rare or charged. Diffraction experiments with low-intensity sources on non-crystalline or ultimately single molecules are substantially limited by radiation damage[2, 3]. That is, accumulating a sufficient number of scattering events takes long exposures during which the huge total radiation dose alters the nuclear skeleton or even destroys the sample-molecule(s). Furthermore, long exposure excludes the temporal resolution required to analyze short-lived intermediate products or fast structural changes by pump-probe schemes.

Intense X-ray pulses of a few femtoseconds (10^{-15} s) duration are predicted to overcome these limitations[1] and first experimental evidence was reported[4–6]. The application of the overdose within a sufficiently short exposure should allow to record useful structural information before the radiation degrades the sample-molecule. The required number of photons to image

a single molecule amounts to the order of 10^{13} per pulse, focused to the size of a large molecule (approximately 0.1 micrometer[1]). At large laser facilities these beam parameters are becoming accessible[5–7]. For example, pulses from the hard X-ray free-electron laser, Linac-Coherent-Light-Source (LCLS), were focused to micrometer sized spots at tens of Hertz repetition rate to approach the required brilliance[5]. Recently, co-author R.K. and colleagues measured the pulse duration at LCLS of a few femtoseconds and have indication that pulses around or shorter than 1 fs are within reach (manuscript in preparation). The challenge is to deliver the ultimate target, a single molecule of choice, deterministically prepared but well isolated from the environment, that can be positioned reliably within each of the pulses of (sub-)micrometer extension and that is replaceable at the repetition rate of the laser source, as illustrated in FIG. 1.

Conventional schemes to achieve a high flux of molecules in vacuum, for example by Electrospray Ionization (ESI)[8, 9], suffer from the molecules being released at random instants, diluted by free expansion and additionally by mutual Coulomb repulsion, in the case of molecular ions. These sources by their own still defy the desired level of control. Ion traps, in contrast, provide

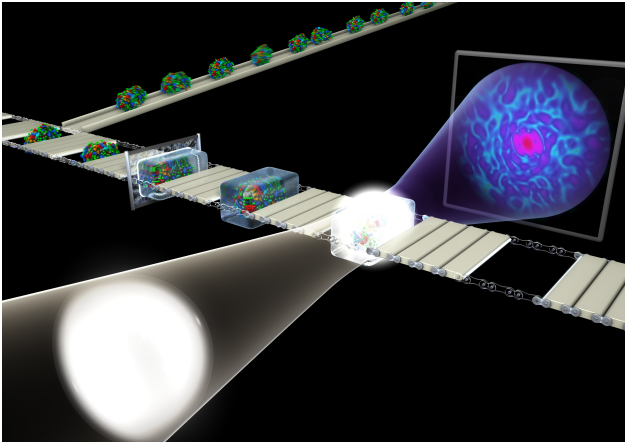


FIG. 1. **Schematic illustration of the setup combining the fields of single particle preparation on the quantum level and single, ultra-short laser pulses.** Generic single molecular ions hover in electric potential wells forming kind of a conveyor belt, visualized here by its mechanical analog. They get container-free embedded with (sub-)micrometer precision into a crystal of laser cooled atomic ions. The trapped molecular ion can subsequently be analyzed, for example, exploring its structure or dynamics. To match the overlap of the analysis-pulses (focused for highest intensity) and the molecules they have to be precisely synchronized in time and space. Spatial precision better than $1\ \mu\text{m}$ and additionally repetition rates of the order of hundred per second are required. Our experimental setup (see also FIG. 2B) is shown to span such a conveyor belt allowing for the accurate control of the internal and external degrees of freedom. To challenge our scheme with few-femtosecond pulse durations, we choose MgH^+ yielding sufficiently fast molecular wave packet dynamics. A straightforward substitution of the target by mid-sized molecules such as protonated Schiff base of retinal would allow to investigate, for example, ultra-fast, light-induced photochemistry of isolated molecules. Molecules up to lysozyme (as depicted) might be provided for the envisioned structural investigations by the diffraction pattern of each X-ray pulse (symbolized in white - temporal delay not to scale).

unique control capabilities for charged particles reaching the quantum limits. They tightly confine and store an atomic ion for days in nearly background-free environment (ultra-high vacuum) and protect it against external disturbance. Their internal (electronic) and external degrees of freedom are controlled to a level that allows both, the observation and the deterministic exploitation of most fragile quantum effects. Examples are superposition states and entanglement for the most accurate optical clocks[10], or quantum computing[11] and teleportation experiments[12]. Laser cooling techniques prepare atomic ions down to the quantum mechanical ground state of motion in the confining potential. Changing the related electric fields allows transferring ions between separable traps at rates of kilohertz and still controlling their absolute position on the sub-10 nm level[12]. A molecular ion of suitable charge to mass ratio can be em-

bedded into an ensemble of directly laser cooled atomic ions that provides a “sympathetic” heat sink[13, 14]. The absolute position of the molecular ion can be measured by detecting the fluorescence light of the atomic ions with an accuracy down to half of its wavelength. Large ensembles of protonated proteins with a mass $m \approx 12400$ amu at charge state $Z = 12$ have been shown to be sympathetically cooled in a radio-frequency trap[14]. By combining these skills for container-free handling we show that a single molecule comes close to the ultimate target described above.

In this paper we present a time resolved experiment on individual molecular ions. To prove our envisioned scheme functional before applying X-ray pulses of highest intensity, we require a molecule providing internal dynamics on the timescale of a few femtoseconds. We therefore sympathetically cool the diatomic molecule MgH^+ featuring correspondingly fast vibrational dynamics with the atomic ion Mg^+ . We perform a pump-probe experiment with two few-cycle ultraviolet pulses. The first pulse triggers an electronic excitation, the second probes the dynamics of the molecular wave packet. This protocol faces identical demands on the handling of the target as for the proposed diffraction experiments using X-ray pulses.

Our experimental setup is depicted in FIG. 2. It includes an ESI source (required for future experiments on generic molecules, see methods summary), followed by a radio frequency (rf) quadrupole[14], selecting a particle distribution with specific Z/m . We join an additional rf-guide of 48 cm length to the filter consisting of electrodes at a mutual distance of ≈ 2 mm that are operated at a frequency of $\Omega_{\text{rf}}/2\pi \approx 7$ MHz. The guide yields tight radial confinement while passing the molecule through two vacuum chambers ($1\ \text{eV}$ potential depth for $\text{MgH}^+ \sim Z^2/m$) and related oscillation frequency $\omega_{\text{radial}}/2\pi \approx 500$ kHz ($\sim Z/m$). Two pairs of ring shaped DC electrodes at the front and at the rear end of the guide can be used to control the transfer of the molecule at 100% efficiency from the preparation chamber to its requested destination within $\approx 200\ \mu\text{s}$. The last pair is alternatively used to turn the section at the rear end of the guide into an ion trap ($\omega_{\text{axial}}/2\pi \approx 30$ kHz ($\sim \sqrt{Z/m}$)) in the ultra-high vacuum (2×10^{-10} mbar). There, several sufficiently laser cooled atomic ions freeze out into ordered structures, so called Coulomb crystals[16]. Their lattice constants amount to the order of $10\ \mu\text{m}$ and each ion is pinned to an individual site. We accomplish Doppler laser cooling with a single turn key laser system[17] on a dipolar allowed, closed transition $S_{1/2} \rightarrow P_{3/2}$ (natural line width $\Gamma/2\pi \approx 43$ MHz) leading to final temperatures of ≈ 1 mK. After transferring the molecule, we embed it into the Coulomb crystal of atomic ions by sympathetically cooling[13] to similar temperatures within milliseconds[18]. Cooling of the internal degrees of freedom of the molecule can be implemented via buffer-gas[19]. We currently exploit comparatively slow (seconds) black body assisted radiative cooling[20]. In equi-

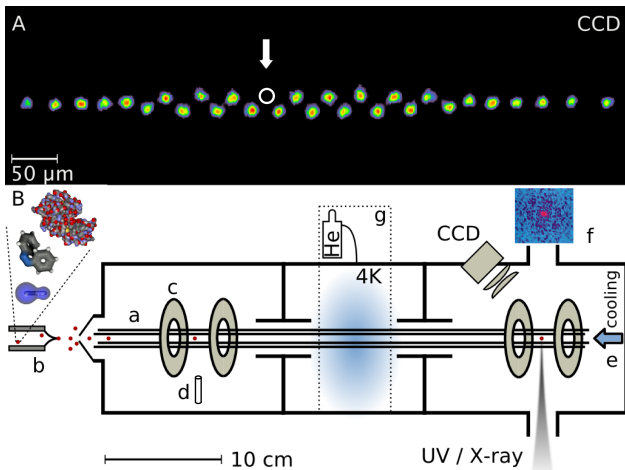


FIG. 2. **Preparation of a single molecular ion as a cold, micro-positioned target.** (A) CCD fluorescence image of atomic ($^{24}\text{Mg}^+$) ions, laser-cooled to form a Coulomb crystal in a linear radio frequency trap. All ion positions are defined to better than $1\ \mu\text{m}$. At the precisely localizable site of the missing bright spot (indicated by a white circle), the molecular ion (MgH^+) is sympathetically cooled by the adjacent, directly laser-cooled atomic ions. (B) Tabletop experimental implementation of the conveyor belt of FIG. 1. Molecular ions can be injected directly into the radio frequency (rf) quadrupole guide (a) by Electrospray Ionization (b) or breded by a photochemical reaction. Ring electrodes (c) at the front and the end of the rf-guide allow for transfer and trapping of the molecule, respectively. An oven (d) produces a thermal beam from which atomic ions can be loaded into the guide/trap by photo-ionization. These are laser cooled (e) to form a sympathetic heat sink for the molecule and to freeze into a Coulomb crystal with the molecule embedded on a lattice site for its precise localization (see (A)). Our experiment is performed with few-femtosecond ultraviolet laser pulses. However, also intense and short X-ray pulses are envisioned to be focused tightly ($< 1\ \mu\text{m}$) onto the single target molecule, predicted to yield diffraction patterns providing atomic resolution (f)[1]. The apparatus is designed to include an additional buffer gas cooling stage (g) and laser-induced, field-free alignment[15].

librium with the thermal background at room temperature, our molecular ion reaches 99.9% occupancy of the vibrational ground state.

The position of the molecular ion can be deduced from the fluorescence light of the atomic ions detected by a CCD camera within milliseconds. The selected molecular ion[21] appears as “dark” spot within the crystalline structure (see FIG. 2A). It can be localized via interpolation between the neighboring “bright” ions to the resolution of the imaging system at the emitted wavelength ($\lambda = 280\ \text{nm}$; motional amplitude for chosen parameters $< 0.25\ \mu\text{m}$). Subsequently, the molecule can be positioned in the focus of the laser, as illustrated in FIG. 1.

MgH^+ is a well suited test candidate, since its vibrational dynamics on the few-femtosecond timescale is

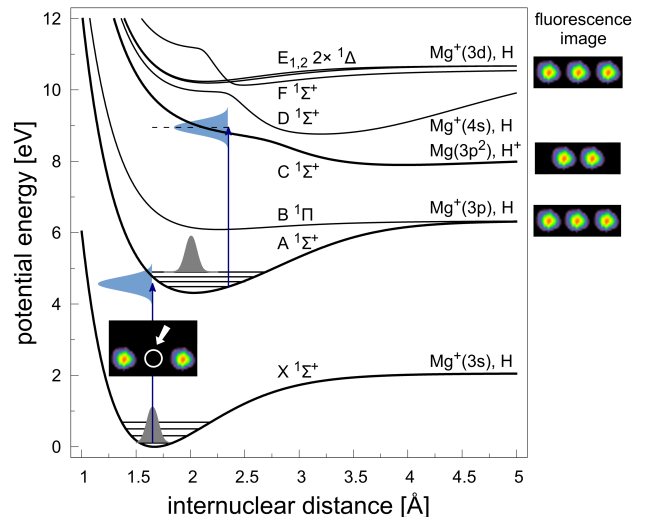


FIG. 3. **Schematic for our experiment on a deterministically positioned single molecule, based on the ab initio potential energy curves of the electronic states involved.** A molecular ion (MgH^+ , indicated by the white circle in the lowest of the four insets depicting fluorescence images of atomic ions) is prepared in the vibrational and electronic ground state (X). Arrows and vertical Gaussian profiles indicate identical ultraviolet pump and probe pulses (4 fs, 285 nm). The spectrally broad pump pulse creates a vibrational wave packet oscillating with 30 fs period in the electronically excited state (A). Its motion is mapped onto the probability for the probe pulse to excite the molecular ion in a second step to the repulsive state (C). Dissociation via (C) results in loss of both product particles.

accurately treatable by theory. Additionally, molecular MgH^+ ions can be generated in the photochemical reaction $\text{Mg}^+ + \text{H}_2 \rightarrow \text{MgH}^+ + \text{H}$ after photoionization of atomic magnesium from a thermal beam in the preparation chamber[22]. However, this experiment requires pulses in the ultraviolet regime. We therefore connected our conveyor belt to an evacuated beam line, providing 100 nJ pulses with a spectrum centered at 285 nm, about 4 fs[23] duration and 117 Hz repetition rate. Each pulse is reflected off a displaceable split mirror, generating two replica of variable delay. Since no other radiation damage than dissociation occurs in the current experiment, we can afford an extended focus of $50\ \mu\text{m}$ leading to an intensity of twice $160\ \text{GW}/\text{cm}^2$ and the identical molecule can be irradiated several times.

The pump-probe scheme is illustrated in FIG. 3. It shows the ab initio potential energy curves of the molecule as a function of the internuclear distance calculated by state-of-the-art quantum chemical methods (see supplementary information). A pump pulse creates a vibrational wave packet oscillating with a period of approximately 30 fs in the potential of the electronically excited, bound state A. Part of this population can be further excited to the repulsive state C by the probe pulse. A molecular ion in this state dissociates accord-

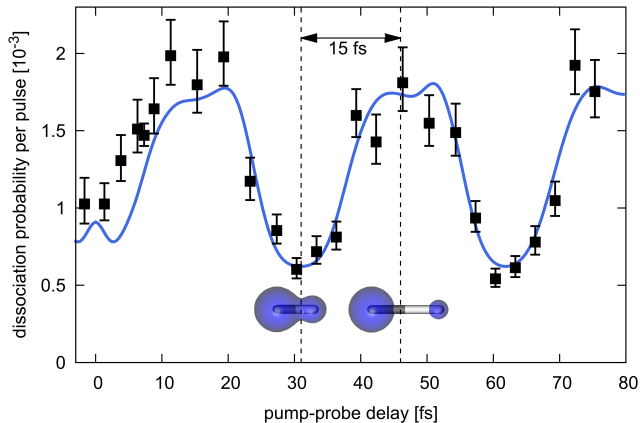


FIG. 4. **Vibrational motion of molecules derived from the dissociation of single molecules as a function of pump-probe delay for 4 fs laser pulses.** Copies of the molecule were repeatedly prepared by the scheme presented in FIG. 1 and FIG. 2, and spatially overlapped with the pulses. The dissociation probability in channel (C) (see FIG. 3) is modulated with a period of 30 femtoseconds. An illustration of the two related electronic probability densities of our molecular ion at the classical turning points is given. Each data point corresponds to the statistical average ($\pm 1\sigma$) of experiments with in total between 50 and 108 molecular ions. Solid line: Result of our theoretical model for the experimental parameters described in the text.

ing to $\text{MgH}^+ \rightarrow \text{Mg} + \text{H}^+$ as proposed for picosecond laser pulses in reference [24]. In this particular reaction channel neither of the two dissociation products remains trapped. The breaking of the chemical bond is signaled by the disappearance of a non-fluorescing dark spot, remarkably detectable with an efficiency of 100% (see FIG. 3). Owing to the slope of the potential energy curve C, the probability for the transition driven by the probe pulse depends on the position of the vibrational wave packet in state A. Described in a simplifying picture, the mean photon energy mismatches with the transition at the wave packet's inner turning point whereas it overlaps well at the outer turning point. That way, the stretching motion periodically modulates the dissociation probability. We vary the pump-probe delay for repeatedly, identically prepared single molecules and derive the binary information whether the molecule remained on its lattice site or dissociated by evaluating fluorescence images. For the given parameters, on average 1 in 1000 ideally matched pump-probe pulse pairs triggers the dissociation. Finally, we average over many dissociation events at each pump-probe-delay setting. From that, we deduce the mean dissociation probability per pulse and its modulation in dependence of the pump-probe delay. Since the pulse duration is shorter than the timescale of the dynamics, we can not only detect the reaction, as proposed in reference [24], but its dynamics within a single molecule and a fidelity close to 100%.

Figure 4 shows the main results of the experiment.

In total, 2477 individual molecules contribute approximately equally to the 26 data points. The theoretical prediction is depicted as a solid line. Here, the dissociation probability is clearly modulated at a period of approximately 30 femtoseconds due to the molecular ion's vibration. Its modulation in time as well as the absolute amplitude of the probability to dissociate is in good agreement with our experimental data. The slight deviation from a sinusoidal modulation in the experimental data is reproduced by the theoretical result and can be attributed to the crosstalk to adjacent potential energy curves (mainly (D), see FIG. 3).

The recovery of the full amplitude after the second oscillation period provides already strong evidence for long coherence times due to minimal environmental disturbances. This is different from intriguing experiments localizing molecules in polymer films[25]. The absence of any decohering environment (solvent or carrier) also explains the good agreement of the experimental data and theory already at zero pulse delay. Overlapping and interfering pump and probe pulses tend to conceal the immediate response of the molecule, for example, by polarizing the environment. Container-free handling of the isolated molecules therefore allows to follow singular processes limited only by the pulse duration.

In the future, the presented scheme will be applied to prototype molecules already provided by our ESI-source. Protonating mid-sized molecules, such as azobenzene and Schiff base of retinal[26], show light induced cis-trans isomerization, a process on the 100 fs timescale of fundamental interest. Experiments on isolated molecular ions would eventually allow to precisely evaluate calculations based on subtle quantum mechanical models that do not take environmental effects into account. Furthermore, exploring molecular ions might be advantageous since biological molecules occur charged in nature[26, 27]. Selecting hydrated molecules ($\approx 10 \text{ H}_2\text{O}$) can simulate a natural surrounding and may stabilize the tertiary structure against radiation damage[9]. If a higher repetition rate was required, a reservoir of many (10 to 100) identical molecules within one Coulomb crystal could be scanned on its individual lattice sites. We could implement the reservoir within a storage ring for molecular ions[28], further extending this approach to crystallized (molecular) ion beams[29]. In our current apparatus we allocate $^{24}\text{Mg}^+$ and $^{138}\text{Ba}^+$, giving already access to a variety of molecular ions, ranging from diatomic via mid-size molecules like retinal[26] ($m \approx 300$ Dalton) to bio-functional organic molecular ions such as cytochrome c ($m \approx 12400$ Dalton) at $Z = +12$ or lysozyme ($m \approx 14000$ Dalton) close to its natural charge state[27] $Z = +8$. A straight forward extension of our method (see methods summary) might allow to follow the development to reach for substantially smaller Z/m or even single viruses[9] and the required waists of 0.1 micrometers[1, 30] and below. The motional amplitude is limited by the quantum mechanical constraint of Heisenberg's uncertainty principle (tens of nanometers for both,

atomic and molecular ions). In addition, the beam parameters could be probed with nanometer resolution using a dedicated (molecular) ion as a sensor.

In the abstract of reference [1] the authors predict that "...ultrashort, high-intensity X-ray pulses from free-electron lasers that are currently under development, in combination with container-free sample handling methods based on spraying techniques, will provide a new approach to structural determination with X-rays." The demonstrated molecular conveyor belt provides the required (sub-)micrometer positioning and the directly related opportunity to reduce the waist of the pulses from 30-10 μm down to 1 μm , allowing to increase the num-

ber of valuable X-ray photons by two to three orders of magnitude, exploiting each single pulse and target, respectively.

The described methodology could be further exploited for involved applications, such as sequencing charged reaction products or fragments and keeping them for subsequent investigation. The identical deterministic methodology would substantially enhance the efficiency of X-ray holography[4] where the molecule and a reference target must be hit simultaneously. Furthermore, the investigation of structural changes during (photo-)chemical reactions not only of one, but between (charged and uncharged) molecules can be envisioned.

-
- [1] Neutze, R., Wouts, R., van der Spoel, D., Weckert, E. & Hajdu, J. Potential for biomolecular imaging with femtosecond x-ray pulses. *Nature* **406**, 752–757 (2000).
- [2] Webster, G. & Hilgenfeld, R. Perspectives on single molecule diffraction using the x-ray free electron laser. *Single Molecules* **3**, 63–68 (2002).
- [3] Henderson, R. The potential and limitations of neutrons, electrons and x-rays for atomic resolution microscopy of unstained biological molecules. *Quarterly Reviews of Biophysics* **28**, 171–193 (1995).
- [4] Chapman, H. N. *et al.* Femtosecond time-delay x-ray holography. *Nature* **448**, 676–679 (2007).
- [5] Young, L. *et al.* Femtosecond electronic response of atoms to ultra-intense x-rays. *Nature* **466**, 56–61 (2010).
- [6] Seibert, M. M. *et al.* Single mimivirus particles intercepted and imaged with an x-ray laser. *Nature* **470**, 78–81 (2011).
- [7] Chapman, H. N. *et al.* Femtosecond x-ray protein nanocrystallography. *Nature* **470**, 73–77 (2011).
- [8] Yamashita, M. & Fenn, J. B. Negative ion production with the electrospray ion source. *The Journal of Physical Chemistry* **88**, 4671–4675 (1984).
- [9] Marklund, E. G., Larsson, D. S. D., Spoel, D. v. d., Patriksson, A. & Caleman, C. Structural stability of electrosprayed proteins: temperature and hydration effects. *Physical Chemistry Chemical Physics* **11**, 8069–8078 (2009).
- [10] Chou, C. W., Hume, D. B., Rosenband, T. & Wineland, D. J. Optical clocks and relativity. *Science* **329**, 1630–1633 (2010).
- [11] Home, J. P. *et al.* Complete methods set for scalable ion trap quantum information processing. *Science* **325**, 1227–1230 (2009).
- [12] Barrett, M. D. *et al.* Deterministic quantum teleportation of atomic qubits. *Nature* **429**, 737–739 (2004).
- [13] Molhave, K. & Drewsen, M. Formation of translationally cold mgh^+ and mgd^+ molecules in an ion trap. *Physical Review A* **62**, 011401 (2000).
- [14] Offenberg, D., Zhang, C. B., Wellers, C., Roth, B. & Schiller, S. Translational cooling and storage of protonated proteins in an ion trap at subkelvin temperatures. *Phys. Rev. A* **78**, 061401 (2008).
- [15] Lee, K. F., Villeneuve, D. M., Corkum, P. B., Stolow, A. & Underwood, J. G. Field-free three-dimensional alignment of polyatomic molecules. *Phys. Rev. Lett.* **97**, 173001 (2006).
- [16] Birkel, G., Kassner, S. & Walther, H. Multiple-shell structures of laser-cooled mg ions in a quadrupole storage ring. *Nature* **357**, 310–313 (1992).
- [17] Friedenauer, A. *et al.* High power all solid state laser system near 280 nm. *Applied Physics B: Lasers and Optics* **84**, 371–373 (2006).
- [18] Schiller, S. & Lämmerzahl, C. Molecular dynamics simulation of sympathetic crystallization of molecular ions. *Physical Review A* **68**, 053406 (2003).
- [19] Gerlich, D. & Borodi, G. Buffer gas cooling of polyatomic ions in rf multi-electrode traps. *Faraday Discussions* **142**, 57–72 (2009).
- [20] Smith, I. W. M. *Low Temperatures And Cold Molecules* (Imperial College Press, 2008).
- [21] Paul, W. Electromagnetic traps for charged and neutral particles. *Reviews of Modern Physics* **62**, 531–540 (1990).
- [22] Kjægaard, N., Hornekær, L., Thommesen, A., Videsen, Z. & Drewsen, M. Isotope selective loading of an ion trap using resonance-enhanced two-photon ionization. *Applied Physics B: Lasers and Optics* **71**, 207–210 (2000).
- [23] Graf, U. *et al.* Intense few-cycle light pulses in the deep ultraviolet. *Optics Express* **16**, 18956–18963 (2008).
- [24] Jørgensen, S., Drewsen, M. & Kosloff, R. Intensity and wavelength control of a single molecule reaction: Simulation of photodissociation of cold-trapped mgh^+ . *Journal of Chemical Physics* **123**, 094302 (2005).
- [25] Brinks, D. e. a. Visualizing and controlling vibrational wave packets of single molecules. *Nature* **465**, 905–908 (2010).
- [26] Hamm, P. *et al.* Femtosecond spectroscopy of the photoisomerisation of the protonated schiff base of all-trans retinal. *ChemPhysChem* **263**, 613–621 (1996).
- [27] Kuehner, D. E. *et al.* Lysozyme net charge and ion binding in concentrated aqueous electrolyte solutions. *The Journal of Physical Chemistry B* **103**, 1368–1374 (1999).
- [28] URL http://www.xfel.eu/sites/site_xfel-gmbh/content/e63594/e63599/e81234/e65128/e76474/sqs-wg-ii-report_eng.pdf.
- [29] Schätz, T., Schramm, U. & Habs, D. Crystalline ion beams. *Nature* **412**, 717–720 (2001).
- [30] Boutet, S. & Williams, G. J. The coherent x-ray imaging (cxi) instrument at the linac coherent light source (lcls). *New Journal of Physics* **12**, 035024 (2010).

METHODS SUMMARY

Extension to biologically relevant molecules Radio-frequency (rf) traps have recently been shown to be suitable to store large ensembles of bio-functional molecules. The protein cytochrome c ($m \sim 12400$ amu; $Z/m \sim 1/1000$) has been confined and sympathetically cooled using a $^{138}\text{Ba}^+$ Coulomb crystal [14].

However, simultaneously trapping a large ensemble of biologically relevant molecules of comparatively small Z/m leads to a substantially reduced coupling to their heat sink because of an increased mutual distance [14]. In contrast, for ions of similar charge and mass, a single atomic ion is sufficient to sympathetically cool and crystallize >10 molecular ions, because sufficient coupling is provided at mutual distances of $d \sim 10 \mu\text{m}$.

Our apparatus is capable of providing such an ensemble as the initial reservoir by its Electro-Spray ionization source [8][9] and the recently demonstrated efficient photoionization scheme for barium atoms [1Meth]. Individual ions have been already separated deterministically from a larger ensemble using the light pressure force and voltages on knife-electrodes [12].

Since the molecular conveyor belt can deliver one molecular- and a single atomic ion, the dilution by space charge is reduced and the stiff confinement allows focusing of the different species sufficiently close to each other to again guarantee efficient cooling and precise positioning. For example, an rf-voltage of 1 kV results in a radial secular frequency of $2\pi \cdot 1.5$ MHz for $^{138}\text{Ba}^+$ and $2\pi \cdot 200$ kHz for cytochrome c at charge state $Z=+12$ [20]. By providing a weaker axial confinement ($2\pi \cdot 400$ kHz and $2\pi \cdot 150$ kHz for $^{138}\text{Ba}^+$ and cytochrome c, respectively) both particles will be forced on the trap axis at a mutual distance of again $d \sim 10 \mu\text{m}$. For these parameters and an equilibrium temperature that could reach up to 20 times the Doppler-cooling limit ($T_{\text{Doppler,barium}} \sim 0.5$ mK), the motional amplitudes would still remain restricted to the order of 0.1 micrometer.

Reaching towards even larger molecules ($> 10^5$ amu) or trying to cool the target to the motional ground state will require to adjoin a tighter trapping section, such as already realized in reference [12][2Meth]. For example, choosing $Z/m = 10/10^5$ requires applying an rf-amplitude of 3 kV at $\Omega_{\text{rf}} = 2\pi \cdot 150$ MHz and a distance of the trap center to the electrodes of $100 \mu\text{m}$ [12] to achieve $d \sim 5 \mu\text{m}$. By potentially adding a few atomic ions, to further increase the coupling, conventional Doppler cooling would suffice for positioning within the $0.1 \mu\text{m}$ scale while already established, sub-Doppler cooling schemes might even reach the motional ground state [3Meth].

[1Meth] Leschhorn, G., Hasegawa, T., Schaetz, T. Efficient photoionization for barium ion trapping using a dipole-allowed resonant two-photon transition *ArXiv e-*

prints:1110.4040 (2011).

[2Meth] Schaetz, T. et al. Towards (scalable) quantum simulations in ion traps *Journal of Modern Optics* **54**, 2317-2325 (2007).

[3Meth] Barrett, M. D. et al. Sympathetic cooling of 9Be^+ and 24Mg^+ for quantum logic *Phys. Rev. A* **68**, 042302 (2003).

SUPPLEMENTARY INFORMATION

The wave packet dynamics is derived by solving the time dependent Schrödinger equation. The potential energy curves provide the basis for the quantum dynamical calculations of the pump-probe process. The eight lowest lying singlet states on the CAS(12/10)/MRCI/ROOS level of theory are derived using the multi reference configuration interaction method provided by MOLPRO 2006.1 [1Supp] with the results being in good agreement with the theoretical prediction presented in reference 24. A Chebychev propagation scheme [2Supp] is used for numerically solving the time dependent Schrödinger equation for the nuclei under influence of the pump- and probe laser fields. The specific experimental situation gives rise to incoherent vibrational heating by repeated excitations followed by spontaneous emissions which is taken into account by linking the wave packet propagation with a rate equation model including the Einstein coefficients for spontaneous emission from the electronic state A as well as from the vibrational states in X (20 vibrational states of the electronic X and A states). Furthermore, we feed our model with the experimental parameters of the pulses, namely the repetition rate (and the phase function of the mirrors), to obtain a highly realistic model.

[1Supp] H.-J. Werner and P. J. Knowles and R. Lindh and F. R. Manby and M. Schütz et al., <http://www.molpro.net>.

[2Supp] H. Tal-Ezer and R.J. Kosloff, *J.Chem.Phys.* **81**, 3967-3971 (1984).

ACKNOWLEDGMENTS

Financial support is gratefully acknowledged by the Deutsche Forschungsgemeinschaft, the DFG cluster of Excellence: Munich Centre for Advanced Photonics, the International Max Planck Research School on Advanced Photon Science (IMPRS-APS) and the EU research project PICC: The Physics of Ion Coulomb Crystals, funded under the European Communities 7th Framework Programme. The authors want to thank J. Britton, W. Schmid, C. Hackenberger, J. Bayerl, M. Schulze, T. Dou and C. Kerzl for their contributions and Prof. Neusser for support of a cw-cooling laser.

A.3 Efficient photoionization for barium ion trapping using a dipole-allowed resonant two-photon transition. *Submitted to Appl. Phys. B, ArXiv:1110.4040*

Efficient photoionization for barium ion trapping using a dipole-allowed resonant two-photon transition

G. Leschhorn · T. Hasegawa · T. Schaetz

Abstract Two efficient and isotope-selective resonant two-photon ionization techniques for loading barium ions into radio-frequency (RF)-traps are demonstrated. The scheme of using the strong dipole-allowed transition $6s^2\ ^1S_0 \rightarrow 6s6p\ ^1P_1$ at $\lambda = 553\text{ nm}$ as a first step towards ionization is compared to the established technique of using a weak intercombination line ($6s^2\ ^1S_0 \rightarrow 5d6p\ ^3D_1$, $\lambda = 413\text{ nm}$). An increase of two orders of magnitude in the ionization efficiency is found favoring the transition at 553 nm. This technique can be implemented using commercial all-solid-state laser systems and is expected to be advantageous compared to other narrowband photoionization schemes of barium in cases where highest efficiency and isotope-selectivity are required.

1 Introduction

Ion traps have become an important tool in a growing number of fields, like precision measurements of fundamental constants[1], testing general relativity[2],

frequency standards[3], quantum information processing[4,5], quantum simulation[6,7] or mass spectrometry[8]. During the last decade, the state-of-the-art loading of ion traps has changed from electron beam bombardment to photoionization of neutral atoms inside the trapping region. The main reasons are a higher efficiency and the isotope selectivity of most of the photoionization schemes presented so far. Additional beneficial effects, like strongly reduced static charging of dielectrics[9], lower motional heating rates of the ions after loading due to the suppression of patch potentials[10] and easier loading of surface-electrode traps with a substantially reduced trap depth[11] is of great advantage in the laboratories. Loading of Paul traps by narrowband cw photoionization[12] has been achieved by several groups on a growing number of atomic species (Ba[13,14], Mg[15], Ca[9,16,17], Yb[18], Sr[19,20], In[21] etc.). Several of these schemes have been applied to photoionization loading techniques that substitute the resistively heated atomic oven as source of neutral atoms. Instead, non-evaporating sources, for instance laser ablation targets [22] or magneto-optical traps[23] are used. These techniques additionally increase the efficiency and the advantages of photoionization loading and were mainly developed to load micro-structured surface traps. Furthermore, non-isotope selective loading schemes, e.g. using ultra-short pulses[24] or laser ablation[25] have been realized which share the advantage of being applicable to most laser-cooled ion species with a further increased efficiency.

In this paper, a novel loading technique for barium by isotope-selective photoionization using a dipole-allowed two-photon transition is demonstrated. A substantial increase in ion loading efficiency compared to established schemes[26] is found. The presented technique promises to provide substantial advantages in experiments that depend on maximizing the efficiency or

G. Leschhorn · T. Schaetz
Max-Planck-Institut for Quantum Optics
Hans-Kopfermann-Str.1
85748 Garching, Germany
Tel.: +49 89-32905-199
Fax: +49 89-32905-200
E-mail: tobias.schaetz@mpq.mpg.de

T. Schaetz
Albert-Ludwigs-Universität Freiburg
Hermann-Herder-Str. 3a
79104 Freiburg, Germany

T. Hasegawa
Faculty of Science and Technology,
Department of Physics, Keio University
3-14-1 Hiyoshi, Kohoku-ku
Yokohama 223, Japan

on a fast, controlled and minimal invasive reloading of ions.

2 Experiment

The ion trap used for the experiments presented in this paper consists of four cylindrical, gold plated copper rods of 2 mm diameter for radial confinement and two additional ring shaped electrodes around the rods providing axial confinement. The rods are arranged in a quadrupole configuration with a minimal distance of 1.12 mm between the trap center and the rod surface. An RF voltage at $\Omega_{\text{RF}} = 2\pi \times 6.8 \text{ MHz}$ is applied on the rod-electrodes. For $^{138}\text{Ba}^+$ the typically used radial secular frequency amounts to $2\pi \times 470 \text{ kHz}$. The 5 mm-thick ring electrodes that are centered around the trap axis are spaced by 15 mm and have an outer diameter of 24 mm and an inner diameter of 8 mm. A DC voltage applied to these ring electrodes leads to a static, nearly harmonic confinement potential along the axis of the linear Paul trap. The trap setup is housed in an ultra-high vacuum chamber at a pressure of $2 \times 10^{-8} \text{ Pa}$. Ions confined in the trap can be observed by imaging their fluorescence light during Doppler laser-cooling with a two-lens condenser on an electron-multiplying CCD camera. The magnification factor of the imaging system is approximately 10 and in conjunction with the trap parameters a single and up to approximately 50 individual ions that form a crystalline structure[27,28] can be observed.

Two different, resonant two-step excitations from the ground state $6s^2 1S_0$ of neutral ^{138}Ba to the continuum are used to produce singly ionized barium. Since in both cases, the first step is realized by a resonant transition and the isotope shifts are sufficiently large compared to the laser linewidth and the Doppler and power broadening of the transition, both photoionization schemes are isotope selective. Figure 1a) gives a summary of the relevant transitions of neutral barium. The first scheme requires two photons at 413 nm and is resonant with the weak intercombination line of the $6s^2 1S_0 \rightarrow 5d6p 3D_1$ transition. It was first demonstrated in[26] and will be labeled scheme A in the following. Despite the weak transition strength, this scheme benefits from the fact that light of only one frequency has to be provided that can be generated by a commercial and robust diode laser. Within the framework of this paper, this scheme has been realized for comparison. The 413 nm laser propagates on axis through the trap setup and is focused to a beam waist of $w_{413} = 440 \mu\text{m}$ ($1/e^2$ of intensity) at the trap center.

The second scheme, labeled scheme B, is based on the strong dipole allowed $6s^2 1S_0 \rightarrow 6s6p 1P_1$ transition

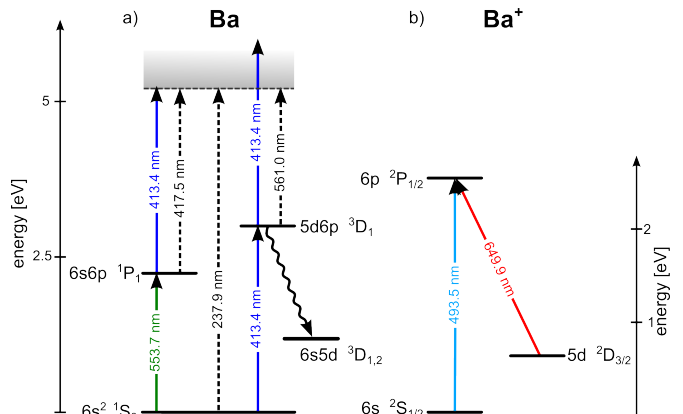


Fig. 1 Energy level scheme of a) neutral and b) singly ionized barium. Only the relevant levels and transitions are shown. Solid lines indicate experimentally realized transition, whereas dashed lines are only given for comparison. For coarse orientation, an energy scale is given for both cases. Photoionization of neutral barium is experimentally realized using two different schemes, that both use one resonant excitation followed by a non-resonant excitation into the continuum. In scheme B, a 553.7 nm photon excites the $1P_1$ state of $2\pi \times 18.9 \text{ MHz}$ natural linewidth, corresponding to 8.4 ns lifetime. Another photon at 413 nm excites the atom above the ionization threshold at 5.21 eV. The other ionization scheme (scheme A) works with two photons at 413 nm. The first one couples the ground state with the $5d6p 3D_1$ level. The second photon excites the electron deeply into the continuum. Note that in scheme A, the atoms are optically pumped (wavy line) to metastable states because the spontaneous emission rate to the states $6s5d 3D_{1,2}$ ($3.8 \times 10^7 \text{ s}^{-1}$ to $3D_1$, $1.9 \times 10^7 \text{ s}^{-1}$ to $3D_2$) is larger than that to the ground state ($1.5 \times 10^6 \text{ s}^{-1}$). Laser cooling on the singly charged ion is done on the Λ -system spanned by the $2S_{1/2}$, $2P_{1/2}$ and $2D_{3/2}$ levels, using photons near 493 nm and near 650 nm.

at 553 nm[29] to provide the first excitation. The second step from the $1P_1$ state to the continuum requires a wavelength $< 418 \text{ nm}$. Therefore, a 413 nm photon is sufficient and the laser of scheme A can be re-used. The laser beam for the first step is generated using a dye laser ($\sim 2\pi \times 500 \text{ kHz}$ linewidth) pumped by a frequency-doubled Nd:YAG laser. The 553 nm beam is focused to a waist of $230 \mu\text{m}$, overlapped with the 413 nm laser and propagates on axis through the trap.

Neutral barium atoms are provided by a thermal beam evaporated into the trapping region by resistively heating a tantalum tube of 1 mm inner diameter filled with barium. A heating current of 3.15 A results in an oven temperature at thermal equilibrium of approximately 600 K. To minimize Doppler broadening and to avoid overall Doppler shifts, a collimated atomic beam perpendicular to the photoionization lasers should be used, especially when a high grade of isotope selectivity is required. However, in the current setup, the atomic barium beam encloses an angle of approximately $100 \pm 5^\circ$ with the direction of laser propagation and

the transition frequency is thus red-shifted. The atomic beam is collimated by a 200 μm wide slit aperture at a distance of 4 cm from the trap axis in the direction perpendicular to the laser beam to ensure a minimal contamination of the trap electrodes with barium.

After ionization, the $^{138}\text{Ba}^+$ ions are laser-cooled on the $^2\text{S}_{1/2} \rightarrow ^2\text{P}_{1/2}$ transition at 493 nm. Figure 1b) shows the relevant electronic levels and transitions of singly ionized barium. The upper state decays with a branching ratio of approximately 3:1 into the ground and a metastable $^2\text{D}_{3/2}$ state[30]. The population in the D state is re-pumped to the P state by an additional laser at 650 nm to approach a closed cycling transition for laser cooling. In addition, a weak magnetic field (0.5 mT) perpendicular to the linear polarization of the laser beam is used to prevent dark states in the Zeeman manifold of the metastable state. The 493 nm light is produced by frequency-doubling a commercial narrow-linewidth (typically $2\pi \times 1$ MHz), tunable diode laser operating in Littrow configuration. Non-critical phase matching in a 10 mm-long KNbO_3 non-linear crystal is used to double the frequency of the light in a home-build second-harmonic generation external ring cavity[31]. The re-pumper light is directly produced by an external cavity diode laser. Both, cooling laser and repumper are overlapped and directed along the axis of the linear trap. Figure 2 shows a two-dimensional fluorescence image of a pure $^{138}\text{Ba}^+$ crystal containing 20 ions loaded into the trap via scheme B. The crystalline structure allows to accurately determine the number of ions of the specific barium isotope that is resonant with the Doppler cooling light. Throughout this paper loading rates of ions are determined by the evaluation of fluorescence images of ions confined in the Paul trap after a certain loading duration. The position and number of non-fluorescing ions within the crystalline structure, for example other barium isotopes or molecular ions can be determined by exploiting the inherent symmetry of Coulomb crystals.

3 Results

In Fig. 3, the ion loading rates are shown as a function of the detuning of the laser from the overall shifted atomic resonance (values in this section are given divided by 2π) coupling the ground and the intermediate state (first step laser) for scheme A and B (the powers of the laser beams providing the first and the second step amount to approximately 1 mW). The zero of the horizontal axis is calibrated by fitting the maximum of the loading rate. The solid lines represent the results of a model. Details of the model and discussions about

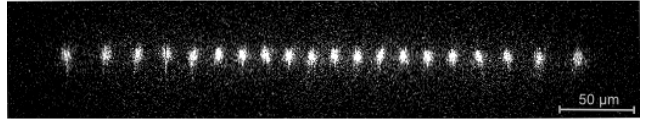
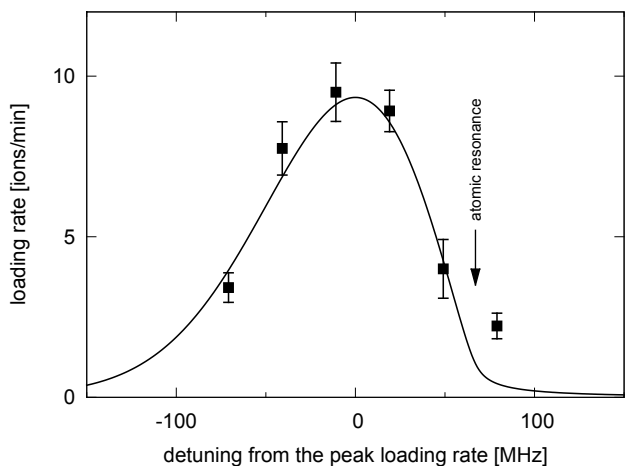


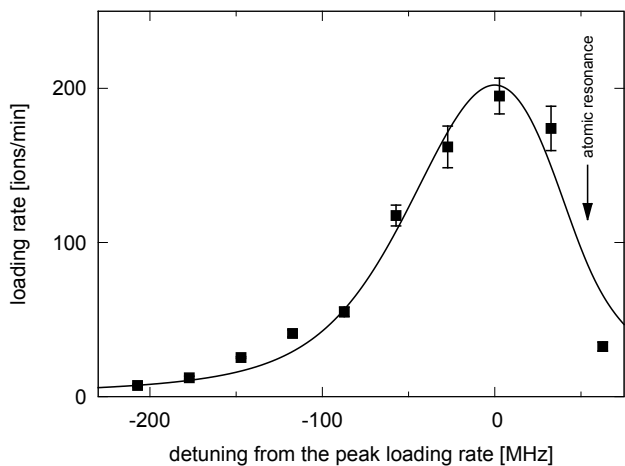
Fig. 2 Fluorescence image of 20 $^{138}\text{Ba}^+$ ions photoionized via a dipole-allowed transition (scheme B) and confined in the Paul trap. The ions are sufficiently laser cooled to form an ion Coulomb crystal. The number of confined particles and the trap parameters lead to a linear chain along the axis of the linear trap. A sufficiently large isotope shift of the transition relative to ^{138}Ba (^{137}Ba : $2\pi \times 215$ MHz; ^{136}Ba : $2\pi \times 128$ MHz; ^{135}Ba : $2\pi \times 259$ MHz; ^{134}Ba : $2\pi \times 143$ MHz[32]) in comparison with the observed Doppler- and power-broadened linewidth allows for a high probability for an isotopically pure crystal. An enhancement of the isotope selectivity can be achieved by a detuning towards lower frequency of the first step photoionization laser because ^{138}Ba has the lowest frequency of all stable isotopes. ^{138}Ba has a natural abundance of 71.7%. The probability to load an isotopically clean ion crystal consisting of 20 $^{138}\text{Ba}^+$ ions (as shown in the figure) with a non-isotope selective technique amounts to $0.717^{20} \approx 0.1\%$.

the broadening of the spectral line can be found in section 4. In the present setup, the atoms have a velocity component along the propagation direction of the laser beams, and hence the transition is Doppler-broadened and the maximum loading rate is Doppler-shifted towards lower frequencies. The center of the unshifted atomic resonance is indicated by an arrow in the figure.

The experimentally derived loading rates of scheme A (B) are shown in dependence of the laser power in Fig. 4 (A: blue circles and B: red squares). The data of scheme A (scheme B) show in principle a dependency on the square of the laser power at 413 nm (product of the laser powers at 413 nm and 553 nm), as to be expected in a process requiring two photons. In scheme B, the laser power of the second laser (413 nm) is kept equal to that of the first laser (553 nm) and therefore, the two schemes are comparable in terms of laser power. This is justified, because scheme B does in principle not require a separate laser system at 413 nm as chosen in the current experiment for simplicity, having the laser source of scheme A available. As shown in [13,14], the transition into the continuum does not have to be of narrow bandwidth (different to the first step in scheme A and B) and can be replaced by an incoherent light source. The solid lines present the results of the calculations based on the model. For the given parameters, the loading rate of scheme B is already about 40 times larger than that of scheme A. As already mentioned in section 2, the beam waists of the two lasers used in scheme B differ considerably at the trap center. Atoms can only be ionized when both required beams overlap, since the lifetime of the excited state is much shorter than the typical transit time of the atom through the beam (see also section 4 and the caption of Fig. 4).



(a) Scheme A



(b) Scheme B

Fig. 3 Loading rate of $^{138}\text{Ba}^+$ ions into the linear Paul trap as a function of the detuning of the laser used in the first ionization step to the peak loading rate. In 3(a), 3(b) the results for scheme A,B are shown respectively. In both cases, the laser powers were set to 1 mW. In the present setup, the atoms have a velocity component along the propagation direction of the laser and therefore, the peak of the loading rate is redshifted with respect to the atomic resonance indicated by an arrow. Note the asymmetry of the fitted model curve (black solid lines) in both photoionization schemes which is also due to the non-perpendicular orientation of the laser beam and atomic oven. The given errorbars represent statistical errors only.

Taking the currently not contributing amount of laser power within the 413 nm beam for scheme B into account, a lower bound for the additionally increase in ionization efficiency can be derived. For the comparison of the two schemes, a homogeneous atom density in the trap volume and an equal probability to trap an ionized atom is assumed. Implying a flat top profile for both beams of different waists would lead to an underestimation of scheme B in the comparison of effi-

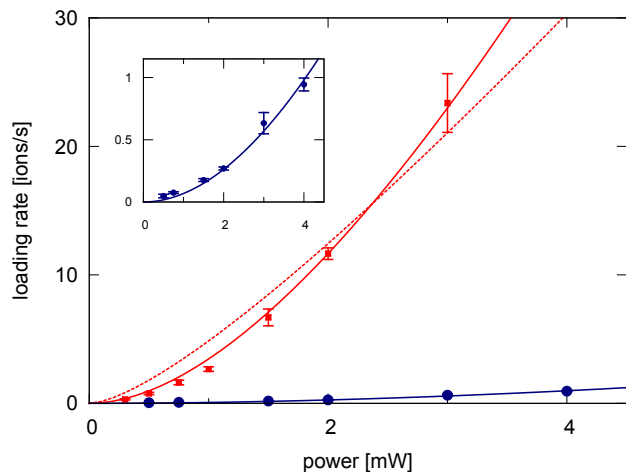


Fig. 4 Loading rate achieved with scheme A (blue circles) and B (red squares) as a function of the laser power used in the first ionization step. For scheme B, the power of the 553 nm and the 413 nm laser are kept equal. The dashed and solid curves represent the results of a calculation, assuming an atomic oven temperature of $T=600$ K. For the dashed red curve, the detuning of the first step laser is set to the frequency at which the loading rate is at its maximum and the angle θ between the laser and the atomic oven is taken to 98.3° . The remaining fitting parameter is the total efficiency α (see main text). The additional solid red curve shows the result of the fit with the model for scheme B when a detuning of +75 MHz from the peak loading rate is assumed. This might explain the discrepancy of the results from the model at low powers. The experimental data show that the ion loading rate in the experiment following scheme B is already about 40 times larger than following scheme A. Due to different beam waists used to realize scheme B, an additional increase of the efficiency by a factor of approximately 2.5 has to be considered, leading to a total enhancement of the efficiency by approximately two orders of magnitude compared to scheme A (for details see main text). The inset shows a close-up of the experimental data derived following scheme A and the corresponding curve fitted according to the model with the laser frequency set to the value where the loading rate is maximal.

ciencies by a factor of $(w_{553}/w_{413})^2 \approx 4$. Considering, more realistically, gaussian beams and assuming a concentric overlap, the measured ionization rate achieved via scheme B has to be multiplied at least with a factor of 2.5 for comparison with scheme A. This allows to derive an increase of the total efficiency via scheme B by two orders of magnitude.

In Fig. 5, the dependence of the loading rate on the power of the first laser (553 nm) is shown when the power of the second laser is kept again constant at 1 mW. Taking saturation effects into account allows to explain the deviation from a linear dependency of the laser power at 553 nm. The power dependence is similar to that described in reference [13] (Fig.6) and follows in principle a dependency on the square root of the power, as to be expected for an increased saturation of the

transition. The solid lines represent the results of the calculations based on the model and will be explained in detail in the next section.

4 Model

In the present setup, the Doppler broadening of the spectral lines is caused by the temperature T of the atomic ensemble in combination with the angle θ between the atomic and the laser beam. The derived spectral line of scheme A (Fig. 3(a)) has a full-width-at-half-maximum (FWHM) of 110 MHz. If this effect was caused by Doppler broadening at the given angle θ , the FWHM achieved via scheme B should amount to 82 MHz. The experimental result, however, shows an even larger width (Fig. 3(b)). This effect is caused by power broadening, because the transition dipole moment μ exploited in scheme B is much larger than in scheme A. This is in agreement with the non-linear dependency of the loading rate depicted as a function of laser power in Fig. 5. Here a model is introduced in order to describe and explain the broadening of the spectral lines and the power dependence of the ion loading rate for scheme B with a set of three parameters (θ , T , detuning from the resonance frequency of an atom at rest) that provides a consistent description of the experimental situation. A similar model for scheme A will be introduced afterwards.

For convenience, Cartesian coordinates (x, y, z) are used. The laser beams and the atomic oven are placed in the $x - z$ plane. The origin of the coordinate system is chosen at the atomic oven, and the center of the laser beams is at $x = X_0$ and $y = 0$, extended along the z -axis. The ion loading rate η at a specific position (x, y, z) is assumed to be proportional to the atom population at the intermediate state ($6s6p^1P_1$) and to the intensity of the second laser beam transferring the population from the intermediate state to the continuum. The population of the intermediate state ρ depends on the intensity of the first laser beam driving the transition from the ground to the intermediate state.

The transverse intensity distribution of the laser beam is assumed to be gaussian: $I_i e^{-2[(x-X_0)^2+y^2]/w_i^2}$ ($i = 1$ (2) for the first (second) step laser, I_i represents the intensity at the center of the laser beam with a beam waist w_i). The ionization probability for an atom leaving the oven at $t = 0$ with velocity (v_x, v_y, v_z) is given by

$$\eta(v_x, v_y, v_z) = \alpha \int_0^\infty I_2 e^{\Delta} \rho(v_x t - X_0, v_y t, v_z t) dt, \quad (1)$$

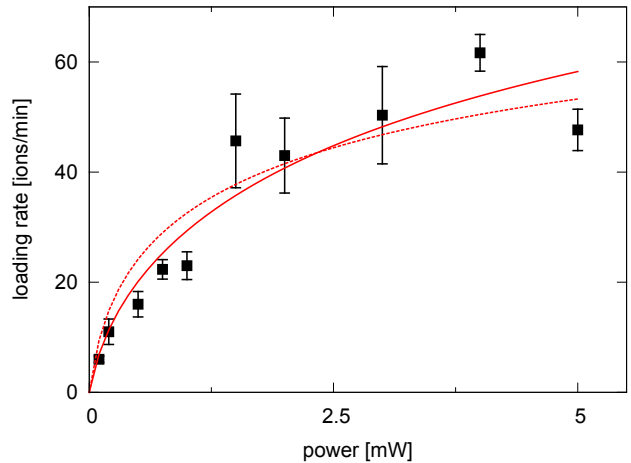


Fig. 5 Loading rate achieved via scheme B as a function of the laser power used in the first ionization step. The power of the laser used by the second step is kept at 1 mW, and the temperature of the atomic oven is assumed to be 550 K for the calculation, to account for a reduced heating current of the atomic oven compared to the one chosen to obtain the results presented in Figs. 3 and 4. The red dashed curve is the result of fitting the model with parameter α and the frequency set at the maximum loading rate. The red solid line is the result of the fit when a detuning of -50 MHz from this frequency is assumed (see main text).

$$\Delta = -\frac{2[(v_x t - X_0)^2 + (v_y t)^2]}{w_2^2}$$

where α is a constant of proportionality (see also caption of Fig. 4). The peak intensity is related to the laser power P_i by $I_i = 2P_i / (\pi w_i^2)$.

The population ρ of an atom in the intermediate state is assumed to be stationary. The lifetime in the intermediate state (inverse of the natural linewidth Γ) is much shorter than the typical transit time of the atom across the laser beam. For example, assuming a Maxwell-Boltzmann distribution for $T = 600$ K, the most probable speed of Ba atoms is about 200 m/s, and the transit time through the laser beam ($2w_1 = 460 \mu\text{m}$) amounts to $2.3 \mu\text{s}$, which is much longer than the lifetime of the $6s6p^1P_1$ state (8 ns). Therefore, ρ can be expressed as [33],

$$\rho = \frac{1}{4} \frac{\Omega_0(v_x t, v_y t)^2}{(\delta - kv_z)^2 + \frac{\Gamma^2}{4} + \frac{\Omega_0(v_x, v_y)^2}{2}}, \quad (2)$$

where δ is the detuning of the laser from the atomic resonance frequency at rest, k is the wavenumber of the laser beam driving the transition at the Rabi frequency Ω_0 which is a function of the spatial coordinates:

$$\Omega_0(x, y)^2 = \frac{2\mu^2}{\hbar^2 \varepsilon_0 c} I_1 \exp\left\{-\frac{2}{w_1^2} [(x - X_0)^2 + y^2]\right\}. \quad (3)$$

In Eq. (3), \hbar is the reduced Planck constant, ε_0 is the electric constant and c is the speed of light in vacuum.

The total ion loading rate is obtained by integrating over the atomic velocity for an appropriate velocity distribution function $f(v_r, v_y)$:

$$\eta_0 = \int_0^\infty v_r dv_r \int_{-\infty}^\infty dv_y \int_{\theta-\delta\theta}^{\theta+\delta\theta} d\theta f(v_r, v_y) \cdot \eta(v_r \sin \theta, v_y, v_r \cos \theta). \quad (4)$$

Here the coordinates (r and θ), defined as $x = r \sin \theta$ and $z = r \cos \theta$, are introduced and v_x and v_z are replaced by $v_r \sin \theta$ and $v_r \cos \theta$, respectively. The azimuthal angle θ is the angle included by the direction of the atomic and the laser beam. For a thermal beam of atoms with mass M , a Maxwell-Boltzmann distribution can be assumed:

$$f(v_r, v_y) = \frac{1}{N} \exp\left(-M \frac{v_r^2 + v_y^2}{2k_B T}\right), \quad (5)$$

where k_B is the Boltzmann constant, and N is a normalization factor. In the present experimental setup, the slit aperture collimates the beam in the y -direction. However, the diverging angle of the atomic beam in the x - z -plane is negligible compared to the velocity distribution of atoms in a thermal beam. Therefore, the divergence $\delta\theta$ in Eq. (4) approaches zero and θ is assumed to be at one value in the following.

In the case of scheme A the spontaneous emission from the intermediate state ($5d6p^3D_1$) mainly leads to metastable states such as $6s5d^3D_{1,2}$. The maximal spontaneous emission rate from $5d6p^3D_1$ to the ground state ($6s^2^1S_0$) amounts to $1.5 \times 10^6 \text{ s}^{-1}$, whereas that to $6s5d^3D_1$ is $3.8 \times 10^7 \text{ s}^{-1}$ and that to $6s5d^3D_2$ is $1.9 \times 10^7 \text{ s}^{-1}$. Therefore, the atoms are optically pumped to the metastable states, and the stationary value of ρ approaches zero. By changing the definition of ρ to be the transition probability from the ground state to the intermediate state, it is possible to use the same formulae as in Eqs. (1-5), except for the value of the constant of proportionality α . Thus, applying the present model does not allow for comparing the absolute value of the loading rates achieved via the two schemes.

By substituting Eqs. (1-3) and (5) into Eq. (4), the theoretical curves in Fig. 3 are obtained. In the case of scheme A, the temperature of the atomic beam is assumed to be $T=600 \text{ K}$, the spontaneous emission rate is $5.85 \times 10^7 \text{ s}^{-1}$, and the parameters of the laser providing the first and the second step of ionization are identical. For scheme B, the temperature is also set to $T=600 \text{ K}$, but the spontaneous emission rate is $1.2 \times 10^8 \text{ s}^{-1}$, and the parameters of the first and second step lasers are set independently. In the calculation, the parameters θ , α , and the center frequency of the resonance are left as

fitting parameters for the data presented in Fig. 3(a) and $\theta = 98.3$ degrees is deduced. The center of the resonance is pointed at by an arrow in the figure. In Fig. 3(b), θ is fixed to the obtained value above, and only the center frequency of the resonance and α remain as fitting parameters.

Using the same model, the results of the derivation for the dependency of the ion loading rate on the power is also depicted in Figs. 4 and 5. Here the only fitting parameter is α , and the detuning is set to the frequency at which the loading rate is at its maximum. In Fig. 5, however, the red dashed curve derived from the model does not fit the experimental result at small laser power very well. Scrutinizing the experimental data, it turned out that the laser frequency has drifted a few tens of megahertz to the red of the frequency for the peak loading rate. Assuming a detuning of -50 MHz from the frequency of maximal loading rate, the result of the model (red solid line) is in better agreement with the experimental findings.

5 Conclusions and outlook

In conclusion, this work demonstrated a novel, isotope-selective resonant two-photon photoionization scheme for barium using a dipole-allowed transition. The loading rates into a linear Paul trap was compared to an established scheme using a weak intercombination line. An increase in efficiency by two orders of magnitude was found. This allows to enhance the advantages of photoionization for barium like minimal charge build-up on insulators compared to electron bombardment ionization or patch potentials caused by a contamination of the trap electrodes. Reducing these effects might have a great impact in experiments that rely on high efficiency such as in cavity quantum-electrodynamics with ion coulomb crystals[34], one-dimensional surface traps for quantum information processing[11], two-dimensional trapping arrays for quantum simulations[35,36] or the recently realized optical trapping of ions[37]. The direct, efficient photoionization of an optically trapped barium atom reduces detrimental charging effects, followed by a loss of the ion out of the shallow, compared to RF-potentials, optical potential. This might allow, for example, to study cold-chemistry processes[38] and to simultaneously avoid micro-motion that normally occurs in conventional ion traps[39]. In addition, providing loading rates of 10^4 ions/s are required to allow for experiments at repetition rates of the order of 0.1-1 kHz, for example, exploring controlled molecular ions that are sympathetically cooled via Ba ions. The devices combining the species, a storage ring[40-42] or a

molecular conveyor belt[43], will substantially depend on the sufficient efficiency of the Ba-ion source.

The presented technique can be further advanced by exploiting the tuneability of the 413 nm laser and its proximity to the ionization threshold. An increase in efficiency is expected by tuning the laser on resonance with a transition to either a field ionized Rydberg state[9] or with an autoionization resonance[44, 45]. The presented technique can be simplified because the dye laser used to generate the 553 nm light can be substituted by a low maintenance, all-solid-state laser system. Very recently, a commercial frequency-doubled diode laser system with the required wavelength and power became available. Since the second ionization step does not require a laser of narrow linewidth, substituting the 413 nm laser by an incoherent light source is possible[13, 14] and the presented highly efficient photoionization scheme could thus be implemented with modest effort and a robust setup.

Acknowledgements Financial support is gratefully acknowledged by the Deutsche Forschungsgemeinschaft, the DFG cluster of Excellence: Munich Center for Advanced Photonics, the International Max Planck Research School on Advanced Photon Science (IMPRS-APS) and the EU research project PICC: The Physics of Ion Coulomb Crystals, funded under the European Communitys 7th Framework Programme. The authors would like to thank S. Kahra for his contributions to the barium trapping setup and M. Albert for carefully reading the manuscript. We would also like to thank J. Bayerl, C. Kerzl and T. Dou for their contributions and the Quantum Optics and Spectroscopy Group in Innsbruck especially R. Blatt and D. Rotter for helpful discussions and insights.

References

- Rosenband, T., Hume, D. B., Schmidt, P. O., Chou, C. W., Brusch, A., Lorini, L., Oskay, W. H., Drullinger, R. E., Fortier, T. M., Stalnaker, J. E., Diddams, S. A., Swann, W. C., Newbury, N. R., Itano, W. M., Wineland, D. J., and Bergquist, J. C. *Science* **319**(5871), 1808–1812 3 (2008).
- Chou, C. W., Hume, D. B., Rosenband, T., and Wineland, D. J. *Science* **329**(5999), 1630–1633 (2010).
- Chou, C.-w., Hume, D. B., Koelemeij, J. C. J., Wineland, D. J., and Rosenband, T. *Physical Review Letters* **104**(7), 070802 2 (2010).
- Haefner, H., Roos, C. F., and Blatt, R. *Physics Reports* **469**, 155 (2008).
- Home, J. P., Hanneke, D., Jost, J. D., Amini, J. M., Leibfried, D., and Wineland, D. J. *Science* **325**(5945), 1227–1230 (2009).
- Friedenaauer, A., Schmitz, H., Glueckert, J. T., Porras, D., and Schaetz, T. *Nature Physics* **4**(10), 757–761 July (2008).
- Lanyon, B. P., Hempel, C., Nigg, D., Mller, M., Gerritsma, R., Zhuringer, F., Schindler, P., Barreiro, J. T., Rambach, M., Kirchmair, G., Hennrich, M., Zoller, P., Blatt, R., and Roos, C. F. *Science* (2011).
- Paul, W. *Rev. Mod. Phys.* **62**, 531–540 Jul (1990).
- Gulde, S., Rotter, D., Barton, P., Schmidt-Kaler, F., Blatt, R., and Hogervorst, W. *Applied Physics B: Lasers and Optics* **73**, 861–86tur (2001). 10.1007/s003400100749.
- Turchette, Q. A., Kielpinski, King, B. E., Leibfried, D., Meekhof, D. M., Myatt, C. J., Rowe, M. A., Sackett, C. A., Wood, C. S., Itano, W. M., Monroe, C., and Wineland, D. J. *Phys. Rev. A* **61**, 063418 May (2000).
- Stick, D., H. W. O. S. M. M. S. K. M. C. *Nature Physics* **2**(1), 36–39 (2006).
- Hurst, G. S., Payne, M. G., Kramer, S. D., and Young, J. P. *Rev. Mod. Phys.* **51**, 767–819 Oct (1979).
- Steele, A. V., Churchill, L. R., Griffin, P. F., and Chapman, M. S. *Physical Review A* **75**(5), 053404 5 (2007).
- Wang, B., Zhang, J. W., Gao, C., and Wang, L. J. *Opt. Express* **19**(17), 16438–16447 Aug (2011).
- Kjaergaard, N., Hornekaer, L., Thommesen, A., Videsen, Z., and Drewsen, M. *Applied Physics B: Lasers and Optics* **71**(2), 207–210 August (2000).
- Lucas, D. M., Ramos, A., Home, J. P., McDonnell, M. J., Nakayama, S., Stacey, J.-P., Webster, S. C., Stacey, D. N., and Steane, A. M. *Phys. Rev. A* **69**(1), 012711 Jan (2004).
- Tanaka, U., Matsunishi, H., Morita, I., and Urabe, S. *Applied Physics B: Lasers and Optics* **81**, 795–799 (2005). 10.1007/s00340-005-1967-2.
- Johanning, M., Braun, A., Eiteneuer, D., Paape, C., Balzer, C., Neuhauser, W., and Wunderlich, C. *Applied Physics B: Lasers and Optics* **103**, 327–338 (2011). 10.1007/s00340-011-4502-7.
- Brownutt, M., Letchumanan, V., Wilpers, G., Thompson, R., Gill, P., and Sinclair, A. *Applied Physics B: Lasers and Optics* **87**, 411–415 (2007). 10.1007/s00340-007-2624-8.
- Vant, K., Chiaverini, J., Lybarger, W., and Berkeland, D. J. (2006).
- Ludsteck, V. *Experimente mit einer linearen Ionenkette zur Realisierung eines Quantencomputers*. PhD thesis, Fakultt fuer Physik, Ludwig-Maximilians-Universitaet Muenchen, May (2004).

22. Hendricks, R., Grant, D., Herskind, P., Dantan, A., and Drewsen, M. *Applied Physics B: Lasers and Optics* **88**, 507–513 (2007). 10.1007/s00340-007-2698-3.
23. Cetina, M., Grier, A., Campbell, J., Chuang, I., and Vuletić, V. *Phys. Rev. A* **76**(4), 041401 Oct (2007).
24. Deslauriers, L., Acton, M., Blinov, B. B., Brickman, K.-A., Haljan, P. C., Hensinger, W. K., Hucul, D., Katnik, S., Kohn, R. N., Lee, P. J., Madsen, M. J., Maunz, P., Olmschenk, S., Moehring, D. L., Stick, D., Sterk, J., Yeo, M., Younge, K. C., and Monroe, C. *Phys. Rev. A* **74**(6), 063421 Dec (2006).
25. Leibbrandt, D. R., Clark, R. J., Labaziewicz, J., Antohi, P., Bakr, W., Brown, K. R., and Chuang, I. L. *Phys. Rev. A* **76**(5), 055403 Nov (2007).
26. Rotter, D. *Quantum feedback and quantum correlation measurements with a single Barium ion*. PhD thesis, (2008).
27. Diedrich, F., Peik, E., Chen, J. M., Quint, W., and Walther, H. *Physical Review Letters* **59**(26), 2931 12 (1987).
28. Wineland, D. J., Bergquist, J. C., Itano, W. M., Bollinger, J. J., and Manney, C. H. *Physical Review Letters* **59**(26), 2935 12 (1987).
29. Armstrong, D. J. and Cooper, J. *Phys. Rev. A* **47**, R2446–R2449 Apr (1993).
30. Davidson, M. D., Snoek, L. C., Volten, H., and Doenzelmann, A. *Astronomy And Astrophysics* **255**(1-2), 457–458 February (1992).
31. Friedenauer, A., Markert, F., Schmitz, H., Petersen, L., Kahra, S., Herrmann, M., Udem, T., Haensch, T., and Schaetz, T. *Applied Physics B: Lasers and Optics* **84**(3), 371–373 January (2006).
32. Baird, P. E. G., Brambley, R. J., Burnett, K., Stacey, D. N., Warrington, D. M., and Woodgate, G. K. *Proceedings of the Royal Society of London. Series A, Mathematical and Physical Sciences* **365**(1723), pp. 567–582 (1979).
33. Metcalf, H. J. and Van der Straten, P. *Laser cooling and trapping*. Springer, New York , London, (1999).
34. Albert, M., Dantan, A., and Drewsen, M. *Nat Photon advance online publication*, 2011/09/04/online (2011).
35. Schaetz, T., Friedenauer, A., Schmitz, H., Petersen, L., and Kahra, S. *J. Mod. Opt.* **54**, 2317–2325 Nov (2007).
36. Schneider, C., Porras, D., and Schaetz, T. *arXiv:1106.2597v1* (2011).
37. Schneider, C., Enderlein, M., Huber, T., and Schaetz, T. *Nature Photonics* **4**(October), 5 (2010).
38. Krych, M., Skomorowski, W., Pawłowski, F., Moszynski, R., and Idziaszek, Z. *Phys. Rev. A* **83**, 032723 Mar (2011).
39. Cormick, C., Schaetz, T., and Morigi, G. *New Journal of Physics* **13**(4), 043019 (2011).
40. <http://www.xfel.eu/sites/site-xfel-gmbh/content/e63594/e63599/e81234/e65128/e76474/sqs-wg-ii-report-eng.pdf>.
41. Schramm, U., Schaetz, T., and Habs, D. *Phys. Rev. Lett.* **87**, 184801 Oct (2001).
42. Schramm, U., Schaetz, T., and Habs, D. *Phys. Rev. E* **66**, 036501 Sep (2002).
43. Kahra, S. and Leschhorn, G. Controlled delivery of single molecules into ultra-short laser pulses: a molecular conveyor belt, to be published.
44. Hudson, R. D., Carter, V. L., and Young, P. A. *Phys. Rev. A* **2**, 643–648 Sep (1970).
45. van Leeuwen, R., Ubachs, W., and Hogervorst, W. *Journal of Physics B: Atomic, Molecular and Optical Physics* **27**(17), 3891 (1994).

List of Tables

1.1	Steady state positions for up to five $^{24}\text{Mg}^+$ -ions in a common trap potential	15
2.1	ESI-source: dig. I/O and analog out voltages of boards #0 and #1.	58
2.2	Quadrupole: analog I/O and dig. out voltages of boards #2 and #3.	59
2.3	Constant parameters used in the ESI characterization experiments.	60
2.4	Parameters applied to the quadrupole setup, with the help of the GUI.	63
4.1	DC-voltages on the electrodes of trap 2 for trapping of barium ions.	96

List of Figures

1.1	The quadrupole potential for a fixed time instant.	8
1.2	Lowest lying part of the stability a-q diagram.	8
1.3	Detailed zoom to the stability diagram near the a-q origin.	10
1.4	Degenerate fine structure manifold of the $3S_{1/2}$ and $3P_{3/2}$ states of $^{24}\text{Mg}^+$	13
1.5	Level scheme of $^{138}\text{Ba}^+$ with Zeeman splitting in an external magnetic field.	14
1.6	Crystalline structures in a trapping potential with cylindrical symmetry.	16
1.7	Two pulses with an absolute carrier to envelope phase that differs by $\pi/2$	18
1.8	Electric field of a pulse with envelope function $\epsilon(t)$ and temporal phase $\zeta(t)$	19
2.1	Top view of the vacuum chamber for trapping single molecular ions.	27
2.2	Overview of the most important inside-vacuum parts of the setup.	29
2.3	Transmission vs. wavelength for the YFP-excitation filter.	33
2.4	The relevant part of the energy level diagram of ^{24}Mg and $^{24}\text{Mg}^+$	34
2.5	Schematic experimental setup, including the lasers for magnesium.	35
2.6	Recorded iodine absorption and polarization spectroscopy spectrum.	36
2.7	Schematic of the frequency doubling resonator and the stabilization scheme.	37
2.8	Schematic layout of the barium laser system.	39
2.9	Layout of the SHG-resonator producing the light for $^{138}\text{Ba}^+$ Doppler cooling.	40
2.10	Transmission vs. wavelength for the red-reflector mirror in the $^{138}\text{Ba}^+$ -setup.	41
2.11	Signal after the opto-galvanic sensor, illuminated with resonant 493 nm light.	43
2.12	Initial loading: 493 nm signal after the barium absorption discharge plasma.	44
2.13	Schematic of the laser system that produces few-cycle NIR/VIS pulses.	45
2.14	Reflectivity vs. wavelength for the metallic mirrors used in the UV-beamline.	47
2.15	Schematic of the femtosecond UV-laser beamline.	48

2.16	The main chambers of the ultra-short pulse laser beamline.	49
2.17	Reflectivity vs. wavelength of the dielectric mirrors used in the delay chamber.	50
2.18	Picture of the dye cuvette, taken by the monitoring CCD camera.	51
2.19	Coarse alignment of the spatial overlap on the cuvette.	52
2.20	Coarse alignment of the temporal overlap on the cuvette.	52
2.21	Schematic illustration of the Electro-Spray Ionization process.	55
2.22	Computer drawing of the refurbished ESI hardware.	56
2.23	Computer drawing of the quadrupole mass filter part of the ESI-setup.	57
2.24	Screen-shot of the GUI, controlling the ESI-source and the mass filter.	59
2.25	Measurements on the total ion current of the ESI-source.	61
2.26	Mass scan of a L-arginin Hydrochlorid solution.	62
3.1	Fluorescence images of crystalline ion structures confined in trap 2.	65
3.2	Count rate of the PMT detecting the fluorescence emitted from $^{24}\text{Mg}^+$ -ions.	67
3.3	Time evolution of atomic and molecular composition of Coulomb crystals.	69
3.4	Simulation of the axial electric potential of trap 1.	70
3.5	Schematic of methods to decelerate and trap ions at the end of their transfer.	71
3.6	Transfer efficiencies vs. switching time for an ensemble from trap 1 to trap 2.	72
3.7	Illustration on the potential energy curves of $^{24}\text{MgH}^+$	76
3.8	Vibrational heating mechanism of multiple excited molecular ions.	81
3.9	Dissociation probability per pulse vs. delay time for 280 nm pulses.	83
3.10	Dissociation probability per pulse vs. delay time for 260 nm pulses.	84
4.1	Energy level scheme of neutral and singly ionized barium.	87
4.2	Measurement of the beam waist for the 553 nm and the 413 nm laser.	88
4.3	Loading rate of $^{138}\text{Ba}^+$ ions into trap 2 vs. detuning of the laser.	90
4.4	Loading rate achieved with scheme A and B vs. laser power.	93
4.5	Loading rate of scheme B vs. laser power used in the first ionization step.	94
4.6	Fluorescence images of pure $^{138}\text{Ba}^+$ crystals using identical trap parameters.	97
4.7	Fluorescence images of Coulomb-crystals in a linear chain configuration.	98
5.1	Schematic illustration of topological defects in ion traps.	102

5.2	Zig-zag and extended kink for equal trapping parameters and number of ions.	104
5.3	Zig-zag and extended kink configuration compared to theory.	106
5.4	Spectrum of normal modes for the zig-zag and extended kink configuration.	107
5.5	Observed localized kink and the first attempt of a comparison to theory. . .	108
5.6	Spectrum of normal modes for the zig-zag and localized kink configuration.	109
5.7	Radial cooling beam in trap 2: experimental results.	111
5.8	Observation of two kinks in one crystal	113

Bibliography

- [1] Bilderback, D. H., Elleaume, P. & Weckert, E. Review of third and next generation synchrotron light sources. *Journal of Physics B: Atomic, Molecular and Optical Physics* **38**, S773 (2005).
- [2] Henderson, R. The potential and limitations of neutrons, electrons and x-rays for atomic resolution microscopy of unstained biological molecules. *Quarterly Reviews of Biophysics* **28**, 171–193 (1995).
- [3] Kim, K.-J. Characteristics of synchrotron radiation. *AIP Conference Proceedings* **184**, 565–632 (1989).
- [4] Webster, G. & Hilgenfeld, R. Perspectives on single molecule diffraction using the x-ray free electron laser. *Single Molecules* **3**, 63–68 (2002).
- [5] Cheetham, A. K. & Wilkinson, A. P. Synchrotron x-ray and neutron diffraction studies in solid-state chemistry. *Angewandte Chemie International Edition in English* **31**, 1557–1570 (1992).
- [6] Spence, J. C. H. & Doak, R. B. Single molecule diffraction. *Physical Review Letters* **92**, 198102 (2004).
- [7] Benvenuti, M. & Mangani, S. Crystallization of soluble proteins in vapor diffusion for x-ray crystallography. *Nature Protocols* **2**, 1633 – 1651 (2007).
- [8] Raymond, C. & Stevens. High-throughput protein crystallization. *Current Opinion in Structural Biology* **10**, 558 – 563 (2000).
- [9] Warren, B. E. X-ray diffraction in random layer lattices. *Phys. Rev.* **59**, 693–698 (1941).
- [10] Klug, H. P. & Alexander, L. E. *X-Ray Diffraction Procedures: For Polycrystalline and Amorphous Materials, 2nd Edition* (1974).
- [11] Chapman, H. N. *et al.* Femtosecond diffractive imaging with a soft-x-ray free-electron laser. *Nature Physics* **2**, 839–843 (2006).
- [12] Gaffney, K. J. & Chapman, H. N. Imaging atomic structure and dynamics with ultrafast x-ray scattering. *Science* **316**, 1444–1448 (2007).

- [13] van der Veen, F. & Pfeiffer, F. Coherent x-ray scattering. *Journal of Physics: Condensed Matter* **16**, 5003 (2004).
- [14] Feldhaus, J., Arthur, J. & Hastings, J. X-ray free-electron lasers. *Journal of Physics B: Atomic, Molecular and Optical Physics* **38**, S799 (2005).
- [15] Neutze, R., Wouts, R., van der Spoel, D., Weckert, E. & Hajdu, J. Potential for biomolecular imaging with femtosecond x-ray pulses. *Nature* **406**, 752–757 (2000).
- [16] Seibert, M. *et al.* Single mimivirus particles intercepted and imaged with an x-ray laser. *Nature* **470**, 78–81 (2011).
- [17] Young, L. *et al.* Femtosecond electronic response of atoms to ultra-intense x-rays. *Nature* **466**, 56–61 (2010).
- [18] Chapman, H. N. *et al.* Femtosecond time-delay x-ray holography. *Nature* **448**, 676–679 (2007).
- [19] Chapman, H. N. *et al.* Femtosecond x-ray protein nanocrystallography. *Nature* **470**, 73–77 (2011).
- [20] Boutet, S. & Williams, G. J. The coherent x-ray imaging (cxi) instrument at the linac coherent light source (lcls). *New Journal of Physics* **12**, 035024 (2010).
- [21] Fuchs, M. *et al.* Laser-driven soft-x-ray undulator source. *Nature Physics* **5**, 826–829 (2009).
- [22] Yamashita, M. & Fenn, J. B. Negative ion production with the electrospray ion source. *The Journal of Physical Chemistry* **88**, 4671–4675 (1984).
- [23] Marklund, E. G., Larsson, D. S. D., Spoel, D. v. d., Patriksson, A. & Caleman, C. Structural stability of electrosprayed proteins: temperature and hydration effects. *Physical Chemistry Chemical Physics* **11**, 8069–8078 (2009).
- [24] Kuehner, D. E. *et al.* Lysozyme net charge and ion binding in concentrated aqueous electrolyte solutions. *The Journal of Physical Chemistry B* **103**, 1368–1374 (1999).
- [25] Hamm, P. *et al.* Femtosecond spectroscopy of the photoisomerisation of the protonated schiff base of all-trans retinal. *ChemPhysChem* **263**, 613–621 (1996).
- [26] Chou, C. W., Hume, D. B., Rosenband, T. & Wineland, D. J. Optical clocks and relativity. *Science* **329**, 1630–1633 (2010).
- [27] Home, J. P. *et al.* Complete methods set for scalable ion trap quantum information processing. *Science* **325**, 1227–1230 (2009).
- [28] Barrett, M. D. *et al.* Deterministic quantum teleportation of atomic qubits. *Nature* **429**, 737–739 (2004).
- [29] Rohde, H. *et al.* Sympathetic ground-state cooling and coherent manipulation with two-ion crystals. *Journal of Optics B: Quantum and Semiclassical Optics* **3**, S34 (2001).

- [30] Barrett, M. D. *et al.* Sympathetic cooling of ${}^9\text{Be}^+$ and ${}^{24}\text{Mg}^+$ for quantum logic. *Phys. Rev. A* **68**, 042302– (2003).
- [31] Kahra/Leschhorn *et al.* Controlled delivery of single molecules into ultra-short laser pulses: A molecular conveyor belt. *accepted for publication in Nature Physics* (2011).
- [32] Offenberg, D., Zhang, C. B., Wellers, C., Roth, B. & Schiller, S. Translational cooling and storage of protonated proteins in an ion trap at subkelvin temperatures. *Phys. Rev. A* **78**, 061401 (2008).
- [33] Gerlich, D. & Borodi, G. Buffer gas cooling of polyatomic ions in rf multi-electrode traps. *Faraday Discussions* **142**, 57–72 (2009).
- [34] Schneider, T., Roth, B., Duncker, H., Ernsting, I. & Schiller, S. All-optical preparation of molecular ions in the rovibrational ground state. *Nature Physics* **6**, 275–278 (2010).
- [35] Sta anum, P. F., Hojbjerg, K., Skyt, P. S., Hansen, A. K. & Drewsen, M. Rotational laser cooling of vibrationally and translationally cold molecular ions. *Nature Physics* **6**, 271–274 (2010).
- [36] Diedrich, F., Peik, E., Chen, J. M., Quint, W. & Walther, H. Observation of a phase transition of stored laser-cooled ions. *Physical Review Letters* **59**, 2931 (1987).
- [37] Wineland, D. J., Bergquist, J. C., Itano, W. M., Bollinger, J. J. & Manney, C. H. Atomic-ion coulomb clusters in an ion trap. *Phys. Rev. Lett.* **59**, 2935–2938 (1987).
- [38] Fishman, S., De Chiara, G., Calarco, T. & Morigi, G. Structural phase transitions in low-dimensional ion crystals. *Phys. Rev. B* **77**, 064111 (2008).
- [39] Okada, K., Wada, M., Takayanagi, T., Ohtani, S. & Schuessler, H. A. Characterization of ion Coulomb crystals in a linear Paul trap. *Physical Review A* **81**, 013420+ (2010).
- [40] Hasse, R. W. & Schiffer, J. P. The structure of the cylindrically confined coulomb lattice. *Annals of Physics* **203**, 419–448 (1990).
- [41] James, D. F. V. Quantum dynamics of cold trapped ions with application to quantum computation. *Applied Physics B: Lasers and Optics* **66**, 181–190 (1998).
- [42] Landa, H., Marcovitch, S., Retzker, A., Plenio, M. B. & Reznik, B. Quantum coherence of discrete kink solitons in ion traps. *Phys. Rev. Lett.* **104**, 043004– (2010).
- [43] del Campo, A., De Chiara, G., Morigi, G., Plenio, M. B. & Retzker, A. Structural Defects in Ion Chains by Quenching the External Potential: The Inhomogeneous Kibble-Zurek Mechanism. *Phys. Rev. Lett.* **105**, 075701 (2010).
- [44] Kibble, T. Some implications of a cosmological phase transition. *Physics Reports* **67**, 183 – 199 (1980).

- [45] Zurek, W. Cosmological experiments in superfluid helium. *Nature* **317**, 505 (1985).
- [46] Kibble, T. Testing cosmological defect formation in the laboratory. *ArXiv:cond-mat/0111082* (2001).
- [47] Bäuerle, C., Bunkov, Y., Fisher, S., Godfrin, H. & Pickett, G. Laboratory simulation of cosmic string formation in the early universe using superfluid ^3He . *Nature* **382**, 332 (1996).
- [48] Ruutu, V. Vortex formation in neutron-irradiated superfluid ^3He as an analogue of cosmological defect formation. *Nature* **382**, 334 (1996).
- [49] Chuang, I. Cosmology in the laboratory: Defect dynamics in liquid crystals. *Science* **251**, 1336 (1991).
- [50] Ducci, S., Ramazza, P. L., González-Viñas, W. & Arecchi, F. T. Order parameter fragmentation after a symmetry-breaking transition. *Phys. Rev. Lett.* **83**, 5210–5213 (1999).
- [51] Chiara, G. D., del Campo, A., Morigi, G., Plenio, M. B. & Retzker, A. Spontaneous nucleation of structural defects in inhomogeneous ion chains. *New Journal of Physics* **12**, 115003 (2010).
- [52] Dehmelt, H. G. Radiofrequency spectroscopy of stored ions i: Storage. vol. Volume 3, 53–72 (Academic Press, 1968).
- [53] Paul, W. & Steinwedel, H. Ein neues Massenspektrometer ohne Magnetfeld. *Zeitschrift Naturforschung Teil A* **8**, 448– (1953).
- [54] Paul, W. Electromagnetic traps for charged and neutral particles. *Reviews of Modern Physics* **62**, 531–540 (1990).
- [55] Metcalf, H. J. & Van der Straten, P. *Laser cooling and trapping* (Springer, New York , London, 1999).
- [56] Reiss, D., Lindner, A. & Blatt, R. Cooling of trapped multilevel ions: A numerical analysis. *Phys. Rev. A* **54**, 5133– (1996).
- [57] Gray, H. R., Whitley, R. M. & C. R. Stroud, J. Coherent trapping of atomic populations. *Opt. Lett.* **3**, 218–220 (1978).
- [58] Davidson, M. D., Snoek, L. C., Volten, H. & Dönszelmann, A. Oscillator-strengths and branching ratios of transitions between low-lying levels in the barium-ii spectrum. *Astronomy And Astrophysics* **255**, 457–458 (1992).
- [59] Oberst, H. *Resonance fluorescence of single barium ions*. Master’s thesis, Leopold-Franzens-Universität Innsbruck (1999).
- [60] Hornekaer, L. & Drewsen, M. Formation process of large ion coulomb crystals in linear paul traps. *Phys. Rev. A* **66**, 013412 (2002).

- [61] Mølhave, K. & Drewsen, M. Formation of translationally cold MgH^+ and MgD^+ molecules in an ion trap. *Phys. Rev. A* **62**, 011401– (2000).
- [62] Ostendorf, A. *et al.* Sympathetic cooling of complex molecular ions to millikelvin temperatures. *Physical Review Letters* **97**, 243005 (2006).
- [63] Diels, J.-C. & Rudolph, W. *Ultrashort laser pulse phenomena* (Elsevier/Academic Press, Amsterdam, London, 2006), 2nd edn.
- [64] Gollub, C. *Femtosecond quantum control studies on vibrational quantum information processing*. Ph.D. thesis, Fakultät für Chemie und Pharmazie, Ludwig-Maximilians-Universität München (2009).
- [65] Born, M. & Oppenheimer, R. Zur Quantentheorie der Moleküle. *Ann. Phys. (Leipzig)* **84**, 457 (1927).
- [66] Werner, H.-J., Knowles, P. J., Knizia, G., Manby, F. R. & *et al.*, M. S. Molpro, version 2010.1, a package of ab initio programs (2010).
- [67] Knowles, P. J. & Werner, H.-J. An efficient method for the evaluation of coupling coefficients in configuration interaction calculations. *Chemical Physics Letters* **145**, 514–522 (1988).
- [68] Werner, H.-J. & Knowles, P. J. An efficient internally contracted multiconfiguration–reference configuration interaction method. *J. Chem. Phys.* **89**, 5803–5814 (1988).
- [69] McNaught, A. D. & Wilkinson, A. *Compendium of Chemical Terminology, 2nd ed.* (Blackwell Scientific Publications, 1997).
- [70] Widmark, P.-O., Persson, B. J. & Roos, B. O. Density matrix averaged atomic natural orbital (ano) basis sets for correlated molecular wave functions. *Theoretical Chemistry Accounts: Theory, Computation, and Modeling (Theoretica Chimica Acta)* **79**, 419–432 (1991). 10.1007/BF01112569.
- [71] Aymar, M., Guerout, R., Sahlaoui, M. & Dulieu, O. Electronic structure of the magnesium hydride molecular ion. *Journal of Physics B: Atomic, Molecular and Optical Physics* **42**, 154025 (2009).
- [72] Balfour, W. J. Rotational Analysis of the $\text{A}^1\Sigma^+ \rightarrow \text{X}^1\Sigma^+$ and $\text{B}^1\Pi \rightarrow \text{X}^1\Sigma^+$ Systems of $^{24}\text{MgH}^+$, $^{25}\text{MgH}^+$, and $^{26}\text{MgH}^+$. *Canadian Journal of Physics* **50**, 1082–1091 (1972).
- [73] Ezer, T. H. & Kosloff, R. An accurate and efficient scheme for propagating the time dependent schroedinger equation. *The Journal of Chemical Physics* **81**, 3967–3971 (1984).
- [74] Kahra, S. *Trapping and cooling of single molecular ions for time resolved experiments*. Ph.D. thesis, Ludwig-Maximilians Universität München, Fakultät für Physik (2011).

- [75] Leschhorn, G. *Speichern und Kühlen molekularer Ionen in einer linearen Paulfalle*. Diplomarbeit, Ludwig-Maximilians-Universität München, Fakultät für Physik (2007).
- [76] Leschhorn, G., Kahra, S. & Schaetz, T. Deterministic delivery of externally cold and precisely positioned single molecular ions. *ArXiv e-prints:1110.4254* (2011). 1110.4254.
- [77] Rangwala, S. A., Junglen, T., Rieger, T., Pinkse, P. W. H. & Rempe, G. Continuous source of translationally cold dipolar molecules. *Phys. Rev. A* **67**, 043406 (2003).
- [78] Bell, M. T., Gingell, A. D., Oldham, J. M., Softley, T. P. & Willitsch, S. Ion-molecule chemistry at very low temperatures: cold chemical reactions between coulomb-crystallized ions and velocity-selected neutral molecules. *Faraday Discussions* **142**, 73–91 (2009).
- [79] Madsen, D. *et al.* Measurements on photo-ionization of $3s3p\ ^1P_1$ magnesium atoms. *Journal of Physics B: Atomic, Molecular and Optical Physics* **33**, 4981 (2000).
- [80] Kjaergaard, N., Hornekaer, L., Thommesen, A., Videsen, Z. & Drewsen, M. Isotope selective loading of an ion trap using resonance-enhanced two-photon ionization. *Applied Physics B: Lasers and Optics* **71**, 207–210 (2000).
- [81] Leschhorn, G., Hasegawa, T. & Schaetz, T. Efficient photoionization for barium ion trapping using a dipole-allowed resonant two-photon transition. *ArXiv e-prints:1110.4040* (2011). 1110.4040.
- [82] Schaetz, T. *Kristalline Ionenstrahlen*. Ph.D. thesis, Fakultät für Physik, Ludwig-Maximilians-Universität München (2001).
- [83] Fenn, J. B., Mann, M., Meng, C. K., Wong, S. F. & Whitehouse, C. M. Electrospray ionization for mass spectrometry of large biomolecules. *Science* **246**, 64–71 (1989).
- [84] Friedenauer, A. *Simulation of the Quantum Ising Model in an Ion Trap*. Ph.D. thesis, Ludwig-Maximilians Universität München: Fakultät für Physik (2010).
- [85] Ostendorf, A. *Sympathetische Kühlung von Molekülionen durch lasergekühlte Bariumionen in einer linearen Paulfalle*. Ph.D. thesis, Heinrich-Heine-Universität Düsseldorf, Mathematisch- Naturwissenschaftliche Fakultät (2006).
- [86] Bothschafter, E. *Collinear Generation and Characterization of Ultrashort UV and XUV Laser Pulses*. Diplomarbeit, Universität Stuttgart (2009).
- [87] Fieß, M. *Advancing attosecond metrology*. Ph.D. thesis, Ludwig-Maximilians Universität München, Fakultät für Physik (2010).
- [88] Kramida, A. & Fuhr, J. Atomic transition probability bibliographic database. National Institute of Standards and Technology, Physical Measurement Laboratory, Atomic Physics Division.

- [89] Friedenauer, A. *et al.* High power all solid state laser system near 280 nm. *Applied Physics B: Lasers and Optics* **84**, 371–373 (2006).
- [90] Smith, P. W. & Hänsch, T. W. Cross-Relaxation Effects in the Saturation of the 6328 Å Neon-Laser Line. *Phys. Rev. Lett.* **26**, 740– (1971).
- [91] Wieman, C. & Hänsch, T. W. Doppler-free laser polarization spectroscopy. *Phys. Rev. Lett.* **36**, 1170– (1976).
- [92] Batteiger, V. *et al.* Precision spectroscopy of the 3s-3p fine-structure doublet in Mg⁺. *Phys. Rev. A* **80**, 022503– (2009).
- [93] Beverini, N. *et al.* Wavelength, isotopic shift, and transition rate of the MgI resonance line. *Optics Communications* **77**, 299–302 (1990).
- [94] Hänsch, T. & Couillaud, B. Laser frequency stabilization by polarization spectroscopy of a reflecting reference cavity. *Optics Communications* **35**, 441–444 (1980).
- [95] Graf, U. *et al.* Intense few-cycle light pulses in the deep ultraviolet. *Opt. Express* **16**, 18956–18963 (2008).
- [96] Nisoli, M. *et al.* Compression of high-energy laser pulses below 5 fs. *Opt. Lett.* **22**, 522–524 (1997).
- [97] Bothschafter, E. M. *et al.* Collinear generation of ultrashort uv and xuv pulses. *Opt. Express* **18**, 9173–9180 (2010).
- [98] Yamashita, M. & Fenn, J. B. Electrospray ion source. another variation on the free-jet theme. *Journal of Physical Chemistry* **88**, 4451–4459 (1984).
- [99] Dole, M. *et al.* Molecular beams of macroions. *The Journal of Chemical Physics* **49**, 2240–2249 (1968).
- [100] Roth, B., Ostendorf, A., Wenz, H. & Schiller, S. Production of large molecular ion crystals via sympathetic cooling by laser-cooled Ba⁺. *Journal of Physics B: Atomic, Molecular and Optical Physics* **38**, 3673 (2005).
- [101] Wang, G. Charged residue versus ion evaporation for formation of alkali metal halide cluster ions in esi. *Analytica Chimica Acta* **406**, 53–65 (2000).
- [102] Kebarle, P. & Peschke, M. On the mechanisms by which the charged droplets produced by electrospray lead to gas phase ions. *Analytica Chimica Acta* **406**, 11–35 (2000).
- [103] Drewsen, M., Mortensen, A., Martinussen, R., Staantum, P. & Sørensen, J. L. Non-destructive identification of cold and extremely localized single molecular ions. *Phys. Rev. Lett.* **93**, 243201 (2004).
- [104] Zhang, C. B., Offenber, D., Roth, B., Wilson, M. A. & Schiller, S. Molecular-dynamics simulations of cold single-species and multispecies ion ensembles in a linear paul trap. *Phys. Rev. A* **76**, 012719– (2007).

- [105] Roth, B., Blythe, P. & Schiller, S. Motional resonance coupling in cold multispecies coulomb crystals. *Phys. Rev. A* **75**, 023402– (2007).
- [106] Buck, U. & Lauenstein, C. Electron bombardment fragmentation of size selected NH_3 clusters. *The Journal of Chemical Physics* **92**, 4250–4255 (1990).
- [107] Jorgensen, S., Drewsen, M. & Kosloff, R. Intensity and wavelength control of a single molecule reaction: Simulation of photodissociation of cold-trapped MgH^+ . *J. Chem. Phys.* **123**, 094302–9 (2005).
- [108] Brinks, D. *et al.* Visualizing and controlling vibrational wave packets of single molecules. *Nature* **465**, 905–908 (2010).
- [109] Schramm, U., Schaetz, T. & Habs, D. Bunched crystalline ion beams. *Phys. Rev. Lett.* **87**, 184801 (2001).
- [110] Luo, C. W., Wang, Y. T., Chen, F. W., Shih, H. C. & Kobayashi, T. Eliminate coherence spike in reflection-type pump-probe measurements. *Opt. Express* **17**, 11321–11327 (2009).
- [111] Balk, M. W. & Fleming, G. R. Dependence of the coherence spike on the material dephasing time in pump-probe experiments. *The Journal of Chemical Physics* **83**, 4300–4307 (1985).
- [112] Rotter, D. *Quantum feedback and quantum correlation measurements with a single Barium ion*. Ph.D. thesis, Leopold-Franzens-Universität Innsbruck (2008).
- [113] Brownnutt, M. *et al.* Controlled photoionization loading of $^{88}\text{Sr}^+$ for precision ion-trap experiments. *Applied Physics B: Lasers and Optics* **87**, 411–415 (2007).
- [114] Gulde, S. *et al.* Simple and efficient photo-ionization loading of ions for precision ion-trapping experiments. *Applied Physics B: Lasers and Optics* **73**, 861–86tur (2001).
- [115] Turchette, Q. A. *et al.* Heating of trapped ions from the quantum ground state. *Phys. Rev. A* **61**, 063418 (2000).
- [116] Stick, D. *et al.* Ion trap in a semiconductor chip. *Nature Physics* **2**, 36–39 (2006).
- [117] Baird, P. E. G. *et al.* Optical isotope shifts and hyperfine structure in lambda 553.5 nm of barium. *Proceedings of the Royal Society of London. Series A, Mathematical and Physical Sciences* **365**, pp. 567–582 (1979).
- [118] Tanaka, U., Matsunishi, H., Morita, I. & Urabe, S. Isotope-selective trapping of rare calcium ions using high-power incoherent light sources for the second step of photo-ionization. *Applied Physics B: Lasers and Optics* **81**, 795–799 (2005).
- [119] Kelly, F. M. & Mathur, M. S. The density dependence of the hanle effect in the resonance line of atomic barium. *Canadian Journal of Physics* **55**, 83–91 (1977).
- [120] Armstrong, D. J. & Cooper, J. Isotope-selective photoionization spectroscopy of barium. *Phys. Rev. A* **47**, R2446–R2449 (1993).

- [121] Steele, A. V., Churchill, L. R., Griffin, P. F. & Chapman, M. S. Photoionization and photoelectric loading of barium ion traps. *Physical Review A* **75**, 053404 (2007).
- [122] Wang, B., Zhang, J. W., Gao, C. & Wang, L. J. Highly efficient and isotope selective photo-ionization of barium atoms using diode laser and led light. *Opt. Express* **19**, 16438–16447 (2011).
- [123] Albert, M., Dantan, A. & Drewsen, M. Cavity electromagnetically induced transparency and all-optical switching using ion coulomb crystals. *Nature Photonics* **5**, 633 (2011).
- [124] Schaetz, T., Friedenauer, A., Schmitz, H., Petersen, L. & Kahra, S. Towards (scalable) quantum simulations in ion traps. *Journal of Modern Optics* **54**, 2317–2325 (2007).
- [125] Schneider, C., Porras, D. & Schaetz, T. Many-body physics with trapped ions. *arXiv:1106.2597v1* (2011).
- [126] Schneider, C., Enderlein, M., Huber, T. & Schaetz, T. Optical trapping of an ion. *Nature Photonics* **4**, 5 (2010).
- [127] Krych, M., Skomorowski, W., Pawłowski, F., Moszynski, R. & Idziaszek, Z. Sympathetic cooling of the Ba^+ ion by collisions with ultracold Rb atoms: Theoretical prospects. *Phys. Rev. A* **83**, 032723 (2011).
- [128] Cormick, C., Schaetz, T. & Morigi, G. Trapping ions with lasers. *New Journal of Physics* **13**, 043019 (2011).
- [129] Hudson, R. D., Carter, V. L. & Young, P. A. Absorption spectrum of Ba I in the region of autoionization from 2382 to 1700 Å. *Phys. Rev. A* **2**, 643–648 (1970).
- [130] van Leeuwen, R., Ubachs, W. & Hogervorst, W. Autoionization of low-lying 5dng states in barium. *Journal of Physics B: Atomic, Molecular and Optical Physics* **27**, 3891 (1994).
- [131] Johnsen, R., Brown, H. L. & Biondi, M. A. Ion–molecule reactions involving N_2^+ , N^+ , O_2^+ , and O^+ ions from 300°K to ~ 1 eV. *The Journal of Chemical Physics* **52**, 5080–5084 (1970).
- [132] Spears, K. & Fehsenfeld, F. Termolecular Association Reactions of Mg, Ca, and Ba Ions. *J. Chem. Phys* **56**, 5698–5705 (1972).
- [133] Armentrout, P. & Beauchamp, J. Experimental and theoretical studies of the reaction $\text{Ba}^+(\text{D}_2, \text{D})\text{BaD}^+$: sequential impulse model for endothermic reactions. *Chemical Physics* **48**, 315 – 320 (1980).
- [134] Drewsen, M., Brodersen, C., Hornekaer, L., Hangst, J. S. & Schiffer, J. P. Large ion crystals in a linear paul trap. *Physical Review Letters* **81**, 2878 (1998).
- [135] Liang, J. & Haljan, P. C. Hopping of an impurity defect in ion crystals in linear traps. *Phys. Rev. A* **83**, 063401 (2011).

- [136] Shimshoni, E., Morigi, G. & Fishman, S. Quantum zigzag transition in ion chains. *Phys. Rev. Lett.* **106**, 010401 (2011).
- [137] Schiffer, J. P. Phase transitions in anisotropically confined ionic crystals. *Phys. Rev. Lett.* **70**, 818–821 (1993).
- [138] Piacente, G., Schweigert, I. V., Betouras, J. J. & Peeters, F. M. Generic properties of a quasi-one-dimensional classical wigner crystal. *Phys. Rev. B* **69**, 045324 (2004).
- [139] Rajaraman, R. *Solitons and instantons : an introduction to solitons and instantons in quantum field theory / R. Rajaraman* (North-Holland Pub. Co. ; sole distributors for the USA and Canada, Elsevier Science Pub. Co., Amsterdam ; New York : New York, N.Y. :, 1982).
- [140] Braun, O. M. & Kivshar, Y. S. *The Frenkel-Kontorova model: concepts, methods, and applications* (Springer-Verlag, Berlin, 2004).
- [141] Carter, S. J., Drummond, P. D., Reid, M. D. & Shelby, R. M. Squeezing of quantum solitons. *Phys. Rev. Lett.* **58**, 1841–1844 (1987).
- [142] Drazin, P. G. & Johnson, R. S. *Solitons : an introduction / P.G. Drazin, R.S. Johnson* (Cambridge University Press, Cambridge [England] ; New York :, 1989).
- [143] Frenkel, J. & Kontorova, T. *Phys. Z. Sowjet.* **13** (1938).
- [144] Braun, O. M. & Kivshar, Y. S. Zigzag kinks in the frenkel-kontorova model with a transversal degree of freedom. *Phys. Rev. B* **44**, 7694–7697 (1991).
- [145] Braun, O., Chubykalo, O., Kivshar, Y. S. & Valkering, T. The Frenkel-Kontorova model with a transverse degree of freedom: kinks structures. *Physica D: Nonlinear phenomena* **113**, 152–156 (1998).
- [146] Landa, H. *Coherence properties of discrete static kinks*. Master’s thesis, Tel Aviv university (2009).
- [147] Wallraff, A. *et al.* Quantum dynamics of a single vortex. *Nature* **425**, 155–158 (2003).
- [148] Eisenberg, H. S., Silberberg, Y., Morandotti, R., Boyd, A. R. & Aitchison, J. S. Discrete spatial optical solitons in waveguide arrays. *Phys. Rev. Lett.* **81**, 3383–3386 (1998).
- [149] Rosenbluh, M. & Shelby, R. M. Squeezed optical solitons. *Phys. Rev. Lett.* **66**, 153–156 (1991).
- [150] Trombettoni, A. & Smerzi, A. Discrete solitons and breathers with dilute bose-einstein condensates. *Phys. Rev. Lett.* **86**, 2353–2356 (2001).
- [151] Cirac, J. I. & Zoller, P. Quantum computations with cold trapped ions. *Physical Review Letters* **74**, 4091 (1995).

- [152] Wineland, D. J. *et al.* Experimental issues in coherent quantum-state manipulation of trapped atomic ions. *Journal of Research of the National Institute of Standards and Technology* **103**, 259–328 (1998).
- [153] Wineland, D. J. Quantum information processing and quantum control with trapped atomic ions. *Physica Scripta* **2009**, 014007 (2009).
- [154] Haeffner, H., Roos, C. F. & Blatt, R. Quantum computing with trapped ions. *Physics Reports* **469**, 155 (2008).
- [155] Schmitz, H. *Über Quantensimulationen in einer linearen Paul-Falle*. Ph.D. thesis, Fakultät für Physik, Ludwig-Maximilians-Universität München (to be submitted).
- [156] Herskind, P. F., Dantan, A., Marler, J. P., Albert, M. & Drewsen, M. Realization of collective strong coupling with ion coulomb crystals in an optical cavity. *Nat Phys* **5**, 494–498 (2009).
- [157] Lee, K. F., Villeneuve, D. M., Corkum, P. B., Stolow, A. & Underwood, J. G. Field-free three-dimensional alignment of polyatomic molecules. *Physical Review Letters* **97**, 173001 (2006).
- [158] El-Batanouny, M. & Wooten, F. *Symmetry and Condensed Matter Physics, Landau's theory of phase transitions* (Cambridge University Press, 2008).
- [159] Dziarmaga, J. & Rams, M. M. Dynamics of an inhomogeneous quantum phase transition. *New Journal of Physics* **12**, 055007 (2010).
- [160] Zurek, W. H. Causality in condensates: Gray solitons as relics of BEC formation. *Phys. Rev. Lett.* **102**, 105702 (2009).
- [161] Küpper, J., Filsinger, F. & Meijer, G. Manipulating the motion of large neutral molecules. *Faraday Discussions* **142**, 155–173 (2009).
- [162] Junglen, T., Rieger, T., Rangwala, S. A., Pinkse, P. W. H. & Rempe, G. Two-dimensional trapping of dipolar molecules in time-varying electric fields. *Phys. Rev. Lett.* **92**, 223001– (2004).
- [163] Wall, T. E. *et al.* Transport of polar molecules by an alternating-gradient guide. *Physical Review A* **80**, 043407 (2009).
- [164] Englert, B. G. U. *et al.* Storage and adiabatic cooling of polar molecules in a microstructured trap. *PRL* (2011).
- [165] Junglen, T., Rieger, T., Rangwala, S. A., Pinkse, P. W. H. & Rempe, G. Slow ammonia molecules in an electrostatic quadrupole guide. *The European Physical Journal D - Atomic, Molecular, Optical and Plasma Physics* **31**, 365–373 (2004).
- [166] Willitsch, S., Bell, M. T., Gingell, A. D., Procter, S. R. & Softley, T. P. Cold reactive collisions between laser-cooled ions and velocity-selected neutral molecules. *Physical Review Letters* **100**, 043203 (2008).

- [167] Wester, R. Radiofrequency multipole traps: tools for spectroscopy and dynamics of cold molecular ions. *Journal of Physics B: Atomic, Molecular and Optical Physics* **42**, 154001 (2009).

Acknowledgements

These pages are dedicated to the people who helped making this work a success.

I want to thank Prof. Dr. T. Schätz for giving me the opportunity to be part of such an interesting field of research. His encouragement and support was always there when I needed it the most. I greatly appreciate his ability to be a boss, a post-doc, a supervisor and a friend in one person.

I want to thank Dr. S. Kahra. With him, I had the best partner one can have when starting a new research project. We joined countless hours in the lab and shared many of the most exciting moments during our time at the MPQ. I really appreciated his expertise and friendship.

I want to thank M. Kowalewski and Prof. Dr. R. de Vivie-Riedle for their great theoretical support during this work.

Thanks to my dear colleagues and friends that are or have been part of the group for their help and for making the years at MPQ such a wonderful time: M. Enderlein, H. Schmitz, Dr. A. Friedenauer, C. Schneider, T. Huber, M. Mielenz, R. Matjeschk, Dr. M. Albert, J. -Glückert, L. Petersen, C. Kerzl, S. Düwel, J. Ströhle, T. Dou, A. Steyer and the associated group members and group lunch participants: Prof. Dr. T. Hasegawa (thanks for helping with the barium paper), Dr. W. Schmid (A big thank you for building the ESI-source with me), Dr. W. Fuß, C. Hahn and B. Englert

I also want to thank: All the members of the group of Prof. Dr. G. Rempe for their support and in particular Prof. Dr. P. Pinkse for answers to a lot of questions. The staff of technicians who always had a good solution to a technical problem. J. Bayerl for making the technical drawings of the vacuum apparatus.

Thanks to T. Strobl and his team at the MPQ-Werkstatt for a fabulous job when building the parts for the experiment and for dealing with all the urgent requests.

I want to thank my colleagues of the group of Prof. Dr. F. Krausz and Prof. Dr. R. Kienberger for so much support with issues of the laser and the beamline, especially E. Bothschafter, Dr. A. Schiffrin and Dr. R. Ernstorfer.

Thanks to all of my fiends at LMU and MPQ for a lot of nice coffee breaks.

Thanks to all members of IMPRS-APS for years of fun, especially M. Wild for dealing with all the "impossible" issues and the coordinators Prof. Dr. T. Schätz, Prof. Dr. M. Kling and Dr. P. Hommelhoff.

I want to give a special thank you to my family. A lot of love and support from my parents, my brother and from S. Paché did make this project possible.
